Macro-Scale Lithium-Ion Battery Simulation by Means of the Finite Element Method and Concentrated Solution Theory

by

Cameron James Fenske

A thesis submitted in partial fulfillment of the requirements for the degree of

Master of Science

Department of Mechanical Engineering
University of Alberta

Abstract

Lithium-ion batteries are the leading contender for high density energy storage for applications such as electric vehicles and personal electronic devices. While they promise well over 4 V of potential per cell, actually realizing such high voltages is quite difficult, given the many modes of energy loss during discharge. One dominant loss, especially at high currents (e.g., fast-charging) is losses due to ionic transport in the electrolyte.

Mathematical models and their computational implementation have been used to simulate Lithium-ion battery discharge to better understand its complex physics and to optimize its design. Because of the complex and dynamic nature of Lithium-ion batteries, these models are transient and highly non-linear. A difficulty arises in that the scales on which key physics occurs varies over many orders of magnitude, meaning simulations often decouple scales to some degree to conserve computational resources.

In this thesis, a transient and non-linear numerical model is developed for the lithium-ion battery macro-scale, that is, the scale on which heterogeneities due to microscopic components can be ignored. Additionally, the electrolyte is studied separately by isolating the separator contribution by modelling a symmetric Li-foil cell. The numerical model is supported by a rigorous set of mathematical derivations for the governing equations. This process utilizes concentrated solution theory and the finite element method.

First the symmetric cell system is verified by reproducing the voltage response to a constant current step reported from experiments in the literature. A sensitivity analysis is performed for the electrolyte characteristics and discussed in terms of their

influence on cell performance. After concluding that the electrolyte model accurately reproduces the real-world system, the model is applied to a novel electrolyte for which no previous numerical modelling has been performed. It is concluded that the experimental results do not match what is expected from the model, due to the non-reproducibility of the experimental data.

The full macro-scale battery model is analyzed in terms of its voltage response and solution variable profiles during a constant current discharge. Following a study of the cell's hysteresis, the battery's capacity and efficiency are calculated. Another sensitivity analysis provides insight into the importance of the active material's characteristics on cell performance. Finally, running the battery at different current densities confirms that increasing the rate of cell charge/discharge will negatively impact the efficiency of the system.

Keywords: Lithium-ion battery, Numerical simulation, Macro-scale, Electrolyte, Finite element method, Concentrated solution theory

Preface

This thesis is an original work by Cameron James Fenske. No part of this thesis has been previously published.

"So we fix our eyes not on what is seen but what is unseen. For what is seen is temporary but what is unseen is eternal."

-2 Corinthians 4:18

Dedicated to my lovely wife, Tiana: who reminds me that beauty is more than just an equation.

Acknowledgements

I would like to offer my deepest thanks to my primary supervisor, Dr. Marc Secanell. His guidance, support, collaboration, and example were paramount for my research and I would probably still be wondering what an electrolyte was without him. It is rare to meet such a person as Dr. Secanell, let alone to have as a supervisor, whose passion for learning so obviously permeates all he does and even manages to percolate down to those whom he supervises.

I would also like to thank my co-supervisor, Dr. Ge Li, for her collaboration, resources, and time. Thank you to Pengcheng Li of the MACE Lab for providing the experimental results in section 3.1.2. Also, I thank all of my colleagues in the Energy Systems Design Laboratory. In particular Aslan Kosakian, Mohamad Ghadban, and Micheal Moore for their knowledge, time, and investment in my work.

Finally, I thank the Lord Jesus: For from Him and through Him and to Him are all things. To Him be glory forever. Amen.

Table of Contents

List of Tables

List of Figures

List of Symbols

Constants

F	Faraday's constant	96 485 C/mol
k_B	Boltzmann's constant	$1.38{\cdot}10^{-23}$ J/K
R	Ideal gas constant	8.314 J/(kg · K)

Latin

a_i	Activity of ionic species	–
A_v	Interficial area per unit volume	m^2/m^3
C_{dl}	Volumetric double layer capacitance	F/m^3
c_i	Concentration of ionic species	M
c_T	Total concentration	M
D	Measurable electrolyte diffusion	m^2/s
$\mathscr{D}_e$	Salt diffusion coefficient	m^2/s
$\mathcal{D}_i$	Ionic self-diffusion coefficient	m^2/s
D	Diffusion coefficient in dilute solution theory	m^2/s
$\mathscr{D}_{ij}$	Ionic mutual diffusion coefficient	m^2/s
D_s	Diffusion in solid phase	m^2/s
E^{eq}	Equilibrium voltage	V
f_{+-}	Molar activity of ionic salt	–

$\mathbf{i}$	Current density	$\mathrm{A/m^2}$
i_{eq}	Equilibrium current density	$\mathrm{A/m^2}$
i_{ref}	Li-foil reference exchange current density	$\mathrm{A/m^2}$
$i_{ref,c}$	Cathode active material reference exchange current density	$\mathrm{A/m^2}$
k_i	Reaction rate constant	variable
K_{ij}	Frictional coefficient between species i and j	$\mathrm{J \cdot s/m^5}$
M_i	Molar mass of species i	mol/kg
m_i	Molality of ionic species i	mol/kg
N	Number of degrees of freedom for spatial discretization	–
N	Number of distinct species in solution	–
n	Moles of electrons transferred per mole of Lithium	–
n	Number of equations in system	–
$\boldsymbol{N}_i$	Flux of ionic species i	$\mathrm{mol/(m^2 \cdot s)}$
r_i	Reaction rate for species i	$\mathrm{mol/(m^3 \cdot s)}$
r_{ref}	Reaction rate at the reference state equilibrium	$\mathrm{mol/(m^3 \cdot s)}$
S_i	Source term for species i	$\mathrm{A/m^3}$
T	Temperature	K
t	Time	s
t_i	Transport number for species i	–
t_i^0	Transference number for species i	–
U	Open-cell voltage of electrode with $\mathrm{Li/Li^+}$ reference electrode	V
u	Ionic mobility	$\mathrm{m^2/(s \cdot V)}$
$\bar{v}_i$	Specific volume of species i	$\mathrm{m^3/mol}$

$\mathbf{v}_i$	Average velocity of species i	m/s
z_i	Ionic charge	–

Greek

α	Li-foil charge-transfer coefficient	–
α_c	Cathode active material charge-transfer coefficient	–
γ_i	Molal activity coefficient	kg/mol
δ	Cell thickness	m
δ_c	Cathode layer thickness	m
ϵ	Volume fraction of pore	–
ϵ_s	Volume fraction of conductive phase	–
ϵ_{AM}	Volume fraction of active material	–
θ	Ratio of filled reaction sites to saturation	–
κ	Measurable conductivity of electrolyte phase	S
$\lambda_i^{\ominus}$	Property expressing secondary reference state for species i	–
$\bar{\mu}_i$	Electrochemical potential of species i	J/mol
μ_i	Chemical potential of species i	J/mol
ν_i	Stoichiometric prefactor in ionic salt for species i	–
σ_s	Conductivity of the solid phase	S
ϕ_m	Quasi-electrostatic "solution-phase" potential	V
ϕ_R	Solid potential of a reference electrode	V
ϕ_s	Solid potential of a porous electrode	V
ϕ_{sp}	Solid potential of a planar electrode	V
ρ	Charge density	C/cm^3

Sub/Superscripts

$+$	Cation
$-$	Anion
0	Solvent
$\ominus$	Reference state
e	Ionic salt pair
e^-	Corresponding to an electron
Li^+	Lithium ion
$Li_{(s)}$	Solid Lithium
P	Product in Butler-Volmer reaction
R	Reactant in Butler-Volmer reaction
R	Reference electrode
ref	Concentrations at reference
s	Solid phase
sat	At saturation

Abbreviations

BC Boundary Condition.

BDF Backward Differentiating Formulae.

BV Butler-Volmer.

CST Concentrated Solution Theory.

DC Direct Current.

DEC Diethyl Carbonate.

DFN Doyle-Fuller-Newman.

DL Double Layer.

DMC Dimethyl Carbonate.

DOF Degree of Freedom.

DST Dilute Solution Theory.

EC Ethylene Carbonate.

EMC Ethyl Methyl Carbonate.

EV Electric Vehicle.

FEM Finite Element Method.

FIB-SEM Focused-Ion-Beam Scanning Electron Microscopy.

HP2D Homogeneous Pseudo 2-Dimensional.

ISE Inorganic Solid Electrolytes.

LFP Lithium Iron Phosphate.

LHS Left Hand Side.

LiB Lithium-ion Battery.

LiTFSI Lithium bis(trifluoromethanesulfonyl)imide, $LiC_2F_6NO_4S_2$.

NMC Nickel Manganese Cobalt.

NP Nernst-Planck.

OCV Open Cell Voltage.

ODE Ordinary Differential Equation.

OSM Onsager-Stefan-Maxwell.

P2D Pseudo 2-Dimensional.

PC Propylene Carbonate.

PDE Partial Differential Equation.

PEO Poly-Ethylene Oxide.

PVdF Poly(vinylidenefluoride).

RAM Random Access Memory.

RHS Right Hand Side.

SATP Standard Atmospheric Temperature and Pressure.

SEI Solid Electrolyte Interface.

SEMP Simplified Electrochemical Multi-Particle.

SHE Standard Hydrogen Electrode.

SPM Single Particle Model.

SS Steady State.

XCT X-ray Computed Tomography.

Chapter 1

Introduction

1.1 Motivation

Ever since the invention of the first battery, the Volta-pile, by Italian physicist Alessandro Volta in 1800, the world has been thrust into the age of portable electricity. With the ability to store electric energy in the form of a chemical potential for use at a later time, one now had a convenient method of harnessing raw electrical energy with the ability to use it for new and greatly diverse applications.

Whether breakthroughs in battery technology drove industrial innovation or vise versa, the emerging field of electrochemistry has produced newer and more powerful batteries, capable of keeping up with society's ever increasing demand for effective energy storage. Examples of such breakthroughs would include Gaston Planté's invention of the first rechargeable lead-acid battery in 1860 and Carl Gassner's first dry-cell in 1887. With the development of the first modern Lithium-based battery due to Whittingham, Goodenough, and Yoshino's development of porous electrode intercalation in 1974, the world was presented with the possibility of harnessing the most electronegative atom on the periodic table. Theoretically, this technology would be able to deliver over 4 V of potential; allowing for power densities that far exceed all other battery options. Additionally, Lithium-ion batteries (LiB) promise large energy densities [1], negligible self-discharge [2], good thermal stability [3], and minor hysteresis [4]. Realistically, however, the practicality of realizing those potentials in

a safe and cost effective manner has proven to be incredibly illusive. The challenges facing LiB development include the cost of materials, safety due to dendrite growth, mass transport loses, and cell expansion.

As the world today looks to green energy sources and storage techniques to assist in mitigating the global climate change crisis, a renewed conquest is being waged to finally unlock the full potential of LiBs. However, with new materials, geometries, and operating conditions emerging each day, it is neither efficient nor effective to experimentally measure all battery configurations in order to direct and streamline future research. One solution to this issue is to create a comprehensive continuum-based multi-physics framework of the battery that can be used to simulate its performance. Such a mathematical model can also be used to understand the internal characteristics of a cell in operation, which is something that is very challenging experimentally due to poor accessibility to the electrode and the micron-size thicknesses of the components. Furthermore, this framework could be computationally adapted, allowing for a "virtual twin" battery simulation for design optimization.

A suitable continuum model will accurately describe the cell's physics on both a cell-level (macro-scale) and a pore/agglomerate/particle level (micro-scale). The macro-scale physics model will track general concentration and potential profiles within all phases of each layer in the cell. Not only will a strong macro-scale model need to account for the kinetic reactions between phases, but should also consider any relevant porosity, thermal, and strain effects. On the pore/particle scale, the model must account for the composition and structure of the pores, how solid Lithium diffuses radially into the active material particles, and how Lithium intercalation may non-uniformly cover the reacting surface due a variety of mechanical factors. The two scales must be completely coupled through the dependencies of the macro-scale coefficients on the micro-scale physics, and vise versa. Additionally, a complete model will also tackle the molecular scale, with the use of either molecular or quantum theories.

Although West *et al.* [5] did propose a strictly 1D macro-scale model, currently

the most common approach to modelling LiBs is based on the pseudo 2-dimensional (P2D) formulation [6, 7], also known as the Doyle-Fuller-Newman (DFN) model. Because this model balances strong agreement to experimental results [8] with relative ease in computation (due to the micro-scale not being fully resolved), it has become the standard in the LiB modelling community. However, because the P2D model is 1-dimensional in the macro-scale, it precludes any study of multi-dimensional effects due, for example, to non-homogeneous heating of the cell (due to a short) or local changes in transport lengths (due to layer heterogeneities during manufacturing or expansion of the active material during operation). Also, the approximations made about the particles eliminates any opportunity of investigating how characteristics within the microstructure might effect cell performance on both a micro- and macro-scale. A considerable number of models have been proposed to either simplify or expand the P2D model [9–27], but few have been suggested that would lift the P2D approximations for the micro-scale altogether as well as allow for multi-dimensional macro-scale modelling. Therefore, there exists a gap in the literature for a comprehensive and streamlined approach to studying the fully-resolved physics within a LiB.

1.2 Background

Batteries work by harnessing the chemical potential of oxidation-reduction (redox) reactions and converting it into electrical energy. A redox reaction is one in which the oxidation numbers of the reactants change, which can result in either a positive or negative energy release, depending on the electrochemical potentials of the reactants versus the products. For a battery, the reaction is split into two half-cell reactions, which, when combined, create the full reaction. Batteries isolate these two half-cell reactions to separate electrodes, separated by an electrically insulating porous media in which ions can travel, and connected by an electrical circuit which allows electrons to be externally transferred between them. Therefore, unlike other redox reactions,

such as corrosion or combustion, the energy is not lost to heat but can instead be harnessed as usable electricity. Additionally, electrochemical conversion devices can be much more efficient than other methods of harnessing chemical energy, as they are not bounded by the Carnot cycle [28].

The cell is the basic building block on which battery stacks are built. They always have three main components: an anode, a cathode, and a separator. A schematic of the cell and reactions are given in Figure 1.1. The anode is the electrode at which electrons are lost through oxidation, resulting in the reacting species increasing its oxidation number. The cathode is the electrode at which electrons are received through reduction, which decreases the reacting species oxidation number. The separator is the medium between the two electrodes in which ions are transferred, but which inhibits the transfer of electrons. The separator electrolyte is often a liquid with dissolved salts, however, recently cells are being developed with solid electrolytes [29] or even molten salts [30].

Electrodes are chosen based on numerous factors, including being an effective oxidizing/reducing agent, having good conductivity and stability, the low cost of materials and fabrication, and being light-weight. For certain battery configurations, it may be advantageous to create a porous electrode, in which reactions occur volumetrically, instead of at a planar interface. The most common types of anodes being researched and actively developed are graphite, silicon-based compounds, and Lithium metal [31]. Graphite anodes work by allowing Lithium-ions to intercalate into the gaps created within the molecular structure. Graphite has the advantage of not allowing dendrites to form, however, it has a relatively low capacity compared to other options. While silicon-based anodes theoretically have a larger capacity than graphite, instead of intercalating, the Lithium-ions react with the silicon to produce an entirely new structure. This causes swelling of the anode, resulting in cracking and lost capacity after multiple charge/discharge cycles. A planar Lithium-foil anode has the largest capacity, however, it must contend with dendrite growth and higher material costs.

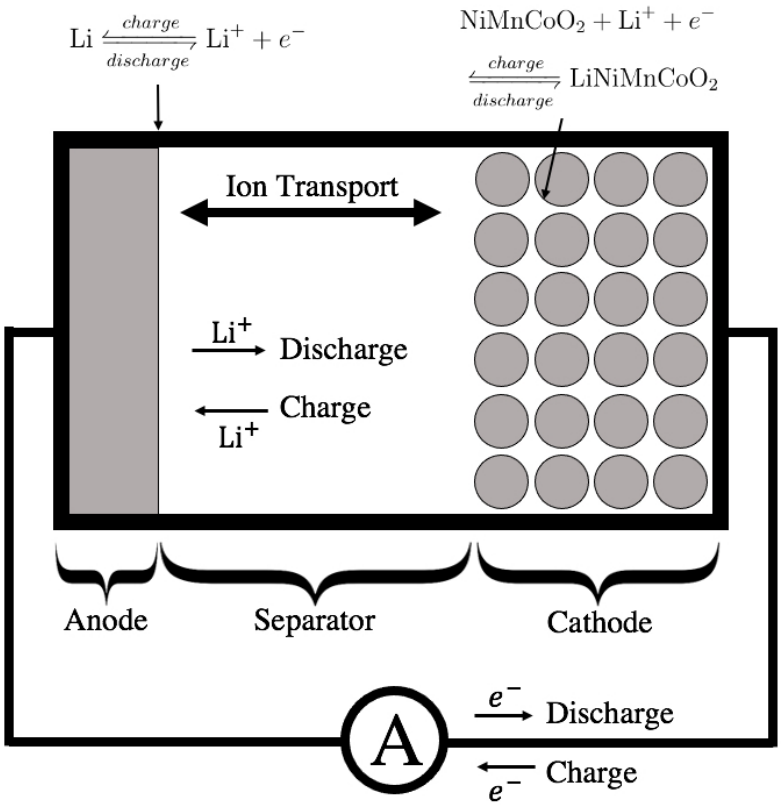

Figure 1.1: Schematic of Lithium-ion battery containing Lithium foil anode and NMC cathode.

The cathode is currently the limiting component in LiB design [32] and, therefore, dominates the research in this field. Porous electrodes contain active material particles, connected by a conductive additive and binder. During fabrication, these components are combined to create what's known as the electrode slurry. This slurry is coated onto Aluminium current collectors, dried, and compressed to create the desired porosity [33]. The reactions occur at the surface of the active material. During discharge, a free electron existing in the solid phase and a positively-charged Lithium-ion combine in a reaction site. The solid Lithium, can then diffuse inside the active material particle lattice, freeing up the surface reaction site for future reactions to occur. During charging, the opposite occurs, where Lithium atoms at the surface of the active material will split with the electron and be released into the electrolyte. The active material is a metal oxide (i.e., XO_2) in various molecular

structures, including layered oxides, spinal oxides, and polyanion oxides [34]. Two of the most common layered compositions, particularly for electric vehicle applications, are Lithium Nickel Manganese Cobalt Oxide ($LiNiMnCoO_2$, or NMC) and Lithium Iron Phosphate ($LiFePO_4$, or LFP). While both have taken significant portions of the LiB industry, they do differ and are useful for different applications. NMC has higher power densities and is less susceptible to temperature variance, whereas LFP has a higher energy density, is more cost effective, and experiences less deterioration over time, both with and without use.

A suitable electrolyte is chosen based on the criteria of being a good ionic conductor, not being reactive or easily flammable, inhibiting the growth of dendrites, and being low cost and not prone to change properties or density when heated. The types of available electrolytes include liquid electrolytes, solid polymer electrolytes, gel polymer electrolytes, solid inorganic electrolytes, and hybrid electrolytes (being a combination of the others) [35]. Liquid electrolytes dissolve an electrolyte in either an organic or aqueous solution, allowing ions to move past one another as current is passed through the cell. Organic electrolytes dissolve Lithium hexafluorophosphate ($LiPF_6$) in a mixture of organic carbonates, such as ethylene carbonate (EC) with dimethyl carbonate (DMC), propylene carbonate (PC), diethyl carbonate (DEC), or ethyl methyl carbonate (EMC) [36]. Each mixture offers its own advantages and disadvantages, and is chosen based on the situation. Polymer electrolytes have the advantage of a diminished risk of dendrite growth, however, tend to suffer from low ionic conductivities. Solid polymers generally use Lithium salts (such as LiTf, LiTFSI, LiBETI, LiClO4, and LiBOB), dissolved in Poly(ethylene oxide) (PEO). Gel polymer electrolytes, typically Poly(vinylidenefluoride) (PVdF), offer an additional option, with increased safety compared to solid polymer electrolytes, but with the downside of reduced mechanical strength (i.e. the ability to withstand physical strain). Inorganic solid electrolytes (ISE) are used for all-solid-state batteries; a promising option for increased energy and power densities, safety, and durability [37]. Finally, hybrid

electrolytes incorporate a combination of the aforementioned electrolytes to tailor the electrolyte for specific needs.

A full cell design must also account for how each component of the system will interact, which configuration the battery will take (e.g., cylindrical, button, pouch, etc.), and whether the battery is a primary (non-rechargeable) or secondary (rechargeable) battery.

During the discharge of a LiB, the Lithium-ions are created at a solid Lithium foil anode when Lithium undergoes the oxidation half-cell reaction. This reaction, given as a reduction, is,

$$\mathrm{Li}^+ + e^- \underset{discharge}{\overset{charge}{\rightleftharpoons}} \mathrm{Li}_{(s)} \tag{1.1}$$

The electrons are carried through the external circuit due to the potential difference that will develop between the two electrodes. The Lithium-ions, on the other hand, are transferred through the electrolyte separator until they react back into solid Lithium at the cathode,

$$\mathrm{Li}^+ + e^- + \Theta \underset{charge}{\overset{discharge}{\rightleftharpoons}} \mathrm{Li}_{(s)}\text{—}\Theta \tag{1.2}$$

where Θ is a reaction site in the active material. For the NMC composition, which will be used in this work, the reaction at the surface of the active material particles will be,

$$\mathrm{Li}^+ + e^- + \mathrm{NiMnCoO_2} \underset{charge}{\overset{discharge}{\rightleftharpoons}} \mathrm{LiNiMnCoO_2} \tag{1.3}$$

Each half-cell reaction has an associated potential, with respect to an arbitrary standard. Generally, this is the Standard Hydrogen Electrode (SHE), however, in this work, for reasons discussed in detail in Chapter 2, it will be with respect to a $\mathrm{Li/Li^+}$ reference electrode. Reaction (1.1) will have a half-cell potential of 0 V. The cathode half cell-potential for a NMC cathode is 4.3 V at standard atmospheric temperature and pressure (SATP) [38]. The open cell voltage (OCV) is the difference of the two half-cell reduction potentials. For NMC, at SATP and 1 M electrolyte concentration, this value is 4.3 V.

Once the cell begins to pass current, the realized voltage will always be less than the OCV, as losses will occur due to ionic transport and overpotential. The transport of Lithium-ions occurs through diffusion, being the propagation of a species from regions of high concentration to low concentration; and migration, being the response of a charged particle to an electric field. Both of these modes of transport accompanies an energy loss. Transport via convection, which is due to the bulk motion of the fluid, is not considered as the battery solvent is static. An overpotential is the step in electrochemical potential that will develop at an interface in which reactions occur and will dictate the speed and direction that the reactions proceed. The overpotential is non-reversible and will therefore decrease the cell voltage based on the current density passing through the cell.

Battery performance is generally characterized by investigating the cell discharge curve created by measuring the cell voltage as a function of the dimensionless state of charge (SOC) of the active material. The SOC of the active material during discharge can be calculated, assuming constant current and that the system is fully charged at $t = 0$, through the equation,

$$SOC(t) = 1 - \frac{\mathbf{i}}{F\delta_c\epsilon_c c_{sat}}t \tag{1.4}$$

where $\mathbf{i}$ is the current, F is Faraday's constant, δ_c is the thickness of the cathode, ϵ_c is the cathode porosity, c_{sat} is the saturation concentration of Lithium in the active material, and t is the time. Additionally, the discharge curve will be highly dependant on the current density at which the cell was run. Generally, the current is expressed in terms of a non-dimensional C-rate; a measure of the number of identical batteries that could be charged or discharged in one hour, given a constant current density. While batteries are usually rated at 1C (meaning it takes exactly one hour to discharge the battery), C-rates can cover several orders of magnitude, both larger and smaller, based on the application. The definition of C-rate is given by,

$$\text{C-rate} = \frac{\mathbf{i}(1\text{ hr})}{z_{Li^+}F\delta_c\epsilon_c c_{sat}} \tag{1.5}$$

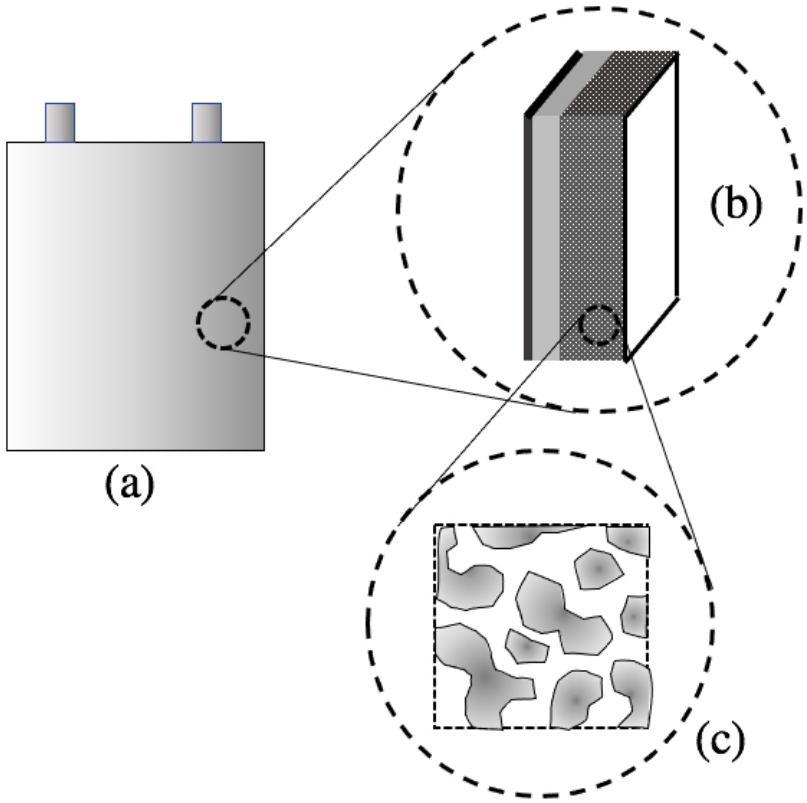

Figure 1.2: Schematic of the Lithium-ion battery at different scales, i.e., (a) battery stack level, (b) cell level (macro-scale), and (c) particle level (micro-scale).

The derivation for both equations is provided in Appendix A.1.

Because of the complexity of the battery system, its analysis and modelling has generally been divided into three spatial scales [27], as presented in Figure 1.2. Each scale will play a crucial role in increasing battery performance, decreasing cost, and maintaining safety during operation. The first level is the full battery stack. The challenges of this level are to ensure equal utilization of each cell in the stack, proper thermal management, and account for geometric constraints. The middle scale, referred to as the macro-scale, corresponds to the continuum mechanics within a single cell. It is concerned with electrode and separator dimensions, electrolyte transport, and spatial variances in concentration and potential, neglecting local heterogeneities. The third scale is the particle level, or micro-scale. This scale concerns individual

active material particles in the cathode and the reactions and solid diffusion within them. It is small enough to assume macro-scale concentration and potential variances are constant and only consider local heterogeneities. Theoretically, there are smaller scales, including molecular and quantum scales, however, these will be left out of this discussion because they are not usually included in battery models and are not investigated in this work.

1.3 Literature Review

This section will provide a brief overview of the literature pertaining to the simulation of Lithium-ion batteries. It will highlight the direction of research, the challenges faced, the common approaches, and any perceived gaps.

First, this review will investigate the models used to simulate a Lithium-ion battery, progressing from heaviest computational expense, to least. Then, a closer investigation will be provided for the homogenized method, outlining previous works and their results. Finally, this review will investigate the use and verification of the concentrated solution theory in LiB simulation.

1.3.1 Electrochemical Models

The performance of a Lithium-ion battery is the result of the interdependent physics operating on vastly different time and length scales. Being able to create a mathematical abstraction of the the holistic system is necessary for understanding the interdependent multi-physics better and for allowing accurate predictions that can supplement and guide experimental research. At the smallest level are atomistic/quantum models, which describe the individual nano-scale interactions within a very small locality and for very short time-scales [39–43]. These scales can provide important information but are not usually included in a full battery model due to the unrealistic fidelity that they would entail. By representing the discrete ions and atoms on a continuum, one can model battery performance on larger time and length scales.

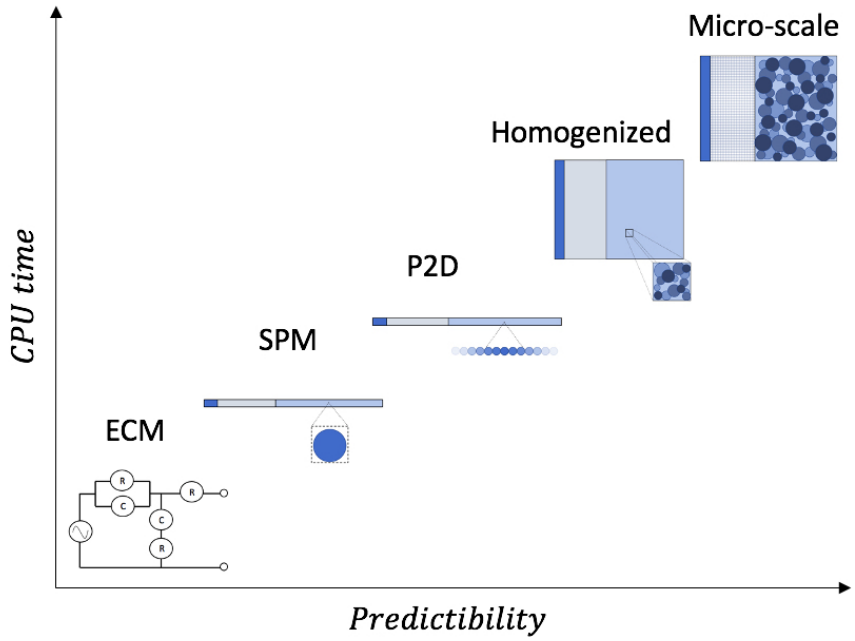

Figure 1.3: Electrochemical models presented in terms of their predictability versus computational time.

On the other extreme are full battery stack models [22, 44–48] and techno-economic models that predict the utilization and degradation of batteries over the span of many years [22]. While models on every scale are important for understanding the battery physics fully, this work will be concerned with modelling the electrochemical system within a single cell.

The compromise that is made when modelling any system is between the degree of accuracy required versus the resulting computational time and resources. Therefore, electrochemical battery models can be arranged in terms of the degree of fidelity to which they are resolved. The various models discussed in this section are presented, from most to least computationally laborious, as outlined in Figure 1.3 [27].

The most complex model, short of resolving the atomistic scale, is known as the micro-scale model [49–51]. This model captures the entire cell domain, yet with a fine enough mesh to model the individual microscopic components, which can be on the order of microns, hence the name. In order for the potential of this model

to be fully realized, an accurate 3D representation of the micro-structure must be obtained. Researchers have used various imaging techniques to recreate the micro-structure, such as X-ray Computed Tomography (XCT) [52] and Focused-Ion-Beam Scanning Electron Microscopy (FIB-SEM) [53]. In the micro-scale model, transport is fully resolved within the porous media, including intercalated Lithium and electron transport in the solid material and electrolyte transport in the pores. The reactions are modelled in the electrodes at the interface between the electrolyte and active material. Because this model is fully resolved, there is no requirement to specify porosity, tortuosity, or effective transport parameters because they are already accounted for through the use of an accurate geometry. Since the micro-scale model is the highest fidelity model, it will provide results closest to reality and can therefore be used for situations where the assumptions made in simpler models will not apply. This includes complicated micro-structures and cell geometries, cases where the micro-structure changes throughout the domain, and the allowances for other battery phenomena to be studied, such as active material cracking. However, this model is extremely computationally demanding, meaning it is unrealistic for most applications, and it requires the accurate micro-structure recreation, which can be very difficult to obtain. Therefore, a simplification to the micro-scale model that will drastically decrease computational resources, while maintaining a significant degree of accuracy, was developed, called the homogenized model.

The homogenized model relies on the observation that most solution variables, when solved using the micro-scale model only change substantially over large length scales (i.e. at the cell-level). Therefore, this model treats the porous media as two over-lapping continua, instead of distinct pore and particle domains. As such, heterogeneities at the microscopic level are neglected, allowing for a much courser mesh and lower computational cost than the micro-scale model. This simplification has three results: first, the gradients in solution variables are no longer calculated at each point but instead averaged over the microscopic domain to describe cell level driving

forces. Second, certain parameters that describe transport will be described in terms of their "effective" value, that is, the value accounting for the porosity and tortuosity of the porous layer. Third, the reactions will no longer be described at the interface between the active material and electrolyte, but instead as a volumetric source term, given the active area per unit volume of the porous media. An issue arises, however, in that the diffusion of intercalated Lithium within the active material is very slow, resulting in substantial gradients within each microscopic particle. Therefore, the concentration of solid Lithium cannot be extended to a volume averaged property. The homogenized model is therefore split into two: the macro-scale model and a representative micro-scale model. The macro-scale model is the continuum based model previously discussed, that governs the cell-level variances in the electrolyte concentration and electric potential. The micro-scale model component is a high fidelity simulation, calculated at each point in the macro-scale domain, in which the micro-structure is fully resolved for a representative volume, given the values of the macro-scale variables at that location. Two methods for coupling these scales are predominant. First, both scales can be resolved simultaneously by concurrently solving the governing equations and transferring the state variables between them in real time [54, 55]. Or alternatively, the surrogate coupling method could be employed which would involve preprocessed micro-scale solutions that are stored in a database and looked up during macro-scale simulation [56]. While the surrogate coupling method reduces computational time, it assumes quasi-static conditions, which is not strictly appropriate for temporal simulations. The representative volume is either, like the micro-scale model, obtained through advanced imaging techniques or it can be artificially recreated based on theory and containing all the features of a real electrode [57–60], i.e., volume fractions, length-scales, and particle shapes. Because the representative volume can be much smaller than the actual volume it represents, this coupled model will have a significant decrease in computational time and cost, regardless of the method used to obtain the micro-structure. The homogenized model

is advantageous because it drastically decreases computation while still allowing for 3D effects at the cell and particle levels to be considered. Disadvantages of this model are that, unlike the micro-scale model, clear and accurate estimations of the effective parameters are necessary for a quality model. Many relations exist for how these parameters can be obtained (such as the Bruggeman correlation which is discussed later), however, it has been concluded that these are highly dependent on the micro-structure and therefore must be reconsidered for each new porous media. Also, for certain applications/geometries in which the fidelity of the homogenized model is not necessary, further simplification can be made. The predominant simplification made is the P2D, or DFN, model.

The pseudo 2-dimensional model, which was originally conceptualized well before the homogenized model [7, 61, 62], can be derived from the homogenized model, given certain simplifications. The main labours of the homogenized model include the resolving of the micro-structure at each location and the use of a 3D geometry. The P2D model assumes one-dimensional cell-level physics only and models intra-particle diffusion using a generic spherical particle. As a result, both major computational costs from the homogenized model are by-passed. The radius of the representative spherical particle describes the diffusion within the active material and constitutes the "pseudo" dimension. Unlike the previous model, the P2D model does not account for the actual micro-structure but instead merely fits the particle radius and porosity to experimental observations. This concept expanded upon the West *et al.* model in which the intra-particle solid Lithium concentration gradients were ignored and the reaction term was instead based off of an experimentally determined correlation with the average solid Lithium concentration [5]. Because of the relative ease in computation for the P2D model and the accuracy at which is captures the battery performance, this model has become the most popular physics-based model for Lithium-ion batteries. The open-source P2D program, *Dualfoil*, which has since become the standard for all other battery simulations [63], was the first computational

model to account for the micro-scale intercalation, and as a result had a significant increase in battery predictability. The P2D concept has also been the framework on which many extended models have been built to account for additional battery complexities (i.e., stress-strain effects, thermal heating and the solid electrolyte interphase (SEI)) [20, 44, 45, 61, 64–88]. Additionally, various groups have extended the P2D model to multiple dimensions using various techniques [16, 32, 89–94].

The most common simplification of the P2D model is the single-particle model (SPM) [9]. The SPM works on a similar principle as the P2D model, in that the diffusion of the solid Lithium radially constitutes the pseudo dimension. However, the SPM differs based on its treatment of the spatial macro-scale dimension. In this model, the variability in SOC of each representative particle is assumed equal, effectively requiring only a single particle to describe the Lithium diffusion throughout the porous electrode. This also means that the reaction rate at all locations in the electrode will be the same, which completely decouples the two phases from one another. The SPM's treatment of the electrolyte varies, depending on the degree of accuracy required. Certain formulations will still spatially resolve the electrolyte according to CST, others will resolve the electrolyte according to DST, and still others will neglect to resolve the spatial variations in the electrolyte properties altogether. Because the SPM model decouples the two phases, it will result in even faster simulations than the P2D model, however, the major simplifications assumed in its formulation will restrict its usage to a very narrow range of applicability, i.e., for applications in which a low level of accuracy is acceptable. One application in which the SPM model returns comparable results, however, is for cases with very thin electrodes and low current densities, as there will not be much spatial variation in active material particles anyway [10]. Another common simplification to the P2D model is the ohmic-porous electrode model, in which the spatial variation in potential is considered and the variation in concentration is disregarded for both the solid and electrolyte phases [11, 12]. While this can be particularly useful when trying to op-

timize electrode dimensions and porosity [13, 62], this simplification is only valid for systems in which mass-transport losses will be minimal (i.e. for thin electrodes and non-viscous electrolytes). An intermediate step between the ohmic porous-electrode model and the P2D model is to use polynomial expressions for the concentration profiles. This expands the usefulness and accuracy of the approximation while retaining quick simulation times [14–16].

Finally, the fastest and least physical method is to model the Lithium-ion battery using an empirical model. The most common approach is to create an equivalent circuit model (ECM) with fitted parameters based on previous experimental observation [95, 96]. Because this model is void of any physical grounding, it is only useful for quickly returning results within the range of its parameterization and, therefore, cannot be used for any novel chemistries, operating conditions, or battery configurations [97].

Each model is important for different applications. It would be irresponsible to use a full micro-scale model when only rough estimates are required and likewise, very unhelpful to use an empirical model when trying to understand the underlying physics during cell discharge. Therefore, there must be research directed into each level of model fidelity, tailored for the relevant application. As this work will focus on the homogenized model implementation, a closer investigation of its implementation be presented in the next section.

1.3.2 Homogenized Model Implementation

Three instances of the implementation of the homogenized model have been identified in the literature. These instances will be discussed in this section.

Kashkooli *et al.* used the homogenized model to study LFP cathode performance under high current densities [54]. It was noted that the P2D model was insufficient at predicting the experimentally observed performance drop because of the substantial influence of the micro-structure on cell behaviour at high current densities [98–101].

Kashkooli *et al.* used XCT to image the 3D LFP micro-structure and virtually recreated its digital twin, saturated with a 1 M $LiPF_6$ electrolyte. The macro-scale was modelled using the 1-dimensional CST formulation. Therefore, this model was only useful for geometries with unidirectional macro-scale transport. These two scales were coupled using state variables, passed iteratively between the two scales until a reasonable threshold was achieved. Their simulation was solved using COMSOL Multiphysics®. Kashkooli *et al.* observed that their homogenized model was considerably more accurate at modelling battery performance compared to the standard P2D model. This was especially noticeable when modelling the method and time-scale of cell failure. Additionally, the homogenized model was more accurate at predicting the spatial SOC within the cathode, noting that there exists larger disparity in solid Lithium concentration within each micro-scale representative volume than was accounted for in other models. Their model provided insight into how the micro-structure effects cell performance, however, because it was developed in 1D only and on a commercial software, it does not allow for complicated macro-scale geometries or the opportunity for other groups to expand upon their model.

Kim *et al.* also used the homogenized model approach to study LFP performance [55]. They used FIB-SEM to reconstruct the representative micro-structure which they implemented into COMSOL Multiphysics®. The macro-scale was modelled in 1D with a $LiPF_6$ in EC-DMC electrolyte, treated with CST. Their simulation also incorporated thermal and mechanical models. Kim *et al.* observed that larger concentrations and concentration gradients were observed at the surface of the particle than at the particle's center. These observances were magnified for larger C-rates. They concluded that higher temperatures and larger C-rates also induce larger stresses on the active material particles. They observed a relationship between capacity fade in particles that were about to crack.

Finally, Du *et al.* created a generic homogenized model, not specific to any particular cathode or electrolyte composition [56]. Unlike the previous two instances

of the homogenized model, Du *et al.* created an artificial micro-structure based on theory, and connected the two through a surrogate coupling. Contrary to Kashkooli *et al.* and Kim *et al.*, Du *et al.* did not observe significant cell performance dependence on the solid Lithium distribution within the active particles and likewise, did not observe much advantage to using the homogenized model over the standard P2D model. While this model offers a unique method of coupling the two scales, which was proven to greatly reduce computational time, it returned conclusions that were contrary to what has been both experimentally and numerically observed. Unfortunately, this work was neither applied to a specific battery configuration nor validated with experiments or with other homogenized models.

Based on this review, it is concluded that the process taken by Kashkooli *et al.* and Kim *et al.* would be used, in which the representative micro-structure is obtained from advanced imaging techniques and the two scales would be coupled directly, instead of through the use of a surrogate coupling. It is also recognized that the homogenized models in this review have not been implemented in three macro-scale dimensions; a characteristic advantage of this model. Therefore, this work will create a framework from which a homogenized model can be developed in three macro-scale dimensions and that is open-sourced, allowing others to expand upon it. Each of these model instances were concerned with the accurate capturing of the micro-scale components and as such, did not consider the importance of the electrolyte on cell performance. The next section will investigate works that have sought to verify the electrolyte adherence to CST in a LiB application.

1.3.3 Concentrated Solution Theory Validation

The modelling of electrolyte transport is paramount in this work. Reference [102] concludes that the formulation concerning transport in dilute solutions falls apart at Lithium-ion concentrations of 0.81 M, and that beyond that, at concentrations in which LiBs tend to operate, a new concentrated solution theory (CST) is required.

Therefore, a literature overview is provided pertaining to the use and validation of the electrolyte models governed by CST.

Numerous studies have been conducted with the intention of parameterizing the transport properties that characterize LiB electrolytes. These studies either attempted to derive the parameterizations from first principles [103, 104] or merely conceded that the physics is too intricate to dissect and, therefore, only gave polynomial fits to experimental data, void of any physical significance [105]. While the former is helpful insofar as to understand the nature of electrochemistry, it has proven difficult to explain and predict experimental observation based solely on first-principles. On the other hand, the latter approach offers trivially accurate approximations to experimentation, however, it fails to predict untested conditions. Another downfall of polynomial fitting is that disagreements may arise based simply on the researchers choice of trend fitting.

Regardless of the choice of parameterization, the issue is that few researchers have validated their model to experimental conditions before introducing more complex components, such as porous electrodes. As a result, the range of applicability of CST is not well understood. A major exception to this trend is the work by Pesko *et al.* in their characterization of the LiTFSI salt in PEO [105]. Pesko first parameterized the relevant electrolyte transport properties and implemented them into a 1D symmetric cell model based on CST. They then ran their model on a symmetric Li-foil cell, passing it through charge and discharge cycles. The results were then compared with experiments conducted under the same conditions. They observed that the model exhibited excellent agreement with experiments for low current densities. At higher densities, it was concluded that results deviated from experimental data due to the influence of more complex phenomena, such as convection and/or dendrite formation.

Lundgren *et al.* also provided a brief experimental validation for their parameterization of a $LiPF_6$ salt in EC:DEC (1:1 by weight) [106]. Unlike Pesko *et al.*, Lundgren provided parameterizations against concentration as well as temperature,

and was able to match relaxation profiles for a Li-foil symmetric cell with those from experiments. Lundgren also compared a model in which the coefficients were derived from first principles with one in which they were merely fitted to data. They concluded that, although the scientifically derived values were less accurate, they were still within error of the experiments and provided confidence in the underlying principles governing transport in concentrated solutions. Lundgren's work, however, described the electrolyte in a much narrower range of concentrations compared to Pesko ($0.5 - 1.5M$ compared to $0.47 - 3.78M$).

The literature aiming at understanding the validity and behaviour of the CST model used to predict the ionic transport in the electrolyte of a LiB has been quite minimal. Furthermore, a sensitivity analysis on the impact of individual physical model coefficients on electrolyte potential and Lithium-ion concentration profiles, as well as cell performance, has not yet been performed.

1.4 Objectives

The objective of this work is to develop a macro-scale continuum based LiB model using FEM and the OpenFCST framework, incorporating a validated CST-based electrolyte model.

Based on the literature review in Section 1.3, the following areas have been identified as gaps in the literature:

- While many studies have parameterized the characteristics of a LiB electrolyte, few have implemented them into a computational framework to verify the applicability of the CST theory. Further, no work has been identified that performs a sensitivity analysis for these parameterizations to discuss their individual impact on cell performance.

- Most CST models in the literature are in 1D; however, a FEM implementation, including a detailed validation, has not yet been provided.

- Many groups have developed full LiB computational models with varying levels of simplification. There exists, however, a gap for a model that couples the 3D macro-scale with a fully-resolved micro-scale.

As a result of these gaps, the following objectives have been defined for the scope of this thesis:

- Create a succinct derivation of the CST governing equations, applied to the electrolyte in an LiB. These equations will then be implemented into the Open-FCST framework using FEM and validated with experimental observations. This electrolyte model will then be used to perform a sensitivity analysis on the influence of the electrolyte characteristics.

- The CST-based model above will then be extended to achieve a volume-averaged, continuum macro-scale LiB model. This model will also be computationally implemented and the results discussed, acting as a precursor to a fully coupled LiB model.

1.5 Outline

The current chapter introduces the motivation for commencing a study of the macro-scale LiB model and specifically the electrolyte. It outlines the current intellectual topography in this field and identifies several gaps in the literature, in particular, the lack of a well-validated, multi-dimensional CST-based electrolyte model and it's multi-dimensional implementation into a full macro-scale battery framework. Finally, this chapter outlines the objectives of the project and the means by which they will be tackled.

Chapter 2 will describe the two systems being modelled in detail: the symmetric cell and macro-scale battery. For each system, this chapter will give a description of the problem being solved along with any assumptions, provide a detailed derivation and summary of the governing equations, and discuss the appropriate boundary

conditions. Then, the input parameters will be discussed, including their physical significance and cited parameters. Finally, this chapter will describe how these equations can be implemented into the computational framework using FEM.

Chapter 3 will provide results for both systems being analyzed. Beginning with the symmetric cell analysis, the model will first be validated by comparison to experimental observation. Then, a parametric analysis will be performed and discussed. Lastly, the electrolyte model will be applied to an electrolyte for which a computational model has not yet been implemented, and the results discussed. For the macro-scale model, the results of a charge/discharge cycle will be discussed, in terms of the discharge curve profile, hysteresis, and transient solution variable profiles. Additionally, a parametric study of the current density, solid conductivity and diffusivity, and exchange current density will be performed and the cell efficiency discussed.

Chapter 4 will then give a brief summary of the work that has been done in this thesis, the conclusions that were reached, and this work's contribution to the literature. It will also provide suggestions for future work.

Chapter 2

Methodology

This chapter will give a description of the systems under analysis, the assumptions and geometries of each system, which solution variables and governing equations will be solved, and a look into the boundary conditions. For each system, the governing equations will be fully derived, as their derivations are neither trivial nor easy to find in the literature. Then, the input parameters will be discussed and a description of how the finite element method can be applied to solve the governing equations will be provided.

The two systems being studied are a symmetric cell and a full cell. The symmetric cell is first implemented to isolate and study the electrolyte. This will allow for the CST based electrolyte model to be verified and to provide a deeper understanding of how the electrolyte parameters influence transport, and under which conditions the cell will operate most effectively. Then, the full macro-scale cell model will be discussed, consisting of a Li-metal anode and an NMC porous cathode, separated by an electrolyte separator layer. The macro-scale cell model will utilize the electrolyte model developed in the symmetric cell system in its electrolyte phase. This cell model will then be useful in studying the behaviour of a cell during charge and discharge.

2.1 Symmetric Cell Analysis

2.1.1 Problem Description

In order to develop an accurate electrolyte model, a symmetric cell with two Lithium foil electrodes separated by the chosen electrolyte is first studied. Figure 2.1 presents a visual schematic of the symmetric system. A separator thickness of 500 μm is displayed because that is the thickness used in Chapter 3. The cell being modelled is a 2032-button cell which is 20 mm in diameter, however, because the current is passed on a per area basis and only in the axial direction (i.e., normal direction to the planar electrodes), the radial dimensions are not resolved. Since both planar electrodes are solid Lithium metal, the cell has a 0 V OCV. Therefore, the potential across the cell is solely a result of the internal resistances. Two binary electrolytes will be modelled in this work. The first one, shown in Figure 2.1, is a $LiPF_6$ salt initially at 0.6 M, dissolved in a polymer mixture of Ethylene Carbonate (EC) and Diethyl Carbonate (DEC) in a one-to-one ratio, by weight. The other electrolyte is LiTFSI in Poly-Ethylene Oxide (PEO). Besides the reactions at the boundary of the cell, the only resistances are a result of mass transport limitations within the electrolyte. Therefore, by creating a domain that isolates for the electrolyte, one can study the impact of the electrolyte characteristics more directly. Once a firm understanding of the electrolyte is achieved, it can be applied with confidence to more complicated models (e.g., the macro-scale full cell model).

When a potential difference is applied to the two electrodes of this system, a number of events will occur which will allow a current to pass between them. First, an overpotential will develop between the Lithium foil and electrolyte layers at either end of the separator. This overpotential will be described using the Butler-Volmer kinetics model and will relate the solid phase potential, electrolyte potential, and current to one another. Within the electrolyte, current will be passed across the domain by the motion of charged particles: Lithium carrying positive charge, and the anion carrying

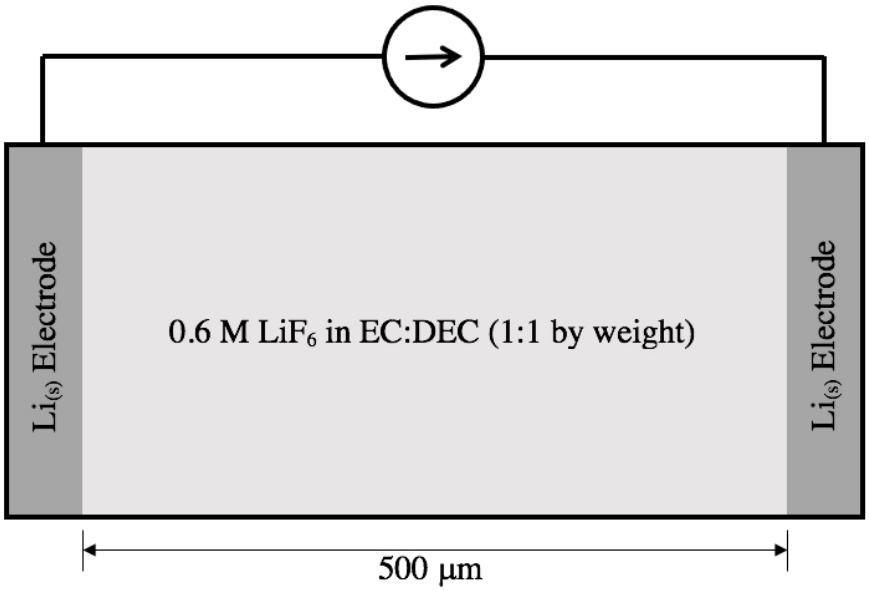

Figure 2.1: Symmetric cell domain schematic. Planar reactions occur at the interface between the separator domain and either electrode.

negative charge. However, because the anion does not participate in the surface reactions, its steady-state flux will have to be zero at either electrode. Therefore, to balance the electric driving force on the anions, a concentration gradient will form, with high concentrations on the side experiencing Lithium oxidation. Because of electroneutrality, the Lithium ions will develop the same profile. There will then be two driving forces on the Lithium ions: the electric field and the ensuing concentration gradient. This concentration gradient will be greatly dependent on the mobility of the Lithium ions with respect to the mobility of the anion. As a result of the concentration gradient, the overpotential will increase at both electrodes to account for the increase in Li^+ concentration at the anode and decrease of Li^+ concentration at the cathode. Therefore, after the initial jump, the cell voltage will increase as the concentration profile develops and then eventually plateau as a steady state is achieved.

Electroneutrality states that within the bulk of a solution the sum of the positive and negative charges must cancel out. This is because an enormous electric charge would need to be applied to separate the positive and negative charges from one

another. Electroneutrality is not, however, a fundamental law, nor even always true at all points in the solution. At the boundaries, an electric "double layer" (DL) can form, in which a surplus of one ion can cause a net charge in the solution to balance the opposite charge developing within the solid.

By convention, the battery community has preferred to use one equation to describe the cation motion and one equation for the solid potential of a reference Li/Li^+ electrode instead of one equation for the anion and one for the cation. The reference electrode potential will change throughout the domain due to the changing activity across the separator.

2.1.2 Governing Equations

The aim of this model is to study the effects of the electrolyte in battery operation. The symmetric cell is therefore used to isolate for the influence of the electrolyte only.

The following assumptions are made for this system:

- The system is isothermal and isobaric.
- The salt is binary and the solvent behaves as if it were a single species.
- The solvent and overall velocity is assumed to be zero. Additionally, the system is incompressible (i.e. the specific volumes are constant).
- All gradients and spatial non-uniformities are assumed to exist only in the normal direction to the reacting surfaces.
- The reactions are uniform across the entire planar electrode surface.
- The double layer capacitance can be neglected due to the short time scales in which it operates.

As discussed in the previous section, the physics being modelled in this system is the motion of the anions and cations, due to an imposed current or voltage. Because

both ionic species are mobile, concentration gradients can be formed, as long as the concentrations of both ions is the same everywhere, due to electroneutrality. An electric field will be a driving force for the ionic species in opposite directions and a concentration gradient will be a driving force for both ionic species in the same direction. Additionally, the current passing through the planar electrodes will be a result of the overpotential created between the electrode and electrolyte potentials. The kinetics will be modelled using the Butler-Volmer equation and will be a function of the concentration of cations at that electrode (Section 2.1.3.2). Instead of deriving an equation for the motion of both ionic species, the system will use the concentration of Lithium ions, c_{Li^+}, and the solid potential of a reference electrode, ϕ_R, as its solution variables. It will use a Lithium ion transport equation (Section 2.1.2.1) and MacInnes equation (Section 2.1.2.2) to describe these variables, respectively.

2.1.2.1 Lithium Ion Transport in Concentrated Solutions

In traditional electrochemical systems, the flux of a charged species in solution is given by the Nernst-Planck equation, i.e.,

$$\boldsymbol{N}_i = -\mathcal{D}_i \nabla c_i - z_i u_i F c_i \nabla \phi_m + c_i \mathbf{v}_0 \tag{2.1}$$

where $\boldsymbol{N}_i$ is the flux of species i, $\mathcal{D}_i$ is the species self-diffusivity, c_i is the species concentration, z_i is the species charge, u_i is the species mobility, ϕ_m is the solution phase potential (discussed in Section 2.2.2.4), and $\mathbf{v}_0$ is the bulk velocity. The three terms on the right hand side of Equation (2.1) represent the three driving forces, i.e., diffusion, migration, and convection, respectively.

This equation is especially useful when a dilute solution can be assumed. However, because the interaction between ions at higher concentrations cannot be neglected, this equation is not valid in this application. Therefore, the development of an equation for species flux in concentrated solutions will be based on Onsager's modification [107] of the Stefan-Maxwell equations: a theory that suggests that the encompassing

driving force for each species, the electrochemical potential, can be expressed in terms of the species' interactions with all other species in solution. A momentum balance of species i leads to [6, 7],

$$c_i \nabla \bar{\mu}_i = \sum_{j \neq i}^{N} K_{ij}(\mathbf{v}_j - \mathbf{v}_i) \tag{2.2}$$

where $\bar{\mu}_i$ is the electrochemical potential of species i, $\mathbf{v}_i$ is the species average velocity, and K_{ij} is the coefficient relating to the drag experienced by species i due to the motion of species j.

The drag coefficient is related to the binary diffusion coefficient, $\mathscr{D}_{ij}$, through,

$$K_{ij} = \frac{RTc_i c_j}{c_T \mathscr{D}_{ij}} \tag{2.3}$$

where c_T is the total concentration of all species, T is the absolute temperature, R is the ideal gas constant, and $\mathscr{D}_{ij}$ is the mutual diffusion coefficient. The mutual diffusion coefficient describes the interaction between each species with all other species in solution and is obtained experimentally by measuring the diffusion rate of species i in species j. The system therefore requires $\frac{1}{2}N(N-1)$ diffusion coefficients and $N-1$ equations to completely describe the system, since, like the drag coefficients, $\mathscr{D}_{ij}$ equals $\mathscr{D}_{ji}$. Because the solvent velocity is taken to be zero, the N^{th} equation is linearly dependent on the others, i.e., its information is redundant, and therefore, is not included.

Given a binary electrolyte within a homogeneous solvent, Equations (2.2) and (2.3) will be expanded for two equations only, corresponding to the motion of the cation and anion. Assuming no bulk convection (i.e. $\mathbf{v}_0 = 0$ and $N_0 = 0$), these equations, respectively, are,

$$c_+ \nabla \bar{\mu}_+ = \frac{RT}{c_T}\left(\frac{1}{\mathscr{D}_{0+}}(-c_0 \boldsymbol{N}_+) + \frac{1}{\mathscr{D}_{+-}}(c_+ \boldsymbol{N}_- - c_- \boldsymbol{N}_+)\right) \tag{2.4}$$

$$c_- \nabla \bar{\mu}_- = \frac{RT}{c_T}\left(\frac{1}{\mathscr{D}_{0-}}(-c_0 \boldsymbol{N}_-) + \frac{1}{\mathscr{D}_{+-}}(c_- \boldsymbol{N}_+ - c_+ \boldsymbol{N}_-)\right) \tag{2.5}$$

where $\boldsymbol{N}_i$ is the species flux, given by,

$$\boldsymbol{N}_i = c_i \mathbf{v}_i \tag{2.6}$$

The assertion that bulk velocity is zero is applicable for the current work, due to the porous matrix and the polymer electrolytes' high viscosity [28, 108]. Additionally, the assumption is made that all solvent species can be regarded as a single species, inasmuch as their thermodynamic diffusion coefficients are concerned.

Combining Equations (2.4) and (2.5), and simplifying the RHS, one obtains an expression for the driving force of the ionic pair,

$$c_+ \nabla \bar{\mu}_+ + c_- \nabla \bar{\mu}_- = -\frac{c_0 RT}{c_T}\Big(\frac{\boldsymbol{N}_+}{\mathscr{D}_{0+}} + \frac{\boldsymbol{N}_-}{\mathscr{D}_{0-}}\Big) \tag{2.7}$$

In doing so, however, information is lost about how each ion interacts with the other. This information will be retrieved in Section 2.1.2.2 with the reintroduction of the above cation equation (Equation (2.4)).

The definition of the total current, which states that the total current being passed through the electrolyte phase is a result of the flux of charged particles in the electrolyte, is used to eliminate $\boldsymbol{N}_-$ from our equation,

$$\mathbf{i} = F(z_+ \boldsymbol{N}_+ + z_- \boldsymbol{N}_-) \tag{2.8}$$

where $\mathbf{i}$ is the total current passing though the electrolyte.

Substituting Equation (2.8) into Equation (2.7), the driving force on the ionic pair is given by,

$$c_+ \nabla \bar{\mu}_+ + c_- \nabla \bar{\mu}_- = -\frac{c_0 RT}{c_T}\left(\Big(\frac{1}{\mathscr{D}_{0+}} - \frac{z_+}{z_-}\frac{1}{\mathscr{D}_{0-}}\Big)\boldsymbol{N}_+ + \frac{1}{z_- \mathscr{D}_{0-}}\frac{\mathbf{i}}{F}\right) \tag{2.9}$$

Shifting focus to the left side of this equation, we will briefly introduce an electrolyte concentration, c_e, such that for binary electrolytes,

$$c_e = \frac{c_+}{\nu_+} = \frac{c_-}{\nu_-} \tag{2.10}$$

where ν_i is the moles of ions per mole of salt. For a binary electrolyte, in which,

$$\mathrm{X}_x\mathrm{Y}_y \leftrightharpoons \nu_x\mathrm{X}^{z_x} + \nu_y\mathrm{Y}^{z_y} \tag{2.11}$$

ν_i for an ion can be expressed in terms of the counter-ion's charge, i.e., $\nu_+ = -z_-$ and $\nu_- = z_+$.

Applying this definition to Equation (2.9),

$$c_e(\nu_+\nabla\bar{\mu}_+ + \nu_-\nabla\bar{\mu}_-) = -\frac{c_0RT}{c_T}\left(\left(\frac{1}{\mathscr{D}_{0+}} - \frac{z_+}{z_-}\frac{1}{\mathscr{D}_{0-}}\right)\boldsymbol{N}_+ + \frac{1}{z_-\mathscr{D}_{0-}}\frac{\mathbf{i}}{F}\right) \tag{2.12}$$

Assuming isobaric and isothermal conditions, the electrochemical potentials can be expanded to [6],

$$\bar{\mu}_i = \mu_i^{\ominus} + RT\ln a_i + z_iF\phi_m \tag{2.13}$$

where $\mu_i^{\ominus}$ is the Gibb's free energy of species i at the reference state and a_i is the molal activity coefficient which can be thought of as a measure of how the ionic activity deviates from ideality and is given by,

$$a_i = m_i\gamma_i\lambda_i^{\ominus} \tag{2.14}$$

where m_i is the ionic molality of each species in moles of solvent per mole of solute, γ_i is the molal activity coefficient with reciprocal units to m_i, and $\lambda_i^{\ominus}$ is a unitless proportionality constant, characteristic of each electrolyte and only dependent on temperature and pressure. Because temperature and pressure are assumed constant, $\lambda_i^{\ominus}$ is also constant. Note, like concentration for a binary electrolyte, the molality of each species can be related to the electrolyte molality through,

$$m_e = \frac{m_+}{\nu_+} = \frac{m_-}{\nu_-} \tag{2.15}$$

where m_e is the electrolyte molality.

By applying these definitions, Equation (2.12) becomes,

$$\begin{aligned} &c_e\big(\nu_+\nabla(\mu_+^{\ominus} + RT\ln(m_+\gamma_+\lambda_+^{\ominus}) + z_+F\phi_m) \\ &\quad + \nu_-\nabla(\mu_-^{\ominus} + RT\ln(m_-\gamma_-\lambda_-^{\ominus}) + z_-F\phi_m)\big) \\ &\quad = -\frac{c_0RT}{c_T}\left(\left(\frac{1}{\mathscr{D}_{0+}} - \frac{z_+}{z_-}\frac{1}{\mathscr{D}_{0-}}\right)\boldsymbol{N}_+ + \frac{1}{z_-\mathscr{D}_{0-}}\frac{\mathbf{i}}{F}\right) \end{aligned} \tag{2.16}$$

Another key characteristic of a liquid electrolyte, is the applicability of electroneutrality, which, for the binary solution in this derivation, is given as,

$$\sum_{i}^{N} z_i c_i = z_+ c_+ + z_- c_- = z_+ \nu_+ + z_- \nu_- = 0 \tag{2.17}$$

This condition will eliminate the ϕ_m terms from Equation (2.16).

Recognizing that the gradient of a constant is zero, Equation (2.16) will reduce to,

$$\begin{aligned} &c_e\big(\nu_+ \nabla \ln\left(m_+ \gamma_+\right) + \nu_- \nabla \ln\left(m_- \gamma_-\right)\big) \\ &\quad = -\frac{c_0}{c_T}\left(\Big(\frac{1}{\mathscr{D}_{0+}} - \frac{z_+}{z_-}\frac{1}{\mathscr{D}_{0-}}\Big)\boldsymbol{N}_+ + \frac{1}{z_- \mathscr{D}_{0-}}\frac{\mathbf{i}}{F}\right) \end{aligned} \tag{2.18}$$

which will further reduce to,

$$c_e \nabla \ln\left(m_+^{(\nu_+ + \nu_-)} \gamma_+^{\nu_+} \gamma_-^{\nu_-}\right) = -\frac{c_0}{c_T}\left(\Big(\frac{1}{\mathscr{D}_{0+}} - \frac{z_+}{z_-}\frac{1}{\mathscr{D}_{0-}}\Big)\boldsymbol{N}_+ + \frac{1}{z_- \mathscr{D}_{0-}}\frac{\mathbf{i}}{F}\right) \tag{2.19}$$

by the derivation in Appendix A.2.

According to the literature [6], the mean molal activity coefficient is related to the ionic molal activity coefficients through, γ_{+-},

$$\gamma_{+-}^{(\nu_+ + \nu_-)} = \gamma_+^{\nu_+} \gamma_-^{\nu_-} \tag{2.20}$$

Equation (2.19) can then be expressed by,

$$(c_+ + c_-) \nabla \ln\left(m_+ \gamma_{+-}\right) = -\frac{c_0}{c_T}\left(\Big(\frac{1}{\mathscr{D}_{0+}} - \frac{z_+}{z_-}\frac{1}{\mathscr{D}_{0-}}\Big)\boldsymbol{N}_+ + \frac{1}{z_- \mathscr{D}_{0-}}\frac{\mathbf{i}}{F}\right) \tag{2.21}$$

given by the derivation in Appendix A.2 as well.

Now utilizing the following relationship,

$$\nabla \ln\left(ab\right) = \nabla \ln a + \nabla \ln b = \left(1 + \frac{\partial \ln b}{\partial \ln a}\right) \nabla \ln a \tag{2.22}$$

we can extract what is known as the thermodynamic factor from the left-hand side of Equation (2.21), to produce,

$$(c_+ + c_-)\left(1 + \frac{\partial \ln \gamma_{+-}}{\partial \ln m_+}\right) \nabla \ln m_+ = -\frac{c_0}{c_T}\left(\Big(\frac{1}{\mathscr{D}_{0+}} - \frac{z_+}{z_-}\frac{1}{\mathscr{D}_{0-}}\Big)\boldsymbol{N}_+ + \frac{1}{z_- \mathscr{D}_{0-}}\frac{\mathbf{i}}{F}\right) \tag{2.23}$$

Equation (2.23) is then rearranged for the cation flux, $\boldsymbol{N}_+$,

$$\begin{aligned}\boldsymbol{N}_+ = &-\frac{c_T c_+}{c_0}\left(\frac{\mathscr{D}_{0+}\mathscr{D}_{0-}(z_+ - z_-)}{z_+\mathscr{D}_{0+} - z_-\mathscr{D}_{0-}}\right)\left(1 + \frac{\partial \ln \gamma_{+-}}{\partial \ln m_+}\right)\nabla \ln m_+ \\ &+ \left(\frac{z_+\mathscr{D}_{0+}}{z_+\mathscr{D}_{0+} - z_-\mathscr{D}_{0-}}\right)\frac{\mathbf{i}}{z_+ F}\end{aligned} \tag{2.24}$$

given the derivation in Appendix A.3.

Next, let's define the diffusion coefficient of the electrolyte, based on the thermodynamically driving force, $\mathscr{D}_e$, as [6],

$$\mathscr{D}_e = \frac{\mathscr{D}_{0+}\mathscr{D}_{0-}(z_+ - z_-)}{z_+\mathscr{D}_{0+} - z_-\mathscr{D}_{0-}} \tag{2.25}$$

and the positive transference number, t_+^0, as [6, 109],

$$t_+^0 = \frac{z_+\mathscr{D}_{0+}}{z_+\mathscr{D}_{0+} - z_-\mathscr{D}_{0-}} \tag{2.26}$$

The positive transference number measures the conductivity fraction contributed by the cation (see Section 2.3.3 for more detail). The negative transference number, t_-^0, is conversely defined and the two must add to unity (i.e. $t_+^0 + t_-^0 = 1$) [110].

The salt diffusion coefficient, D, is related to the electrolyte diffusion coefficient and thermodynamic factor by [111, 112],

$$D = \mathscr{D}_e \frac{c_T}{c_0}\left(1 + \frac{\partial \ln \gamma_{+-}}{\partial \ln m_+}\right) \tag{2.27}$$

The salt diffusion is an experimentally measurable coefficient (see Section 2.3.1), for which parameterized expressions have been developed in the literature [104–106, 110]. By substituting the identities in Equations (2.25), (2.26), and (2.27) into Equation (2.24), one obtains,

$$\boldsymbol{N}_+ = -c_+ D \nabla \ln m_+ + \frac{t_+^0 \mathbf{i}}{z_+ F} \tag{2.28}$$

Because molarity is the solution variable being solved for instead of molality, the identity,

$$m_+ = \frac{c_+}{c_0 M_0} \tag{2.29}$$

will be implemented into Equation (2.28), where M_0 is the molar mass of the solvent. By taking the gradient through the logarithm and applying the relation in Equation (2.22) once again, one can obtain an expression for the flux with respect to the ionic concentration,

$$\boldsymbol{N}_+ = -D\left(1 - \frac{d\ln c_0}{d\ln c_+}\right)\nabla c_+ + \frac{\mathbf{i}t_+^0}{z_+F} \tag{2.30}$$

The bracketed factor in Equation (2.30) can be thought of as a molarity correction factor. This term can be expressed in terms of the specific volumes of the electrolyte pair,

$$1 - \frac{d\ln c_0}{d\ln c_+} = \frac{1}{1 - \bar{v}_e c_+} \tag{2.31}$$

where $\bar{v}_e$ is the specific volume of the solvent. The derivation for the Equation (2.31) identity is given in Appendix A.4.

An equivalent equation to (2.30) can be similarly derived for the flux of anions,

$$\boldsymbol{N}_- = -D\left(1 - \frac{d\ln c_0}{d\ln c_+}\right)\nabla c_- + \frac{\mathbf{i}t_-^0}{z_-F} \tag{2.32}$$

Equation (2.30) can be substituted into the mass conservation equation,

$$\frac{\partial c_i}{\partial t} + \nabla \cdot \boldsymbol{N}_i = 0 \tag{2.33}$$

resulting in an expression for the cation flux,

$$\frac{\partial c_+}{\partial t} = \nabla \cdot \left[D\left(1 - \frac{d\ln c_0}{d\ln c_+}\right)\nabla c_+ - \frac{\mathbf{i}t_+^0}{z_+F}\right] \tag{2.34}$$

Equation (2.34) is the generic form of the cation transport in concentrated solution equation. This equation can be specifically applied to the Lithium-ion battery stoicheometry. The final form of the Lithium transport equation in the electrolyte is then,

$$\boxed{\frac{\partial c_{Li^+}}{\partial t} = \nabla \cdot \left[D\left(1 - \frac{d\ln c_0}{d\ln c_{Li^+}}\right)\nabla c_{Li^+}\right] - \frac{\mathbf{i}\cdot\nabla t_+^0}{F}} \tag{2.35}$$

This equation is equivalent to equation (4) in ref [7], applied to Lithium in a 1:1 binary electrolyte.

2.1.2.2 MacInnes Equation in Concentrated Solutions

Unlike for a system in which one of the ionic species is fixed in place [113], concentration imbalances and gradients can form in the separator electrolyte, acting as a driving force for ionic movement. The electric field imposed by an external source will also act as a driving force, influencing the ionic species proportional to their charge. The concentration gradient will increase until the combination of these two forces will balance each other for the anion species. A steady-state concentration profile will be achieved in which all current will be transported by the cation flux. This equation, therefore, describes how total charge will be carried throughout the domain as a result of the flux of anions and cations. The MacInnes equation describes this relationship, and will be derived in this section. It gives an explicit relationship for how current is related to the gradient of the reference electrode potential and the gradient of the Li+ concentration. The MacInnes equation is presented in two separate forms, differing only semantically, in their use of their electrolyte potential definition.

Nernst-Planck (NP) theory is usually used to describe ion flux in an electrolyte. It is obtained from the definition of the electrochemical potential, i.e.,

$$\bar{\mu}_i = \mu_i^{\ominus} + RT \ln a_i + z_i F \phi_m \tag{2.13}$$

where ϕ_m is the first of these two electrolyte potential definitions and is known as the quasi-electrostatic (or solution-phase) potential.

The second potential definition, based on the Onsager-Stefan-Maxwell (OSM) theory, is the potential, ϕ_R, that would exist within a Li/Li$^+$ reference electrode in equilibrium with the neighbouring solution. Applying Equation (2.13) to the electrons existing within the reference electrode, one can define the reference potential as,

$$\bar{\mu}_{e^-}^R = \mu_{e^-}^{\ominus,R} - F\phi_R \tag{2.36}$$

where $\mu_{e^-}^{\ominus,R}$ is the Gibb's free energy of an electron in the reference electrode.

According to the laws of thermodynamics, at a porous interphase at equilibrium the electrochemical potentials of the reactants in all phases, χ, must be equal to the potential of the products in all phases,

$$\sum_{i=react} \nu_i \bar{\mu}_i^{\chi} = \sum_{j=prod} \nu_j \bar{\mu}_j^{\chi} \tag{2.37}$$

While other reactions would work as well, it is here assumed that the reaction is reversible only with respect to the cation (as is the case for Lithium-ion batteries),

$$M_+^{z_+} + ne^- \leftrightharpoons M_0 \tag{2.38}$$

where n is the number of moles of electrons transferred per mole of reactant. Then, the relationship between the NP solution-phase potential and the OSM reference potential is:

$$\phi_R = \phi_m + \frac{1}{nF}\left[\mu_+^{\ominus} + n\mu_{e^-}^{\ominus,R} - \mu_{M^0}^{\ominus,R} + RT\ln\left(a_+\right)\right] \tag{2.39}$$

However, because the MacInnes equation is concerned with the driving force in charge flux, the relationship between the gradients of the two potentials is the critical comparison, i.e. (assuming isothermal conditions),

$$\nabla\phi_R = \nabla\phi_m + \frac{RT}{nF}\nabla\ln\left(a_+\right) \tag{2.40}$$

From this result, it is evident that the OSM reference potential is a measure of not only the electrostatic potential but also the fluctuating concentration gradients. Its gradient is proportional to the gradient in electrochemical potential of the cation in the electrolyte,

$$\nabla\phi_R = \frac{1}{nF}\nabla\bar{\mu}_+ \tag{2.41}$$

As mentioned in Section 2.1.2.1, by combining the positive and negative momentum equations in the derivation of the Lithium transport equation, information was lost about how the mobility of the cation and anion relate to each other. Therefore, the derivation for the MacInnes equation will begin with this lost information by

reintroducing the cation momentum equation,

$$c_+\nabla\bar{\mu}_+ = \frac{RT}{c_T}\left(\frac{1}{\mathscr{D}_{0+}}(-c_0\boldsymbol{N}_+) + \frac{1}{\mathscr{D}_{+-}}(c_+\boldsymbol{N}_- - c_-\boldsymbol{N}_+)\right) \tag{2.4}$$

First, the derived flux expressions for $\boldsymbol{N}_+$ and $\boldsymbol{N}_-$ (Equations (2.30), (2.32), and (2.27)) are inserted into Equation (2.4) and simplified, i.e.,

$$\begin{aligned} c_+\nabla\bar{\mu}_+ = \frac{RT}{c_T}\Bigg[&\frac{c_+}{\mathscr{D}_{+-}}\left(\frac{z_+c_T\mathscr{D}_e}{z_-c_0}\Big(1+\frac{\partial\ln\gamma_{+-}}{\partial\ln m_+}\Big)\Big(1-\frac{d\ln c_0}{d\ln c_+}\Big)\nabla c_+ + \frac{\mathbf{i}t_-^0}{z_-F}\right) \\ &+\Big(\frac{z_+c_+}{z_-\mathscr{D}_{+-}} - \frac{c_0}{\mathscr{D}_{0+}}\Big)\Big(-\frac{c_T\mathscr{D}_e}{c_0}\Big(1+\frac{\partial\ln\gamma_{+-}}{\partial\ln m_+}\Big)\Big(1-\frac{d\ln c_0}{d\ln c_+}\Big)\nabla c_+ + \frac{\mathbf{i}t_+^0}{z_+F}\Big)\Bigg] \end{aligned} \tag{2.42}$$

Equation (2.42) can be further simplified by combining terms for ∇c_+ and $\mathbf{i}$, and rearranging for current,

$$\begin{aligned} &\mathbf{i}\left[\frac{-RT}{c_Tz_-z_+F^2}\left(\frac{1}{\mathscr{D}_{+-}} + \frac{c_0t_+^0}{c_-\mathscr{D}_{0+}}\right)\right] \\ &= \left[-\frac{1}{z_+F}\nabla\bar{\mu}_+ + \frac{RTt_-^0}{c_+F}\left(\frac{1}{z_+}-\frac{1}{z_-}\right)\left(1+\frac{\partial\ln\gamma_{+-}}{\partial\ln m_+}\right)\left(1-\frac{d\ln c_0}{d\ln c_+}\right)\nabla c_+\right] \end{aligned} \tag{2.43}$$

where the factor multiplying the current is the reciprocal of the ionic conductivity, κ [6]; a coefficient that is experimentally measurable in the absence of a concentration gradient [114], i.e.,

$$\kappa = \left[\frac{-RT}{c_Tz_-z_+F^2}\left(\frac{1}{\mathscr{D}_{+-}} + \frac{c_0t_+^0}{c_-\mathscr{D}_{0+}}\right)\right]^{-1} \tag{2.44}$$

An extended derivation for this step is given in Appendix A.5.

The gradient of cation electrochemical potential in Equation (2.43) was identified earlier as the gradient of the reference potential, i.e., Equation (2.41). Recalling that, according to Equation (2.38), $n = z_+$ and the OSM MacInnes equation with respect to the electric potential of a reference electrode, ϕ_R, is,

$$\mathbf{i} = \kappa\left[-\nabla\phi_R + \frac{RTt_-^0}{c_+F}\left(\frac{1}{z_+}-\frac{1}{z_-}\right)\left(1+\frac{\partial\ln\gamma_{+-}}{\partial\ln m_+}\right)\left(1-\frac{d\ln c_0}{d\ln c_+}\right)\nabla c_+\right] \tag{2.45}$$

Alternatively, the electrochemical potential in Equation (2.43) can be instead substituted by the electrochemical definition in Equation (2.13) and (2.14). This substitution will involve the "solution-phase" potential, thus leading to the NP form of the

MacInnes equation,

$$\mathbf{i} = \kappa\Bigg[- \nabla\big(\mu_+^{\ominus} + RT\ln\left(m_+\gamma_+\lambda_+^{\ominus}\right) + z_+F\phi_m\big) + \frac{RTt_-^0}{c_+F}\left(\frac{1}{z_+} - \frac{1}{z_-}\right)\left(1 + \frac{\partial \ln \gamma_{+-}}{\partial \ln m_+}\right)\left(1 - \frac{d\ln c_0}{d\ln c_+}\right)\nabla c_+\Bigg] \tag{2.46}$$

By simplification of Equation (2.46), as shown in Appendix A.6, we obtain,

$$\mathbf{i} = \kappa\Bigg[- \nabla\phi_m - \frac{RT}{c_+F}\left(\frac{t_-^0}{z_-}\Big(1 + \frac{\partial \ln \gamma_-}{\partial \ln m_+}\Big) + \frac{t_+^0}{z_+}\Big(1 + \frac{\partial \ln \gamma_+}{\partial \ln m_+}\Big)\right)\left(1 - \frac{d\ln c_0}{d\ln c_+}\right)\nabla c_+\Bigg] \tag{2.47}$$

This equation shows how, when using ϕ_m, the only impact the concentration gradient will have on the potential is as a result of a discrepancy between the cation and anion transference numbers and thermodynamic factors. If they were the same for both ions, the coefficient for the concentration gradient term would be zero and ϕ_m would be constant throughout.

The charge conservation equation in the electrolyte is given by,

$$\frac{\partial \rho}{\partial t} + \nabla \cdot \mathbf{i} = 0 \tag{2.48}$$

where ρ is the charge density, given by,

$$\rho = F(z_+c_+ + z_-c_-) \tag{2.49}$$

The first term in (2.48) describes the accumulation of charge in the electrolyte. This occurs when electroneutrality does not apply. In the electrolyte, electroneutrality is broken at the electrode surface due to the development of a double layer, which effectively acts as a capacitor. Given the definition [115] of the volume averaged double-layer capacitance, C_{dl},

$$C_{dl} = \frac{\partial \rho}{\partial(\phi_m - \phi_s)} \tag{2.50}$$

Equation (2.48) can be rewritten [116], as,

$$C_{dl}\frac{\partial(\phi_m - \phi_s)}{\partial t} + \nabla \cdot \mathbf{i} = 0 \tag{2.51}$$

Note, however, for a typical battery charge/discharge, the transient component is minor and only operates on very short time-scales and is therefore dropped in all LiB model discussions [6, 7, 61], as it will be here. Equation (2.51) will then simplify to,

$$\nabla \cdot \mathbf{i} = 0 \tag{2.52}$$

Combining this with the MacInnes equation allows us to fully describe the potential distribution in the system,

$$\begin{aligned} \nabla \cdot \Bigg[-\kappa \nabla \phi_R + \frac{\kappa RT t_-^0}{c_+ F} \left(\frac{1}{z_+} - \frac{1}{z_-} \right) \left(1 + \frac{\partial \ln \gamma_{+-}}{\partial \ln m_+} \right) \\ \left(1 - \frac{d \ln c_0}{d \ln c_+} \right) \nabla c_+ \Bigg] = 0 \end{aligned} \tag{2.53}$$

$$\begin{aligned} \nabla \cdot \Bigg[-\kappa \nabla \phi_m - \frac{\kappa RT}{c_+ F} \left(\frac{t_-^0}{z_-} \left(1 + \frac{\partial \ln \gamma_-}{\partial \ln m_+} \right) + \frac{t_+^0}{z_+} \left(1 + \frac{\partial \ln \gamma_+}{\partial \ln m_+} \right) \right) \\ \left(1 - \frac{d \ln c_0}{d \ln c_+} \right) \nabla c_+ \Bigg] = 0 \end{aligned} \tag{2.54}$$

where the former is obtained with the OSM formulation and the latter with the NP formulation.

Finally, the charge flux equations applied to the Lithium-ion battery application using the OSM and NP theories is, respectively,

$$\boxed{\nabla \cdot \left[-\kappa \nabla \phi_R + \frac{2\kappa RT t_-^0}{c_{Li^+} F} \left(1 + \frac{\partial \ln \gamma_{+-}}{\partial \ln m_{Li^+}} \right) \left(1 - \frac{d \ln c_0}{d \ln c_{Li^+}} \right) \nabla c_{Li^+} \right] = 0} \tag{2.55}$$

$$\boxed{\begin{aligned} \nabla \cdot \Bigg[-\kappa \nabla \phi_m + \frac{\kappa RT}{c_{Li^+} F} \left(t_-^0 \left(1 + \frac{\partial \ln \gamma_-}{\partial \ln m_{Li^+}} \right) - t_+^0 \left(1 + \frac{\partial \ln \gamma_+}{\partial \ln m_{Li^+}} \right) \right) \\ \left(1 - \frac{d \ln c_0}{d \ln c_{Li^+}} \right) \nabla c_{Li^+} \Bigg] = 0 \end{aligned}} \tag{2.56}$$

Due to convention within the battery community, Equation (2.55) will be used for the remainder of this work. This equation is equivalent to equation (18) in reference [105], with the only difference being the use of the molal activity coefficient, γ_{+-}, instead of the molar activity coefficient, f_{+-}. As such, Equation (2.55) contains the molarity correction that is absent in the reference's work. While either form is appropriate, this form was chosen because parametric relations for the molal activity coefficient are more prevalent.

2.1.2.3 Equation Summary

In summary, the two governing equations for the two solution variables, c_{Li^+} and ϕ_R, which fully describe the electrolyte are species transport (2.35) and the MacInnes equation (2.55), i.e.,

$$\frac{\partial c_{Li^+}}{\partial t} = \nabla \cdot \left(D\Big(1 - \frac{d \ln c_0}{d \ln c_{Li^+}}\Big) \nabla c_{Li^+} \right) - \frac{\mathbf{i} \cdot \nabla t_+^0}{F} \tag{2.35}$$

$$0 = \nabla \cdot \left(\kappa \nabla \phi_R - \frac{2\kappa RT t_-^0}{c_{Li^+} F} \Big(1 + \frac{\partial \ln \gamma_{+-}}{\partial \ln m_{Li^+}}\Big) \Big(1 - \frac{d \ln c_0}{d \ln c_{Li^+}}\Big) \nabla c_{Li^+} \right) \tag{2.55}$$

These equations are supported by those published in the literature [6, 7, 91, 105, 117]. The four coefficients, D, t_+^0, κ, and $\left(1 + \frac{\partial \ln \gamma_{+-}}{\partial \ln m_{Li^+}}\right)$, are parameterized in Section 2.3.

The system of governing equations can be written in vector notation,

$$\boldsymbol{A} \frac{\partial \mathbf{u}}{\partial t} = \nabla \cdot \big[\boldsymbol{B}(\mathbf{u}) \nabla \mathbf{u} \big] + \big[\mathbf{i}(\mathbf{u}) \cdot \nabla t_+^0(\mathbf{u}) \big] \mathbf{g} + \mathbf{f}(\mathbf{u}) \tag{2.57}$$

where,

$$\mathbf{u} = \begin{pmatrix} c_{Li^+} \\ \phi_R \end{pmatrix} \tag{2.58}$$

$$\boldsymbol{A} = \begin{pmatrix} 1 & 0 \\ 0 & 0 \end{pmatrix} \tag{2.59}$$

$$\boldsymbol{B}(\mathbf{u}) = \begin{pmatrix} D\Big(1 - \frac{d \ln c_0}{d \ln c_{Li^+}}\Big) & 0 \\ -\frac{2\kappa RT t_-^0}{c_{Li^+} F} \Big(1 + \frac{\partial \ln \gamma_{+-}}{\partial \ln m_{Li^+}}\Big) \Big(1 - \frac{d \ln c_0}{d \ln c_{Li^+}}\Big) & \kappa \end{pmatrix} \tag{2.60}$$

$$\mathbf{g} = \begin{pmatrix} -\frac{1}{F} \\ 0 \end{pmatrix} \tag{2.61}$$

$$\mathbf{f}(\mathbf{u}) = \begin{pmatrix} 0 \\ 0 \end{pmatrix} \tag{2.62}$$

2.1.3 Boundary Conditions

The simplest boundary condition to conceptualize and implement is to impose known values for the solution variables at the boundary; that is, Lithium-ion concentration,

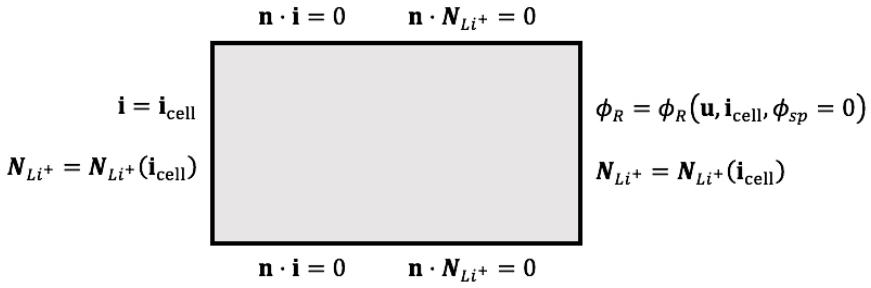

(a)

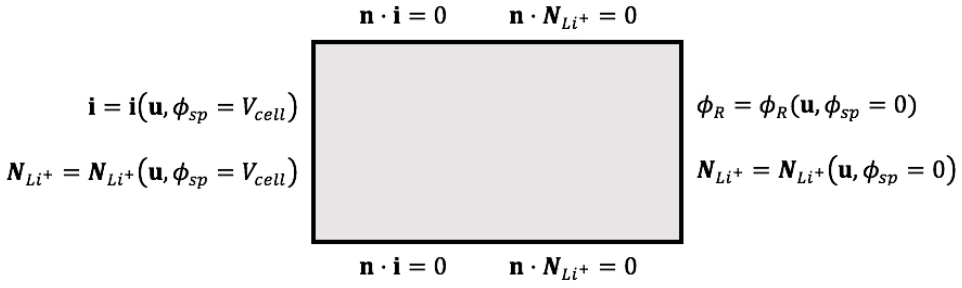

(b)

Figure 2.2: Boundary condition schematic for symmetric cell application for an (a) imposed current and (b) imposed voltage. $\mathbf{i}_{\text{cell}}$ indicates the vector of imposed current and V_{cell} is the scalar imposed voltage.

c_{Li^+}, and the potential of a Li/Li$^+$ reference electrode, ϕ_R. However, although these variables are easily measured, they are not particularly useful boundary conditions (except perhaps when trying to conceptualize the internal physics of the governing equations) because neither variable is easily imposed in a physical system.

Instead, two more realistic boundary conditions would be imposing either a known current through the cell (Section 2.1.3.1) or a known voltage across it (Section 2.1.3.2). Figure 2.2 gives a visual representation of the boundary conditions that would be applied for both imposed current and voltage. Note, the bracketed terms indicates which parameters a particular boundary variable depends on (where $\mathbf{u}$ denotes the solution variable vector).

2.1.3.1 Current Boundary Condition

A flux, or Neumann, boundary condition is required when attempting to model a cell that is operating potentiostatically: with either a constant or known, yet fluctuating, Lithium flux at the boundary. The first application of this would be at the cell walls in which, due to a lack of reaction, it is asserted that the flux of Lithium normal to the surface is zero. At a planar Li electrode, on the other hand, the following electrochemical equation is taking place,

$$\mathrm{Li}^+ + e^- \leftrightharpoons \mathrm{Li}_{(s)} \tag{1.1}$$

and either a known flux of Lithium-ions or a current can be specified. Since anions do not participate in the reaction, it is clear that the current is related to the Li^+ boundary flux only through,

$$\mathbf{i} = F\boldsymbol{N}_{Li^+}\Big|_{(x=0,\delta)} \tag{2.63}$$

where $x = 0$ and $x = \delta$ correspond to the anode and cathode lengths respectively.

By considering the definition of cation flux from Equation (2.30), one can rearrange Equation (2.63) to define the current at the boundary as a function of the mass transport driving force [6],

$$\mathbf{i} = \frac{F}{t_+^0 - 1} D\left(1 - \frac{d\ln c_0}{d\ln c_{Li^+}}\right)\nabla c_{Li^+}\Big|_{(x=0,\delta)} \tag{2.64}$$

where this equation will be used as the boundary term for the Lithium-ion transport equation.

Likewise, Equation (2.45) will be used to define the current as a function of the charge transport driving forces,

$$\mathbf{i} = -\kappa\nabla\phi_R + \frac{2\kappa RT(1-t_+^0)}{c_{Li^+}F}\left(1 + \frac{\partial\ln\gamma_{+-}}{\partial\ln m_{Li^+}}\right)\left(1 - \frac{d\ln c_0}{d\ln c_{Li^+}}\right)\nabla c_{Li^+}\Big|_{(x=0,\delta)} \tag{2.65}$$

where this term will be used as the boundary expression for the MacInnes equation.

2.1.3.2 Voltage Boundary Condition

An alternative to imposing a current through the system would be to impose a known voltage. A known voltage would specify the potential in the planar electrodes, ϕ_{sp}, which can be connected to the solution variables through the use of a reaction equation. In this work, the Butler-Volmer single-electron transfer equation will be derived and utilized, as it ensures versatility at a wide range of operating currents [118].

The reaction kinetics are modelled in this section as a single-electron transfer reaction,

$$\mathrm{R} + e^- \leftrightharpoons \mathrm{P} \tag{2.66}$$

According to rate theory, the rate of forward and backward reactions is given by,

$$r_{\text{forward}} = c_R k_{\text{forward}} \tag{2.67}$$

$$r_{\text{backward}} = c_P k_{\text{backward}} \tag{2.68}$$

where r_i is the reaction rate and k_i is the reaction rate constant. The net rate of reaction in the forward direction would be the difference between these two rates,

$$r_{\text{net}} = r_{\text{forward}} - r_{\text{backward}} = c_R k_{\text{forward}} - c_P k_{\text{backward}} \tag{2.69}$$

The rate constants are given by [119],

$$k_{\text{forward}} = k_{\text{f}}^{\ddagger} \exp\left(-\frac{\alpha F}{RT}\left(E - E^{\ddagger}\right)\right) \tag{2.70}$$

$$k_{\text{backward}} = k_{\text{b}}^{\ddagger} \exp\left(\frac{(1-\alpha) F}{RT}\left(E - E^{\ddagger}\right)\right) \tag{2.71}$$

where $k_i^{\ddagger}$ is the standard state reaction constant based on the standard free energy of the reactions at their transition state, α is the charge transfer coefficient at the Li-foil electrodes, and $E^{\ddagger}$ is the arbitrary reference potential at which $k_i^{\ddagger}$ is determined.

Now, assuming the electrode is existing within an electrolyte at reference conditions ($c_R = c_R^{ref}$, $c_P = c_P^{ref}$), one can imagine that for a given voltage, $E^{eq,ref}$, an equilibrium state can be established. At this state, the rates of forward and backward reactions

are equal. Although the reaction does not progress in either direction, reactions are still taking place. The rate of these reactions, in either direction, can be captured by a new rate constant, r_{ref},

$$\begin{aligned} & k_{\mathrm{f}}^{\ddagger} c_R^{ref} \exp\left(-\frac{\alpha F}{RT}\left(E^{eq,ref} - E^{\ddagger}\right)\right) \\ & \quad = k_{\mathrm{f}}^{\ddagger} c_P^{ref} \exp\left(\frac{(1-\alpha)F}{RT}\left(E^{eq,ref} - E^{\ddagger}\right)\right) = r_{ref} \end{aligned} \tag{2.72}$$

Writing Equations (2.67) and (2.68) in terms of this reference rate gives the relations,

$$r_{\text{forward}} = r_{ref}\left(\frac{c_R}{c_R^{ref}}\right) \exp\left(-\frac{\alpha F}{RT}\left(E - E^{eq,ref}\right)\right) \tag{2.73}$$

$$r_{\text{backward}} = r_{ref}\left(\frac{c_P}{c_P^{ref}}\right) \exp\left(\frac{(1-\alpha)F}{RT}\left(E - E^{eq,ref}\right)\right) \tag{2.74}$$

Finally, by inserting Equations (2.73) and (2.74) into Equation (2.69), the Butler-Volmer equation is,

$$\begin{aligned} r_{net} = r_{ref}\Bigg[& \left(\frac{c_R}{c_R^{ref}}\right) \exp\left(-\frac{\alpha F}{RT}\left(E - E^{eq,ref}\right)\right) \\ & - \left(\frac{c_P}{c_P^{ref}}\right) \exp\left(\frac{(1-\alpha)F}{RT}\left(E - E^{eq,ref}\right)\right)\Bigg] \end{aligned} \tag{2.75}$$

In this section, this equation will be applied to a planar electrode interfacing with the electrolyte and undergoing the same reaction as that used to measure ϕ_R (i.e., an Li/Li^+ electrode).

Due to conservation of charge, at a planar reaction surface, all current passing from the electrolyte must become current within the solid, i.e., at the surface,

$$\nabla \cdot (\mathbf{i}_s + \mathbf{i}) = 0 \tag{2.76}$$

where $\mathbf{i}_s$ is the current passing through the solid phase. Both currents are directly related to the rate of reaction through,

$$\mathbf{i} = \mathbf{i}_s = \mathbf{n} F r_{\text{net}} \tag{2.77}$$

where the vectoral direction of the current density is oriented towards the solid material, normal to the reaction surface, $\mathbf{n}$.

Additionally, the exchange current density, i_{ref}, is merely defined as the current equivalent of the reference rate, r_{ref},

$$i_{ref} = Fr_{ref} \tag{2.78}$$

Substituting Equations (2.77) and (2.78) into Equations (2.75), gives the Butler-Volmer reaction equation for a planar electrode, with respect to the quasi-electrostatic electrolyte potential, ϕ_m,

$$\begin{aligned}\mathbf{i} =&\mathbf{n}i_{ref}\left[\left(\frac{c_R}{c_R^{ref}}\right)\exp\left(-\frac{\alpha F}{RT}(\phi_{sp}-\phi_m-E^{eq,ref})\right)\right.\\&\left.-\left(\frac{c_P}{c_P^{ref}}\right)\exp\left(\frac{(1-\alpha)F}{RT}(\phi_{sp}-\phi_m-E^{eq,ref})\right)\right]\end{aligned} \tag{2.79}$$

One can assume that for any combination of products and reactants, an equilibrium can be established by adjusting the imposed overpotential, that is, the difference between the solid and electrolyte potentials. By definition, this electrode will then be acting as a reference electrode, as no current is being passed to or from the electrolyte. In this specific case, the working electrode is made of the same material as the reference electrode and so ϕ_{sp} must equal ϕ_R. Equation (2.79) can then be written at equilibrium,

$$\begin{aligned}0 =&\mathbf{n}i_{ref}\left[\left(\frac{c_R}{c_R^{ref}}\right)\exp\left(-\frac{\alpha F}{RT}(\phi_R-\phi_m-E^{eq,ref})\right)\right.\\&\left.-\left(\frac{c_P}{c_P^{ref}}\right)\exp\left(\frac{(1-\alpha)F}{RT}(\phi_R-\phi_m-E^{eq,ref})\right)\right]\end{aligned} \tag{2.80}$$

Evidently, the forward and backward rates of reaction must be equal. As such, Equation (2.80) can be rearranged and the magnitude of this current captured with a new variable, i_{eq},

$$\begin{aligned}&i_{ref}\left(\frac{c_R}{c_R^{ref}}\right)\exp\left(-\frac{\alpha F}{RT}(\phi_R-\phi_m-E^{eq,ref})\right)\\&=i_{ref}\left(\frac{c_P}{c_P^{ref}}\right)\exp\left(\frac{(1-\alpha)F}{RT}(\phi_R-\phi_m-E^{eq,ref})\right)=i_{eq}\end{aligned} \tag{2.81}$$

This equilibrium current density, i_{eq}, is specific to the local concentrations of products and reactants. It can be related to the known exchange current density at the reference

concentrations, i_{ref} through,

$$i_{eq} = i_{ref}\left(\frac{c_P}{c_P^{ref}}\right)^{\alpha}\left(\frac{c_R}{c_R^{ref}}\right)^{1-\alpha} \tag{2.82}$$

The derivation for this relationship is developed in Appendix A.7.

By bringing the exponential term in Equation (2.81) to the right-hand side, the concentration ratios in Equation (2.79) can be isolated,

$$i_{ref}\left(\frac{c_R}{c_R^{ref}}\right) = i_{eq}\exp\left(\frac{\alpha F}{RT}(\phi_R - \phi_m - E^{eq,ref})\right) \tag{2.83}$$

$$i_{ref}\left(\frac{c_P}{c_P^{ref}}\right) = i_{eq}\exp\left(-\frac{(1-\alpha)F}{RT}(\phi_R - \phi_m - E^{eq,ref})\right) \tag{2.84}$$

Finally, by substituting Equations (2.83) and (2.84) into Equation (2.79), a Butler-Volmer equation is presented that depends directly on the solution variable, ϕ_R, and can therefore be used in conjuction with Equation (2.55) to define the reactions at the boundary of the domain,

$$\mathbf{i} = \mathbf{n}i_{eq}\left[\exp\left(-\frac{\alpha F}{RT}(\phi_{sp} - \phi_R)\right) - \exp\left(\frac{(1-\alpha)F}{RT}(\phi_{sp} - \phi_R)\right)\right] \tag{2.85}$$

The Butler-Volmer kinetics in Equation (2.85) is still applied to the generic reaction outlined in Equation (2.66). The reaction specific to a solid Lithium-foil electrode is,

$$\mathrm{Li}^+_{(aq)} + e^- \leftrightharpoons \mathrm{Li}_{(s)} \tag{1.1}$$

Since the products do not exist in the electrolyte phase, the forward and backward reaction rates are,

$$\begin{aligned} r_{\text{forward}} &= c_{Li^+}k_{\text{forward}} \\ r_{\text{backward}} &= k_{\text{backward}} \end{aligned} \tag{2.86}$$

Therefore, the reaction governing Lithium-ion reactions at the surface of a $\mathrm{Li}_{(s)}$ planar electrode is,

$$\mathbf{i} = \mathbf{n}i_{eq}\left[\exp\left(-\frac{\alpha F}{RT}(\phi_{sp} - \phi_R)\right) - \exp\left(\frac{(1-\alpha)F}{RT}(\phi_{sp} - \phi_R)\right)\right] \tag{2.87}$$

where,

$$i_{eq} = i_{ref}\left(\frac{c_{Li^+}}{c_{Li^+}^{ref}}\right)^{1-\alpha} \tag{2.88}$$

This form of the BV equation is supported by reference [118].

As in Section 2.1.3, Equations (2.64) and (2.65) can then be used to impose the resulting current boundary condition on the solution variables.

2.2 Macro-Scale Lithium-Ion Battery Analysis

2.2.1 Problem Description

The domain for the macro-scale model of the Lithium-ion battery, consists of a Lithium foil anode and an NMC porous cathode with the separator in between. The separator, as well as the pores of the cathode are filled with the same electrolyte as in the symmetric cell. The solid phase of the cathode consists of an active material, at which the reaction occurs, connected by a conductive binder, that can transport the electronic current to the current collector at the far end of the electrode. Note that the current collector does not itself participate in the reaction. For the scope of this work, the pores are not microscopically resolved and instead each phase is modelled as a homogeneous, overlapping phase, using volume-averaging, in which continuum equations can model the physics. A schematic of the domain for this application is presented in Figure 2.3.

All assumptions made in Section 2.1.1 are also assumed for this system. Additionally, the following assumptions are made for the macro-scale system:

- Heterogeneities are not considered. Locally volume-averaging is applied to obtain representative parameters, such as, porosity, solid diffusion and conductivity, and the interficial area-to-volume ratio.

- Micro-scale intra-particle diffusion is infinitely fast and macro-scale inter-particle diffusion is not constrained by any additional resistances [120]. These assumptions are discussed further in Section 2.3.5.

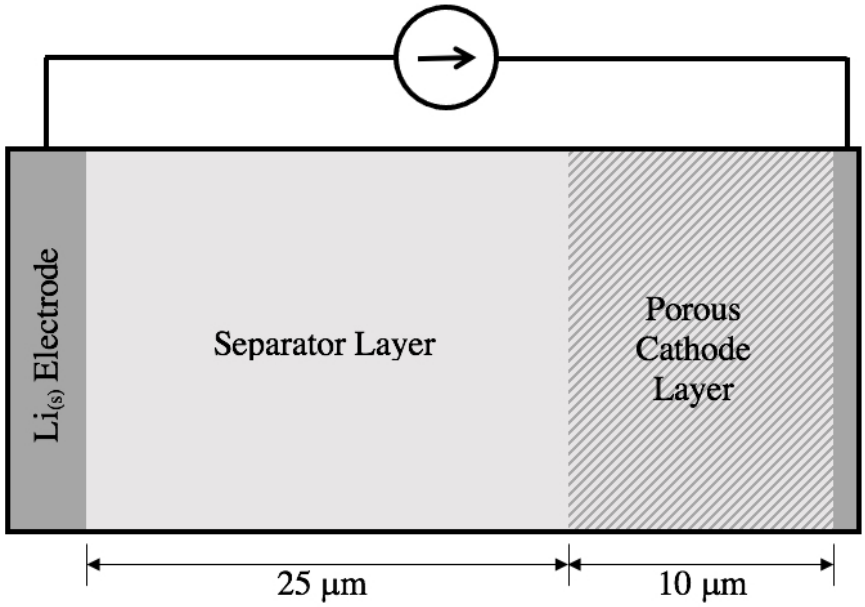

Figure 2.3: Macro-scale battery domain schematic. The anodic reaction occur at the interface between the Lithium foil electrode and the separator and the cathodic reactions occur volumetrically within the porous cathode layer.

- Porosity is constant within each layer. Solid Lithium is only transferred through the active material and electrons are only transferred through the conductive binder.

2.2.2 Governing Equations

In addition to the governing equations describing the transport of Lithium and charge in the electrolyte, this system will need to incorporate an additional two equations to account for the transport of solid Lithium, $c_{Li_{(s)}}$, and charge in the solid phase, ϕ_s. A source term that can couple the solution variables of both phases in the porous electrode will also be implemented into each equation.

2.2.2.1 Lithium Transport in Solid Phase

For an uncharged species in the absence of any convective effects (which is the case in the solid electrode phase), the only driving force would be that of diffusion. Diffusion describes how a species tends to move from a location of high concentration towards

a region of lower concentration. Unimpeded, this process would continue until a uniform concentration is established across the entire domain. The flux of species is directly proportional to the negative of the gradient in concentration, and made equal through the use of a constant diffusion proportionality coefficient, D_s. This is a simplification of the Nernst-Planck equation, that is, Equation (2.1) in Section 2.1.2.1, i.e.,

$$\boldsymbol{N}_i = -D_s \nabla c_i \tag{2.89}$$

which is also known as Fick's Law.

The solid phase in a porous electrode is modelled as a collection of micro-scale particles of active material connected by a conductive matrix. Therefore, the flux of ions, which is on a per unit area of both pore and matrix, must be accounted for to isolate for the flux through the solid phase only. The factor, ϵ_{AM}, describes the volumetric fraction of the active material in the cathode, i.e.,

$$\frac{\boldsymbol{N}_i}{\epsilon_{AM}} = -D_s \nabla c_i \tag{2.90}$$

Furthermore, the diffusion coefficients are multiplied by $\epsilon_{AM}^{0.5}$ to account for tortuosity, as described by Bruggeman [121]. Therefore, an effective diffusion coefficient is established for diffusion within the solid material,

$$D_s^{eff} = \epsilon_{AM}^{1.5} D_s \tag{2.91}$$

Similar to Equation (2.33) in the electrolyte phase, a species balance equation, which enforces concentration continuity in the solid phase (assuming constant porosity), is used as the governing equation, i.e.,

$$\epsilon_{AM} \frac{\partial c_i}{\partial t} + \nabla \cdot \boldsymbol{N}_i = S_i \tag{2.92}$$

where S_i denotes the species source term given in units of $\mathrm{mol}/(\mathrm{cm}^3 \cdot \mathrm{s})$. This term is associated with volumetric reactions occurring between different phases in the same domain (as in a porous electrode) and will be discussed further in Section 2.2.2.5. The

porosity factor in the transient term states that the solid species can only accumulate in the solid phase, as opposed to existing in the electrolyte as well.

Inputting the flux definition into Equation (2.92) returns the equation for species transport within the solid phase,

$$\epsilon_{AM}\frac{\partial c_i}{\partial t} = \nabla \cdot \left(D_s^{eff}\nabla c_i\right) + S_i \tag{2.93}$$

which, for solid Lithium within the active material of an insertion electrode, would be in the form,

$$\boxed{\epsilon_{AM}\frac{\partial c_{Li_{(s)}}}{\partial t} = \nabla \cdot \left(D_s^{eff}\nabla c_{Li_{(s)}}\right) + S_{Li_{(s)}}} \tag{2.94}$$

2.2.2.2 Charge Transport in Solid Phase

Within the solid phase, charge is carried by freely moving electrons. Therefore, unlike the relatively massive solid Lithium atoms, the electron flux is only governed by the influence of an electric field. Electrons pass from a locality of low potential to a locality of high potential. By convention, current is defined as the negative flux of electrons, meaning it proceeds against a potential gradient. This relationship is given by,

$$\mathbf{i}_s = -\sigma_s \nabla \phi_s \tag{2.95}$$

where ϕ_s is the electric potential of the solid phase and σ_s is a constant denoting the conductivity, or proportionality constant, of the solid phase in Siemens ($S = \Omega^{-1}$).

Applying Equation (2.95) to a porous electrode, the effective conductivity of the solid phase has been expressed in the literature [122] as,

$$\sigma_s^{eff} = \epsilon_s^{1.5}\sigma_s \tag{2.96}$$

where ϵ_s is the porosity of the conductive binder.

The charge balance equation, given the source term, S_i, is,

$$\epsilon_s\frac{\partial \rho}{\partial t} + \nabla \cdot \mathbf{i}_s = FS_i \tag{2.97}$$

where the charge density in the solid phase is,

$$\rho = F z_{e^-} c_{e^-} \tag{2.98}$$

Substituting the definition of the DL capacitance in Equation (2.50), the charge equation is,

$$\epsilon_s C_{dl} \frac{\partial(\phi_s - \phi_m)}{\partial t} + \nabla \cdot \mathbf{i}_s = F S_i \tag{2.99}$$

As discussed in Section 2.1.2.2, the transient component will be dropped for the current work, leading to,

$$\nabla \cdot \mathbf{i}_s = F S_i \tag{2.100}$$

Equations (2.95) and (2.100) can be combined to return an equation for charge transport in the solid phase of a Lithium-ion battery porous cathode,

$$\boxed{0 = \nabla \cdot \left(\sigma_s^{eff} \nabla \phi_s\right) + F S_{Li_{(s)}}} \tag{2.101}$$

2.2.2.3 Lithium Ion Transport in Electrolyte Phase

As in Section 2.2.2.1, the flux of ions in the electrolyte phase of the porous cathode must also be corrected for porosity and tortuosity. This will be done by applying a similar effective diffusion coefficient as for the solid phase in Equation (2.91) (except this time being solved within the porous phase, ϵ),

$$D^{eff} = \epsilon^{1.5} D \tag{2.102}$$

The cation flux in Equation (2.30) is then given by,

$$\boldsymbol{N}_+ = -D^{eff}\left(1 - \frac{d \ln c_0}{d \ln c_+}\right)\nabla c_+ + \frac{\mathbf{i} t_+^0}{z_+ F} \tag{2.103}$$

The current term does not contain a porosity term because, like $\boldsymbol{N}_i$ in Equation (2.90), $\mathbf{i}$ only describes the current passing through the pore phase.

The continuity equation for the cation in the electrolyte is also altered to account for porosity through,

$$\epsilon \frac{\partial c_+}{\partial t} + \nabla \cdot \boldsymbol{N}_+ = S_{Li^+} \tag{2.104}$$

In this case, the reaction source term, S_{Li^+}, can be related directly to the divergence of current (outlined in Section 2.2.2.5), as Lithium is the only species undergoing a phase change due to reactions in either electrodes. Finally, combining Equations (2.103) and (2.104) and applying the LiB stoichiometry gives,

$$\boxed{\epsilon\frac{\partial c_{Li^+}}{\partial t} = \nabla\cdot\left[D^{eff}\left(1-\frac{d\ln c_0}{d\ln c_{Li^+}}\right)\nabla c_{Li^+}\right] - \frac{\mathbf{i}\cdot\nabla t_+^0}{F} + (1-t_+^0)S_{Li^+}} \tag{2.105}$$

2.2.2.4 MacInnes Equation in Electrolyte Phase

The MacInnes equation in the electrolyte will also need to consider the porosity of the electrode and the reaction source term. An effective conductivity is defined to correct for this reality. Following the approaches of [6, 121, 123], the following relationship is used as it is proven to be reasonably simple and accurate,

$$\kappa^{eff} = \epsilon^{1.5}\kappa \tag{2.106}$$

Additionally, the charge conservation Equation (2.52) will contain a source term for electron generation due to volumetric reactions, i.e.,

$$\epsilon\frac{\partial\rho}{\partial t} + \nabla\cdot\mathbf{i} = FS_i \tag{2.107}$$

Again, the transient term will be dropped as the DL effects are assumed negligible on the longer time-scales of battery discharge.

Therefore, the OSM MacInnes equation in the porous electrode is,

$$\begin{aligned}\nabla\cdot\Bigg[-\kappa^{eff}\nabla\phi_R + \frac{\kappa^{eff}RTt_-^0}{c_+F}\left(\frac{1}{z_+}-\frac{1}{z_-}\right)\left(1+\frac{\partial\ln\gamma_{+-}}{\partial\ln m_+}\right)\\ \left(1-\frac{d\ln c_0}{d\ln c_+}\right)\nabla c_+\Bigg] = FS_+\end{aligned} \tag{2.108}$$

And finally, the governing equation for the case of a LiB cathode is,

$$\boxed{\nabla\cdot\left[-\kappa^{eff}\nabla\phi_R + \frac{2\kappa^{eff}RTt_-^0}{c_{Li^+}F}\left(1+\frac{\partial\ln\gamma_{+-}}{\partial\ln m_{Li^+}}\right)\left(1-\frac{d\ln c_0}{d\ln c_{Li^+}}\right)\nabla c_{Li^+}\right] = FS_{Li^+}} \tag{2.109}$$

This equation is equivalent to Equation (8) in [61], and Equations (12.27) and (22.5) in [6].

2.2.2.5 Electrochemical Reaction

As mentioned before, the source terms within the governing equations for the battery application will be a result of volumetric reactions in the porous cathode layer. Specifically, this reaction is called Lithiation, in which a positive Lithium ion in the electrolyte phase intercalates into the active material by combining with an electron from the solid phase, and thus creating a solid Lithium atom. As with the P2D model, in this work, the reaction will be modelled using a volume-averaged technique. The surface concentrations will be assumed to be the same as the average solid concentration, as discussed later in this section. Eventually, with the addition of the micro-scale model, this assumption will be lifted by splitting the domain into electrolyte and solid domains, instead of superimposed continua, and coupling them with surface BV kinetics. This extension is discussed further in the Future Work section, i.e., Section 4.3. By assuming equality between the surface and bulk concentration in this work, the reactions will be modelled on a per volume basis instead of solving for the current density on a per area basis at an electrode interface. The source terms for Lithium-ion and solid Lithium are related through the use of charge conservation and based upon the divergence of current in each phase, i.e.,

$$S_{Li_{(s)}} = -S_{Li^+} = \frac{1}{F}\nabla \cdot \mathbf{i}_s = -\frac{1}{F}\nabla \cdot \mathbf{i} \tag{2.110}$$

Practically, this means that any current lost in one phase must be gained in the other phase, as the total current in the system must remain constant.

The equilibrium exchange current density can be related to the source term through the interfacial surface area per unit volume factor, A_v, given in units of cm^2 of reacting surface per cm^3 of volume. The source term for intercalation into the active material of the porous electrode is therefore given by the BV equation,

$$\begin{aligned} S_{Li_{(s)}} = -S_{Li^+} = & \frac{A_v}{F} i_{eq} \Bigg[\exp\left(-\frac{\alpha_c F}{RT}(\phi_s - \phi_R - U) \right) \\ & - \exp\left(\frac{(1-\alpha_c)F}{RT}(\phi_s - \phi_R - U) \right) \Bigg] \end{aligned} \tag{2.111}$$

where α_c is the cathodic charge transfer coefficient and U is the equilibrium potential of the half-cell reaction with respect to a Li/Li^+ electrode at the reference concentrations.

The local reactions taking place at the interfaces between the solid and electrolyte phases will be,

$$Li^+ + e^- + \Theta \leftrightharpoons Li_{(s)}—\Theta \tag{1.2}$$

where Θ denotes a reaction site within the active material. Since these are limited, they will have a significant effect upon the reaction rates at the surface. The line connecting the products indicate that the Lithium atom has filled this site.

The reaction rates for Equation (1.2) are,

$$\begin{aligned} r_{\text{forward}} &= k_{\text{forward}} c_{Li^+} c_\Theta \\ r_{\text{backward}} &= k_{\text{backward}} c_{(Li—\Theta)} \end{aligned} \tag{2.112}$$

noting that the rates of forward and reverse reactions are dependent on the concentration of empty and filled sites respectively.

At this point there are two possible ways to express the reaction kinetics at the active material interface. The approach taken in references [6, 118, 119] is to substitute Equation (2.112) into Equation (2.82). By doing so, the equilibrium current density is given by,

$$i_{eq} = i_{ref,c} \left(\frac{c_{(Li—\Theta)}}{c^{ref}_{(Li—\Theta)}} \right)^{\alpha_c} \left(\frac{c_\Theta}{c^{ref}_\Theta} \right)^{1-\alpha_c} \left(\frac{c_{Li^+}}{c^{ref}_{Li^+}} \right)^{1-\alpha_c} \tag{2.113}$$

where $i_{ref,c}$ is the reference exchange current density for the cathodic reaction. Now, taking the reference concentration for reaction sites to be at its fully saturated state, the ratio of filled sites to saturation can be expressed as a ratio, θ, and conversely, the ratio of empty sites to saturation as $(1-\theta)$, i_{eq} becomes,

$$i_{eq} = i_{ref,c} \theta^{\alpha_c} (1-\theta)^{1-\alpha_c} \left(\frac{c_{Li^+}}{c^{ref}_{Li^+}} \right)^{1-\alpha_c} \tag{2.114}$$

An issue arises in that the potential difference between the reference electrode and the electrolyte does not account for the activity of the filled and empty sites. The

potential difference between the active material electrode and the electrolyte, however, does. According to the derivation in Appendix A.7, the activity terms for filled and empty sites cannot be incorporated into the ϕ_R solution variable. This complexity is avoided by claiming that the reference electrode equilibrium potential, U, accounts for these activities instead, and is therefore cited as being dependent on the extent of Lithiation of the active material and independent of the Lithium-ion concentration in the electrolyte [7, 118, 124, 125].

The alternative form of the Butler-Volmer equation at the active material interface used by Newman [6] is to make the equilibrium current density, i_{eq}, only dependent on the activities of the reactants and products that are common to the reference and active material electrodes (that being Lithium-ion concentration). The remaining ratios are left in front of the exponential term corresponding to its respective reaction direction, i.e.,

$$\begin{aligned} S_{Li_{(s)}} = -S_{Li^+} = \frac{A_v}{F} i_{eq} \Bigg[(1-\theta) \exp\left(-\frac{\alpha_c F}{RT} (\phi_s - \phi_R - U') \right) \\ - \theta \exp\left(\frac{(1-\alpha_c)F}{RT} (\phi_s - \phi_R - U') \right) \Bigg] \end{aligned} \tag{2.115}$$

where,

$$i_{eq} = i_{ref,c} \left(\frac{c_{Li^+}}{c_{Li^+}^{ref}} \right)^{1-\alpha_c} \tag{2.116}$$

Theoretically, this would maintain the reference electrode equilibrium potential as being both concentration and Lithiation independent, hence the distinction between U and U'.

While the two forms of the active material Butler-Volmer equations differ in form and meaning of the equilibrium potential, either form is valid and physically meaningful. However, for this work, Equation (2.115) will be used because U' is simply a constant. Care must be taken to ensure that the correct definition of U or U' is chosen, corresponding to the form of the equation being implemented. The relationship between U and U' is,

$$U' + \frac{RT}{F} \ln\left(\frac{1-\theta}{\theta} \right) = U \tag{2.117}$$

for which a derivation is provided in Appendix A.8.

In this work, a simplification is made, due to its scope only focusing on the macro-scale. Instead of using the θ and $(1-\theta)$ ratios, which correspond to the surface concentration, c_Θ, this work will simply use the locally averaged concentration of Lithium in the solid phase, $c_{Li_{(s)}}$, relative to an assumed saturation concentration, c_{sat}. Having a lower concentration of Lithium in the active material will be assumed proportional to having many open reaction sites, and conversely, having a high concentration of solid Lithium will be assumed proportional to having many filled sites. This simplification would be equivalent to assuming that the microscopic diffusion within the particle is infinitely fast, while maintaining that diffusion macroscopically is still slow. Therefore, the Butler-Volmer equation for intercalating into the active material in this work is,

$$S_{Li_{(s)}} = -S_{Li^+} = \frac{A_v i_{ref,c}}{F}\left(\frac{c_{Li^+}}{c_{Li^+}^{ref}}\right)^{1-\alpha_c}\left[\left(\frac{c_{sat}-c_{Li_{(s)}}}{c_{sat}}\right)\exp\left(-\frac{\alpha_c F}{RT}(\phi_s-\phi_R-U')\right)\right.$$
$$\left.-\left(\frac{c_{Li_{(s)}}}{c_{sat}}\right)\exp\left(\frac{(1-\alpha_c)F}{RT}(\phi_s-\phi_R-U')\right)\right] \tag{2.118}$$

2.2.2.6 Equation Summary

In summary, given the assumptions made about the system, the four governing equations describing the solution variables, $c_{Li_{(s)}}$, ϕ_s, c_{Li^+}, and ϕ_R, within the macro-scale battery are, respectively,

$$\epsilon_{AM}\frac{\partial c_{Li_{(s)}}}{\partial t} = \nabla\cdot\left(D_s^{eff}\nabla c_{Li_{(s)}}\right) + S_{Li_{(s)}} \tag{2.94}$$

$$0 = \nabla\cdot\left(\sigma_s^{eff}\nabla\phi_s\right) + FS_{Li_{(s)}} \tag{2.101}$$

$$\epsilon\frac{\partial c_{Li^+}}{\partial t} = \nabla\cdot\left(\zeta\nabla c_{Li^+}\right) - \frac{\mathbf{i}\cdot t_+^0}{F} + (1-t_+^0)S_{Li^+} \tag{2.105}$$

$$0 = \nabla\cdot\left(\kappa^{eff}\nabla\phi_R + \xi\nabla c_{Li^+}\right) + FS_{Li^+} \tag{2.109}$$

$$\text{where,}\quad \xi = -\frac{2\kappa^{eff}RTt_-^0}{c_{Li^+}F}\left(1+\frac{\partial\ln\gamma_{+-}}{\partial\ln m_{Li^+}}\right)\left(1-\frac{d\ln c_0}{d\ln c_{Li^+}}\right)$$

$$\text{and,}\quad \zeta = D^{eff}\left(1-\frac{d\ln c_0}{d\ln c_{Li^+}}\right)$$

where all four equations are solved in the cathode and only the last two, corresponding to the electrolyte phase equations, are solved in the separator. This system of equations is supported by other works in the literature [54, 117, 126].

Using Equation (2.57) as a template, the terms $\mathbf{u}$, $\boldsymbol{A}$, $\boldsymbol{B}$, $\mathbf{g}$, and $\mathbf{f}$ are defined as,

$$\mathbf{u} = \begin{pmatrix} c_{Li_{(s)}} \\ \phi_s \\ c_{Li^+} \\ \phi_R \end{pmatrix} \tag{2.119}$$

$$\boldsymbol{A} = \begin{pmatrix} \epsilon_{AM} & 0 & 0 & 0 \\ 0 & 0 & 0 & 0 \\ 0 & 0 & \epsilon & 0 \\ 0 & 0 & 0 & 0 \end{pmatrix} \tag{2.120}$$

$$\boldsymbol{B}(\mathbf{u}) = \begin{pmatrix} D_s^{eff} & 0 & 0 & 0 \\ 0 & \sigma_s^{eff} & 0 & 0 \\ 0 & 0 & D^{eff}\left(1 - \frac{d\ln c_0}{d\ln c_{Li^+}}\right) & 0 \\ 0 & 0 & -\frac{2\kappa^{eff}RTt_-^0}{c_{Li^+}F}\left(1 + \frac{\partial \ln \gamma_{+-}}{\partial \ln m_{Li^+}}\right)\left(1 - \frac{d\ln c_0}{d\ln c_{Li^+}}\right) & \kappa^{eff} \end{pmatrix} \tag{2.121}$$

$$\mathbf{g} = \begin{pmatrix} 0 \\ 0 \\ -\frac{1}{F} \\ 0 \end{pmatrix} \tag{2.122}$$

$$\mathbf{f}(\mathbf{u}) = \begin{pmatrix} S_{Li_{(s)}} \\ FS_{Li_{(s)}} \\ (1 - t_+^0)S_{Li^+} \\ FS_{Li^+} \end{pmatrix} \tag{2.123}$$

2.2.3 Boundary Conditions

As with the boundary conditions for the separator cell in Section 2.1.3, Equations (2.64) and (2.65) can be used at the anodic boundary of the domain to describe

the flux conditions for the Lithium-ions, c_{Li^+}, and electrolyte potential, ϕ_R, for an imposed current. For an imposed voltage, Equation (2.87), describing the reactions at a planar-electrode, can be additionally used to relate the potential drop to the current. Because the solid phase only exists in the cathode layer, a zero flux boundary condition can be imposed on the solid Lithium concentration, $c_{Li_{(s)}}$, and the solid phase potential, ϕ_s, at the interface between the separator and the cathode. At the current collector interface, at the far end of the cathode layer, the flux of Lithium-ion, solid Lithium, and electrolyte current are all set to zero. Because electrons are the only component that can penetrate this boundary, the solid potential will be set to zero as a reference. While this value is arbitrarily chosen, it will "anchor" the potential for the whole system from which a potential difference can be measured for the imposed current case, and the current can be measured for the imposed voltage case. Figure 2.4 visually describes how the boundaries conditions are assigned for (a) a constant current and (b) a constant cell voltage.

2.3 Input Parameters

This section will provide physical meaning for the diffusion coefficient, ionic conductivity, transference number, and the thermodynamic factor, it will describe how they can be obtained through experimentation, and it will give their parameterization sourced from the literature. This will be for the two electrolytes used in the simulations, i.e., $LiPF_6$ in EC:DEC (1:1 by weight) and LiTFSI in PEO. The $LiPF_6$ parameters are given at 10, 25, and 40°C for Li^+ concentration between 0.5 and 1.5 M, and the LiTFSI is presented at 90°C for the range of 0.25 to 3.75 M. Because the parameterized equations for LiTFSI were determined from the raw data in ref [105], the original data points are included in the figures as well.

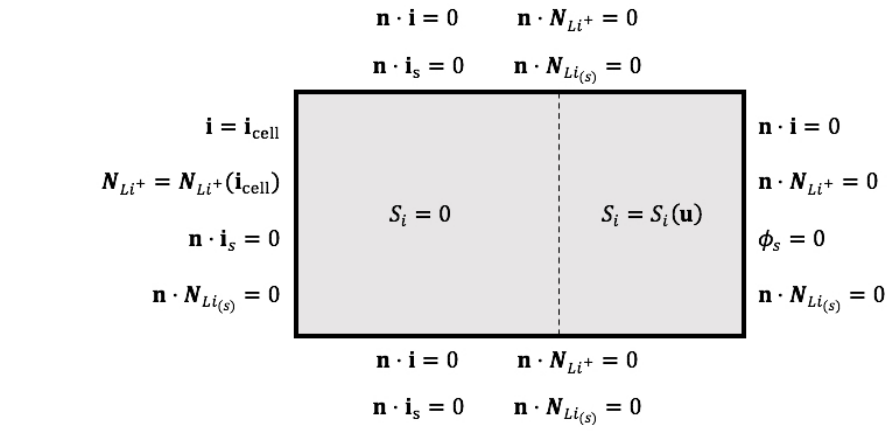

(a)

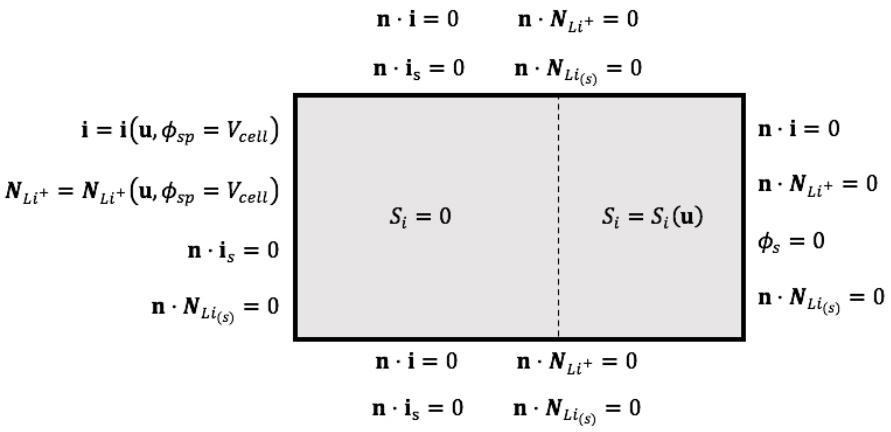

(b)

Figure 2.4: Boundary condition schematic for macro-scale battery application for an (a) imposed current and (b) imposed voltage. The solid phase solution variables are not solved in the separator and therefore their boundary conditions are applied at the interface between the separator and cathode. $\mathbf{i}_{\text{cell}}$ indicates the vector of imposed current and V_{cell} is the scalar imposed voltage.

2.3.1 Diffusion Coefficient

The measurable salt diffusion coefficient, introduced in Equation (2.27), is not an intrinsic property of any one component in solution but instead a byproduct of the exact species and stoichiometries of the electrolyte as a whole. As a result, it is evident that when the stoichiometries change due to concentration differentials in an operable cell, the diffusion at each point in the cell will also change. Parameterization for the diffusion coefficient is obtained through experimental fitting instead of directly from theory because certain parameters for which diffusion is dependent, such as the salt activity coefficients, are not easily obtained from theory alone. Additionally, it has been observed that in concentrated solutions, such as in Lithium-ion batteries, the salt experiences a significant amount of ionic association, resulting in the formation of ionic pairs and triplets, and eventually the precipitation of the salt out of the solution altogether [104]. Some experiments indicate that ionic association is of the order of 40-60% for $LiPF_6$ electrolytes during operation [127, 128]. Changing the electrolyte makeup, by increasing the concentration of ionic pairs, will naturally decrease mobility and thus also decrease the salt diffusion [129]. The salt diffusion, therefore, tends to decrease with increased concentration and subsequently increase with increasing temperatures, due to increased Brownian motion and mobility.

Salt diffusion can be experimentally measured in multiple ways, with varying degrees of accuracy. One such method is the restricted diffusion experiment in which relaxation between two fixed points is measured, after the application of a current or voltage [110]. This method applies a small enough polarization so as to assume constant diffusion across the domain, yet a large enough polarization to mitigate experimental error [130]. Another method is to measure the self-diffusivities of all components in solution (e.g., using nuclear magnetic resonance (NMR) in operando [131, 132]) and using the relationships in Equations (2.25) and (2.27) to parameterize the salt diffusivities for whatever operational range of salt concentrations is required

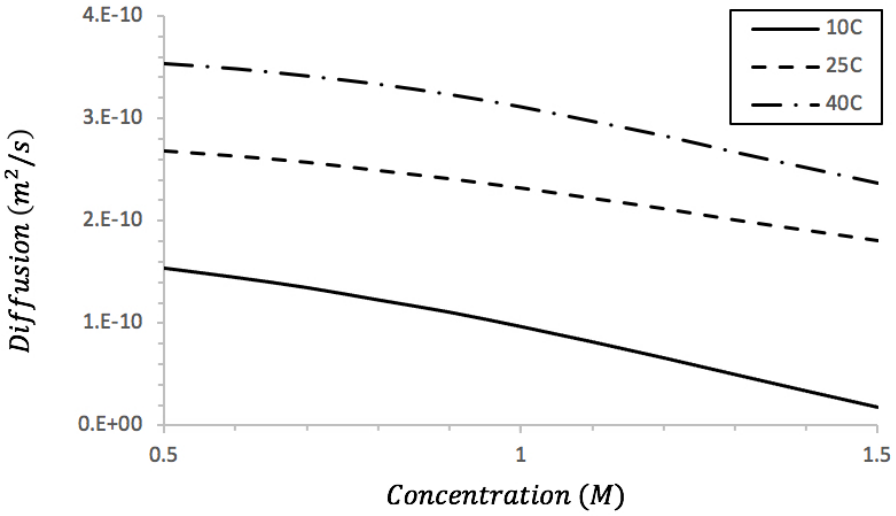

Figure 2.5: Diffusion coefficient given as a function of salt concentration for various temperatures for $LiPF_6$ in EC:DEC 1:1 by weight. Experimental data sourced from ref [106].

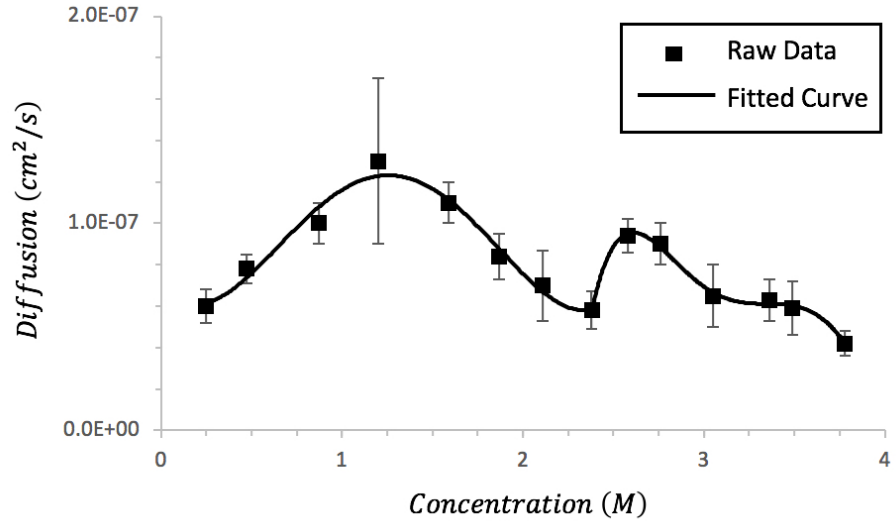

Figure 2.6: Diffusion coefficient given as a function of salt concentration at 90°C for LiTFSI in PEO. Experimental data sourced from ref [105].

[104, 110].

The salt diffusion for $LiPF_6$ in EC:DEC (1:1 by weight) is modelled against concentration in Figure 2.5 and tabulated in Table 2.1, for temperatures of 10°C, 25°C, and 40°C [106]. For the LiTFSI in PEO, the diffusion coefficient was determined from a line of best fit, given the experimental data presented in Figure 2.6 and Table 2.2

Table 2.1: Salt diffusion of $LiPF_6$ in EC:DEC (1:1 by weight).

$D(c) = a_0 + a_1 c_{Li^+} + a_2 c_{Li^+}^2$ [$\times 10^{-11}$ m^2/s]			
	a_0	a_1	a_2
10°C	19.16	-5.170	-4.310
25°C	29.13	-2.932	-3.013
40°C	36.64	6.763	-6.295

Table 2.2: Input parameters for LiTFSI in PEO at 90°C.

$x(c_{Li^+}) = a_0 + a_1 c_{Li^+} + a_2 c_{Li^+}^2 + a_3 c_{Li^+}^3 + a_4 c_{Li^+}^4$						
$x(c_{Li^+})$		a_0	a_1	a_2	a_3	a_4
D [10^{-11} m^2/s]	$c_{Li^+} \geq 2.38$ M	-706.8	1178	-711.3	212.4	-31.35
	$c_{Li^+} < 2.38$ M	0.7165	-1.156	3.603	-2.497	0.4949
κ [mS/cm]	$c_{Li^+} \geq 2.58$ M	-100.7	97.81	-30.68	3.138	
	$c_{Li^+} < 2.58$ M	0.1049	-0.6306	63.62	-4.878	-0.9992
t_+^0	$c_{Li^+} \geq 2.58$ M	-68.22	59.93	-17.25	1.631	
	$c_{Li^+} < 2.58$ M	-0.0874	0.7622	-0.2531	-0.0318	
$\left(1 + \frac{\partial \ln c_0}{\partial \ln c_{Li^+}}\right)$	$c_{Li^+} \geq 2.58$ M	-226.2	193.4	-52.79	4.702	
	$c_{Li^+} < 2.58$ M	-0.1876	1.963	0.5783	-0.3799	

[105].

2.3.2 Conductivity

Like diffusion, the electrolyte conductivity, κ is also highly dependent on ionic concentration, however, in this case, not monotonically. As the ionic concentration decreases, the electrolyte begins to resemble a capacitor and the resistance greatly increases due to less ions being able to carry charge within the electric field. On the other hand, at very high ionic concentrations, the interaction between ions becomes more dominant, due to the mentioned ionic pair formation and potential precipitation, thus also increasing resistance. However, conductivity increases monotonically with temperature

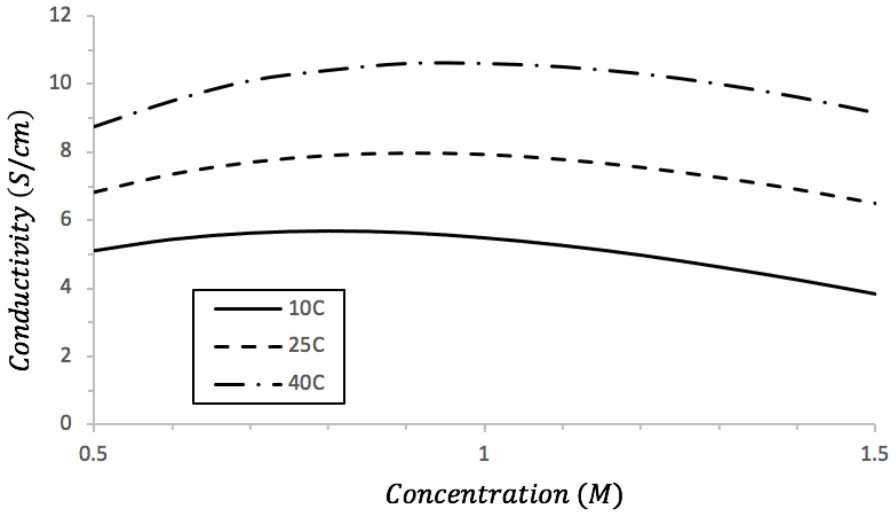

Figure 2.7: Conductivity given as a function of salt concentration for various temperatures for $LiPF_6$ in EC:DEC 1:1 by weight. Experimental data sourced from ref [106].

as a result of increased ionic mobility (see Equation (2.44) for the relationship between conductivity and temperature). The optimal range for maximum conductivity, lies within the $0.8 - 1.0M$ range, depending on the electrolyte and temperature.

Electrolyte conductivity is measured experimentally by performing EIS over a symmetric Li-foil cell [133]. An equivalent circuit can be built, consisting of a constant-phase element (CPE) to account for the capacitive DL, in series with a resistor for conductivity [134]. By fitting the curve of the equivalent circuit to the experimentally achieved results, the resistor element can be isolated and the ionic conductivity calculated by means of the equation,

$$\kappa = \frac{\text{Cell Length}}{\text{Cell Area} \cdot \text{Resistance}} \tag{2.124}$$

The ionic conductivity is given with respect to the $LiPF_6$ in EC:DEC (1:1 by weight) concentration in Figure 2.7 and Table 2.3 [106] and for the LiTFSI in PEO electrolyte in Figure 2.8 and Table 2.2 [105].

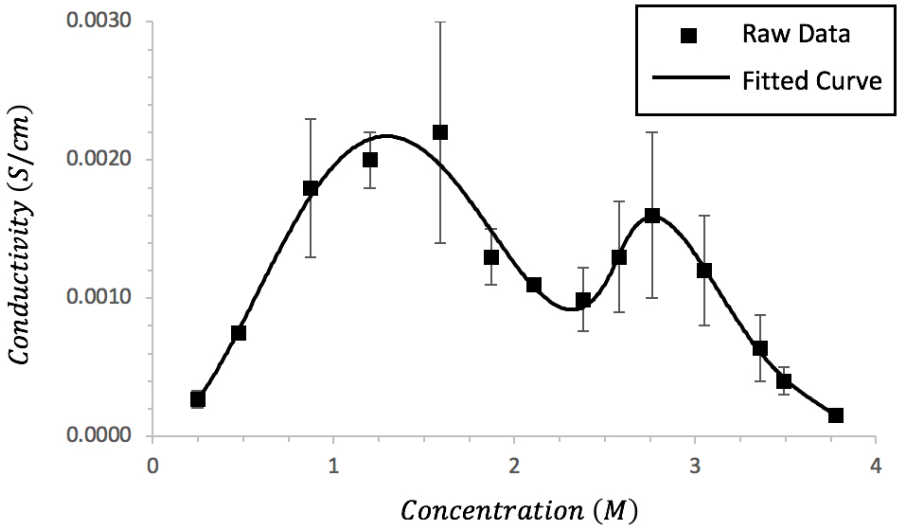

Figure 2.8: Conductivity given as a function of salt concentration at 90°C for LiTFSI in PEO. Experimental data sourced from ref [105].

Table 2.3: Ionic conductivity of $LiPF_6$ in EC:DEC (1:1 by weight).

$\kappa(c) = a_0 c_{Li^+} + a_1 c_{Li^+}^{1.5} + a_2 c_{Li^+}^{3}$ [mS/cm]			
	a_0	a_1	a_2
10°C	23.30	-18.90	1.073
25°C	29.15	-22.38	1.147
40°C	35.95	-26.48	1.149

2.3.3 Transference Number

The transference number, t_i^0, is defined as the number of moles of a species transferred by migration per mole of electrons. For an ideal, fully dissolved solution, this definition could be expressed by Equation (2.26). However, this equation does not hold once the ions start to associate and create ionic pairs. Transference is therefore most easily reported by fitting experimental data.

The transference number is often misunderstood and confused with another parameter: the transport number, t_i. For a binary salt, an ion's transport number corresponds to the ratio of mobility of that ion with respect to its counter ion. As a result, it is often expressed in terms of the self-diffusivities of each ion, i.e. for the cation [135],

$$t_+ = \frac{\mathcal{D}_+}{\mathcal{D}_+ + \mathcal{D}_-} \tag{2.125}$$

The use of the transport number assumes the applicability of the Nernst-Einstein equation, which does not account for the interaction between charged ions. This assumption is valid at the dilute limit, but as concentration increases and ionic interactions become significant, the use of the transport number in place of the transference number will result in errors. Despite this, the transport number is still useful, even for concentrated solution. While one may not obtain a quantitative value that can be implemented into a model, the transport number is easily measurable and its quantitative characteristics are analogous to those of the transference number.

The confusion regarding the transference number often arises through the incorrect usage of certain experiments in reporting its parameterized values. For instance, the Bruce-Vincent method is often performed, in which a constant voltage is applied to a symmetric Li-foil cell and the resulting current is measured [136]. Once a steady state (SS) is obtained, the transport number can be obtained through comparison of the initial current and the final current, i.e.,

$$t_+ = \frac{I_{ss}}{I_0} \tag{2.126}$$

where I_{ss} is the steady state current and I_0 is the initial current. The derivation of this equation, however, assumes the applicability of the Nernst-Einstein relation, and therefore is a measure of the transport number, not the transference number (as is often reported).

An experiment that is used to measure the true transference number is called the Hittorf method [137]. This method bypasses the need for the Nernst-Einstein equation by inserting at least two additional reference electrodes within the separator, and measuring the potential that develops accross them, ensuring that the concentrations between the intermediate electrodes remains constant. Then, by calculating the number of moles of anion passed between the intermediate electrodes, by measuring the anion concentration accumulation in the vicinity of the cathode, one can determine the number of moles of Lithium-ions that are passed. Recognizing that this transport of Lithium between the intermediate electrodes is solely due to migration, the transference number will be the ratio of the number of moles of Lithium passed per mole of charge.

Other sources for discrepancy between reported transference numbers are due to the presence of neutral aggregates [104, 127], moving boundaries due to plating [138], or the assumption of a non-zero bulk velocity [139]. As such, transference numbers vary greatly, with some suggesting concentration independence [140] or even negative values [103, 141]. The majority, however, assert that the transference number is mildly dependent on concentration and temperature and exists in the neighbourhood of $0.2 - 0.3$. The transference number is usually much less than the transport because the Lithium-ion often has a large solvation shell around it, making mobility more difficult.

For this work, the transference number's dependence on concentration is presented in Figure 2.9 and Table 2.4 for $LiPF_6$ in EC:DEC (1:1 by weight) [106] and in Figure 2.10 and Table 2.2 for LiTFSI in PEO [105].

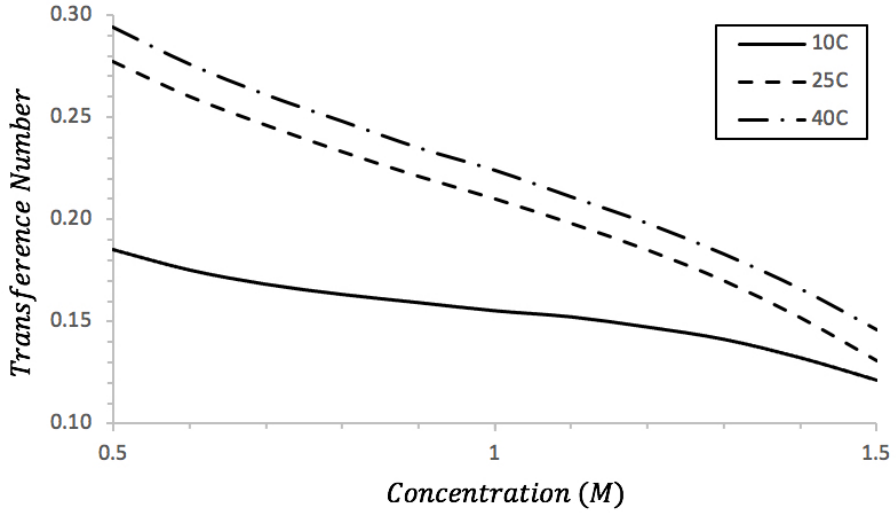

Figure 2.9: Positive transference number coefficient given as a function of salt concentration for various temperatures for $LiPF_6$ in EC:DEC 1:1 by weight. Experimental data sourced from ref [106].

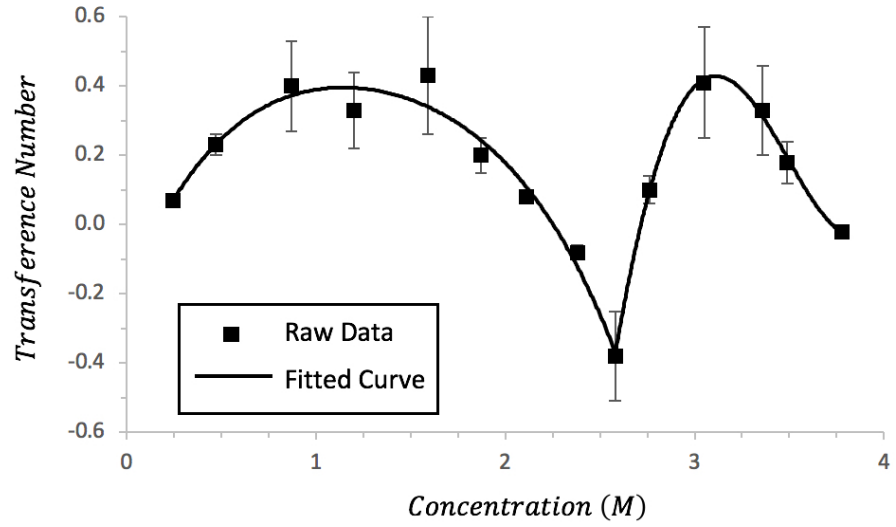

Figure 2.10: Positive transference number given as a function of salt concentration at 90°C for LiTFSI in PEO. Experimental data sourced from ref [105].

Table 2.4: Positive transference number of $LiPF_6$ in EC:DEC (1:1 by weight).

$t_+^0(c) = a_0 + a_1 c_{Li^+} + a_2 c_{Li^+}^2 + a_3 c_{Li^+}^3$				
	a_0	a_1	a_2	a_3
10°C	0.2973	-0.3651	0.3396	-0.1166
25°C	0.4231	-0.4312	0.3373	-0.1197
40°C	0.4467	-0.4450	0.3394	-0.1176

2.3.4 Thermodynamic Factor

Appearing as the bracketed factor containing the molal activity factor in Equations (2.35) and (2.55), i.e.,

$$\left(1 + \frac{\partial \ln \gamma_{\pm}}{\partial \ln m_{Li^+}}\right) \tag{2.127}$$

the thermodynamic factor is a measure of the non-ideality of the electrolyte, specifically with regard to how the salt activity changes with ionic concentration. At low ionic concentrations, as experienced in dilute solution theory, this term will approach unity and can be neglected. But once the ionic concentration exceeds roughly 0.5 M [142], this assumption will introduce significant under-predictions of the open-cell voltage. The thermodynamic factor measures the potential across a concentration cell when no current is being passed. In this case, Equation (2.45) can be rearranged to:

$$\left.\frac{\partial \phi_R}{\partial c_{Li^+}}\right|_{\mathbf{i}=0} = \frac{2RT}{F}\left(1 + \frac{\partial \ln \gamma_{\pm}}{\partial \ln m_{Li^+}}\right)(1 - t_+^0) \tag{2.128}$$

and the thermodynamic factor isolated for.

The concentration dependency for the thermodynamic factor for $LiPF_6$ in EC:DEC (1:1 by weight) is given in Figure 2.11 and Table 2.5 [106] and for LiTFSI in PEO in Figure 2.12 and Table 2.2 [105].

2.3.5 Other Parameters

While the four parameters described so far are the most important for accurately modelling the electrolyte, there are additional parameters for which parameterizations

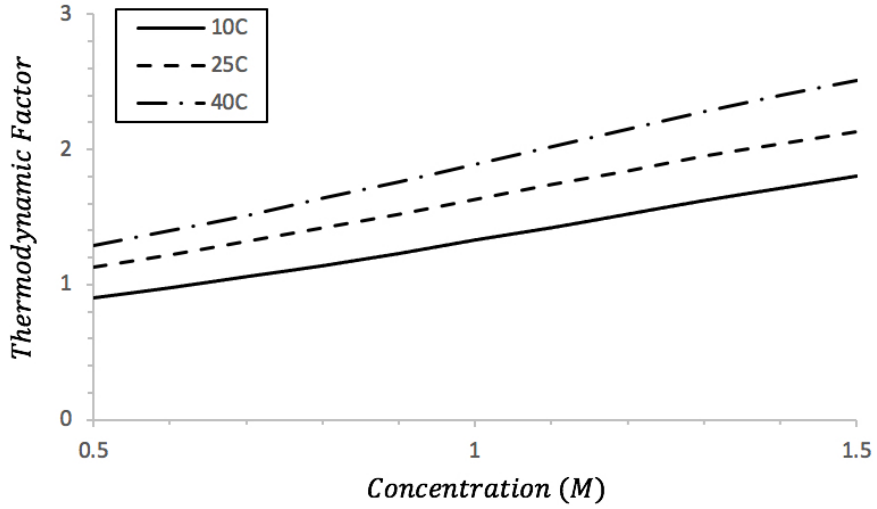

Figure 2.11: Thermodynamic factor given as a function of salt concentration for various temperatures for $LiPF_6$ in EC:DEC 1:1 by weight. Experimental data sourced from ref [106].

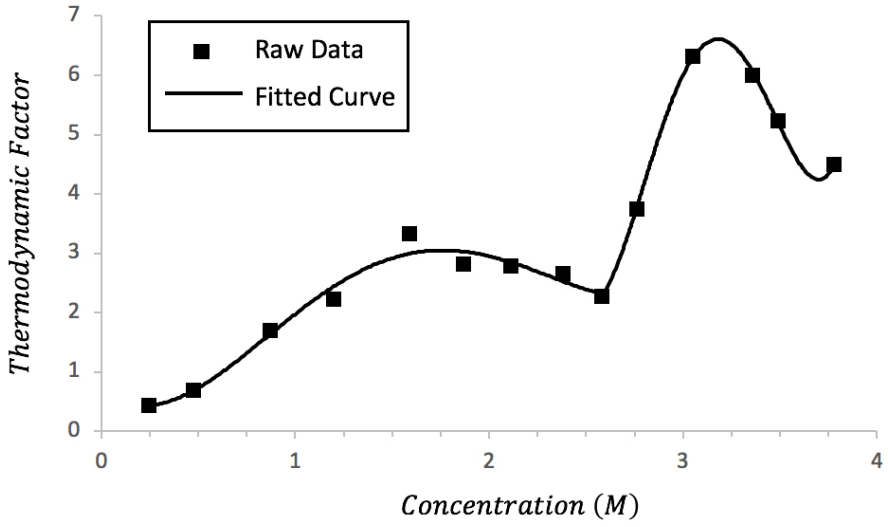

Figure 2.12: Thermodynamic factor given as a function of salt concentration at 90°C for LiTFSI in PEO. Experimental data sourced from ref [105].

Table 2.5: Thermodynamic factor of $LiPF_6$ in EC:DEC (1:1 by weight).

$\left(1+\frac{\partial \ln c_0}{\partial \ln c_{Li^+}}\right)(c) = a_0 + a_1 c_{Li^+} + a_2 c_{Li^+}^2$			
	a_0	a_1	a_2
10°C	0.5167	0.7073	0.1041
25°C	0.6223	0.9968	0.6223
40°C	0.6708	1.199	0.0214

are not provided but are still very important for modelling the symmetric cell system and the full battery system. These are presented in Table 2.6. While each cathodic parameter is with respect to NMC, they are obtained from multiple sources. This is because, unfortunately, it is uncommon for one group to fully parameterize the cathode, given that their research is usually focused at one aspect of the cathode only.

A closer examination of the cathodic micro-structure must be taken for the volumetric parameters pertaining to its nature to be understood. First, the diffusion of solid Lithium occurs in two modes. First, and most substantially, it diffuses radially within each active material particle. The "pseudo" dimension in the P2D model is strictly responsible for this mode of diffusion. However, in this work, because the micro-scale is not being modelled, it is assumed that the radial diffusion rate is infinitely fast, and therefore, the intra-particle diffusion coefficient is infinitely large. The other mode of diffusion is macroscopically, in which solid Lithium is passed between the active material particles, allowing for macro-scale spatial movement of solid Lithium. The transport between particles is often assumed insignificant and therefore not modelled in most electrochemical models [126]. However, reference [120] noted that inter-particle diffusion is likely the cause of decreased heterogeneity within the solid phase, and therefore, a contributing factor in macro-scale transport. As an ongoing area of research, this transport has not yet been quantified for NMC in terms of a diffusion coefficient. Following the examples of references [54, 120], the inter-particle

Table 2.6: Additional simulation parameters

Parameter	**Symbol**	**Value**
Inter-particle solid diffusion coefficient	D_s	$6 \cdot 10^{-12}$ cm^2/s [143]
Intra-particle solid diffusion coefficient		∞ (assumed)
Macro-scale solid conductivity	σ_s	38 mS/cm [143]
Separator pore volume fraction	ϵ	0.55*
Cathode pore volume fraction	ϵ	0.37 [144]
Cathode AM volume fraction	ϵ_{AM}	0.60 [144]
Interfacial area to volume ratio	A_v	8000 cm^2/cm^3 [145]
Li-foil exchange current density	i_{ref}	0.5 mA/cm^2 [146]
Active material exchange current density	$i_{ref,c}$	0.96 mA/cm^2 [32]
Li-foil charge-transfer coefficient	α	0.5 [143]
Active material charge-transfer coefficient	α_c	0.5 [32]
Solid Lithium saturation concentration	c_{sat}	27.380 M [143]
Electrolyte Li^+ reference concentration	c_{ref}	1.0 M
Open cell voltage (OCV)	U	3.3-4.3 V† [147]
$LiPF_6$ specific volume	$\bar{v}_e$	53.49 m^3/mol
LiTFSI specific volume	$\bar{v}_e$	215.85 m^3/mol

* Based on Celgard® 2500 Monolayer Microporous Membrane.

† SOC dependant. See ref [147] for details.

diffusion coefficient will be taken to be the same as the intra-particle diffusion coefficient, accounting for porosity and toruosity, as given in ref [143]. Because this diffusion is acting over such large scales (i.e., the macro-scale cathode domain instead of one active material radius), this inter-particle diffusion will not have a significant impact on cell performance. This is to be expected, given that the main mode of solid diffusion is radially within the active material particle.

The specific volume of the active material and pore phase do not actually comprise the total volume of the cathode, as is suggested in the governing equation derivation. In reality, there are other materials as well, including the conductive additive, binder, and any other doping/enriching compounds. However, because these materials make up a minimal fraction of the total volume, it is lumped in with the active material phase.

The saturation concentration is a measure of the maximum amount of intercalated Lithium that can be extracted back out of the cathode as the cell is run in reverse. Note that this is not the same as the total amount of Lithium in the cathode. The maximum Lithium concentration in the NMC active material is 48.204 M and the minimum amount that must remain when Lithium is being stripped is 20.824 M [143], resulting in a saturation concentration equal to the difference (i.e., 27.380 M).

Finally, the active material exchange current density is obtained from the reaction rate constant cited from reference [32], using the saturation concentration and electrolyte reference concentration presented in the table.

2.4 Implementation

This section outlines the process of implementing the governing equations, in the form,

$$\boldsymbol{A}\frac{\partial \mathbf{u}}{\partial t} = \nabla \cdot \left[\boldsymbol{B}(\mathbf{u})\nabla \mathbf{u}\right] + \left[\mathbf{i}(\mathbf{u}) \cdot \nabla t_+^0(\mathbf{u})\right]\mathbf{g} + \mathbf{f}(\mathbf{u}) \tag{2.57}$$

into the OpenFCST software through the use of the finite element method (FEM) [148]. The solution vector, $\mathbf{u}$, and the coeffieicnts, $\boldsymbol{A}$, $\boldsymbol{B}(\mathbf{u})$, $\mathbf{g}$, and $\mathbf{f}(\mathbf{u})$, are given for the symmetric cell in Equations (2.58) to (2.62) and for the full battery in Equations (2.119) to (2.123). The current, $\mathbf{i}(\mathbf{u})$, is given in Equation (2.45).

2.4.1 Temporal Discretization

Since the temporal and spatial components of Equation (2.57) are independent, a method for solving each can be developed, independent of the other. Given the temporal ODE,

$$\frac{d\mathbf{u}}{dt} = \boldsymbol{f}\big(t, \mathbf{u}(t)\big) \tag{2.129}$$

the function, $\boldsymbol{f}\big(t, \mathbf{u}(t)\big)$, contains the spatial driving forces and source terms from Equation (2.57).

OpenFCST already has a θ-scheme and a backward differentiating formulae (BDF) scheme implemented in its framework. For the θ-scheme, the transient component is replaced by a finite difference and the $\boldsymbol{f}\big(t, \mathbf{u}(t)\big)$ function is implemented by the combination of implicit and explicit terms, i.e.,

$$\frac{\mathbf{u}^{(n+1)} - \mathbf{u}^{(n)}}{\tau} = \theta \boldsymbol{f}^{(n+1)} + (1-\theta)\boldsymbol{f}^{(n)} \tag{2.130}$$

where τ is the step size. When θ is set to 0, one obtain the explicit Euler method and when θ is 1, one obtains implicit Euler, both of which are first order accurate. By setting $\theta = 0.5$, the Crank-Nicolson method is obtained which is second order and unconditionally stable (as is implicit Euler). The BDF scheme is also unconditionally stable for its first and second order ($k = 1$ or 2) but has the possibility of being extended to sixth order accurate, although the higher order schemes are conditionally stable. Implicit Euler is recovered for BDF-1 [116]. In this work, the BDF-1 scheme was chosen as it is unconditionally stable and can be extended to higher orders of accuracy if needed.

Based on the form of the system in Equation (2.129), the BDF discretization definition for order k is given by,

$$\boldsymbol{f}^{(n+1)} = \sum_{p=n-k+1}^{n+1} \frac{\alpha_p}{\tau}\mathbf{u}^{(p)} = \frac{1}{\tau}\big(\alpha_{n+1}\mathbf{u}^{(n+1)} + \alpha_n\mathbf{u}^{(n)} + \cdots + \alpha_{n-k+1}\mathbf{u}^{(n-k+1)}\big) \quad (2.131)$$

The superscript, $(n+1)$, denotes the current time step, and α_p is a mathematically determined prefactor that is dependent on the scheme order.

Applying Equation (2.131) to Equation (2.57), results in the following temporally discretized governing equation,

$$\begin{aligned}\sum_{p=n-k+1}^{n+1} \frac{\boldsymbol{A}\alpha_p}{\tau}\mathbf{u}^{(p)} =& \nabla\cdot\big(\boldsymbol{B}(\mathbf{u}^{(n+1)})\nabla\mathbf{u}^{(n+1)}\big) \\ &+ \big(\mathbf{i}(\mathbf{u}^{(n+1)})\cdot\nabla t_+^0(\mathbf{u}^{(n+1)})\big)\mathbf{g} + \mathbf{f}(\mathbf{u}^{(n+1)})\end{aligned} \quad (2.132)$$

2.4.2 Linearization

The driving force coefficient, $\boldsymbol{B}$, the current, $\mathbf{i}$, and the source term, $\mathbf{f}$, are all functions of the solution variables, and therefore, their values for the current time step cannot be directly determined, as the values on which they depend are unknown. Therefore, an iteration technique within the current time step will be applied that can give an increasingly accurate estimate for the values of the unknown coefficients. This iteration routine will be denoted by a second superscript $(n+1, m+1)$, where $m+1$ denotes the current nonlinear iteration. Note that the values of the solution variables from previous time steps ($p \leq n$) are always given by the final iteration at that time step. Equation (2.132) will then be,

$$\begin{aligned}\sum_{p=n-k+1}^{n+1} \frac{\boldsymbol{A}\alpha_p}{\tau}\mathbf{u}^{(p,m+1)} =& \nabla\cdot\big(\boldsymbol{B}(\mathbf{u}^{(n+1,m+1)})\nabla\mathbf{u}^{(n+1,m+1)}\big) \\ &+ \big(\mathbf{i}(\mathbf{u}^{(n+1,m+1)})\cdot\nabla t_+^0(\mathbf{u}^{(n+1,m+1)})\big)\mathbf{g} + \mathbf{f}(\mathbf{u}^{(n+1,m+1)})\end{aligned} \quad (2.133)$$

The first method implemented in OpenFCST is the Picard method. In this method, the unknown coefficients are merely computed using the solution variables from the previous iteration. This process is repeated until a reasonable tolerance is achieved.

Applying this method gives,

$$\sum_{p=n-k+1}^{n+1} \frac{\boldsymbol{A}\alpha_p}{\tau}\mathbf{u}^{(p,m+1)} = \nabla\cdot\left(\boldsymbol{B}(\mathbf{u}^{(n+1,m)})\nabla\mathbf{u}^{(n+1,m+1)}\right) + \left(\mathbf{i}(\mathbf{u}^{(n+1,m)})\cdot\nabla t_+^0(\mathbf{u}^{(n+1,m)})\right)\mathbf{g} + \mathbf{f}(\mathbf{u}^{(n+1,m)}) \tag{2.134}$$

Alternatively, the Newton-Raphson method was also implemented into OpenFCST. This linearization method involves taking the variation of the equation functional and setting it equal to zero, i.e.,

$$R(\mathbf{u}^{(m+1)}) = R(\mathbf{u}^{(m)}) + \delta R(\mathbf{u}^{(m)}) = 0 \tag{2.135}$$

Applied to Equation (2.133), the linearized form of the governing equation is,

$$\begin{aligned}
0 = &\sum_{p=n-k+1}^{n+1} \frac{\boldsymbol{A}\alpha_p}{\tau}\mathbf{u}^{(p,m)} \\
&+ \frac{\boldsymbol{A}\alpha_{n+1}}{\tau}\delta\mathbf{u} \\
&- \nabla\cdot\left(\boldsymbol{B}(\mathbf{u}^{(n+1,m)})\nabla\mathbf{u}^{(n+1,m)}\right) \\
&- \nabla\cdot\left(\boldsymbol{B}(\mathbf{u}^{(n+1,m)})\nabla\delta\mathbf{u}\right) \\
&- \nabla\cdot\left(\left.\frac{\partial\boldsymbol{B}(\mathbf{u})}{\partial u_k}\right|_{\mathbf{u}=\mathbf{u}^{(n+1,m)}}\delta u_k\nabla\mathbf{u}^{(n+1,m)}\right) \\
&- \left(\left(\left.\frac{\partial\mathbf{i}(\mathbf{u})}{\partial u_k}\right|_{\mathbf{u}=\mathbf{u}^{(n+1,m)}}\delta u_k\right)\cdot\left(\left.\frac{\partial t_+^0(\mathbf{u})}{\partial u_l}\right|_{\mathbf{u}=\mathbf{u}^{(n+1,m)}}\nabla u_l\right)\right)\mathbf{g} \\
&- \left(\mathbf{i}(\mathbf{u}^{(n+1,m)})\cdot\left(\left.\frac{\partial t_+^0(\mathbf{u})}{\partial u_k}\right|_{\mathbf{u}=\mathbf{u}^{(n+1,m)}}\nabla u_k^{(n+1,m)}\right)\right)\mathbf{g} \\
&- \left(\mathbf{i}(\mathbf{u}^{(n+1,m)})\cdot\left(\left.\frac{\partial t_+^0(\mathbf{u})}{\partial u_k}\right|_{\mathbf{u}=\mathbf{u}^{(n+1,m)}}\nabla\delta u_k\right)\right)\mathbf{g} \\
&- \left(\mathbf{i}(\mathbf{u}^{(n+1,m)})\cdot\left(\left.\frac{\partial^2 t_+^0(\mathbf{u})}{\partial u_k\partial u_l}\right|_{\mathbf{u}=\mathbf{u}^{(n+1,m)}}\delta u_k\nabla u_l^{(n+1,m)}\right)\right)\mathbf{g} \\
&- \mathbf{f}(\mathbf{u}^{(n+1,m)}) \\
&- \left.\frac{\partial\mathbf{f}(\mathbf{u})}{\partial u_k}\right|_{\mathbf{u}=\mathbf{u}^{(n+1,m)}}\delta u_k
\end{aligned} \tag{2.136}$$

An approximation of $\mathbf{u}^{(n+1)}$ is obtained by successfully solving for $\delta\mathbf{u}$ and updating $\mathbf{u}^{(n+1,m+1)} = \mathbf{u}^{(n+1,m)} + \delta\mathbf{u}$. This will continue until the residual tolerance is satisfied, at which point the algorithm will advance in time. The derivation for this linearization is provided in Appendix A.9.

In this case, the disadvantage of using the Newton-Raphson method is that the derivatives of the $\boldsymbol{B}$, $\mathbf{i}$, and $\mathbf{f}$ terms need to be determined and implemented for each variable. This will cause derivative terms to appear off the main diagonal of the solution matrix, thus making matrix inversion generally more difficult. For this application, however, in which certain equations are driven by multiple solution variables, the system-matrix is already non-symmetric and using the Newton-Raphson method will not make it worse. The advantage of this method, and the reason it was chosen for this application, is that it converges significantly faster than the Picard iteration, thus reducing computational expense.

2.4.3 Weak Formulation and Spatial Discretization

The linearized equations will be spatially discretized using the Bubnov-Galerkin finite-element method. Each term is multiplied by a test function [116], v, and the equation

is integrated over the domain, Ω, i.e.,

$$
\begin{aligned}
0 = & \int_{\Omega} v \sum_{p=n-k+1}^{n+1} \frac{\boldsymbol{A}\alpha_p}{\tau}\mathbf{u}^{(p,m)} d\Omega \\
& + \int_{\Omega} v \frac{\boldsymbol{A}\alpha_{n+1}}{\tau}\delta\mathbf{u} d\Omega \\
& - \int_{\Omega} v \nabla \cdot \big(\boldsymbol{B}(\mathbf{u}^{(n+1,m)})\nabla\mathbf{u}^{(n+1,m)}\big) d\Omega \\
& - \int_{\Omega} v \nabla \cdot \big(\boldsymbol{B}(\mathbf{u}^{(n+1,m)})\nabla\delta\mathbf{u}\big) d\Omega \\
& - \int_{\Omega} v \nabla \cdot \left(\left.\frac{\partial \boldsymbol{B}(\mathbf{u})}{\partial u_k}\right|_{\mathbf{u}=\mathbf{u}^{(n+1,m)}} \delta u_k \nabla\mathbf{u}^{(n+1,m)}\right) d\Omega \\
& - \int_{\Omega} v \left(\left(\left.\frac{\partial \mathbf{i}(\mathbf{u})}{\partial u_k}\right|_{\mathbf{u}=\mathbf{u}^{(n+1,m)}} \delta u_k\right) \cdot \left(\left.\frac{\partial t_+^0(\mathbf{u})}{\partial u_l}\right|_{\mathbf{u}=\mathbf{u}^{(n+1,m)}} \nabla u_l\right)\right)\mathbf{g} d\Omega \\
& - \int_{\Omega} v \left(\mathbf{i}(\mathbf{u}^{(n+1,m)}) \cdot \left(\left.\frac{\partial t_+^0(\mathbf{u})}{\partial u_k}\right|_{\mathbf{u}=\mathbf{u}^{(n+1,m)}} \nabla u_k^{(n+1,m)}\right)\right)\mathbf{g} d\Omega \\
& - \int_{\Omega} v \left(\mathbf{i}(\mathbf{u}^{(n+1,m)}) \cdot \left(\left.\frac{\partial t_+^0(\mathbf{u})}{\partial u_k}\right|_{\mathbf{u}=\mathbf{u}^{(n+1,m)}} \nabla \delta u_k\right)\right)\mathbf{g} d\Omega \\
& - \int_{\Omega} v \mathbf{i}(\mathbf{u}^{(n+1,m)}) \cdot \left(\left.\frac{\partial^2 t_+^0(\mathbf{u})}{\partial u_k \partial u_l}\right|_{\mathbf{u}=\mathbf{u}^{(n+1,m)}} \delta u_k \nabla u_l^{(n+1,m)}\right)\mathbf{g} d\Omega \\
& - \int_{\Omega} v \mathbf{f}(\mathbf{u}^{(n+1,m)}) d\Omega \\
& - \int_{\Omega} v \left.\frac{\partial \mathbf{f}(\mathbf{u})}{\partial u_k}\right|_{\mathbf{u}=\mathbf{u}^{(n+1,m)}} \delta u_k d\Omega
\end{aligned}
\tag{2.137}
$$

One can then apply integration by parts and Gauss' theorem, i.e.,

$$
\begin{aligned}
\int_{\Omega} s\big(\nabla \cdot \mathbf{v}\big) d\Omega &= -\int_{\Omega} (\nabla s) \cdot \mathbf{v} d\Omega + \int_{\Omega} \nabla \cdot \big(s\mathbf{v}\big) d\Omega \\
&= -\int_{\Omega} (\nabla s) \cdot \mathbf{v} d\Omega + \oint_{\partial\Omega} \mathbf{n} \cdot \big(s\mathbf{v}\big) d\Gamma
\end{aligned}
\tag{2.138}
$$

to Equation (2.137) to reduce the order of the derivative by one. Here, s is a scalar, $\mathbf{v}$ is a vector, and $\partial\Omega$ denotes the domain boundary.

The weak form of the governing equation is then,

$$
\begin{aligned}
&\int_\Omega v\frac{\boldsymbol{A}\alpha_{n+1}}{\tau}\delta\mathbf{u}d\Omega \\
&+\int_\Omega(\nabla v)\cdot\big(\boldsymbol{B}(\mathbf{u}^{(n+1,m)})\nabla\delta\mathbf{u}\big)d\Omega \\
&+\int_\Omega(\nabla v)\cdot\left(\left.\frac{\partial\boldsymbol{B}(\mathbf{u})}{\partial u_k}\right|_{\mathbf{u}=\mathbf{u}^{(n+1,m)}}\delta u_k\nabla\mathbf{u}^{(n+1,m)}\right)d\Omega \\
&-\int_\Omega v\left(\left(\left.\frac{\partial\mathbf{i}(\mathbf{u})}{\partial u_k}\right|_{\mathbf{u}=\mathbf{u}^{(n+1,m)}}\delta u_k\right)\cdot\left(\left.\frac{\partial t_+^0(\mathbf{u})}{\partial u_l}\right|_{\mathbf{u}=\mathbf{u}^{(n+1,m)}}\nabla u_l\right)\right)\mathbf{g}d\Omega \\
&-\int_\Omega v\left(\mathbf{i}(\mathbf{u}^{(n+1,m)})\cdot\left(\left.\frac{\partial t_+^0(\mathbf{u})}{\partial u_k}\right|_{\mathbf{u}=\mathbf{u}^{(n+1,m)}}\nabla\delta u_k\right)\right)\mathbf{g}d\Omega \\
&-\int_\Omega v\left(\mathbf{i}(\mathbf{u}^{(n+1,m)})\cdot\left(\left.\frac{\partial^2 t_+^0(\mathbf{u})}{\partial u_k\partial u_l}\right|_{\mathbf{u}=\mathbf{u}^{(n+1,m)}}\delta u_k\nabla u_l^{(n+1,m)}\right)\right)\mathbf{g}d\Omega \\
&-\int_\Omega v\left.\frac{\partial\mathbf{f}(\mathbf{u})}{\partial u_k}\right|_{\mathbf{u}=\mathbf{u}^{(n+1,m)}}\delta u_k d\Omega \\
&=-\int_\Omega v\sum_{p=n-k+1}^{n+1}\frac{\boldsymbol{A}\alpha_p}{\tau}\mathbf{u}^{(p,m)}d\Omega \\
&-\int_\Omega(\nabla v)\cdot\big(\boldsymbol{B}(\mathbf{u}^{(n+1,m)})\nabla\mathbf{u}^{(n+1,m)}\big)d\Omega \\
&+\int_\Omega v\left(\mathbf{i}(\mathbf{u}^{(n+1,m)})\cdot\left(\left.\frac{\partial t_+^0(\mathbf{u})}{\partial u_k}\right|_{\mathbf{u}=\mathbf{u}^{(n+1,m)}}\nabla u_k^{(n+1,m)}\right)\right)\mathbf{g}d\Omega \\
&+\int_\Omega v\mathbf{f}(\mathbf{u}^{(n+1,m)})d\Omega \\
&+\oint_{\partial\Omega}\mathbf{n}\cdot\big(v\boldsymbol{B}(\mathbf{u}^{(n+1,m+1)})\nabla\mathbf{u}^{(n+1,m+1)}\big)d\Gamma
\end{aligned}
\tag{2.139}
$$

Note that the boundary term is computed at the $m+1$ nonlinear iteration. This can be achieved as the boundary conditions are either Dirichlet, in which case the whole term will become zero (as $v=0$), or Neumann/complex, in which case the flux is imposed and the whole term can be replaced (see Section 2.4.4 for more detail).

Determining functions that closely approximate the solution over the whole domain would be tedious and incredibly difficult. As such, the domain will be spatially discretized over a predetermined mesh. The intention being, that the solution over these cells can be approximated by a set of given shape functions to a reasonable degree of accuracy. By increasing the number of cells (and therefore decreasing the size of each cell), along with changing the number of shape functions in each cell,

the error in the final approximation can be reduced to within a required threshold. The shape function definition for the solution variance, δu_c, and test functions, v, are given as,

$$\delta u_c \approx \sum_{j=1}^{N} \psi^j \delta \bar{u}_c^j \qquad v \approx \sum_{i=1}^{N} \psi^i \bar{v}^i \tag{2.140}$$

where ψ^j is a first order Lagrangian polynomial and N is the DOF of the shape functions. The indices are given as superscripts to distinguish them as DOF indices instead of indices denoting the equation number, which are given as subscripts.

For these discretizations to be applied to Equation (2.139), it is convenient to write this equation in index notation, as a fourth order matrix in tensor notation could be misleading. The discretized weak form is then,

$$\begin{aligned}
&\Bigg[\int_{\hat{\Omega}} \frac{A_{ac}\alpha_{n+1}}{\tau} \psi^i \psi^j d\hat{\Omega} \\
&+ \int_{\hat{\Omega}} B_{ac}(\mathbf{u}^{(n+1,m)}) \big(\nabla \psi^i \cdot \nabla \psi^j \big) d\hat{\Omega} \\
&+ \int_{\hat{\Omega}} \left(\left. \frac{\partial B_{ab}(\mathbf{u})}{\partial u_k} \right|_{\mathbf{u}=\mathbf{u}^{(n+1,m)}} \delta_{kc} \right) \big(\nabla \psi^i \cdot \nabla u_b^{(n+1,m)} \big) \psi^j d\hat{\Omega} \\
&- \int_{\hat{\Omega}} \left(\left. \frac{\partial t_+^0(\mathbf{u})}{\partial u_l} \right|_{\mathbf{u}=\mathbf{u}^{(n+1,m)}} \right) \left(\left(\left. \frac{\partial \mathbf{i}(\mathbf{u})}{\partial u_k} \right|_{\mathbf{u}=\mathbf{u}^{(n+1,m)}} \delta_{kc} \right) \cdot \nabla u_l \right) g_a \psi^i \psi^j d\hat{\Omega} \\
&- \int_{\hat{\Omega}} \left(\left. \frac{\partial t_+^0(\mathbf{u})}{\partial u_k} \right|_{\mathbf{u}=\mathbf{u}^{(n+1,m)}} \delta_{kc} \right) \Big(\mathbf{i}(\mathbf{u}^{(n+1,m)}) \cdot \nabla \psi^j \Big) g_a \psi^i d\hat{\Omega} \\
&- \int_{\hat{\Omega}} \left(\left. \frac{\partial^2 t_+^0(\mathbf{u})}{\partial u_k \partial u_l} \right|_{\mathbf{u}=\mathbf{u}^{(n+1,m)}} \delta_{kc} \right) \Big(\mathbf{i}(\mathbf{u}^{(n+1,m)}) \cdot \nabla u_l^{(n+1,m)} \Big) g_a \psi^i \psi^j d\hat{\Omega} \\
&- \int_{\hat{\Omega}} \left(\left. \frac{\partial f_a(\mathbf{u})}{\partial u_k} \right|_{u=u^{(n+1,m)}} \delta_{kc} \right) \psi^i \psi^j d\hat{\Omega} \Bigg] \delta \bar{u}_c^j \\
&= - \int_{\hat{\Omega}} \sum_{p=n-k+1}^{n+1} \frac{A_{ab}\alpha_p}{\tau} u_b^{(p,m)} \psi^i d\hat{\Omega} \\
&- \int_{\hat{\Omega}} B_{ab}(\mathbf{u}^{(n+1,m)}) \big(\nabla \psi^i \cdot \nabla u_b^{(n+1,m)} \big) d\hat{\Omega} \\
&+ \int_{\hat{\Omega}} \left(\left. \frac{\partial t_+^0(\mathbf{u})}{\partial u_k} \right|_{\mathbf{u}=\mathbf{u}^{(n+1,m)}} \right) \Big(\mathbf{i}(\mathbf{u}^{(n+1,m)}) \cdot \nabla u_k^{(n+1,m)} \Big) g_a \psi^i d\hat{\Omega} \\
&+ \int_{\hat{\Omega}} f_a(\mathbf{u}^{(n+1,m)}) \psi^i d\hat{\Omega}
\end{aligned} \tag{2.141}$$

where δ_{lk} is the Kronecker delta function, defined as,

$$\delta_{lk} = \begin{cases} 1 & k = l \\ 0 & k \neq l \end{cases} \tag{2.142}$$

At this point, the LHS is an $n \times n$ square matrix with indices a and c, where n is the number of equations in the system. Each element contains the corresponding equation's a'th Jacobian matrix with respect to the c'th solution variable variance. The Jacobians are $N \times N$ matrices with indices i and j. Likewise, the RHS is a vector with index a and length n, where each element is the residual vector for that equation, with index i and size N. The domain of integration becomes the domain of each cell, $\hat{\Omega}$. This step is not trivial but does not offer much towards understanding. Therefore a derivation is provided in Appendix A.10.

The boundary terms drop out of the equation for the cells that do not share an edge with the edge of the simulation domain. As such, they have been left out of the derivation and will be considered further in Section 2.4.4.

The discretized form of an arbitrary governing equation, α, in the system is now in the linear form,

$$\left(\boldsymbol{M}\delta\bar{\mathbf{u}}\right)_{\alpha} = \mathbf{b}_{\alpha} \tag{2.143}$$

and can be directly implemented into the application. OpenFCST then uses various linear solver techniques to obtain a solution for the shape function coefficients for that time step, i.e., $\delta\bar{\mathbf{u}}$. The guess for the next iteration will then use the previous iteration's guess plus the variance, $\mathbf{u}^{(n+1,m+1)} = \mathbf{u}^{(n+1,m)} + \delta\mathbf{u}$, obtained using Equation (2.140). Once a reasonable tolerance has been achieved, the program will save the solution for that time step and move on to the next time step using this solution as its initial guess.

2.4.4 Boundary Conditions

This section outlines the use and implementation of each type of boundary condition into the OpenFCST program. Recall that the boundary term omitted in Section 2.4.3

for an arbitrary equation, α, is given by,

$$\left(\oint_{\partial\hat{\Omega}} \mathbf{n} \cdot \left(\boldsymbol{B}(\mathbf{u}^{(n+1,m+1)}) \nabla \mathbf{u}^{(n+1,m+1)} \right) \psi^i d\Gamma \right)_\alpha \tag{2.144}$$

The following subsections outline the various methods of applying this boundary term to the boundary conditions outlined in Sections 2.1.3 and 2.2.3.

2.4.4.1 Dirichlet Boundary Condition

A Dirichlet boundary condition is one in which the value of the solution variable at that boundary is directly imposed, such as the solid phase potential at the cathodic current collector. The process of implementing this condition is to ensure that the initial solution guess meets the requirements of this boundary, and then forcing the solution update to zero at those points. Since the solution is known, the test function is forced to zero such that the integral in Equation (2.144) will disappear, and thus not be used at all. This boundary condition can account for temporally fluctuating boundary values by imposing values of the affected solution variables prior to the first iteration in each new time step.

2.4.4.2 Neumann Boundary Condition

A Neumann boundary condition describes the flux of a solution variable across the boundary of the domain. Examples of this would be the no-flux boundary condition at the lateral domain walls or the imposed current at the planar anodic electrode.

For the no-flux current or concentration boundaries, the boundary integral (2.144) will become zero and can be neglected all-together.

An imposed current is accounted for through the use of Equations (2.64) and (2.65). By applying these equations to the boundary integral (2.144), the following equations can be used to impose the current boundary condition for the species transport and

MacInnes equations, respectively:

$$\left(\oint_{\partial\hat{\Omega}} \mathbf{n} \cdot \left(\boldsymbol{B}(\mathbf{u}^{(n+1,m+1)}) \nabla \mathbf{u}^{(n+1,m+1)} \right) \psi^i d\Gamma \right)_1 = \frac{t_+^0 - 1}{F} \oint_{\partial\hat{\Omega}} \mathbf{n} \cdot \mathbf{i}^{(n+1)} \psi^i d\Gamma \tag{2.145}$$

$$\left(\oint_{\partial\hat{\Omega}} \mathbf{n} \cdot \left(\boldsymbol{B}(\mathbf{u}^{(n+1,m+1)}) \nabla \mathbf{u}^{(n+1,m+1)} \right) \psi^i d\Gamma \right)_2 = - \oint_{\partial\hat{\Omega}} \mathbf{n} \cdot \mathbf{i}^{(n+1)} \psi^i d\Gamma \tag{2.146}$$

Since the current will remain constant within the nonlinear iterations, the $m+1$ superscript can be dropped. The transient superscript, however, will remain because the current may be time dependant (e.g. for EIS or potentiostatic ramp tests).

2.4.4.3 Complex Boundary Condition

When applying a cell voltage, no direct information is given about the solution variables being solved for (neither their values, nor their fluxes). What is provided, however, is the potential of the out-of-domain electrode, ϕ_{sp}. Equation (2.87) describes how a current can be calculated through the use of the Butler-Volmer kinetics, given values for the solution variables, $\mathbf{u}$. Therefore, $\mathbf{i}(\mathbf{u})$ is an implicit term and must be solved for within the Newton loop. Using Equations (2.145) and (2.146), the boundary integral terms become,

$$\left(\oint_{\partial\hat{\Omega}} \mathbf{n} \cdot \left(\boldsymbol{B}(\mathbf{u}^{(n+1,m+1)}) \nabla \mathbf{u}^{(n+1,m+1)} \right) \psi^i d\Gamma \right)_1 \tag{2.147}$$

$$= \frac{t_+^0 - 1}{F} \oint_{\partial\hat{\Omega}} \mathbf{n} \cdot \mathbf{i}(\mathbf{u}^{(n+1,m+1)}) \psi^i d\Gamma \tag{2.148}$$

$$\left(\oint_{\partial\hat{\Omega}} \mathbf{n} \cdot \left(\boldsymbol{B}(\mathbf{u}^{(n+1,m+1)}) \nabla \mathbf{u}^{(n+1,m+1)} \right) \psi^i d\Gamma \right)_2 \tag{2.149}$$

$$= - \oint_{\partial\hat{\Omega}} \mathbf{n} \cdot \mathbf{i}(\mathbf{u}^{(n+1,m+1)}) \psi^i d\Gamma \tag{2.150}$$

for the species flux and current terms, respectively. Applying the linearization technique in Equation (2.133), these equations become,

$$\begin{aligned}\left(\oint_{\partial\hat{\Omega}} \mathbf{n} \cdot \left(\boldsymbol{B}(\mathbf{u}^{(n+1,m+1)}) \nabla \mathbf{u}^{(n+1,m+1)} \right) \psi^i d\Gamma \right)_1 \\ = \frac{t_+^0 - 1}{F} \oint_{\partial\hat{\Omega}} \mathbf{n} \cdot \left(\mathbf{i}(\mathbf{u}^{(n+1,m)}) + \left(\frac{\partial \mathbf{i}(\mathbf{u})}{\partial u_k} \right) \Big|_{u=u^{(n+1,m)}} \psi^j \delta \bar{u}_k^j \right) \psi^i d\Gamma\end{aligned} \tag{2.151}$$

$$\begin{aligned}\left(\oint_{\partial\hat{\Omega}} \mathbf{n} \cdot \left(\boldsymbol{B}(\mathbf{u}^{(n+1,m+1)}) \nabla \mathbf{u}^{(n+1,m+1)} \right) \psi^i d\Gamma \right)_2 \\ = - \oint_{\partial\hat{\Omega}} \mathbf{n} \cdot \left(\mathbf{i}(\mathbf{u}^{(n+1,m)}) + \left(\frac{\partial \mathbf{i}(\mathbf{u})}{\partial u_k} \right) \Big|_{u=u^{(n+1,m)}} \psi^j \delta \bar{u}_k^j \right) \psi^i d\Gamma\end{aligned} \tag{2.152}$$

The first term in the integral can be incorporated into the residual vector of Equation (2.143), and the derivative term can be included in the Jacobian matrix.

Chapter 3

Results

3.1 Symmetric Cell Analysis

Before an effective model for the macro-scale LiB can be developed and analyzed, the correctness of the electrolyte equations and their implementation must first be confirmed. These equations were isolated by eliminating the porous electrode altogether and only considering the separator layer, sandwiched between two planar Li-foil electrodes. First, the model described in Section 2.1 was used to reproduce the experimental results by Pesko *et al.* in reference [105]. Then, a sensitivity analysis of each input parameter in the model was conducted. This provided insights that would be used to discuss the differences between the computational model and the results from the literature. Finally, the OpenFCST model is applied to an electrolyte for which no computational study has yet been performed. This is compared with experimental results and discussed.

Since the symmetric cell was built using a coin cell configuration, transport is assumed uniform in the radial direction of the cell and varying only in the axial direction (i.e. the x-coordinate). While the edges of the cell will impact the cell performance in a real system, the larger the diameter of the cell, the smaller this effect will be and the closer the model will become to reality. The simulation domain for this application can therefore be modelled in one-dimension only. OpenFCST is designed to operate in either 2- or 3-dimensions. Therefore, for this analysis, a

2-dimensional equally sized quadrilateral mesh with a width in the y-direction of only one cell was used.

3.1.1 Validation

The system was validated by reproducing experimental results obtained from the literature for the geometry and conditions described in Section 2.1.

Using the various experimental methods described in Section 2.3, Pesko *et al.* measured the input parameters for LiTFSI in PEO for various Li^+ concentrations at 90°C [103, 105]. The data points presented in the figures in Section 2.3 are directly obtained from their published work. While they also provided piece-wise polynomial expressions for the input parameters, these did not match the data points provided in the same paper; in some cases, being orders of magnitude different. Therefore, new polynomial expressions were created for this work, shown visually by the solid trend line in the aforementioned figures.

Pesko *et al.* also ran galvanostatic experiments of a symmetric cell containing various concentrations of LiTFSI in PEO at various current densities. Using the input parameters mentioned, the OpenFCST model could be validated by comparing its results with the results from these experiments.

The domain of the OpenFCST simulation was 500 μm, refined into 500 cells (therefore, making each cell 1 μm thick). This domain thickness was chosen as it is wide enough for spatial variations to be detected for relatively low current densities. The refinement was chosen because it is fine enough not to introduce significant numerical error while still large enough to keep computational times low. By decreasing the cell thickness to 0.5 μm (i.e., 1000 cells), the cell voltage at steady-state changed by only 0.00001%. The simulation time step was progressed at 1 s intervals, for a total simulation time of 4 hours. Decreasing the time step to 0.5 s only decreased the steady-state cell voltage by 0.001%.

The direct linear solver used in this analysis is the MUltifrontal Massively Parallel

Solver (MUMPS) [149] and the numerical integration was performed using the deal.II library [150]. The tolerance of the nonlinear solver, as outlined in Section 2.4.2, is 10^{-8}. The simulation was run on 12 AMD cores using an MSI computer with 32GB of RAM. The simulations in Section 3.1.1 averaged 48 s to complete and the simulations in Section 3.1.2 averaged 27 s, both using the fuel_cell-2D executable.

3.1.1.1 Comparison with the Literature

Pesko *et al.* presented experimental results for the symmetric cell application in reference [105] using LiTFSI in PEO. Because of the dendrite growth at higher current densities, leading to inaccurate results and eventually short circuiting, Pesko's work focused on very low current densities. Low current densities result in gradual concentration and potential gradients, therefore the separator thickness in their study was significantly extended to allow for larger changes in the solution variables across the domain (i.e., 500 μm instead of a typical 25 μm).

Figure 7a in ref [105] provides their experimental cell voltage responses over time when running the symmetric cell with an initial Li^+ concentration of 2.76 M at varying current densities, ranging from 0.02 to 0.25 mA/cm^2. Figure 7b isolates the effect of the electrolyte by removing the overpotential effects. This was done by performing EIS tests, fitting the model to an equivalent circuit, and determining the overpotential contribution from the low frequency range. This contribution could then be subtracted from the cell potential to isolate for the electrolyte contribution only, i.e., the ohmic voltage. Additionally, Figure 7b scales this voltage response by dividing by the separator thickness. This scaling was performed because one would expect that, by scaling the cell thickness, the ohmic voltage would scale by the same factor, allowing for a more general analysis.

The OpenFCST model was run under the same conditions as Pesko *et al.*, given the model described in Section 2.1 and the input parameters in Section 2.3. The main.prm and data.prm configuration files for this simulation are given in Appendix B.1. The

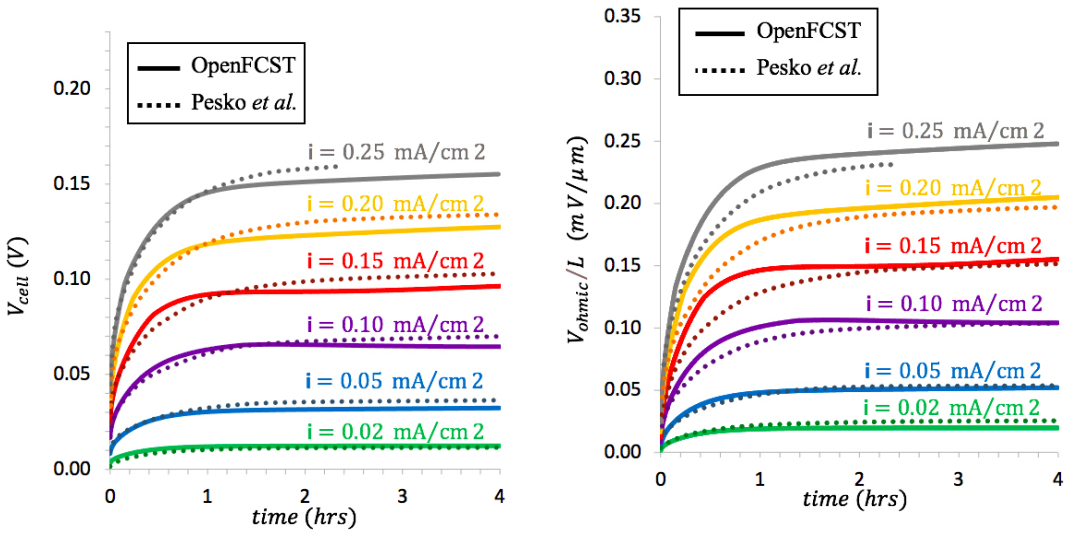

(a) Cell voltage

(b) Scaled cell voltage, isolating for electrolyte influence only.

Figure 3.1: Symmetric cell discharge with varying current densities and a 2.76 M initial Li^+ concentration using OpenFCST simulation results and Pesko *et al.* experimental results [105].

results are presented in Figure 3.1, alongside Pesko *et al.*'s experimental results. Figure 3.1a is the cell voltage response (equivalent to Figure 7a in ref [105]) and Figure 3.1b is the ohmic voltage response (obtained by eliminating the overpotential due to surface kinetics) scaled by the separator thickness (which is equivalent to Figure 7b in ref [105]). The overpotential was eliminated in the OpenFCST model by replacing the Robin boundary conditions described in Section 2.4.4.3 by Dirichlet and Newman conditions on either side. Because the solution variable, ϕ_R, is the solid potential of a reference electrode, its difference across the cell will be exactly equal to the ohmic voltage. Note the experimental curve for a current density of 0.25 mA/cm^2 abruptly ends at about two hours. This is due to the cell experiencing failure at this point, likely due to dendrite growth.

While not perfect, the simulation results do an adequate job of replicating the experimental results. As expected, the cell voltage increases as current density increases and the cell voltage within each test initially increases sharply before approaching a steady state value. In particular, the steady-state cell voltage in Figure 3.1b is re-

markably similar for the simulation and experimental results. These results provide validation that the model presented in Section 2.1 is applicable for this system.

Figure 3.2 provides insight into the steady-state simulations by plotting the solution variable profile's within the simulation domain for three current densities: 0.02, 0.05, and 0.10 mA/cm^2. From Figure 3.2a, it is clear that the average concentration remains at 2.76 M, regardless of the current density. This is because the anions cannot leave the electrolyte and, because of electroneutrality, there cannot be an accumulation of charge (neglecting the DL). This means that for every Li^+ ion that leaves the electrolyte, one must enter. The downward slope is expected, as discussed in Section 2.1.1. The stronger the current, and therefore the electric field, the steeper the gradient must be for the anion to balance the electric attraction. The ϕ_R plot in Figure 3.2b demonstrates the losses that occur spatially due to Li^+ transport. As current density increases, the losses become more pronounced as energy is lost to the environment via heat. These plots demonstrate that the model does produce realistic results.

Given the variability of the input parameters with Li^+ concentration, the question arises as to whether one would observe the same agreement with experiments for a different initial concentration. In Figure 8 of reference [105], Pesko *et al.* provides the SS voltage from experimentally testing a symmetric cell with a 0.02 mA/cm^2 current density for different initial Li^+ concentrations. These results are presented in Figure 3.3, along with the simulated results for the same concentrations, using the developed OpenFCST model. The error bars represent the standard deviation of the experimental data.

The OpenFCST model provides strong agreement with experiments for concentrations between 1 M and 3 M. The data points fall within or very close to the error bars and the general trend, including the local peak at 2.38 M, is also captured.

The SS cell voltage at both Li^+ concentration extremes deviate from experimental observations, especially at higher concentrations. One possible explanation for this

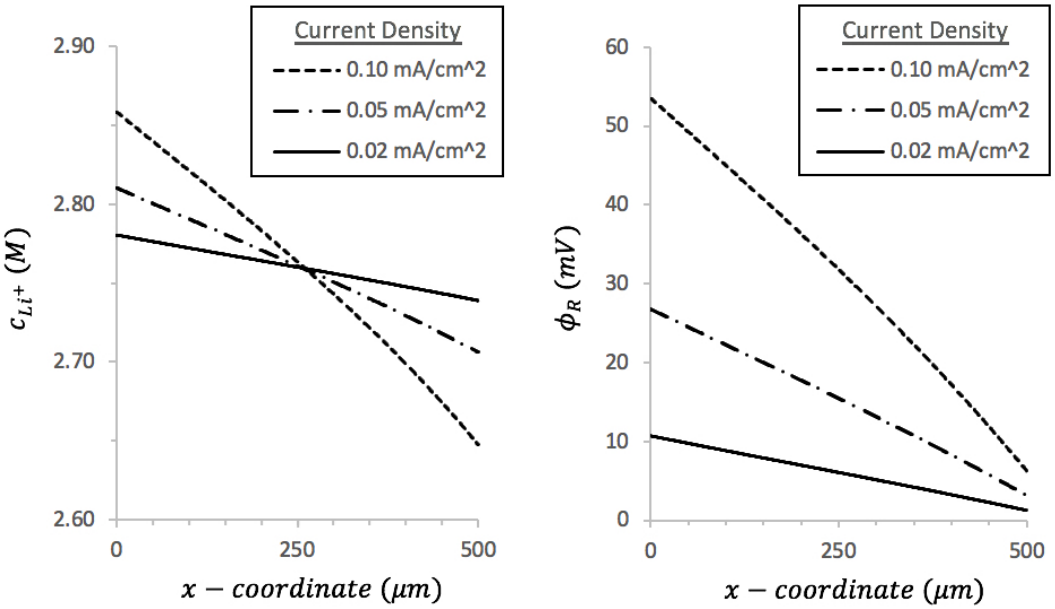

(a) Li^+ concentration (b) Reference Li/Li^+ electrode potential.

Figure 3.2: Steady state spatial profiles due to varying current densities for (a) the Li^+ concentration and (b) solid potential of a reference Li/Li^+ electrode.

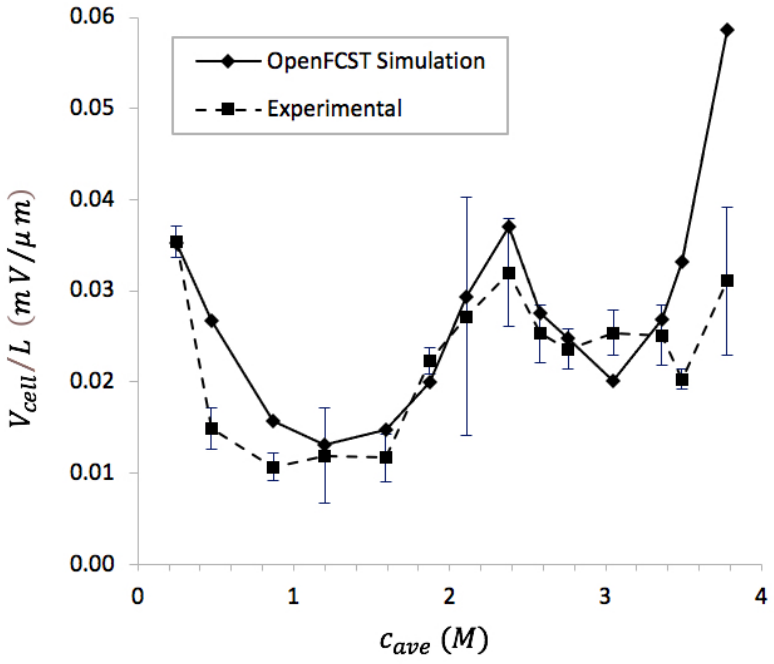

Figure 3.3: Symmetric cell steady-state voltage response to a 0.02 mA/cm^2 current for varying initial concentrations. Comparing experimental results with OpenFCST model. Experimental results reproduced from ref [105].

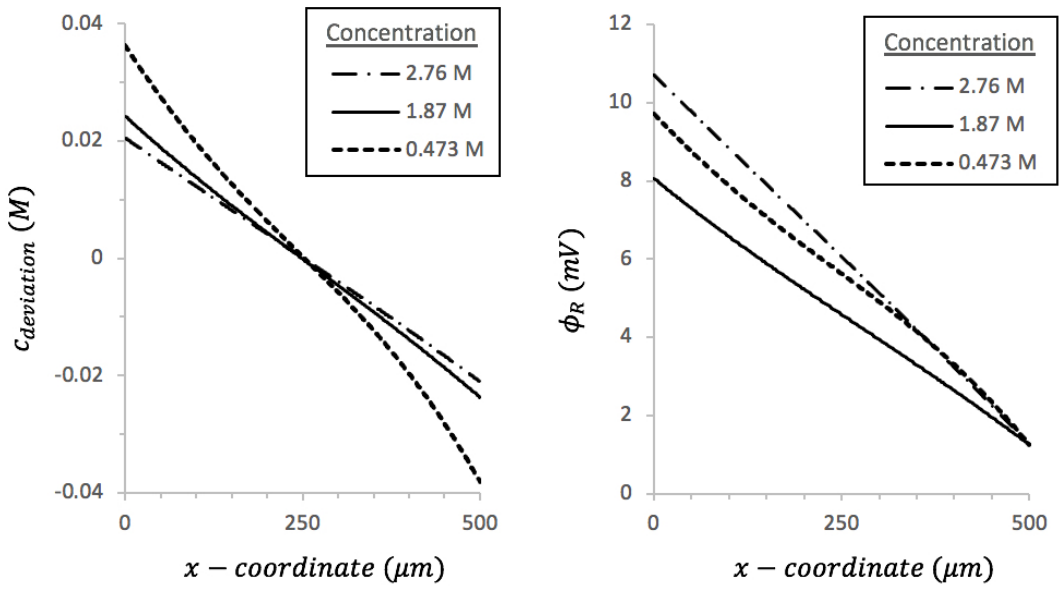

(a) Li^+ concentration deviation (b) Reference Li/Li^+ electrode potential.

Figure 3.4: Steady state spatial profiles due to varying average Li^+ concentration for (a) the deviation in Li^+ concentration from the average and (b) solid potential of a reference Li/Li^+ electrode.

is that the input variables are not parameterized below 0.25 M and above 3.78 M and therefore, although the average Li^+ concentration is within the defined range, the concentration gradient will force the extremities to operate at concentrations for which the parameters are not defined.

The valleys in the SS cell voltage profile occur in the vicinity of 1 M and 3 M. These ranges are of practical importance as they are the concentration ranges for which batteries are designed to operate. The local maxima at low and high concentrations and at 2.38 M correspond to regions in which internal resistance is increased due to hindered Lithium transport. This is a result of either a low diffusion coefficient or low transference number.

Figure 3.4 provides the internal solution variable profiles at steady state for the symmetric cell undergoing a 0.02 mA/cm^2 current density with average Li^+ concentrations of 0.473, 1.87, and 2.76 M. For readability, the concentration profiles are displayed as their deviation from the average current. As expected, each plot shows a

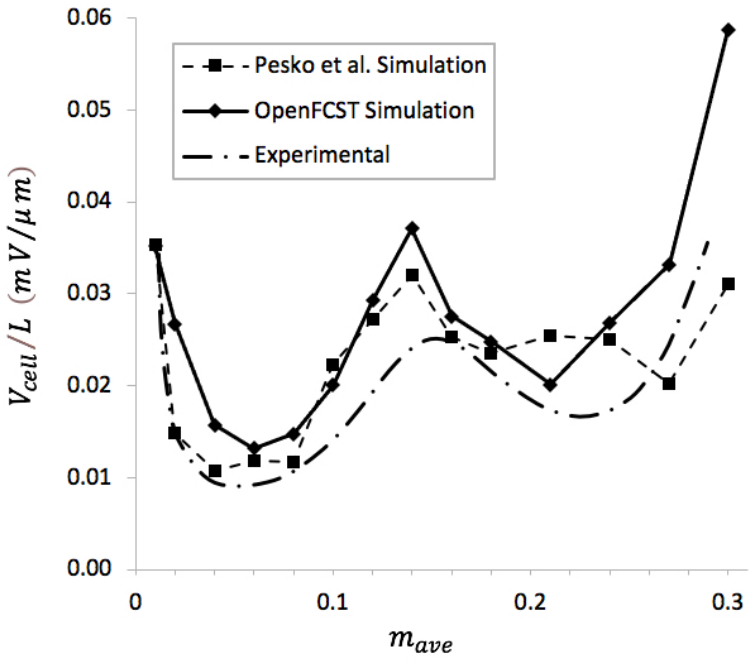

Figure 3.5: Symmetric cell steady-state voltage response to a 0.02 mA/cm^2 current for varying initial concentrations. Comparing experimental results with Pesko *et al.* SS model. Reproduced from ref [105].

downward trend between electrodes. The fluctuation in each profile is a result of the input parameter's Li^+ concentration dependencies. The gradient of concentration for the 0.473 M symmetric cell exhibits the strongest slope. This is to be expected considering the role that the thermodynamic factor plays in the boundary conditions, i.e., Equation (2.64). The thermodynamic factor for the 0.473 M case is much smaller than the other two, meaning the magnitude of the gradient in concentration must increase to compensate.

Figure 3.5 shows the results produced using Pesko *et al.*'s SS computational model for the SS voltage responses to a 0.02 mA/cm^2 current density at varying Li^+ concentrations. Note in this figure, the cell voltages are given as a function of molality instead of molarity. This is because the simulation results presented in ref [105] were given with respect to molality. It is clear that, despite only being a steady state model, they too observe a comparable error with the experimental results.

The key differences between the OpenFCST model and the model used in Pesko

et. al.'s work, besides the OpenFCST model being multi-dimensional, is the transient versus steady-state capability, the boundary condition equations, and perhaps the input parameterization.

The steady-state result for the OpenFCST model was obtained by running a transient simulation and recording the cell voltage when the system has achieved a steady-state solution. Pesko's model for obtaining the plot in Figure 3.5 does not contain transient elements, and therefore directly solves for the steady state. While, in theory, this should lead to the same result, it will also magnify other differences.

Perhaps the most significant difference between the two models is Pesko's choice of boundary conditions. In ref [105] they state that the 1D boundary conditions with respect to the species transport equation are,

$$-D\frac{dc_{Li^+}}{dx}\bigg|_{x=0} = \frac{1-t_+^0}{F}\mathbf{i}_{SS} \qquad \text{(16) in ref [105]}$$

$$-D\frac{dc_{Li^+}}{dx}\bigg|_{x=\delta} = -\frac{1-t_+^0}{F}\mathbf{i}_{SS} \qquad \text{(17) in ref [105]}$$

From the derivation in Section 2.1.3.1, it is clear that the LHS of these two equations should be multiplied by the molality correction factor, as in Equation (2.64). It is known that this factor is not merely lumped into the diffusion coefficient, D, in these reported equations because it is present in their Li^+ transport equation (that is, Equation (15) in ref [105]), from which the two BCs should derive. Figure 3.6 demonstrates the effect of not including the molality correction factor, by simulating the same conditions using the OpenFCST model but with the boundary conditions described in Equations (16) and (17) of reference [105]. It is clear that these boundary conditions will cause a significant error in predicted SS voltage, when comparing the two OpenFCST models. Unlike the actual OpenFCST model, which exceeds the voltages expected from Pesko *et al.*, the model with the alternative BCs shows diminished SS voltages, but to a similar degree. Therefore, it is inconclusive as to whether Pesko's model did in fact use incorrect BCs or whether they were correctly implemented and only reported incorrectly in the article.

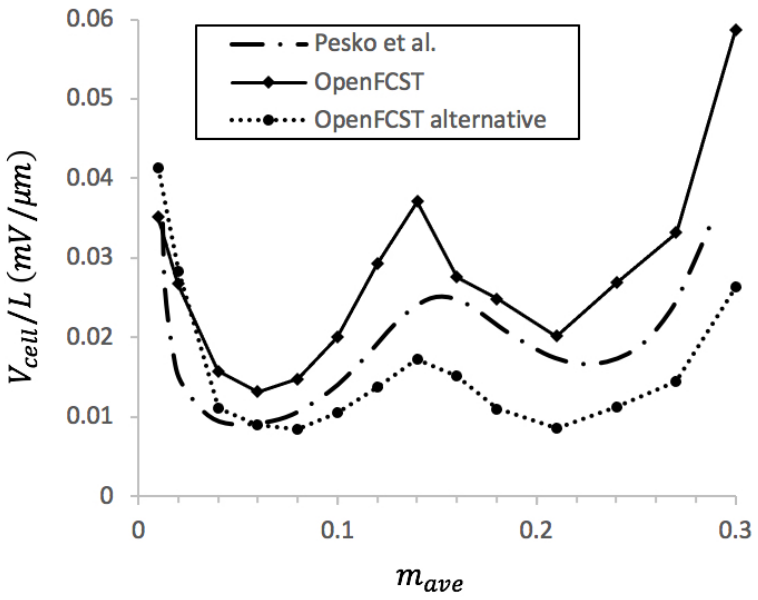

Figure 3.6: Comparison between model implementations of steady state voltage for the symmetric cell system with varying Li^+ concentrations at a constant current density of 0.02 mA/cm^2. Models include Pesko *et al.*'s model, the OpenFCST model, and the OpenFCST model using the same boundary conditions as in Equations (16) and (17) or ref [105], denoted as OpenFCST alternative.

Finally, the equations provided in ref [105] describing the relationship between the input parameters and the Li^+ concentration for LiTFSI in PEO do not match their own data points. Additionally, these equations are given in piece-wise notation and they are very discontinuous between the two defined regions. The parameterization that was used in this work was based on the best-fit line for the raw data points that were also provided in the same article. Therefore, it is very likely that the OpenFCST parameterizations are slightly (or perhaps significantly) different to those implemented in Pesko's model.

3.1.1.2 Parametric Studies

This section provides a better understanding of how each input parameter influences the performance of the cell by simulating and comparing the cell response to an instantaneous step in current for varying electrolyte input parameters. The influence of each parameter was isolated and studied by simulating LiTFSI in PEO and increasing

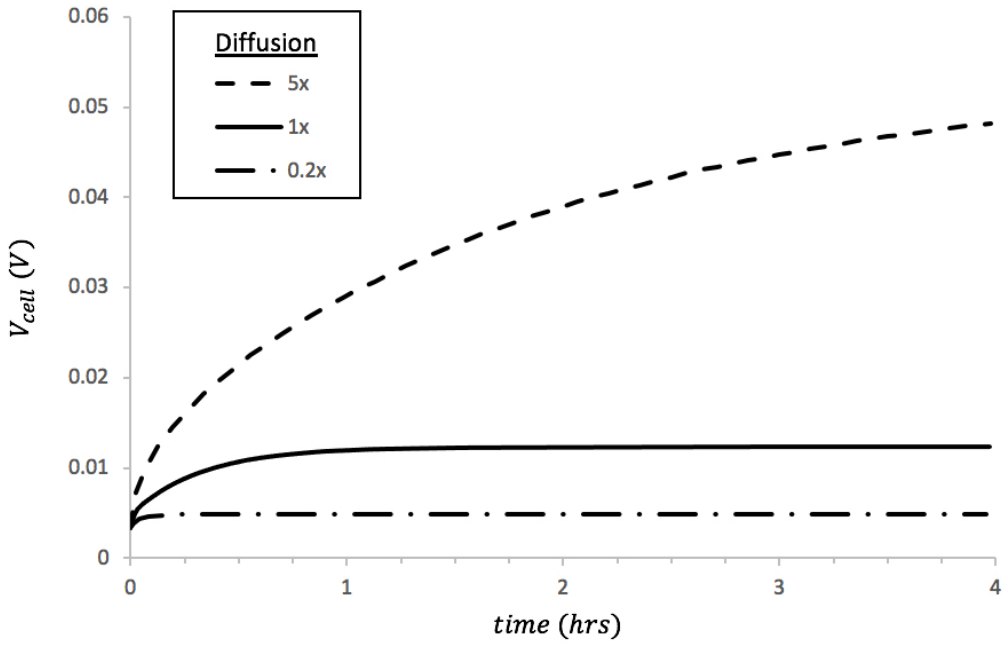

Figure 3.7: Characteristic curve from a 0.02 mA/cm^2 current density for LiTFSI in PEO electrolyte in symmetric-cell configuration with varying salt diffusion coefficient at 90°C. All other input parameters are held constant.

or decreasing the parameter in question while keeping all other parameters the same. These simulations were all performed at 0.02 mA/cm^2 and 2.76 M, as these are the conditions at which Pesko *et al.* studied the cell.

3.1.1.2.1 Diffusion Coefficient

The parametric study for the salt diffusion coefficient is presented in Figure 3.7. The nominal value for diffusion, for the LiTFSI in PEO electrolyte, is $9{\cdot}10^{-8}$ cm^2/s for an Li^+ concentration of 2.76 M. These values were adjusted from one fifth to five times its nominal value.

Evidently, the diffusion coefficient has a significant effect on cell performance for both the SS voltage of the cell and the time scales required to obtain this steady state. By decreasing the diffusion coefficient, it is observed that the cell voltage required to achieve the same current density increases. Mathematically, this follows from the diffusion coefficient being the proportionality factor between the gradient of

concentration and the diffusion driving force. By increasing the diffusion coefficient, the influence of a concentration gradient increases and therefore a lower gradient is required to maintain the same current.

The time scale also increases as diffusion decreases (stretching the plot horizontally), for two reasons. The first is a result of this need to create a larger concentration gradient when decreasing the diffusion coefficient. Naturally, it would take longer to create a steep gradient. The second is that, by decreasing diffusion, the mobility of the ions decreases, thus slowing the development of the concentration gradient profile. This is supported by the Einstein relation [151, 152], i.e.,

$$D = k_B T u \tag{3.1}$$

where u is the ionic mobility and k_B is the Boltzmann constant. While this equation is only strictly true of DST, it is a valuable approximation for the relationship between diffusion and mobility.

3.1.1.2.2 Conductivity

Figure 3.8 shows the parametric study for conductivity values ranging from one tenth to ten times its nominal value (which, for LiTFSI in PEO is $1.6{\cdot}10^{-3}$ S/cm for an Li^+ concentration of 2.76 M).

Because both driving force terms in Equation (2.55) contain a pre-factor of κ, the increased potential required to account for the developing concentration gradient will remain constant, regardless of conductivity. This explains why, besides the vertical shift, the cell voltage response profiles in Figure 3.8 look the same. The vertical shift exists because the ionic conductivity quantifies the ohmic resistance (i.e. the proportionality between the current and potential gradient). This means that a decreased conductivity will increase ohmic resistance thus shifting the cell potential vertically upwards, and vice versa.

As will be discussed in Section 3.1.1.2.5, altering the exchange current density will have a similar effect on the cell voltage profile as conductivity does. The influences of

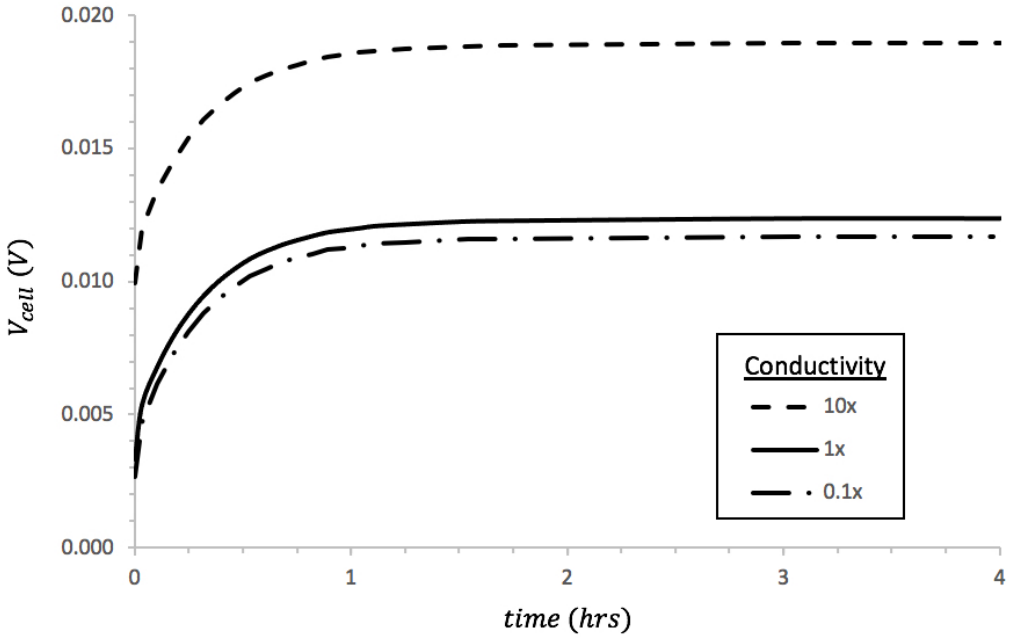

Figure 3.8: Characteristic curve from a 0.02 mA/cm^2 current density for LiTFSI in PEO electrolyte in symmetric-cell configuration with varying ionic conductivity at 90°C. All other input parameters are held constant.

these parameters are easily distinguished from one another by considering the effect of linearly scaling the thickness of the cell. Because the conductivity will influence the potential gradient, by enlarging the size of the cell, the cell voltage will also increase, proportional to the conductivity. The exchange current density, on the other hand, affects only the overpotential developing at the reaction surfaces and therefore will be independent of the thickness of the cell.

3.1.1.2.3 Transference Number

The parametric study for the positive transference number is given in Figure 3.9. The study is conducted by altering the transference number of LiTFSI in PEO by its nominal value plus 0.3 to the nominal value minus 0.3. The value nominal value is 0.1 for a Li^+ concentration of 2.76 M.

The transference number appears in both governing equations and boundary conditions of the symmetric cell system. In the boundary conditions, Equation (2.64)

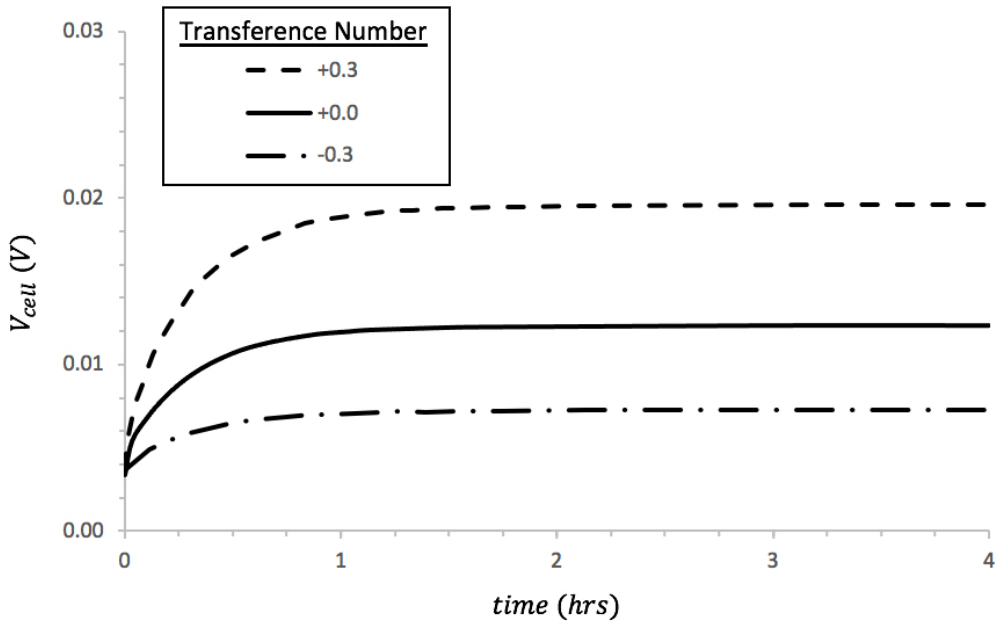

Figure 3.9: Characteristic curve from a 0.02 mA/cm^2 current density for LiTFSI in PEO electrolyte in symmetric-cell configuration with a varying positive transference number at 90°C. All other input parameters are held constant.

states that the magnitude of the gradient in Li^+ concentration increases when transference decreases. This is due to the mobility of Lithium ions decreasing compared to the anions. Further, the transference number also appears in the pre-factor for the concentration gradient term in Equation (2.55). By decreasing the transference number, the concentration gradient will provide a greater contribution to the current passing through the cell. Because both of these effects will contribute to the potential in the same way, the linear decrease in transference number will result in a quadratic increase in the cell potential. This quadratic relationship is observable in Figure 3.9 in that there is a larger gap between the nominal value and the +0.3 plot than between the nominal value and -0.3 plot.

3.1.1.2.4 Thermodynamic Factor

Figure 3.10 displays the parametric response of increasing the thermodynamic factor of the LiTFSI in PEO electrolyte from one fifth to five times its nominal value. The

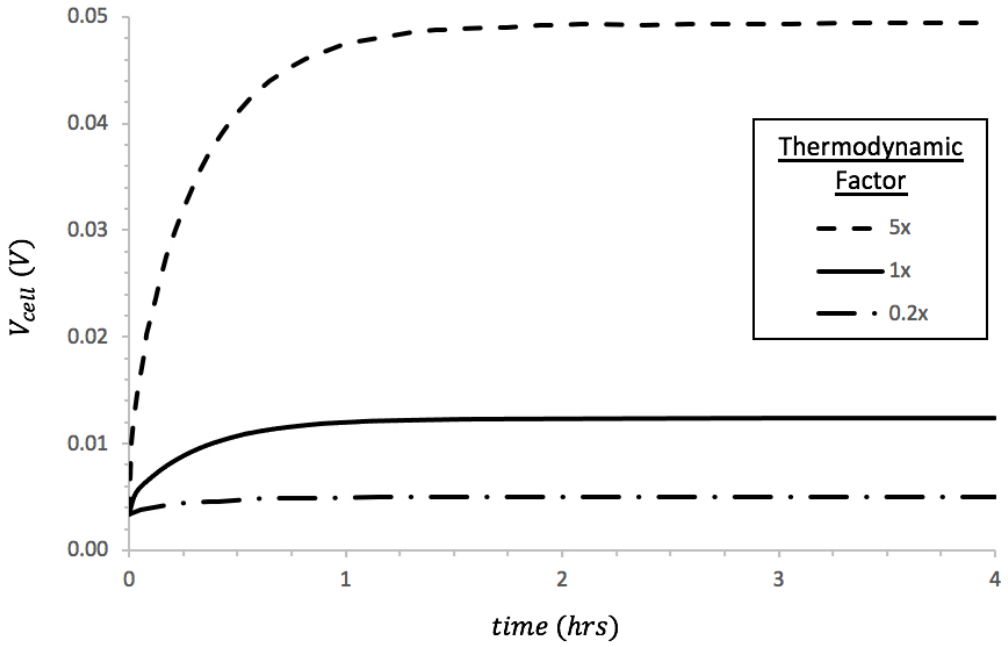

Figure 3.10: Characteristic curve from a 0.02 mA/cm^2 current density for LiTFSI in PEO electrolyte in symmetric-cell configuration with varying thermodynamic factor at 90°C. All other input parameters are held constant.

nominal value is 3.74 for an Li^+ concentration of 2.76 M.

The response to increasing the thermodynamic factor of the electrolyte is a vertical stretch in the cell potential. This is because the thermodynamic factor merely adjusts the relationship between the concentration and potential gradients. Note that the effect of the thermodynamic factor and the transference number will be similar. One way to distinguish between the influence of each parameter, is to investigate the Li^+ concentration profile in the cell during discharge. While changing the transference number will impact the concentration gradient, changing the thermodynamic factor will have no effect on the developed gradient.

3.1.1.2.5 Exchange Current Density

Finally, although the exchange current density is not a characteristic of the electrolyte itself but rather of the reaction at the electrode surface, it is still parameterized and discussed in this section because its effect can be easily confused with that of the ionic

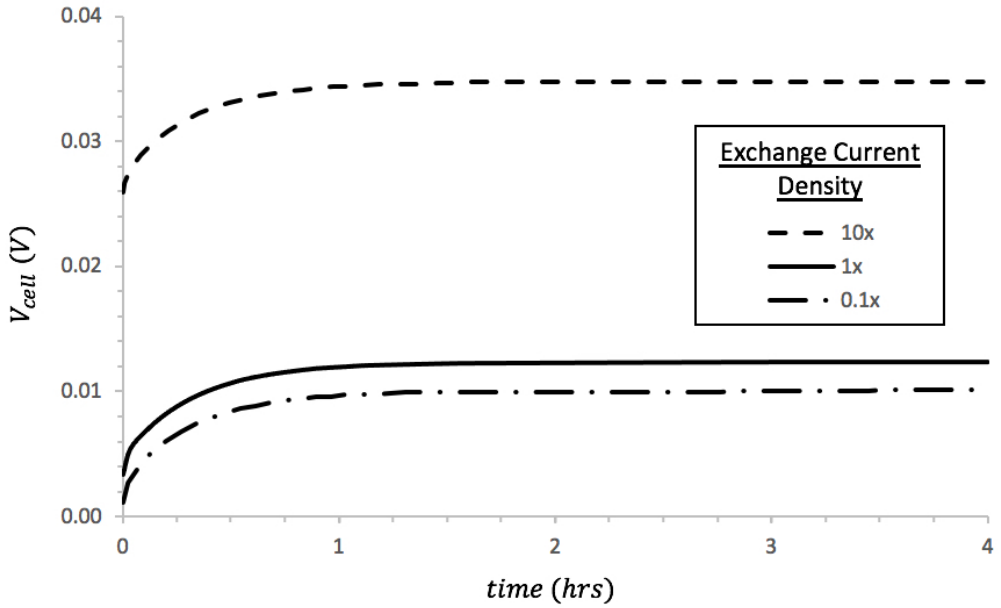

Figure 3.11: Characteristic curve from a 0.02 mA/cm^2 current density for LiTFSI in PEO electrolyte in symmetric-cell configuration with varying exchange current density at 90°C. All other input parameters are held constant.

conductivity, as discussed in Section 3.1.1.2.2. Figure 3.11 shows the cell response to altering the exchange current density by a factor of ten larger and smaller than its nominal value of 0.5 mA/cm^2.

As with the conductivity, the exchange current density parametric study shows simply a vertical shift in the voltage response profile. This is because, with a smaller current density, a larger overpotential is required to supply the same current at the planar electrodes. As stated, this overpotential is dependent on the reaction itself and will remain constant with a changing cell thickness. The current density may be increased or decreased based on the electrode/electrolyte pairing, or the surface roughness of the electrode. A rougher surface will have more reaction surface area per cm^2 of electrode, thus increasing the reaction rate and exchange current density.

3.1.1.3 Input Parameter Discussion

By comparing the experimental and simulation results in the two plots in Figure 3.1 and in light of the information gleaned from Section 3.1.1.2, one can make assertions about the accuracy of the input values proposed in ref [105]. First, it is evident that the differences between the SS voltages obtained at sequential current densities in Figure 3.1a are closer together for the simulation results then they are for the experimental results. This, however, is the opposite in Figure 3.1b, where the simulated SS voltages are further apart. Besides scaling with cell thickness, which would have no effect on this relationship, the only adjustment between the two figures is the elimination of the surface overpotential. Due of this observation, it is concluded that the overpotential has a larger impact on cell voltage than was expected. Therefore, assuming the validity of the BV equation, the exchange current density is likely slightly larger in reality than that implemented in the numerical model. This conclusion is not surprising, as any roughness to the surface of the Lithium foil would increase its surface area and effectively increase the exchange current density.

Focusing more directly on Figure 3.1b, the major difference between the experimental and simulation results is in regard to the rate at which the system approaches a steady state. The numerical results begin to plateau at around one hour, whereas the experimental results are more gradual and plateau closer to two hours. The only input parameter associated with changing the cell voltage reaction profiles with respect to time (i.e. horizontally) is the salt diffusion coefficient. Therefore, the more gradual development of the cell voltage may suggest that the diffusion coefficient is, in reality, slightly less than that reported in ref [105]. However, this cannot be the only adjustment that would be required to match the experimental results, as a decreased diffusion coefficient would also increase the SS current, which is not observed. Therefore, by decreasing either the positive transference number or the thermodynamic factor, the SS cell voltage could once again re-approach the correct value. Which

one of these two quantities would need altering cannot be known with confidence because information about the experimental Li^+ concentration profile is not available in ref [105]. That being said, in Pesko's earlier paper [103], the transference number was obtained by fitting data, given the already determined values of the diffusion coefficient and thermodynamic factor. Therefore, because the transference number is wholly dependent on the value of diffusion, which appears to be over-estimated, it is logically concluded that this value is the culprit and is actually less than reported.

Finally, the reported value of ionic conductivity appears to agree with experiments. This is concluded by recognizing that the experimental and simulation results have similar initial cell voltages at the beginning of each test, prior to the formation of a concentration gradient.

3.1.2 Application to a Novel Electrolyte

Having validated the symmetric cell model in Section 3.1.1, this model will now be applied to a new electrolyte chemistry that is commonly used in battery applications, i.e., $LiPF_6$ in EC:DEC (1 to 1 by weight), for which previous numerical simulations have not been performed.

This electrolyte is slightly viscous, allowing for an effective study of the mass transfer phenomena. Additionally, it is one chemistry that is easily made using the experimental resources readily available for this work and for which parameterized values are available in the literature. The electrolyte is parameterized based on Lundgren et al.'s work in reference [106], which is summarized in Section 2.3. As with the model in Section 3.1.1, the cell consists of a 500 μm separator, saturated with the electrolyte and pressed between two planar Li-foil electrodes. In this case, a steady-state was reached far quicker than with the LiTFSI in PEO simulations, as a result of the increased diffusion coefficient. Therefore, the time of simulation was limited to 15 minutes, with a time step, τ, of 0.1 s. By decreasing the time step further, to 0.05 s, the steady state voltage only decreases by 0.002%.

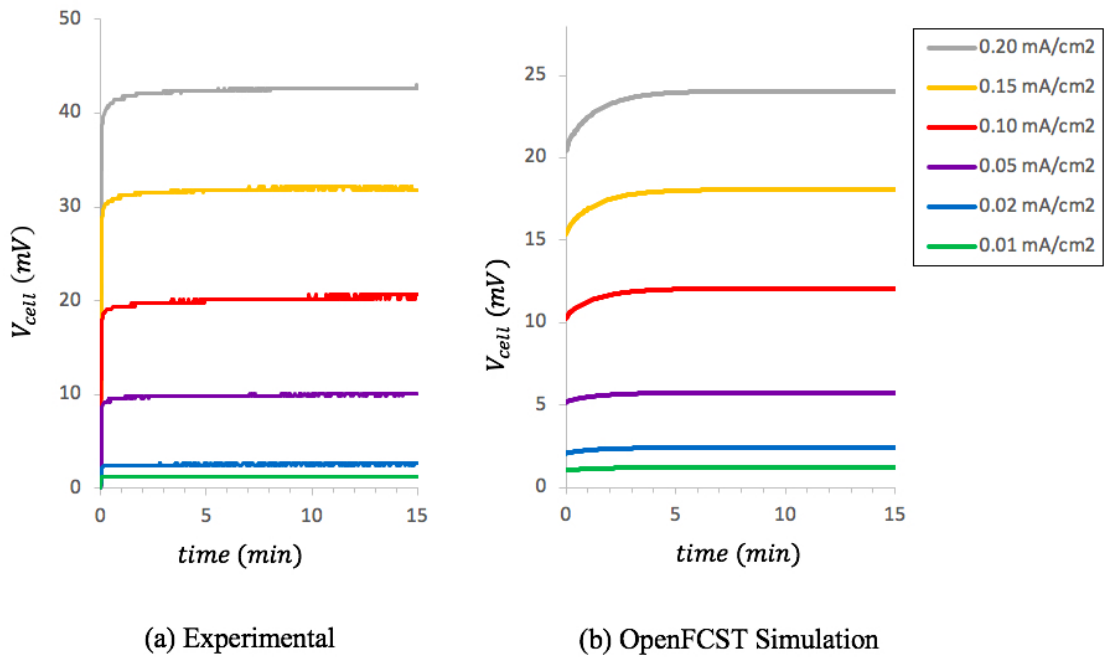

(a) Experimental (b) OpenFCST Simulation

Figure 3.12: Cell voltage response to varying current densities applied to a 500 μm symmetric cell with 0.6 M $LiPF_6$ in EC:DEC (1:1 by weight). Results presented for (a) experimental cell and (b) the OpenFCST model.

While the simulated cell was operable within a wide range of operating conditions, the experimental cell experienced difficulties at high concentrations and current densities. Eventually, testing conditions were chosen to be a constant current of 0.01 to 0.2 mA/cm^2 for a cell with 0.6 M Li^+ concentration and 25°C, and the resulting voltage response was recorded. Even for these conditions, however, the experimental setup did not always create reproducible or even steady results. Nevertheless, a set of experimental results are presented in Figure 3.12 alongside the OpenFCST simulated results.

It is apparent that the initial voltage of the symmetric cell, before the concentration gradient profile is established, is nearly twice as large for the experimental results than it is in for the simulation results. As discussed in Section 3.1.1.2, this can be attributed to one of two parameters in the electrolyte: the ionic conductivity or the exchange current density. It was earlier remarked that the cause of this large initial voltage could be determined by changing the separator thickness and observing the

result. If the exchange current density was the issue, the initial voltage would not scale with thickness and if it was the ionic conductivity, it would. Three new experimental cells with thicknesses of 125, 250, and 500 μm were created and subjected to a current density of 0.20 μm/cm^2. This same test was run for the numerical model and the results for both are presented in Figure 3.13. The simulated results show the expected change in the voltage response profile. The numerical model predicted that, by decreasing the size of the domain, the cell voltage would drop. It is evident that the overpotential constitutes the largest loss component, evident in how little the initial voltage changes between cell thicknesses. By extrapolation, the theoretical voltage loss due to overpotential is 0.0205 V. The experimental results, however, did not produce the expected result. The 125 μm cell did experience a decrease in voltage, but the 250 μm cell actually showed an increase in voltage. Additionally, the 250 μm cell profile also requires more time than the 500 μm cell profile to plateau; a relationship that should be the opposite. Finally, the 500 μm cell produced very different results than those from the identical experiment in Figure 3.12, both in magnitude and time-scale. It is therefore concluded that the experimental analysis does not create reproducible results. This likely has to do with the process in which the batteries were constructed, as the results in Figure 3.12 that are taken from a single cell show physically realistic relationships between each test but when analyzing different cells, comparison is not cohesive. One potential source of experimental error could be attributed to surface imperfections or SEI layer development. These non-idealities are not considered in the OpenFCST model and could be the source of the nonconformity between the OpenFCST model and the experimental cells and also between experimental cells.

It was decided that the narrow operating conditions and variability of the experimental results for this electrolyte were such that further investigation using the OpenFCST model could not be validated. Instead, the focus was shifted to modelling and investigating the full macro-scale battery model.

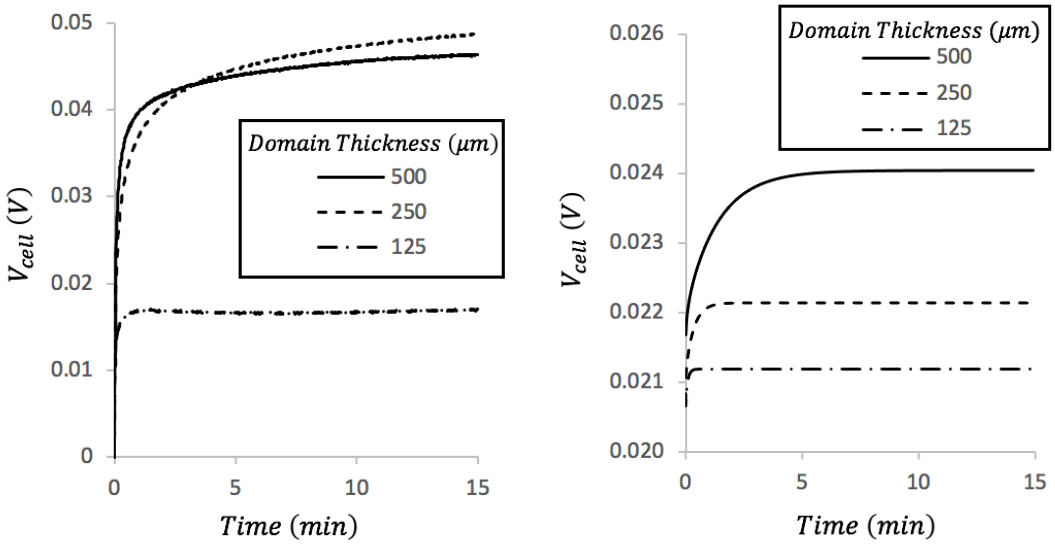

(a) Experimental Results.

(b) Numerical Results.

Figure 3.13: Cell voltage response for symmetric cell with varying thicknesses, subjected to a 0.20 mA/cm^2 current density with 0.6 M $LiPF_6$ in EC:DEC (1:1 by weight).

3.1.3 Summary

The electrolyte was modelled using the formulation of concentrated solution theory outlined in Section 2.1. It was studied by creating a symmetric cell in which the electrolyte saturated a separator sandwiched between two Lithium-foil electrodes. First, the electrolyte, LiTFSI in PEO, was used to reproduce the experimental results produced by Pesko *et al.* The discharge profiles at varying current densities matched the experiments very closely, providing confidence in the transient implementation of the model. The steady-state voltages reproduced those from experiments to a comparable degree as Pesko *et al.*'s own model. The differences between Pesko *et al.*'s model and the OpenFCST model were discussed, especially with regard to the incorrect boundary conditions in their article. Then the model was run through a set of parametric tests to determine each parameter's influence on cell performance. This information was used to comment on possible reasons why the OpenFCST model may have diverged from the experiments. Finally, a novel electrolyte was investigated for which no computational model has yet been developed. Unfortunately, the experi-

mental results were not reproducible, resulting in inconclusive agreement between the OpenFCST simulations and reality.

3.2 Macro-Scale Lithium-Ion Battery Analysis

The full cell analysis is based on the macro-scale model developed in Section 2.2. This analysis contains a major simplification, namely not modelling the micro-scale, and therefore is not expected to predict cell performance well unless transport within the active material particle is not dominant, i.e., if the particles are very small or the solid diffusion coefficient very large. However this study is still important as it provides insight into the electrolyte behaviour within a more complex application: especially in modelling volumetric reactions and multi-layer transport.

Two possible options were available in the analysis of this model. Either the model could be applied to a hypothetical battery, in which the electrolyte and solid material parameters are sourced separately from the literature, or applied to a battery chemistry for which experimental results have been obtained in the literature. While the latter option would quantitatively provide an argument for whether the micro-scale model is required to reproduce experiments, the first option was ultimately chosen, as it allows the direct application of the electrolyte characteristics gleaned from the previous section. Additionally, this approach is likely more realistic, as sources that present parameters for the solid phase often disregard the electrolyte, and vise versa.

The domain of simulation is one-dimensional with a thickness of 35 μm, divided into a 25 μm separator and 10 μm porous cathode. The width of the separator was chosen as that is the width of the standard Celgard® 2500 separator used in button cells. The width of the cathode was chosen as that is the common width used in a laboratory setting for studying LiBs. This domain is parcelled into 700 cells, each 0.1 μm wide. This cell width was chosen based on the mesh independence study, provided in Figure 3.14. If the cell size is decreased by a factor of 2, the

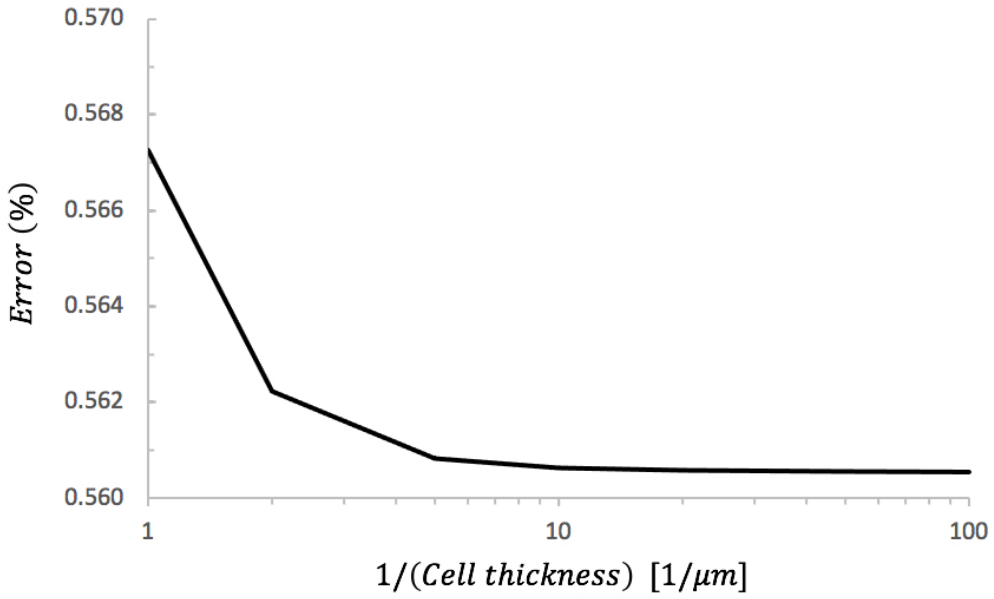

Figure 3.14: Mesh independence study for macro-scale simulations. Tested at 8C using 0.1 s time step intervals. Error quantified using average Li^+ concentration at 50% SOC.

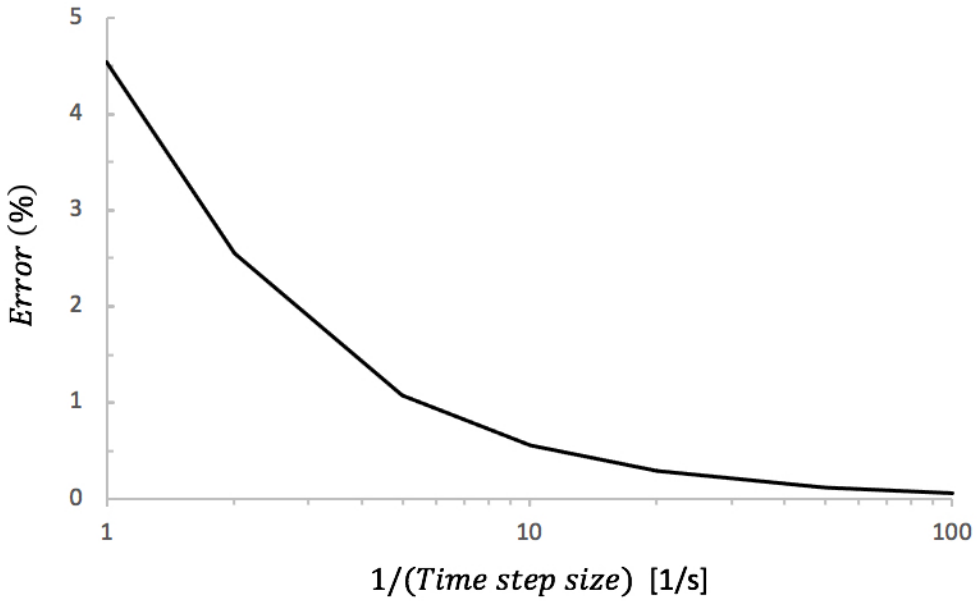

Figure 3.15: Time step independence study for macro-scale simulations. Tested at 8C using a mesh with 0.1 μm thick cells. Error quantified using average Li^+ concentration at 50% SOC.

error diminishes by only 0.00006%. The method for which error was determined is based on the error investigation in Section 3.2.1. The simulation time step of 0.02 s was chosen for this simulation, based on the time step independence study in Figure 3.15. Decreasing the step size to 0.01 s would only decrease the error by 0.05%. The electrolyte being modelled is LiTFSI in PEO at an average Li^+ concentration of 1 M, for which parameterized coefficients are provided in Section 2.3, and all other simulation parameters are summarized in Table 2.6. The anode is modelled as a planar Li-foil electrode, similar to the symmetric model, and the cathode is chosen to be made of NMC active material, connected to a current collector at its far end. While the current collectors may introduce minor ohmic losses, they are not considered in this model. The simulation is run until the cell discharges fully; that is, when the cell can no longer provide a positive voltage.

First, this section will provide the voltage response for a discharge simulation at a constant current density. Additionally, the requirement of a constant average Li^+ concentration will be discussed and verified. The transient profiles of the solution variables will be discussed. Then, the cell will be recharged and the hysteresis discussed, along with the cell efficiency and capacity. Finally, a parametric study is performed and the effect of changing the current density is discussed in terms of cell efficiency.

3.2.1 Discharge Curve

A discharge simulation was conducted at a constant current of 8C (2.172 mA/cm^2), meaning that it took 7.5 min for the cathode material to became fully saturated and not allow any more current to pass. This C-rate was chosen as it provides deeper insight into the challenges facing batteries when pushed to higher current densities. The main.prm and data.prm configuration files for this simulation are given in Appendix B.2. The resulting discharge curve is presented in Figure 3.16.

The OCV of this cell at 90°C is 4.3 V [147] which, because this is an ideal sys-

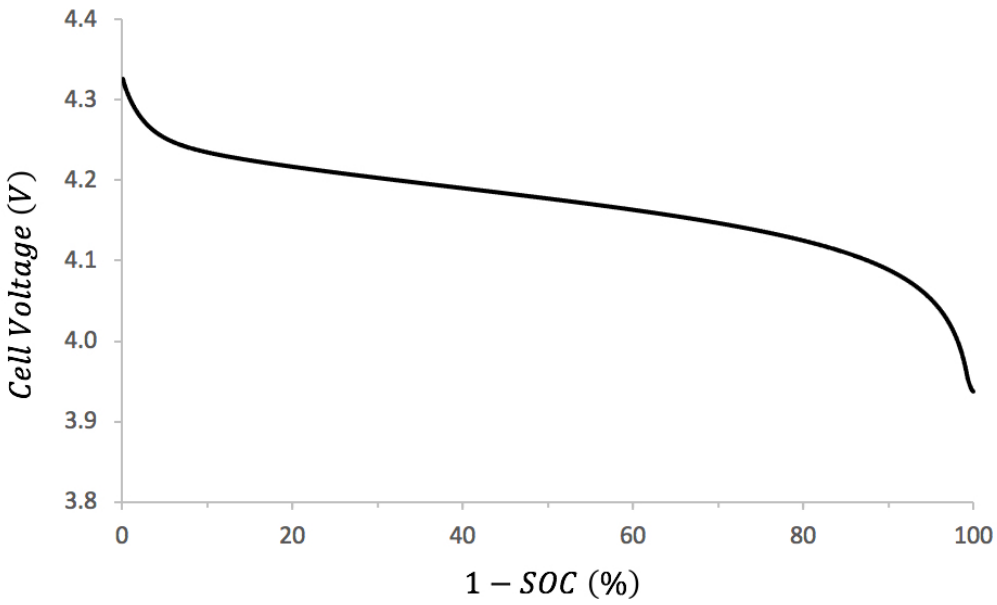

Figure 3.16: Discharge curve of macro-scale LiB at 8C using OpenFCST simulation.

tem, is equal to the thermodynamic voltage. The discrepancy between this value and the starting cell voltage of 4.32 V is a result of the solid Lithium concentration in the active material being well below the reference value of 1 M. The relatively steep decrease in voltage in the first 10% of discharge is the result of the developing Lithium-ion concentration gradient, as discussed thoroughly in the previous system (Section 3.1). Then, the majority of the discharge is characterized by a gradual decrease in cell voltage due to there being fewer reaction sites in the active material into which Lithium can intercalate, and therefore slower kinetics. This gradual decrease becomes more pronounced in the later stages of discharge as Lithium-ions travel further through the cathode to regions with lower solid Lithium concentrations. Finally, the sharp decrease in cell potential that characterizes the last 10% of discharge is a result of the solid phase reaching its saturation concentration of solid Lithium. The distribution of all solution variables and reactions within the cell will be discussed in Section 3.2.2.

The plot in Figure 3.16 provides confidence in the effectiveness of this macro-scale model in that it shows a very similar trend to those reported in the literature (e.g.,

Figure 26.52 in ref [28]). Understandably, however, it is likely to fail to accurately model any real battery, as the micro-scale contribution is neglected. For this reason, the quantitative comparison to experimental discharge curves will be reserved for when the two model scales can be combined.

Without comparing with experiments, answering the question of whether the equations presented in Section 2.2.2.6 were correctly implemented into the OpenFCST model becomes paramount. In this case, an alternative metric can be used to verify the model implementation. By neglecting the double layer effects, as discussed in Chapter 2, charge cannot be stored in the system. Additionally, the anion does not participate in the reaction and therefore the average anodic concentration is always constant. Due to these two postulates, it can be concluded that, for the 1:1 binary electrolyte modelled in this section, the average concentration of Lithium ions must everywhere be equivalent to that of the anion, thus requiring that its average does not change throughout the operation of the cell. This principle is not imposed by boundary conditions but instead a conservative property of the modelled equations and, therefore, should be observed at all times. This value will be the metric to ensure that the discretized form of the equations and their numerical implementation are correct. It is also the metric used for the mesh and grid independence analysis in the previous section.

The average concentration at any time can be calculated from the area under the plot of the concentration profile throughout time, accounting for the different porosity in each layer. Figure 3.17 shows how the average concentration remains relatively even throughout the experiment, with a few intermittent fluctuations. Importantly, however, is the magnitude by which the average concentration deviates from the expected value. Recognizing that the fluctuations in this figure are incredibly minimal and therefore likely just numerical noise (e.g. having a maximum error of only 0.2%) gives confidence to the correct implementation of the discretized form of the equations outlined in Section 2.2.2.6. Had the equations been incorrectly implemented, or the

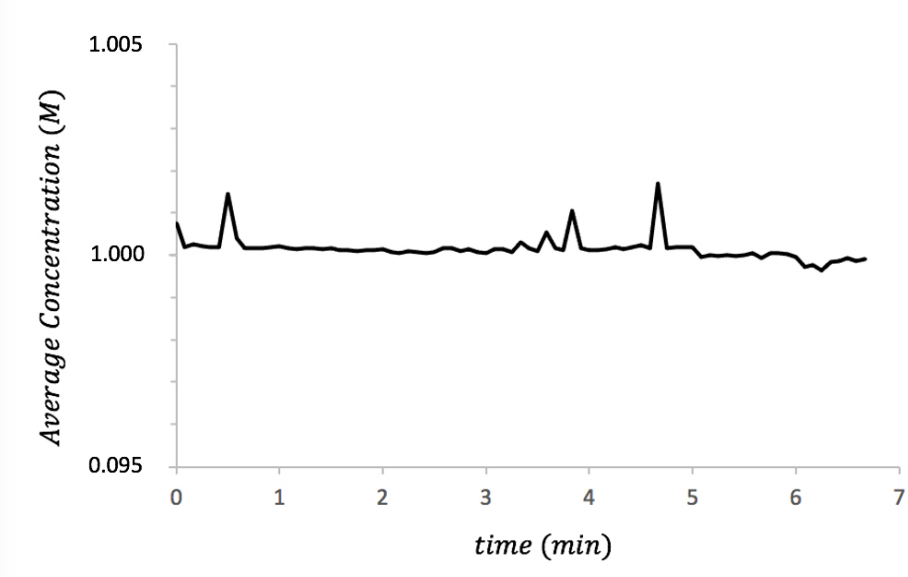

Figure 3.17: Average Lithium-ion concentration throughout cell discharge.

time step/mesh size too large, one would observe a steady increase or decrease in average concentration throughout the simulation.

3.2.2 Transient Profiles

The visualization of the behaviour of each solution variable can provide deeper insight into the physical processes occurring in the cell during discharge. As such, this section will provide and discuss the transient profiles of the solution variables and reaction distribution.

3.2.2.1 Lithium-ion Concentration

Figure 3.18 gives the profile evolution of the Lithium-ion concentration throughout cell discharge. Each line corresponds to a 30 s time step, trending from light to dark as the discharge progresses. The dashed vertical line at 25 μm indicates the interface between the separator layer and the porous cathode layer.

The magnitude of the concentration gradient rapidly increases at the beginning of the test. As mentioned in Section 2.1.1 and 2.1.2.2, this slope produces a driving force on the anion that is countered by the electrical field across the system. After

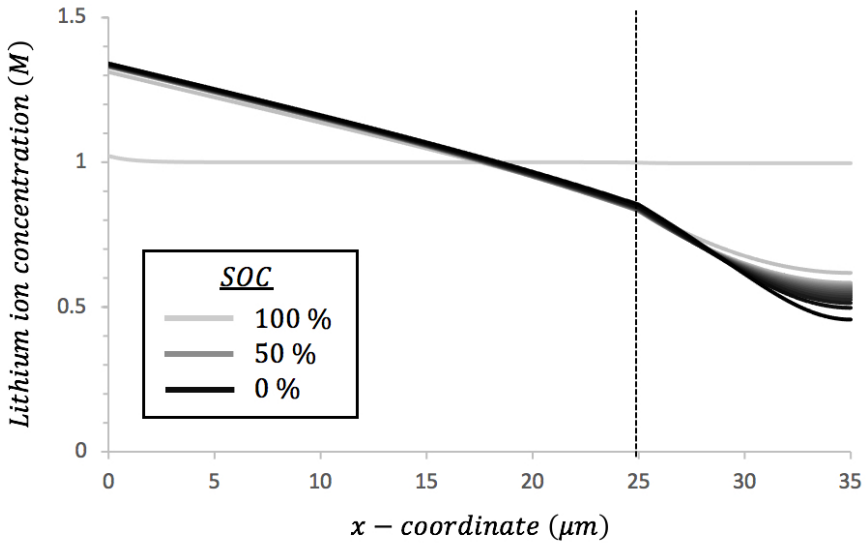

Figure 3.18: Lithium-ion concentration profiles in the electrolyte throughout 8C discharge of macro-scale cell. The dashed line indicates interface between separator layer and cathode layer.

roughly 30 s, this slope reaches a steady-state.

The cathode exhibits a similar negative gradient in Lithium-ion concentration. At the interface with the separator, it is evident that the slope is even steeper than in the separator. This is a result of the cathode layer being less porous than the separator and therefore having a smaller effective diffusion coefficient. Also, the concentration gradient in the cathode layer vanishes as it approaches the cathodic current collector, until the profile becomes completely horizontal. This is to be expected, as Lithium-ions are being consumed in the volumetric reactions, resulting in less and less current in the electrolyte phase until, at the current collectors, no current is being passed at all. Figure 3.19 illustrates the current passing through the electrolyte phase. As stated, it is observed that the current is constant throughout the separator and then trends to zero in the cathode layer. The difference between plots throughout time is a result of the reaction rate profile, which will be discussed further in Section 3.2.2.5.

As the concentration of Lithium-ions decreases in the cathode over time, the cathodic overpotential must increase. This is one of the contributing factors for the

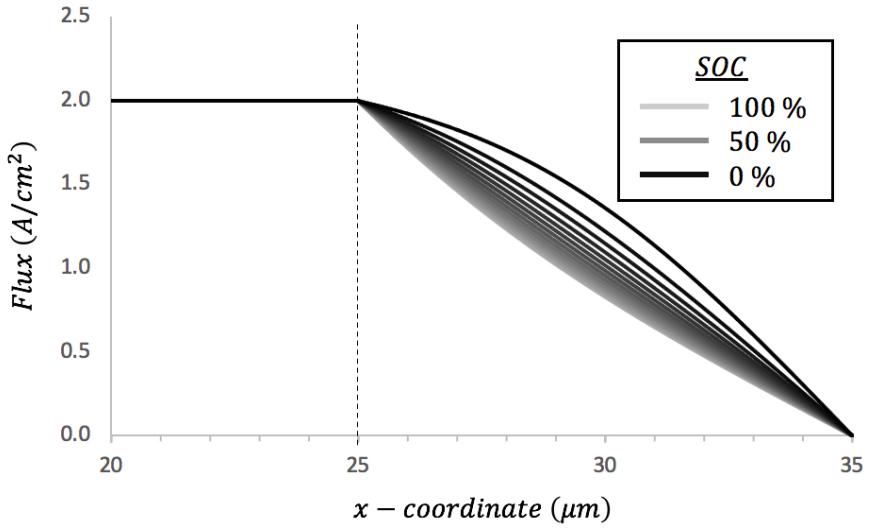

Figure 3.19: Profile of current passing through electrolyte phase at throughout 8C discharge of macro-scale cell. Dashed line indicates the interface between the separator and cathode layers.

decreasing cell voltages in Figure 3.16, particularly in the first 10% of discharge.

3.2.2.2 Solid Potential of a Reference Electrode

The development of the solid potential for a Li/Li^+ reference electrode in the electrolyte is illustrated in Figure 3.20.

The first thing to notice is that the potential is generally in the range of -4.0 to -4.3 V for this discharge. The significant negative values are due to the OCV of the battery, being around 4.3 V for this chemistry at 90°C. The values are negative because reduction is assumed. The potential increases above the -4.3 V because of the potential losses due to resistance in the solid phase and the reaction overpotential. Likewise, the reference electrode potential increases throughout the test because the overpotential has to increase to compensate for the depletion of Lithium-ions and active material reaction sites in the cathode layer.

The negative gradient in the potential profiles is a result of the concentration profile discussed in the previous section. They mimic the concentration profiles in that the slope is accentuated due to the decreased porosity in the cathode and they trend to

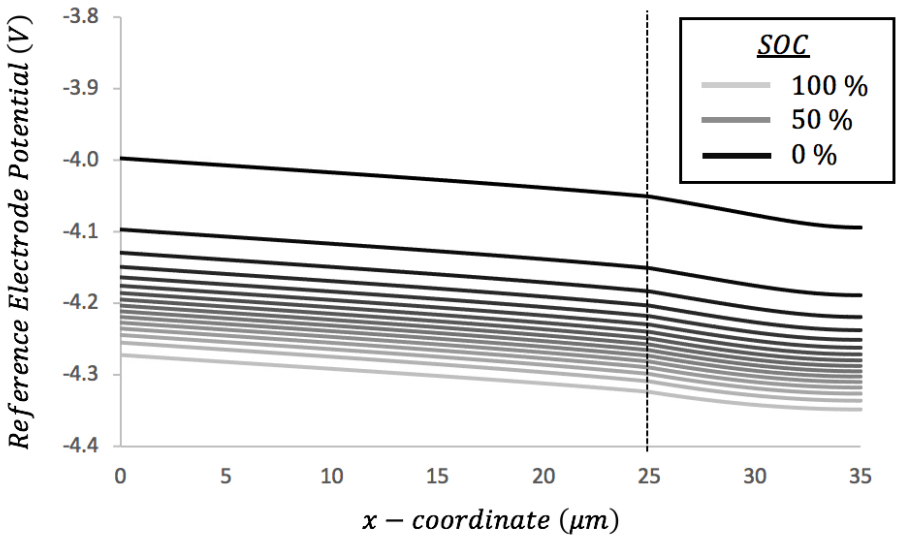

Figure 3.20: Potential profile of electrolyte reference electrode throughout 8C discharge of macro-scale cell. The dashed line indicates interface between separator layer and cathode layer.

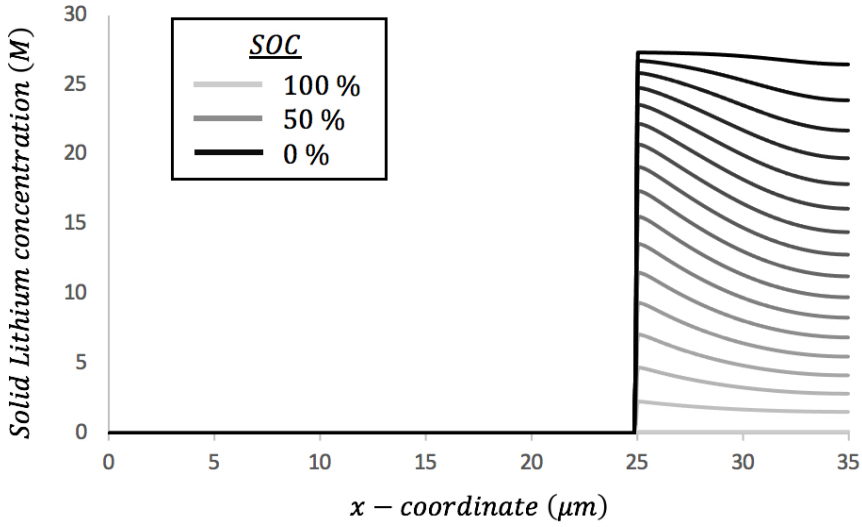

Figure 3.21: Solid Lithium concentration profiles throughout 8C discharge of macro-scale cell.

horizontal at the cathodic current collector.

3.2.2.3 Solid Lithium Concentration

Figure 3.21 gives the transient profile of the solid Lithium concentration throughout cell discharge.

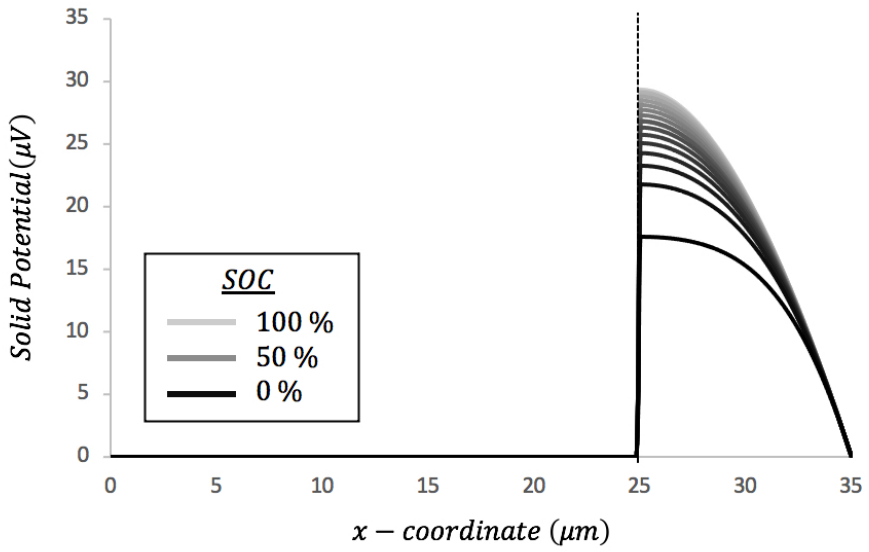

Figure 3.22: Solid potential profiles throughout 8C discharge of macro-scale cell. The dashed line indicates the interface between the separator and cathode layers.

The solid concentration is zero in the separator layer, as there is no solid phase for which the Lithium can intercalate. The average concentration of solid Lithium in the cathode steadily increases as Lithium ions react to create solid Lithium. The solid Lithium cannot leave the cathode as the flux in either direction is zero. Since the current is constant throughout and therefore solid Lithium is produced at a constant rate, the area created between sequential lines in Figure 3.21 is always the same.

Initially, the reactions are favoured at the LHS of the cathode layer as a result of the larger overpotential. However, as time progresses, this switches on account of a depletion in active material reaction sites on the LHS.

3.2.2.4 Solid Potential

The electronic potential profiles are given for progressing time in Figure 3.22.

The gradient in the solid phase is considerably smaller than the other solution variables, having a maximum difference on the order of 0.03 mV, on account of the high conductivity in the solid phase. As with the solid Lithium profiles, the electronic potential is forced to zero in the separator layer, as there is no solid through which

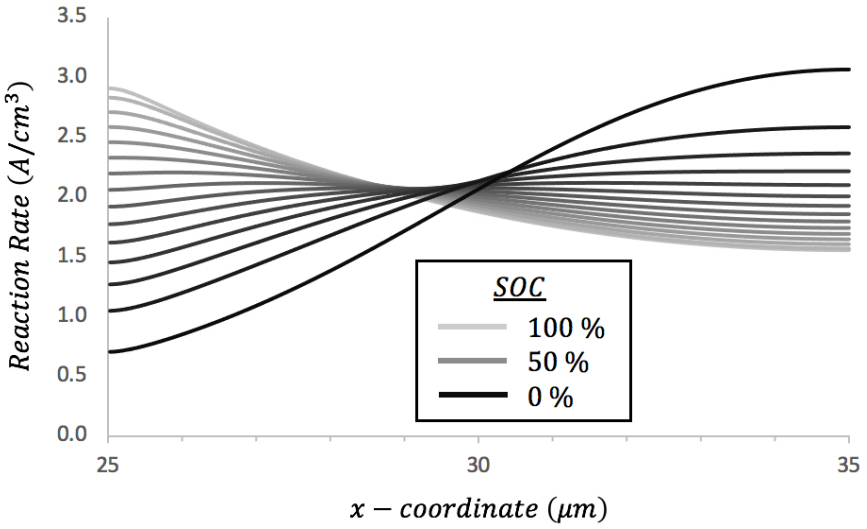

Figure 3.23: Reaction rate profiles throughout 8C discharge of macro-scale cell.

electrons can move. Also, at all time steps, the RHS of the profile is forced to zero. This is because the RHS is directly connected to the cathodic current collector, which serves as the reference potential for which all other potentials are measured against.

As time progresses, the LHS of the electronic potential profile decreases. This is because relatively fewer reactions are occurring at this side of the cathode, on account of the depletion of active material reaction sites on that side. Because the majority of the reactions are shifted to the RHS, there is a smaller current being passed through the RHS and thus a smaller potential gradient. The gradient of electronic potential right at the current collector interface is always constant, as this gradient drives the constant current through Ohm's law,

$$\mathbf{i}_s = -\sigma_s \nabla \phi_s \tag{2.95}$$

3.2.2.5 Reaction Rate

Due to the constantly changing potentials and concentrations within the simulation domain, the reaction rate within the cathode will also change spatially over time. Figure 3.23 gives the progression of the reaction rate profile throughout cell discharge.

As with the previous two profiles, the reaction rate in the separator layer is zero

at all times because there is no solid phase for which the electrolyte can intercalate into. The area under the graph would correspond to the current density being passed through the battery. As expected, this is equal to 2.172 mA/cm^2 (8C) for all times.

At the beginning of discharge, the reactions favour the LHS of the cathode, as this region has a larger overpotential while maintaining similar concentrations as the RHS. As time progresses, the LHS overpotential remains larger, however, the solid Lithium concentration approaches saturation and slows the reaction. This results in the reaction rate becoming more uniform throughout the cell and eventually, when the LHS begins to reach saturation, strongly favouring the RHS of the cathode.

3.2.3 Hysteresis

A hysteresis study was conducted by charging the cell at the same current density as discharge, but in the opposite direction, beginning with a fully saturated cathode and stripping it of the Lithium until it reaches the lower limit. The results are presented in Figure 3.24, where the charge curve is compared directly to the discharge curve by comparing the cell voltage magnitudes, recognizing that the delithiation process produces a negative cell voltage.

From the plot, it is evident that there is a large difference in voltage magnitude for the charge versus discharge curves. This is understandable in that the losses due to transport and overpotential will be significant for the relatively high current densities in this study. These losses will decrease the available potential of the discharge curve and increase the required potential for the charge curve, thus increasing the space between curves and decreasing the reversibility of the cell.

Using the charge/discharge curves, one can calculate the energy supplied by the cell, as well as the energy required to recharge it. As such, one can determine the energy lost to thermal effects and the efficiency of the cell. The DC power, P, either produced by the cell or supplied to the cell on a per area basis is equal to the cell

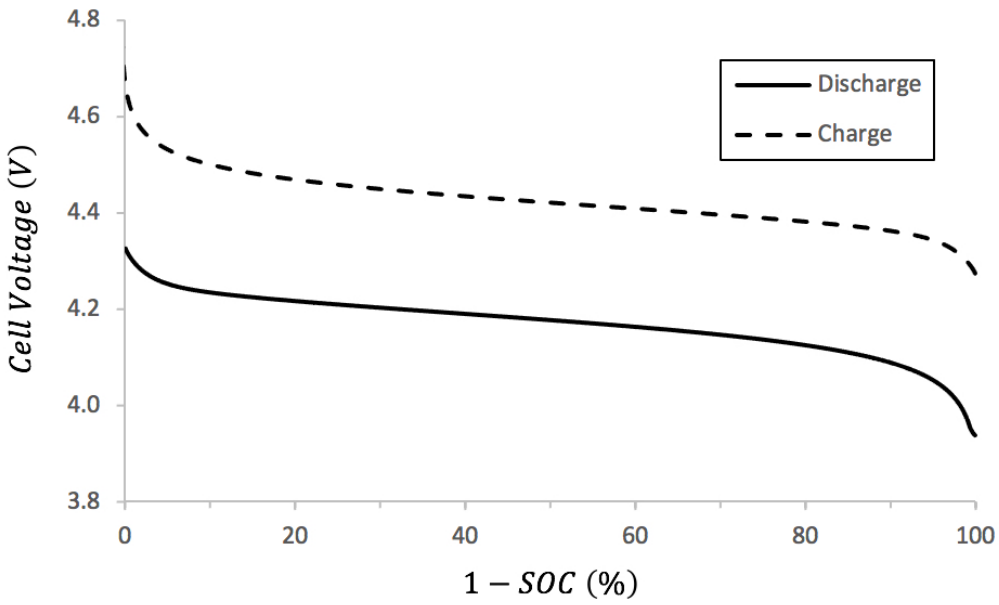

Figure 3.24: Hysteresis study for charge and discharge of macro-scale model. Cell is operated at 8C for charge and discharge processes.

voltage multiplied with the current density, i.e.,

$$P = V_{cell}(t)\mathbf{i}A \tag{3.2}$$

where A is the cell area, assumed here to be 1 cm^2. The electrical energy, E is just the power multiplied by the time for which that power is applied,

$$dE = P(t)dt \tag{3.3}$$

Therefore, the total energy is equal to,

$$E(t) = \int_0^t V_{cell}\mathbf{i}dt \tag{3.4}$$

From the simulation in question, the energy required to charge the cell, using Equation (3.4), is 0.8855 J. Likewise, the energy produced by the cell discharge is 0.8338 J. Therefore, the energy lost in the charge/discharge cycle is 0.0517 J and the efficiency, defined as,

$$\eta_{cell} = \frac{E_{out}}{E_{in}} \tag{3.5}$$

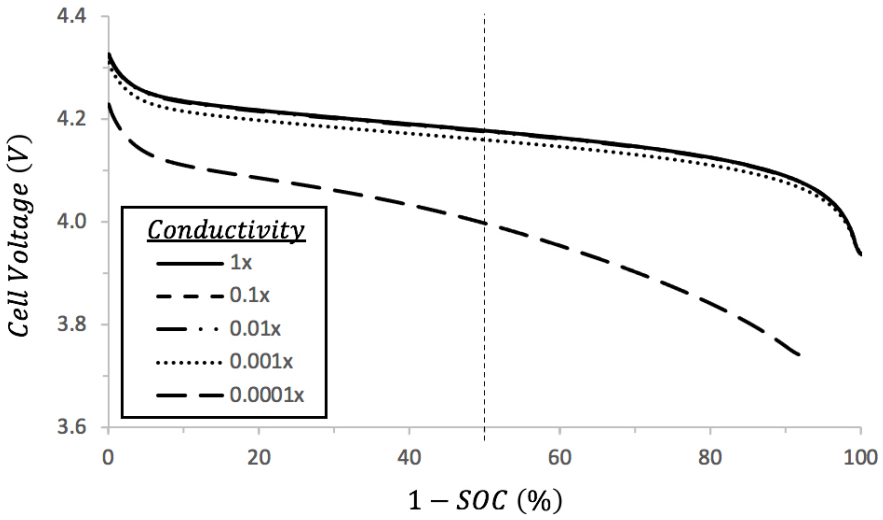

Figure 3.25: Characteristic curve at 8C for macro-scale battery system with varying solid conductivity. All other input parameters are held constant. The dashed line corresponds to 50% SOC.

is 94.2%. This cell produces such a small amount of energy because the cathode material and thickness were chosen to resemble laboratory conditions and therefore store far less Lithium than in most real applications.

3.2.4 Parametric Studies

This section is provided to enrich the understanding of the influence of the solid phase input parameters, having already performed a parametric study of the electrolyte parameters in Section 3.1.1.2. Each study was performed under the same conditions outlined in Section 2.2 but with one parameter changed, i.e., solid conductivity, solid diffusion, exchange current density, or the current density passing through the system.

3.2.4.1 Solid Conductivity

The discharge curves for the solid conductivity parametric study are presented in Figure 3.25 for conductivities 1 to 10 000 times less than in ref [144].

Decreasing the conductivity 100 times makes a negligible impact on the discharge curve, emphasizing the ease at which electrons pass through the solid. If the conduc-

tivity is decreased further, one begins to observe cell voltage losses that are comparable and may even exceed the methods of voltage loss that are usually more dominant, e.g., overpotential and transport in the electrolyte phase.

Figure 3.26 offers more insight into the effects of decreasing the solid phase conductivity to the point that it alters the internal physics of the system. Specifically, this figure provides the solid potential, overpotential, and solid Lithium profiles within the cathode layer at 50% SOC, indicated by the dashed line in the discharge plot.

The solid potential is presented in Figure 3.26a on a logarithmic plot in the vertical direction. The solid potential profile increases roughly proportional to the decrease in conductivity. The steps make sense in that the gradient of potential is proportional to the current being passed. The profiles are not, however, merely stretched copies of one another, as the reaction rate profile changes as well.

The overpotential plot, in Figure 3.26b is very interesting and will offer valuable insight into why the solid Lithium concentration develops in the manner that it does for low conductivities. Recalling that the gradient of potential is proportional to the current being passed, it is expected that ϕ_R, though also containing other dependencies, will transition from a steep gradient at the separator interface, where it is transporting all the current, to flat at the end of the cathode, where it is no longer passing any current, resulting in the bowed profile observant in Figure 3.20. Conversely, the solid potential would have a similar bow, but trending in the opposite direction as it carries more charge the further it is from the separator interface. Figure 3.26b then correctly depicts why the overpotential (defined here as the difference between the two) also shows this bow. As the conductivity decreases, this bow shifts from being electrolyte dominant (i.e., downward sloping) to solid dominant (i.e., upward sloping). This change is easily understood as the transition from greater losses occurring due to transport in the electrolyte, to transport in the solid. When the conductivity is decreased 1000 times, it can be seen that the two phases offer comparable transport losses, as the trend decreases on the left, plateaus, and then clearly increases on the

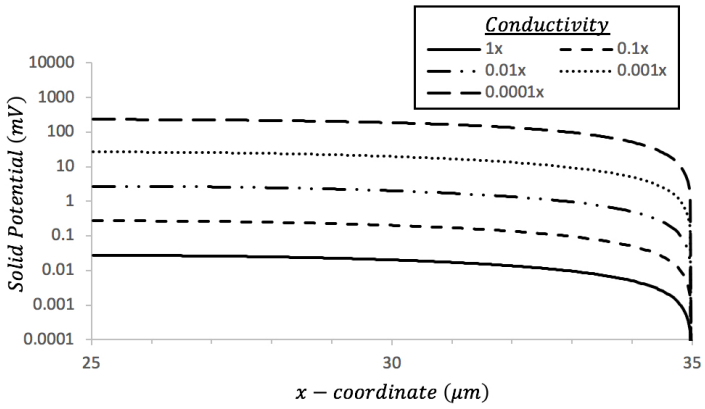

(a) Solid potential profile.

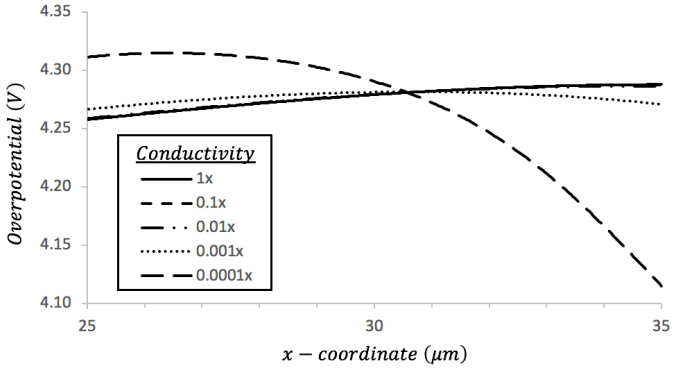

(b) Overpotential profile.

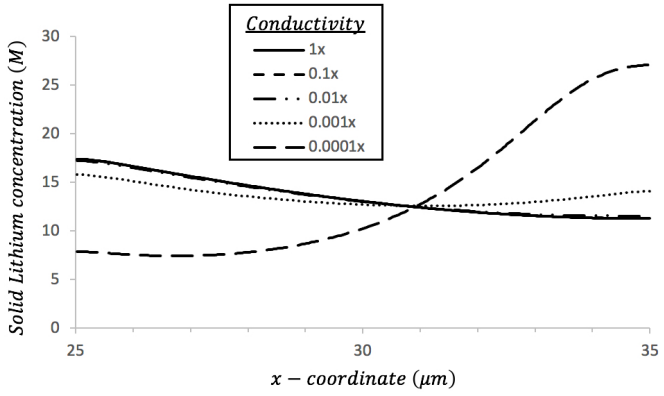

(c) Solid Lithium concentration

Figure 3.26: Solution variable profiles for macro-scale battery system discharge at 8C in porous cathode layer at 50% SOC with varying solid conductivity. All other input parameters are held constant.

right. It is evident, however, that decreasing the conductivity 10 000 times results in the solid phase losses greatly exceeding those in the electrolyte.

Finally, the solid Lithium profile, in Figure 3.26c, demonstrates how the Lithium accumulates in the region of the cathode with the larger overpotential. At normal conductivities, the Lithium profile develops a downward sloping trend due to more reactions closer to the separator layer where overpotential is greater. When conductivity is very low, the accumulation develops close to the cathodic current collector. For the 10 000 times decrease, this accumulation is so significant that the right side of the cathode begins to experience saturation while the cathode as a whole is still at 50% SOC.

3.2.4.2 Solid Diffusion

The solid phase in a real battery is composed of active material particles, into which Lithium intercalates and diffuses. Lithium seldomly passes between particles as a response to a macro-scale concentration gradient. Therefore, the solid phase diffusion coefficient has been reported to be very small. For the simulations in previous sections, solid Lithium is nearly static. Figure 3.27 contains the discharge plots, in which it is allowed that solid Lithium is more mobile and influenced by macro-scale concentration gradients. The discharge curves correspond to simulations with diffusion coefficients 100 to 10 000 times greater than reported in reference [143].

Although diffusion is allowed in the solid phase, the discharge curve shows that this allowance has minimal effect on the cell voltage. If anything, losses are minimized as the solid diffusion coefficient increases. This is because diffusion can aid in transporting solid Lithium from regions of high Lithium solid concentration to lower concentrations, allowing for reactions to resume in these regions with larger overpotential. The difference in discharge curves may be accentuated if the cathode thickness was larger, as larger solid Lithium differentials would exist in the cathode.

Figure 3.28 demonstrates that, with an increased diffusion coefficient, the concen-

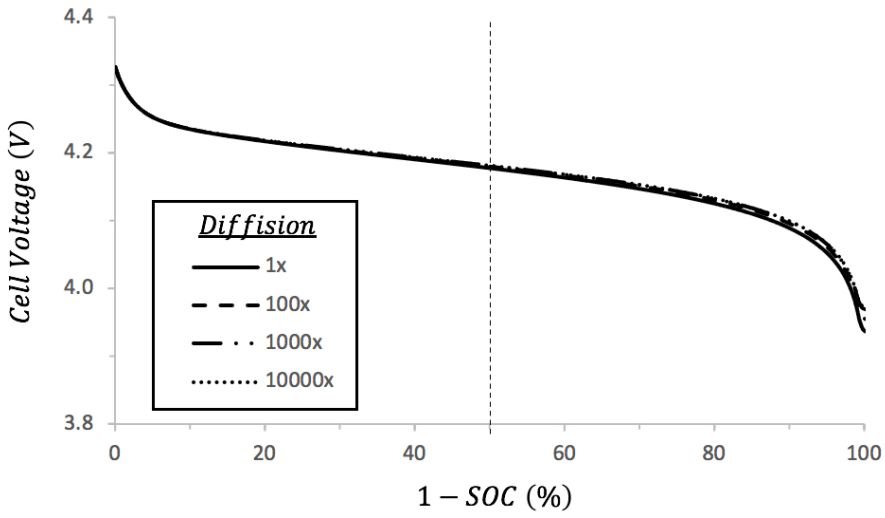

Figure 3.27: Characteristic curve at 8C for macro-scale battery system with varying solid diffusion. All other input parameters are held constant. The dashed line corresponds to 50% SOC.

tration profile will smooth from a distinct slope to completely horizontal, at which point any gradient in solid Lithium concentration created by nonuniform reaction rates is completely leveled due to macro-scale diffusion. Note that studying these large diffusion coefficients helps to gain a better understanding of each parameter and is not necessarily realistic for modelling actual battery conditions, as no solid material can transport Lithium this effectively.

3.2.4.3 Exchange Current Density

The cathodic exchange current density is a measure of the proportionality between the kinetics exponential to the rate at which reactions occur within the cathode. Figure 3.29 shows the discharge curve for varying exchange current densities. Figure 3.30 shows the solid potential of a Li/Li^+ reference electrode across the whole battery domain at the point when the SOC is at 50%.

It is clear from Figure 3.29 that the exchange current density does impact the discharge curve, but only insomuch as a linear translation in cell voltage. Figure 3.30 shows a similar linear translation for the reference electrode potential. While not

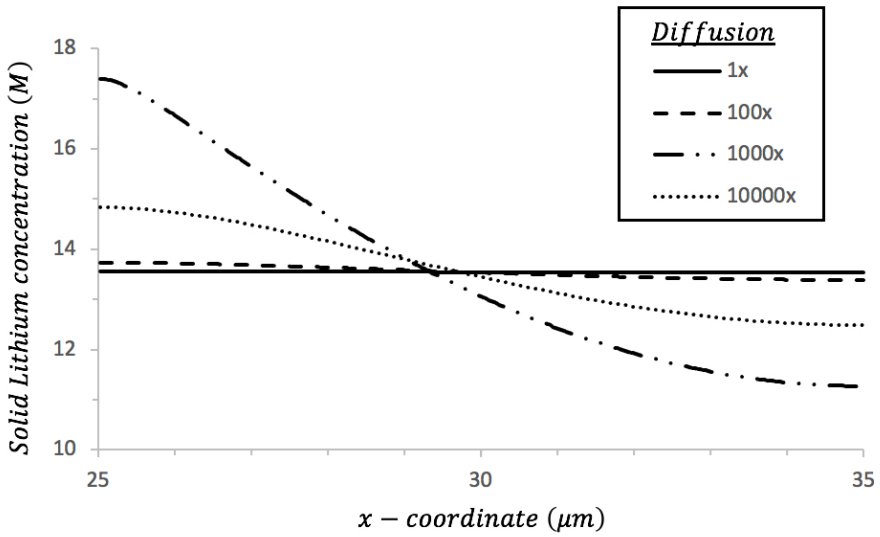

Figure 3.28: Solid Lithium profile for macro-scale battery system discharge at 8C in porous cathode layer at 50% SOC with varying solid diffusion coefficients. All other input parameters are held constant.

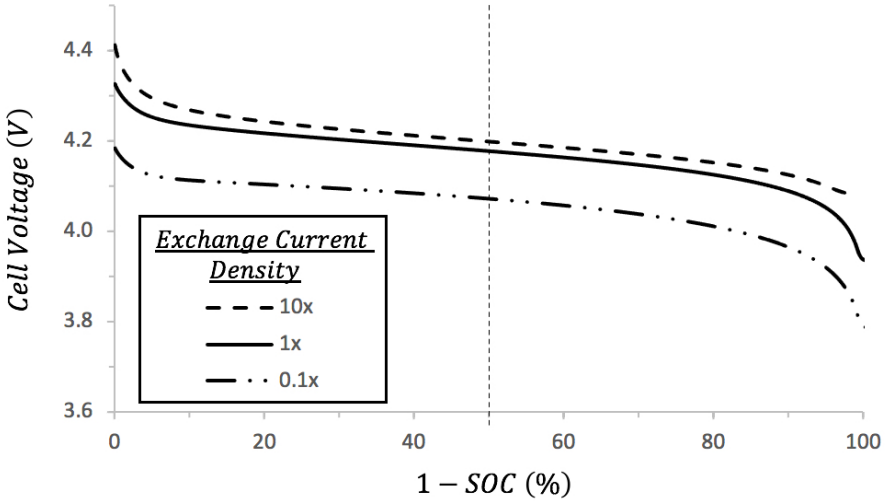

Figure 3.29: Characteristic curve at 8C for macro-scale battery system with varying cathodic exchange current densities. All other input parameters are held constant. The dashed line corresponds to 50% SOC.

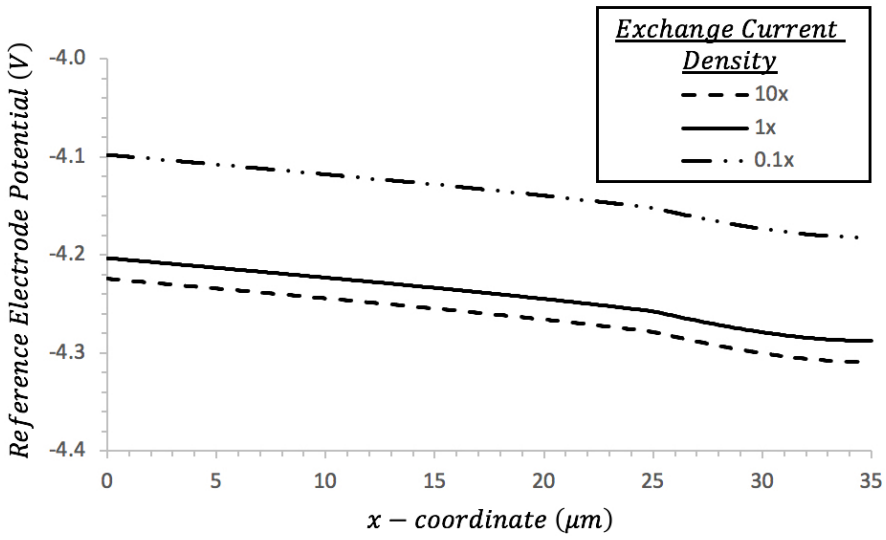

Figure 3.30: Li/Li^+ reference electrode profiles for macro-scale battery system discharge at 8C at 50% SOC with varying exchange current. All other input parameters are held constant.

shown, all other solution variable profiles remain the exact same given this variance in exchange current density. This is because, as mentioned, the exchange current density is the relationship between the kinetics exponential and the reaction rate, and therefore, to sustain the same current density, the solid and electrolyte potential difference needs to compensate. Due to the exponential in this relationship, this difference will increase linearly as exchange current density is increased exponentially. Then, because the solid potential is anchored at the cathode, the reference electrode potential will linearly decrease and the cell voltage linearly increase, as observed in the figures. If the exchange current density is increased to infinity, the discharge curve will only give the ohmic losses, allowing one to study the electrolyte induced losses in isolation. Unfortunately, a study with infinite exchange current density cannot be run using the current simulation framework. This is because the reference electrode potential is only anchored by its relationship to the solid potential. If the exchange current density is increased to infinity, the reference electrode potential will not be able to be expressed in terms of the solid potential and the simulation will fall apart.

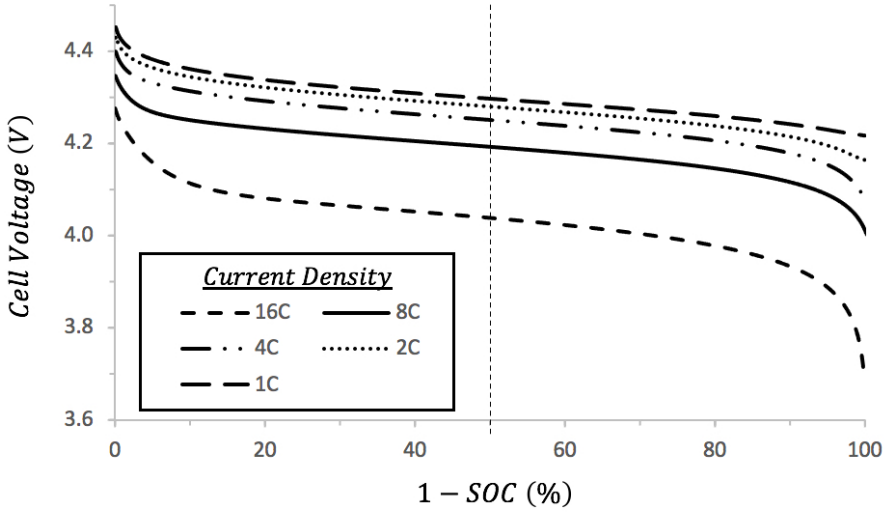

Figure 3.31: Discharge curves at varying current densities for macro-scale model. The dashed line indicates 50% SOC.

3.2.4.4 Current Density

The current density being passed through the cell will strongly dictate the behaviour of the cell, affecting the cell voltage, transient profiles, and overall time-scale. This analysis was performed with current densities of 16C, 8C, 4C, 2C, and 1C at an average Li^+ concentration of 1.5 M. The resulting discharge curves are presented in figure 3.31.

As expected, as the current density increases, the available cell voltage decreases. This is because all modes by which potential is lost (i.e., mass transport, overpotential, and ohmic losses), are being exacerbated. This concept will be investigated at 50% SOC, as indicated by the dashed line in Figure 3.31. The solution variable profiles for all three current densities at this SOC are presented in Figure 3.32.

As the current density increases, the Lithium-ion concentration gradient and electrolyte potential gradient get progressively steeper. Interestingly, the electrolyte profiles for the 16C case are far less linear in the separator layer than they are for the lower current densities; a result of the complex concentration dependencies of the coefficients in the electrolyte transport equations. The gradient of the solid potential is

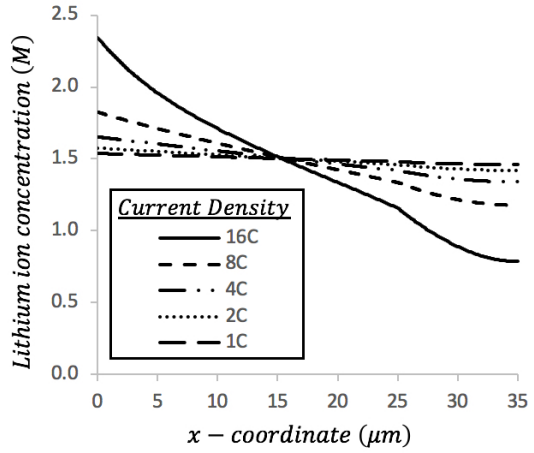

(a) Lithium-ion concentration

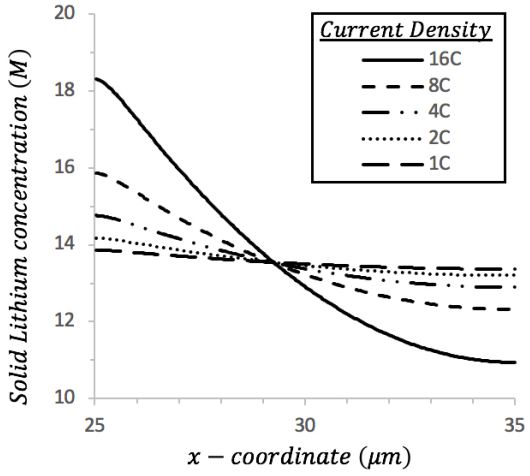

(b) Solid Lithium concentration

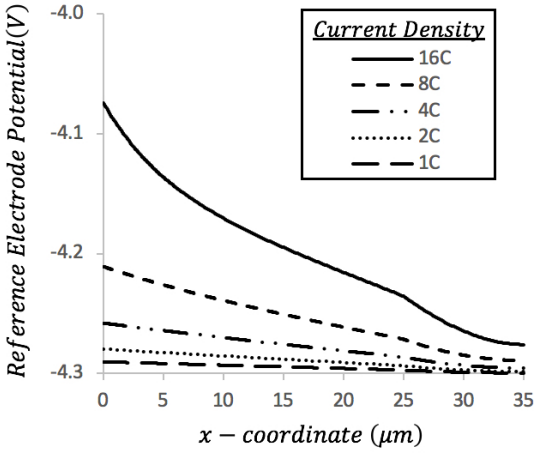

(c) Reference electrode potential

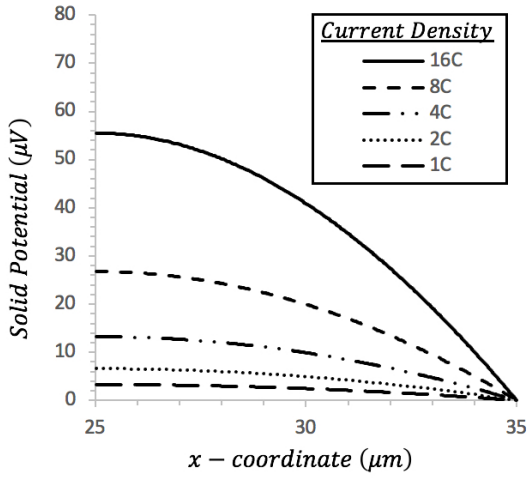

(d) Solid potential

Figure 3.32: Solution variable profiles for macro-scale battery system discharge at 8C and 50% SOC for various current densities.

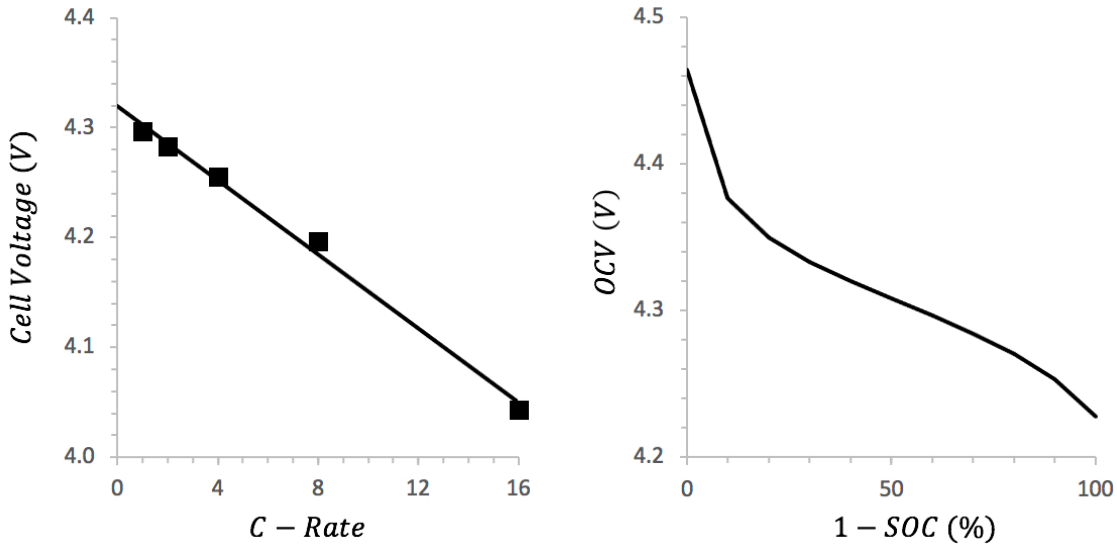

(a) (b)

Figure 3.33: OCV study for macro-scale LiB simulation. (a) Cell voltages at 50% SOC for varying current densities. Trendline slope and vertical intercept correspond to the equivalent circuit's internal resistance and OCV. (b) OCV of the cell as a function of the SOC of the active material.

also much steeper in the cathode layer for larger current densities. The solid Lithium concentration gradient is also more exaggerated, but unlike the others, which are a result of larger fluxes, this gradient is a result of accumulation over time due to the larger overpotential and thus more reactions created at the LHS of the cathode.

Figure 3.33a shows the slice taken at 50% SOC from Figure 3.31, as a function of the current density. Within this phase of the discharge curve, the increased current density will have a linear effect on the available cell voltage. The vertical intercept of this plot gives the OCV at that SOC. The slope is the effective internal resistance of the battery system. Therefore, the cell voltage will be,

$$V_{cell} = OCV - R_{internal}\mathbf{i}$$

where, at 50% SOC, the OCV is 4.308 V and the internal resistance is 62.2 $\Omega{\cdot}\text{cm}^2$.

Extending this approach to the entire discharge of the battery, Figure 3.33b demonstrates how the OCV of the cell sharply decreases at first, then plateaus slightly, and then drops as the active material becomes fully saturated. The potentials above 4.3 V

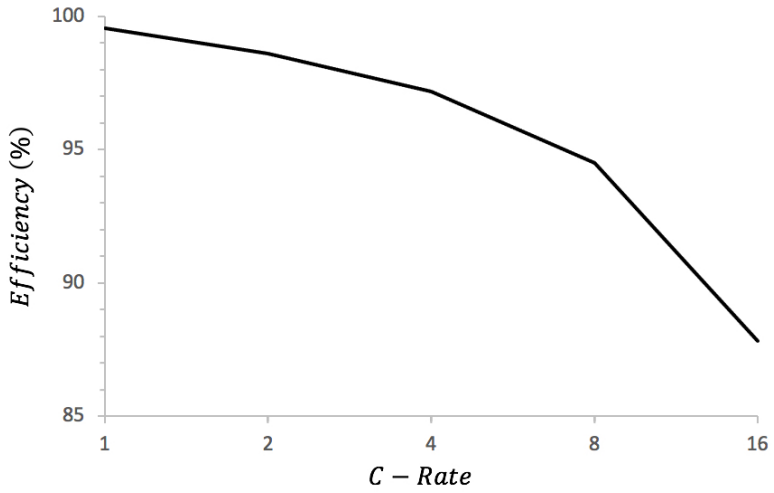

Figure 3.34: Efficiency of macro-scale battery model for various C-rates.

are allowable, given that the rate of forward and reverse reactions will equal each other for an applied voltage of 4.3 V only when the concentration of filled sites equals the concentration of empty sites, which is evident in Equation (2.118). This will occur 50% of the way through discharge, meaning the OCV before this point will be larger than 4.3 V and afterwards, will be less than 4.3 V. The reason the cell voltage at zero current does not equal 4.3 V, given the trend line intercept in Figure 3.33a, is that the point at 16C is not directly inline with the others, and is therefore shifting the intercept up.

Figure 3.34 gives the cell efficiency, using Equation (3.5), for varying C-rates. It demonstrates how the cell efficiency decreases as current density increases. Therefore, in addition to the fact that fast-charging an EV's battery can be detrimental to the batteries health, it is also far less efficient; which is paramount to EV usage. As expected, slowing the discharge of the battery will bring the efficiency closer and closer to fully reversible. In reality, the battery will be less efficient than the model predicts at these low C-rates, since the battery will experience self-discharge due to parasitic reactions.

3.2.5 Summary

The macro-scale system was built, based on the description in Section 2.2, to function as one of the building blocks, along with a micro-scale model, for the development of a multi-dimensional multi-scale LiB model. First, this system was run under realistic conditions and the discharge curve presented and discussed. It was concluded that its resemblance to experimental curves and the minimal deviance in average Li^+ concentration were strong markers that this model correctly captures the macro-scale. The physical processes occurring during discharge were further investigated by analyzing how the solution variables and reaction profiles developed throughout cell discharge. This was supplemented with a parametric study of the exchange current density, solid conductivity and diffusion, and current density. The cell was then run in reverse to detect hysteresis, and the cell capacity determined. Finally, the cell efficiency as a function of current density was plotted and discussed.

Chapter 4

Conclusion

The focus of this work was to create a computational framework for the macro-scale model of a Lithium-ion battery that can be extended with the addition of a micro-scale model to physically model a full cell.

This objective was achieved by,

- Providing an extensive derivation of CST and the Lithium-ion battery governing equations as well as their finite element implementation.
- Create an electrolyte model that could be validated with the literature and applied to experiments.
- Expand the electrolyte model to a full macro-scale battery model.
- Discuss the transient profiles, hysteresis, and the effects of each input parameter on cell performance.

4.1 Summary of Work Completed

Two systems used to study Lithium-ion batteries were implemented into OpenFCST. The first was a symmetric cell with Lithium foil electrodes separated by an electrolyte separator. The purpose of this system was to isolate the electrolyte's influence on cell performance. The electrolyte transport equations are based on the DFN concentrated solution theory formulation. Using the concentration of Lithium-ions and the solid

potential of a Li/Li^+ reference electrode as the solution variables, two equations were derived that fully describe the system, that is, the Li^+ species transport equation and the MacInnes equation. Additionally, an equation relating the reaction rate at the two planar electrodes with the potential difference of the working and reference electrodes was developed using the Butler-Volmer formulation.

The other model was for a full macro-scale Lithium-ion battery. This model used Lithium foil as the anode and a porous NMC layer as the cathode, sandwiching the electrolyte separator. The porous media is modelled as superimposed continua coupled through volumetric reactions. The addition of the solid phase required two additional equations to describe the solid phase concentration and electron transfer; enter Fick's law and Ohm's law respectively. The reaction source term is again formulated using BV kinetics.

Although the electrolyte equations are obtained from first-principles, the equation coefficients are most easily determined through experimentation. Two electrolytes were parameterized, i.e., $LiPF_6$ in EC:DEC (1:1 by weight) [105] and LiTFSI in PEO [106]. Additional parameters were sourced from the literature for the solid phase and reaction kinetics at both electrodes.

The governing equations were temporally discretized using the backward differentiation formulae, linearized using the Newton-Raphson method, and then presented in their finite-element, spatially discretized weak form using the Bubnov-Galerkin method. The boundary terms were discretized separately and related to their Newman and complex boundary conditions. The equations and boundary conditions were then implemented into their respective OpenFCST applications.

The first system to be simulated was the symmetric cell. It was first validated by reproducing experimental results in the literature [105]. Using a 2.76 M LiTFSI in PEO electrolyte in a 500 μm thick button-cell, the system was subjected to a constant 20 $\mu A/cm^2$ current density and the transient cell voltage response recorded. This was repeated for increasing current densities up to 250 $\mu A/cm^2$. The results

matched those from experiments very closely. The cell was then simulated with an applied 20 μA/cm^2 current density for varying Li^+ concentration; spanning from 0.473 M to 3.78 M. The steady-state voltages obtained from these tests were compared to experiments and to a SS electrolyte model created by Pesko *et al.* It was concluded that the OpenFCST implementation was comparable to Pesko *et al.*'s SS model at reproducing the experimental results. The difference between the two models was also discussed, especially in regard to the incorrect boundary conditions used by Pesko *et al.*'s model. The same cell configuration at 2.76 M and 20 μA/cm^2 was used for a sensitivity analysis, in which the input parameters were adjusted to discern their individual influence on the electrolyte performance. While each parameter had a different impact on the cell voltage, each played a crucial role in mitigating losses. Using this information, a commentary was provided on the likely culprit in any nonconformity between the OpenFCST model and experiments. The OpenFCST model was then applied to an electrolyte for which no previous computational implementation has yet been performed. The experimentation had a very difficult time creating reproducible results. Even though numerical results are physical, experiments performed to validate the model were not reproducible. Therefore, the validation of the OpenFCST model for this new electrolyte could not be completed.

The focus was then shifted to the macro-scale Lithium-ion battery system. This system considered a button cell containing a 25 μm separator layer sandwiched between a Lithium foil anode and a porous 10 μm NMC cathode. The electrolyte used in this investigation was LiTFSI in PEO at an initial concentration of 1 M. The system was first operated at 10C and the resultant discharge curve plotted and discussed. The curve created the same trend that has been reported in the literature. The average Li^+ concentration throughout the discharge was plotted and it was noted that it remained within 0.2% of the original value, providing confidence in the numerical accuracy of the model. The transient profiles of the solution variables as well as the reaction rate and current density were then plotted and discussed. Each plot provided

realistic results and allowed for a deeper understanding of the battery physics. Then, the model was charged after discharge and the hysteresis plotted. Using this plot, the cell capacity and efficiency were deduced. A parametric analysis was then performed for parameters not considered in the symmetric system (i.e., solid conductivity and diffusion, exchange current density, and the applied current density). It was found that minor changes in solid diffusivity and conductivity had a minimal impact on cell performance, while decreasing exchange current density had a significant impact. Finally, the cell efficiency was modelled for increasing current densities and the general trend noted for conforming well to reality.

In conclusion, both systems returned realistic results and allowed for a deeper understanding of the LiB physics and internal cell profiles. This information can be used in future applications to understand limiting conditions and facilitate battery design. The macro-scale battery system provides a framework for which future models can extend upon (i.e. a micro-scale and thermal model).

4.2 Contributions

This work contributed to the literature in the following ways:

- The equations governing CST are highly non-trivial. Certain works provide the scientific grounding for these equations, however, none could be found that provide a rigorous derivation. This work fully outlines how the equations are developed, what the relevant first principles are, and how they are be applied based on certain assumptions. This work sheds light on the non-intuitive terms such as the conductivity definition, thermodynamic factor, and molality correction factor. Additionally, this work discusses the confusion surrounding the use of ϕ_R instead of ϕ_m to describe the electrolyte potential, and how this usage will impact the BV equations.

- Most works simplify the model by either implementing only first order equations,

assuming one-dimensionality, or using a commercial FEM solver, and thus not allowing for other groups to verify or expand on their work. This work, however, provides an open-sourced FEM framework and the discretized weak form of the implemented multi-dimensional governing equations. This is provided for the symmetric cell system, in which an electrolyte can be studied using CST, and for the full macro-scale cell model. The fully documented and verifiable software can then be used as is, or expanded for future works.

- Multiple boundary conditions for the CST electrolyte have been proposed in the literature. Based on the derivation provided in this work, one formulation was preferred and validated by experimental results. Additionally, the alternative boundary conditions that have been reported were also implemented in the model. The differences were compared and discussed in the context of the literature that proposes these alternative boundary conditions.

- Creating a computational LiB framework can have advantages in itself, such as being able to verify the governing equations and understanding the relevant physics, but the main objective of all models is to supplement design by guiding experimental research. This is done by investigating the interior physical profiles that are unobtainable during experimentation, or by providing accurate results faster than experimentation and therefore guiding design optimization. This work provided insight into the interior solution variable and reaction rate profiles which helped in understanding where and by what means losses were most significant. This work also provided parametric studies for a host of electrolyte and solid phase parameters. This helped understand which material characteristic would be most important for improving battery performance.

4.3 Future Work

The current work has the following limitations:

- The use of the solid potential for a reference Li/Li^+ electrode as a solution variable in the electrolyte complicates the use of the BV equations and is not common in the field of electrochemistry, outside of battery research.

- The discussion of the results is not exhaustive in what was chosen to be studied, given the capability of the model.

- The full battery system makes the major assumption of infinitely fast intra-particle diffusion, which is known to cause major inaccuracies in predicting battery performance.

Therefore, the areas of future research proposed are using alternative solution variables, conducting further macro-scale investigations, and adding the micro-scale model.

4.3.1 Alternative Solution Variables

In Section 2.1.2.2, two forms of the MacInnes equation were presented: one with respect to the reference potential, ϕ_R, and one with respect to the electrolyte potential, ϕ_m. In battery modelling using CST, the convention is to use ϕ_R because it reduces the need for two thermodynamic factors to only one. Not only that, but the thermodynamic factor in Equation (2.55), i.e.,

$$\left(1 + \frac{\partial \ln \gamma_{+-}}{\partial \ln m_{Li^+}}\right)$$

is characteristic of the electrolyte salt combination and is therefore likely easier to experimentally measure than either thermodynamic terms in Equation (2.56), i.e.,

$$\left(1 + \frac{\partial \ln \gamma_{+}}{\partial \ln m_{Li^+}}\right), \quad \left(1 + \frac{\partial \ln \gamma_{-}}{\partial \ln m_{Li^+}}\right)$$

as they are with respect to the individual ionic species in the electrolyte salt. Despite these advantages, ϕ_m is traditionally used in the field of electrochemistry as a whole because it is directly derived from NP theory and is far simpler to use in conjunction with the BV equations.

Future work could be to investigate a macro-scale model in which ϕ_m is used as the solution variable instead of ϕ_R. Not only would this greatly reduce the complexity surrounding the BV equation, but it would also allow direct comparison between the CST battery system to other applications in electrochemistry; namely DST, in which ϕ_m is consistently used. Further research would need to be conducted to determine the importance of differentiating the two thermodynamic factors from the one in Equation (2.55). If they could be assumed similar or if a convenient method of measuring them could be found, this framework may be much more useful than the one outlined in this work.

The system of governing equations that would describe this alternative macro-scale model, obtained from Chapter 2, would be,

$$
\begin{aligned}
(1-\epsilon)\frac{\partial c_{Li_{(s)}}}{\partial t} &= \nabla\cdot\left(D_s^{eff}\nabla c_{Li_{(s)}}\right) && + S_{Li_{(s)}} && (2.94)\\
0 &= \nabla\cdot\left(\sigma_s^{eff}\nabla\phi_s\right) && + FS_{Li_{(s)}} && (2.101)\\
\epsilon\frac{\partial c_{Li^+}}{\partial t} &= \nabla\cdot\left(\zeta\nabla c_{Li^+}\right) && - \frac{\mathbf{i}\cdot t_+^0}{F} \quad + (1-t_+^0)S_{Li^+} && (2.105)\\
0 &= \nabla\cdot\left(\kappa^{eff}\nabla\phi_m + \xi\nabla c_{Li^+}\right) && + FS_{Li^+} && (4.1)
\end{aligned}
$$

$$
\text{where,}\quad \xi = -\frac{\kappa^{eff}RT}{c_{Li^+}F}\left(t_-^0\left(1+\frac{\partial\ln\gamma_-}{\partial\ln m_{Li^+}}\right)-t_+^0\left(1+\frac{\partial\ln\gamma_+}{\partial\ln m_{Li^+}}\right)\right)\left(1-\frac{d\ln c_0}{d\ln c_{Li^+}}\right)
$$

$$
\text{and,}\quad \zeta = D^{eff}\left(1-\frac{d\ln c_0}{d\ln c_{Li^+}}\right)
$$

The reaction source terms would be,

$$
\begin{aligned}
S_{Li_{(s)}} = \frac{A_v i_{ref,c}}{F}\Bigg[&\left(\frac{c_{Li^+}}{c_{Li^+}^{ref}}\right)\left(\frac{c_{sat}-c_{Li_{(s)}}}{c_{sat}}\right)\exp\left(-\frac{\alpha_c F}{RT}(\phi_s-\phi_m-E^{eq,ref})\right)\\
&-\left(\frac{c_{Li_{(s)}}}{c_{sat}}\right)\exp\left(\frac{(1-\alpha_c)F}{RT}(\phi_s-\phi_m-E^{eq,ref})\right)\Bigg]
\end{aligned}
\tag{4.2}
$$

and the reactions at the planar electrode would be,

$$
\begin{aligned}
\mathbf{i} = \mathbf{n}i_{ref}\Bigg[&\left(\frac{c_R}{c_R^{ref}}\right)\exp\left(-\frac{\alpha F}{RT}(\phi_{sp}-\phi_m-E^{eq,ref})\right)\\
&-\left(\frac{c_P}{c_P^{ref}}\right)\exp\left(\frac{(1-\alpha)F}{RT}(\phi_{sp}-\phi_m-E^{eq,ref})\right)\Bigg]
\end{aligned}
\tag{2.79}
$$

4.3.2 Further Macro-Scale Investigations

Further macro-scale investigations could also be performed, given the implementation already existing in OpenFCST.

In Section 3.2, the approach taken was to model a battery using the already implemented electrolyte model and sourcing the remaining parameters from the literature. The other approach would have been to find an article with a full set of input parameters and reproduce the experimental results using the macro-scale system. This would allow for a quantitative measure of how important it is to include the micro-scale model in the battery simulation. By pursuing this avenue of research, the question of how valid the assumption of infinitely fast particle diffusion could be answered.

Another investigation could be to alter the temperature or Li^+ saturation concentration, thickness, or porosity of the cathode layer and examine the responding discharge curves and solution variable profiles. Other electrolytes could also be implemented to understand under which conditions the optimal cell performance can be achieved.

Additionally, the double layer capacitance could be reintroduced to examine the cell's voltage response at short time scales and for EIS studies.

Finally, the macro-scale model could be run in 2D or 3D with nontrivial geometries. Little research has been carried out for complicated geometries. Optimizing cell dimensions and shapes, especially when combined with the micro-scale model, could help in battery design.

4.3.3 Addition of the Micro-Scale Model

Finally, the most important extension to this work is the addition of the micro-scale model. Research would need to be conducted on the most effective means by which this could be done, but a couple potential solutions are provided here:

- Using the 3D micro-structure, the electrolyte could be solved in the pores only.

Instead of modelling the reactions as source terms, they could be modelled as boundary conditions at the interface with the active particle (similar to the planar electrode BC). The micro-scale model could be solved simultaneously in the solid phase, thus fully coupling the two phases through the reaction kinetics. This method would be very computationally demanding as the micro-structure would need to be resolved completely and thus the domain must have an incredibly fine mesh. This is the approach taken by references [49–51].

- Similar to the previous suggestion, except the two phases would be solved separately, iterating between them to reduce the residual of the reaction equation. This would have the added complication, however, of not directly imposing the requirement for a constant Li^+ concentration within the electrolyte. No previous work has been found that uses this approach.

- Continue modelling the macro-scale on a volumetric averaging basis, where the reaction source term is location dependant and a result of the micro-scale output. The micro-scale model could be solved using a representative volume at each location in the macro-scale, using the concentration and potential values at that location. This would allow the two scales to be solved simultaneously but would save time in that the micro-structure would not need to be fully resolved. This is the approach followed by references [54, 55] in their work with homogenized models.

- Model the macro-scale on the continuum basis, as described in this work. The micro-scale could incorporate a surrogate coupling scheme in which it is parameterized in pre-processing and stored in a database so that, during simulation, the macro-model use the micro-scale solutions on a look-up basis. This is the approach followed by reference [56].

Based on the research conducted in the literature review of this work, the third option

is the best path forward, however, future work may have a different application in mind, in which higher fidelity solution are required. In this case, one of the other options, or perhaps a different one all-together, would be the most appropriate. Once completed, this full scale model could be validated with experimental and literature sourced results. It could be used to aid battery design and predict performance.

Bibliography

[1] B. Dunn, *et al.*, "Electrical energy storage for the grid: A battery of choices," *Science*, vol. 334, no. 6058, pp. 928–935, 2011.

[2] B.A. Johnson, R.E White, "Characterization of commercially avaliable lithium-ion batteries," *Power Sources*, vol. 70, no. 1, pp. 48–54, 1998.

[3] A. Jokar *et al.*, "Review of simplified pseudo-two-dimensional models of lithium-ion batteries," *Journal of Power Sources*, vol. 327, pp. 44–55, 2016.

[4] M.S.M. Farag, "Lithium-ion batteries: Modelling and state of charge estimation," Ph.D. dissertation, McMaster University, 2013.

[5] K. West, *et al.*, "Modeling of porous insertion electrodes with liquid electrolyte," *Journal of Electrochemical Society*, vol. 129, pp. 1480–1485, 1982.

[6] J. Newman, N. Balsara, *Electrochemical Systems*, 4th ed. John Wiley and Sons, 2020.

[7] M. Doyle *et al.*, "Modeling of galvanostatic charge and discharge of the lithium/polymer/insertion cell," *Journal of The Electrochemical Society*, vol. 140, no. 6, pp. 1526–1533, 1993.

[8] M. Doyle, *et al.*, "Comparison of modeling predictions with experimental data from plastic lithium ion cells," *Journal of Electrochemical Society*, vol. 143, no. 6, pp. 1890–1903, 1996.

[9] D. Zhang, *et al.*, "Modeling lithium intercalation of a single spinel particle under potentiodynamic control," *Journal of Electrochemical Society*, vol. 147, no. 3, pp. 831–838, 2000.

[10] M. Guo, *et al.*, "Single-particle model for a lithium-ion cell: Thermal behavior," *Journal of Electrochemical Society*, vol. 158, no. 2, A122–A132, 2011.

[11] V. Ramadesigan, *et al.*, "Optimal porosity distribution for minimized ohmic drop across a porous electrode," *Journal of Electrochemical Society*, vol. 157, no. 13, A1328, 2010.

[12] M. Doyle, J. Newman, "Modeling the performance of rechargeable lithium-based cells: Design correlations for limiting cases," *Journal of The Power Sources*, vol. 54, no. 1, pp. 46–51, 1995.

[13] M. Doyle, J. Newman, "The use of mathematical modeling in the design of lithium/polymer battery systems," *Electrochemica Acta*, vol. 40, p. 2191, 1995.

[14] S.K. Rahimian, *et al.*, "Extension of physics-based single particle model for higher charge-discharge rates," *Power Sources*, vol. 224, pp. 180–194, 2013.

[15] T.R. Tanim, *et al.*, "A temperature dependent, single particle, lithium ion cell model including electrolyte diffusion," *Journal of Dynamic Systems, Measurement, and Control*, vol. 137, no. 1, p. 011 005, 2015.

[16] M. Mastali, *et al.*, "Simplified electrochemical multi-particle model for LiFePO4 cathodes in lithium-ion batteries," *Journal of Power Sources*, vol. 275, pp. 633–643, 2015.

[17] T.S. Dao, *et al.*, "Simplification and order reduction of lithium-ion battery model based on porous-electrode theory," *Journal of Electrochemical Society*, vol. 198, pp. 329–337, 2012.

[18] R. Klein, *et al.*, "Electrochemical model based observer design for a lithium-ion battery," *IEEE Transactions on Control Systems Technology*, vol. 21, no. 2, pp. 289–301, 2013.

[19] L. Cai, R.E. White, "Reduction of model order based on proper orthogonal decomposition for lithium-ion battery simulations," *Journal of Electrochemical Society*, vol. 156, no. 3, A153–A161, 2009.

[20] V.R. Subramanian, *et al.*, "Mathematical model reformulation for lithium-ion battery simulations: Galvanostatic boundary conditions," *Journal of Electrochemical Society*, vol. 156, no. 4, A260–A271, 2009.

[21] K. Smith, *et al.*, "Model-based electrochemical estimation and constraint management for pulse operation of lithium ion batteries," *IEEE Transactions on Control Systems Technology*, vol. 18, no. 3, pp. 654–663, 2010.

[22] V. Ramadesigan, *et al.*, "Efficient reformulation of solid-phase diffusion in physics-based lithium-ion battery models," *Journal of Electrochemical Society*, vol. 157, no. 7, A854–A860, 2010.

[23] J.C. Forman, *et al.*, "Reduction of an electrochemistry based li-ion battery model via quasi-linearization and pade approximation," *Journal of Electrochemical Society*, vol. 158, no. 2, A93–A101, 2011.

[24] J.L. Lee, *et al.*, "One-dimensional physics-based reduced order model of lithium-ion dynamics," *Journal of Power Sources*, vol. 220, pp. 430–448, 2011.

[25] W. Luo, *et al.*, "An approximate solution for electrolyte concentration distribution in physics-based lithium-ion cell models," *Microelectronics Reliability*, vol. 53, no. 6, pp. 797–804, 2013.

[26] J. Marcicki, *et al.*, "Design and parametrization analysis of a reduced-order electrochemical model of graphite/LiFePO4 cells for SOC/SOH estimation," *Journal of Power Sources*, vol. 237, pp. 310–324, 2013.

[27] F. Brosa Planella, *et al.*, "A continuum of physics-based lithium-ion battery models reviewed," *Progress in Energy*, vol. 4, p. 042 003, 2022.

[28] D. Linden, T.B. Reddy, *Handbook of Batteries*, 3rd ed. McGraw-Hill Book Co., 2001.

[29] P. Albertus *et al.*, "Challenges for and Pathways toward Li-Metal-Based All-Solid-State Batteries," *ACS Energy Letters*, vol. 6, no. 4, pp. 1399–1404, 2021.

[30] S. Fujiwara *et al.*, "New molten salt systems for high temperature molten salt batteries: Ternary and quaternary molten salt systems based on LiF–LiCl, LiF–LiBr, and LiCl–LiBr," *Journal of Power Sources*, vol. 196, no. 8, pp. 4012–4018, 2011.

[31] P.U. Nzereogu, *et al.*, "Anode materials for lithium-ion batteries: A review," *Applied Surface Science Advances*, vol. 9, p. 100 233, 2022.

[32] K. Higa, *et al.*, "Comparing macroscale and microscale simulations of porous battery electrodes," *Journal of The Electrochemical Society*, vol. 164, no. 11, E3473–E3488, 2017.

[33] W.B. Hawley, J. Li, "Electrode manufacturing for lithium-ion batteries—analysis of current and next generation processing," *Journal of Energy Storage*, vol. 25, p. 100 862, 2019.

[34] A. Manthiram, "A reflection on lithium-ion battery cathode chemistry," *Nature Communications*, vol. 11, p. 1550, 2020.

[35] A. Ahniyaz, *et al.*, "Progress in solid-state high voltage lithium-ion battery electrolytes," *Advances in Applied Energy*, vol. 4, p. 100 070, 2021.

[36] Q. Li, *et al.*, "Progress in electrolytes for rechargeable Li-based batteries and beyond," *Green Energy Environment*, vol. 1, no. 1, pp. 18–42, 2016.

[37] T. Famprikis, *et al.*, "Fundamentals of inorganic solid-state electrolytes for batteries," *Nature Materials*, vol. 18, pp. 1278–1291, 2019.

[38] Q.Q. Yu *et al.*, "A Comparative Study on Open Circuit Voltage Models for Lithium-ion Batteries," *Chinese Journal of Mechanical Engineering*, vol. 31, p. 65, 2021.

[39] S.H Garofalini, "Molecular dynamics simulations of li transport between cathode crystals," *Journal of Power Sources*, vol. 110, no. 2, pp. 412–415, 2002.

[40] W.Q. Li, S.H Garofalini, "Molecular dynamics simulation of lithium diffusion in Li2O–Al2O3–SiO2 glassess," *Journal of Power Sources*, vol. 166, no. 3, pp. 365–373, 2004.

[41] K.R. Kganyago, P.E. Ngoepe, "Structural and electronic properties of lithium intercalated graphite LiC6," *Physical Review B*, vol. 68, p. 205 111, 2003.

[42] Y. Qi, *et al.*, "Threefold increase in the young's modulus of graphite negative electrode during lithium intercalation," *Journal of Electrochemical Society*, vol. 157, no. 5, A558, 2010.

[43] K. Tasaki, *et al.*, "Decomposition of LiPF6 and stability of PF5 in li-ion battery electrolytes: Density functional theory and molecular dynamics studies," *Journal of Electrochemical Society*, vol. 150, no. 12, A1628, 2003.

[44] Y. Chen, J.W. Evans, "Three-dimensional thermal modeling of lithium-polymer batteries under galvanostatic discharge and dynamic power profile," *Journal of Electrochemical Society*, vol. 141, no. 11, p. 2947, 1994.

[45] C.R. Pals, J. Newman, "Thermal modeling of lithium/polymer battery ii: Thermal profiles in a cell stack," *Journal of Electrochemical Society*, vol. 142, no. 10, p. 3282, 1995.

[46] Y. Chen, J.W. Evans, "Thermal analysis of lithium-ion batteries," *Journal of Electrochemical Society*, vol. 143, p. 2708, 1996.

[47] Z. Wang, *et al.*, "Theoretical simulation and modeling of three-dimensional batteries," *Cell Reports Physical Science*, vol. 1, no. 6, p. 100 078, 2020.

[48] P. Northrop *et al.*, "Coordinate transformation, orthogonal collocation, model reformulation and simulation of electrochemical-thermal behavior of lithium-ion battery stacks," *Journal of Electrochemical Society*, vol. 158, no. 12, A1461, 2011.

[49] G.B. Less, *et al.*, "Micro-Scale Modeling of Li-Ion Batteries: Parameterization and Validation," *Journal of The Electrochemical Society*, vol. 159, no. 6, A697–A704, 2016.

[50] X. Lu, *et al.*, "3D microstructure design of lithium-ion battery electrodes assisted by X-ray nano-computed tomography and modelling," *Nature Communications*, vol. 11, p. 2079, 2020.

[51] A. Shodiev, *et al.*, "4D-resolved physical model for Electrochemical Impedance Spectroscopy of Li(Ni1-x-yMnxCoy)O2-based cathodes in symmetric cells: Consequences in tortuosity calculations," *Journal of Power Sources*, vol. 454, p. 227 871, 2020.

[52] R. Thiedmann, *et al.*, "Graph-based simulated annealing: a hybrid approach to stochastic modeling of complex microstructures," *Modelling and Simulation in Materials Science and Engineering*, vol. 50, p. 3365, 2012.

[53] M. Ender, *et al.*, "Three-dimensional reconstruction of a composite cathode for lithium-ion cells," *Electrochemical Communications*, vol. 13, no. 2, p. 166, 2011.

[54] A.G. Kashkooli *et al.*, "Multiscale modeling of lithium-ion battery electrodes based on nano-scale x-ray computed tomography," *Journal of Power Sources*, vol. 307, pp. 496–509, 2016.

[55] S. Kim, *et al.*, "Multiphysics coupling in lithium-ion batteries with reconstructed porous microstructures," *The Journal of Physical Chemistry*, vol. 122, no. 10, pp. 5280–5290, 2018.

[56] W. Du, *et al.*, "A Surrogate-Based Multi-Scale Model for Mass Transport and Electrochemical Kinetics in Lithium-Ion Battery Electrodes," *Journal of the Electrochemical Society*, vol. 161, no. 8, E3086–E3096, 2014.

[57] K.C. Smith, *et al.*, "Columnar order in jammed LiFePO4 cathodes: ion transport catastrophe and its mitigation," *Physical Chemistry Chemical Physics*, vol. 14, p. 7040, 2012.

[58] G.M. Goldin, *et al.*, "Three-dimensional particle-resolved models of Li-ion batteries to assist the evaluation of empirical parameters in one-dimensional models," *Electrochemica Acta*, vol. 64, p. 118, 2012.

[59] W. Dreyer, *et al.*, "The behavior of a many-particle electrode in a lithium-ion battery," *Physica D Nonlinear Phenomena*, vol. 240, no. 12, p. 1008, 2011.

[60] C.W. Wang, A.M. Sastry, "Mesoscale Modeling of a Li-Ion Polymer Cell," *Journal of Electrochemical Society*, vol. 154, no. 11, A1035, 2007.

[61] T. Fuller *et al.*, "Simulation and optimization of the dual lithium ion insertion cell," *Journal of The Electrochemical Society*, vol. 141, no. 1, pp. 1–10, 1994.

[62] J. Newman, "Optimization of porosity and thickness of a battery electrode by means of a reaction-zone model," *The Electrochemical Society*, vol. 142, p. 97, 1995.

[63] J. Mao, *et al.*, "Simulation of li-ion cells by dualfoil model under constant-resistance load," *ECS Transactions*, vol. 58, p. 71, 2014.

[64] T. Fuller *et al.*, "Relaxation phenomena in lithium-ion-insertion cells," *Journal of The Electrochemical Society*, vol. 141, no. 4, pp. 982–989, 1994.

[65] M. Gomadam, *et al.*, "Mathematical modeling of lithium-ion and nickel battery systems," *Journal of Power Sources*, vol. 110, no. 2, pp. 267–284, 2002.

[66] P. Ramadass *et al.*, "Mathematical modeling of the capacity fade of li-ion cells," *Journal of Power Sources*, vol. 123, pp. 230–240, 2003.

[67] P. Ramadass *et al.*, "Development of first principles capacity fade model for li-ion cells," *Journal of Electrochemical Society*, vol. 151, A196, 2004.

[68] K. Thomas, J. Newman, "Thermal modeling of porous insertion electrodes," *Journal of Electrochemical Society*, vol. 150, no. 2, A176, 2003.

[69] G. Botte, *et al.*, "Mathematical modeling of secondary lithium batteries," *Electrochemica Acta*, vol. 45, no. 15, pp. 2595–2609, 2000.

[70] G. Ning, *et al.*, "A generalized cycle life model of rechargeable li-ion batteries," *Electrochemica Acta*, vol. 51, no. 10, pp. 2012–2022, 2006.

[71] V. Sulzer, *et al.*, "Python battery mathematical modelling (pybamm)," *Journal of Open Research Software*, vol. 9, no. 1, p. 14, 2017.

[72] S. Al Hallaj, *et al.*, "Thermal modeling and design considerations of lithium-ion batteries," *Journal of Power Sources*, vol. 83, no. 1, pp. 1–8, 1999.

[73] D. Bernardi, *et al.*, "A general energy balance for battery systems," *Journal of Electrochemical Society*, vol. 132, no. 1, p. 5, 1985.

[74] T.I. Evans, R.E. White, "A thermal analysis of a spirally wound battery using a simple mathematical model," *Journal of Electrochemical Society*, vol. 136, no. 8, p. 2145, 1989.

[75] Y. Chen, J.W. Evans, "Heat transfer phenomena in lithium/polymer-electrolyte batteries for electric vehicle application," *Journal of Electrochemical Society*, vol. 140, no. 7, p. 1833, 1993.

[76] C.R. Pals, J. Newman, "Thermal modeling of lithium/polymer battery i: Discharge behaviour of single cell," *Journal of Electrochemical Society*, vol. 142, no. 10, p. 3274, 1995.

[77] G. Botte, *et al.*, "Influence of some design variables on the thermal behavior of a lithium-ion cell," *The Electrochemical Society*, vol. 146, no. 3, p. 914, 1999.

[78] D.R. Baker, M.W.Verbrugge, "Temperature and current distribution in thin-film batteries," *Journal of Electrochemical Society*, vol. 146, no. 7, p. 2413, 1999.

[79] L. Song, J.W. Evans, "Electrochemical-thermal model of lithium polymer batteries," *Journal of Electrochemical Society*, vol. 147, no. 6, p. 2086, 2000.

[80] M.K. Verbrugge, "Three-dimensional temperature and current distribution in a battery module," *AIChE*, vol. 41, no. 6, p. 1550, 1995.

[81] H. Huang, T.V. Nguyen, "A transient non-isothermal model for valve-regulated lead-acid batteries under float," *Journal of Electrochemical Society*, vol. 144, no. 7, p. 2420, 1997.

[82] P. De Vidts, *et al.*, "A nonisothermal nickel-hydrogen cell model," *Journal of Electrochemical Society*, vol. 145, no. 11, p. 3874, 1998.

[83] W.Gu, C. Wang, "Thermal-electrochemical modeling of battery systems," *Journal of the Electrochemcial Society*, vol. 147, no. 8, pp. 2910–2922, 2000.

[84] J. Christensen, J. Newman, "A mathematical model of stress generation and fracture in lithium manganese oxide," *Journal of Electrochemical Society*, vol. 153, no. 6, A1019, 2006.

[85] X. Zhang *et al.*, "Numerical simulation of intercalation-induced stress in li-ion battery electrode particles," *Journal of Electrochemical Society*, vol. 154, no. 10, A910, 2007.

[86] R.E. Garcia *et al.*, "Microstructural modeling and design of rechargeable lithium-ion batteries," *Journal of Electrochemical Society*, vol. 152, no. 1, A255, 2005.

[87] L. Wu *et al.*, "Three-dimensional finite element study on Li diffusion induced stress in FIB-SEM reconstructed LiCoO2 half cell," *Electrochimica Acta*, vol. 222, pp. 814–820, 2016.

[88] K. Leung, J.L. Budzien, "Ab initio molecular dynamics simulations of the initial stages of solid–electrolyte interphase formation on lithium ion battery graphitic anodes," *Physical Chemistry Chemical Physics*, vol. 12, no. 25, p. 6583, 2010.

[89] B.L. Trembacki, *et al.*, "Fully coupled simulation of lithium ion battery cell performance," *Laboratory Directed Research and Development*, p. 7997, 2015.

[90] B.L. Trembacki, *et al.*, "Mesoscale electrochemical performance simulation of 3d interpenetrating lithium-ion battery electrodes," *Journal of The Electrochemical Society*, vol. 166, no. 6, A923–A934, 2019.

[91] S. Allu *et al.*, "A new open computational framework for highly-resolved coupled three-dimensional multiphysics simulations of Li-ion cells," *Journal of Power Sources*, vol. 246, pp. 876–886, 2014.

[92] R.W. Hart, *et al.*, "3-d microbatteries," *Electrochemical Communications*, vol. 5, no. 2, pp. 120–123, 2003.

[93] V. Zadin, *et al.*, "Modelling electrode material utilization in the trench model 3d-microbattery by finite element analysis," *Journal of The Power Sources*, vol. 195, no. 18, pp. 6218–6224, 2010.

[94] D.J. Noelle *et al.*, "Internal resistance and polarization dynamics of lithium-ion batteries upon internal shorting," *Applied Energy*, vol. 212, no. 15, pp. 796–808, 2018.

[95] Q. Yang, *et al.*, "A simplified fractional order impedance model and parameter identification method for lithium-ion batteries," *Plos One*, vol. 12, no. 2, p. 0 172 424, 2017.

[96] B.Y. Liaw, *et al.*, "Modeling of lithium ion cells—a simple equivalent-circuit model approach," *Solid State Ionics*, vol. 175, no. 1–4, pp. 835–839, 2004.

[97] V. Ramadesigan, *et al.*, "Modeling and simulation of lithium-ion batteries from a systems engineering perspective," *Journal of Electrochemical Society*, vol. 159, no. 3, R31–R45, 2012.

[98] B. Yan *et al..*, "Three dimensional simulation of galvanostatic discharge of licoo2 cathode based on x-ray nano-ct images," *Journal of Electrochemical Society*, vol. 159, A1604–A1614, 2012.

[99] B. Yan *et al..*, "Simulation of heat generation in a reconstructed licoo2 cathode during galvanostatic discharge," *Electrochim. Acta*, vol. 100, pp. 171–179, 2013.

[100] C. Lim *et al..*, "Simulation of diffusion-induced stress using reconstructed electrodes particle structures generated by micro/nano-ct," *Electrochim. Acta*, vol. 75, pp. 279–287, 2012.

[101] A.A. Franco, "Multiscale modelling and numerical simulation of rechargeable lithium ion batteries: Concepts, methods and challenges," *RSC Adv.*, vol. 3, pp. 13 027–13 058, 2013.

[102] P. Georen, G. Lindbergh, "Characterisation and modelling of the transport properties in lithium battery polymer electrolytes," *Electrochimica Acta*, vol. 47, pp. 577–587, 2001.

[103] D. Pesko *et al.*, "Negative transference numbers in poly(ethylene oxide)-based electrolytes," *Journal of Electrochemical Society*, vol. 164, no. 11, E3569–E3575, 2017.

[104] D. Bazak *et al.*, "Mapping of lithium-ion battery electrolyte transport properties and limiting currents with in situ MRI," *Journal of The Electrochemical Society*, vol. 167, no. 14, p. 140 518, 2020.

[105] D. Pesko *et al.*, "Comparing cycling characteristics of symmetric lithium-polymer-lithium cells with theoretical predictions," *Journal of Electrochemical Society*, vol. 165, no. 13, A3186–A3194, 2018.

[106] H. Lundgren *et al.*, "Electrochemical characterization and temperature dependency of mass-transport properties of LiPF6 in EC:DEC," *Journal of Electrochemical Society*, vol. 162, no. 3, A413–A420, 2015.

[107] L. Onsager, "Theories and problems of liquid diffusion," 1945.

[108] K.E. Thomas *et al.*, *Mathematical modeling of lithium batteries, in: W.A.V. Schalkwijk, B. Scrosati (Eds.), Advances in Lithium-ion Batteries*. Springer Science and Business Media, 2002.

[109] K. Fong *et al.*, "Ion transport and the true transference number in nonaqueous polyelectrolyte solutions for lithium ion batteries," *ACS Central Science*, vol. 5, no. 7, pp. 1250–1260, 2019.

[110] A. Wang *et al.*, "Review of parameterisation and a novel database (LiionDB) for continuum Li-ion battery models," *Progress in Energy*, 2022.

[111] J. Newman *et al.*, "Mass transfer in concentrated binary electrolytes," *Berichte der Bunsengesellschaft*, vol. 69, no. 7, pp. 608–612, 1965.

[112] M. Farkhondeh, C. Delacourt, "Mathematical modeling of commercial LiFePO4 electrodes based on variable solid-state diffusivity," *Journal of The Electrochemical Society*, vol. 159, no. 2, A177–A192, 2011.

[113] L. Cabras *et al.*, "A two-mechanism and multiscale compatible approach for solid state electrolytes of (Li-ion) batteries," *Journal of Energy Storage*, vol. 48, p. 103 842, 2022.

[114] A. Bizeray *et al.*, "Resolving a discrepancy in diffusion potentials, with a case study for li-ion batteries," *Journal of The Electrochemical Society*, vol. 163, no. 8, E223–E229, 2016.

[115] G.A. Martynov, R.R. Salem, *Electrical Double Layer at a Metal-dilute Electrolyte Solution Interface*. Springer-Verlag, 1983.

[116] A. Kosakian, "Transient numerical modeling of proton-exchange-membrane fuel cells," Ph.D. dissertation, University of Alberta, 2021.

[117] M. Mastali *et al.*, "Three-dimensional multi-particle electrochemical model of LiFePO4 cells based on a resistor network methodology," *Electrochimica Acta*, vol. 190, pp. 574–587, 2016.

[118] E. Dickinson, A. Wain, "The butler-volmer equation in electrochemical theory: Origins, value, and practical application," *Journal of Electroanalytical Chemistry*, vol. 872, p. 114 145, 2020.

[119] A.J. Bard, L.R.Faulkner, *Electrochemical Methods: Fundamentals and Applications*, 2nd ed. John Wiley and Sons, 2001.

[120] M. Ferraro, *et al.*, "Electrode Mesoscale as a Collection of Particles: Coupled Electrochemical and Mechanical Analysis of NMC Cathodes," *Ionics*, vol. 167, no. 1, p. 013 543, 2022.

[121] B Tjaden *et al.*, "On the origin and application of the bruggeman correlation for analysing transport phenomena in electrochemical systems," *Current Opinion in Chemical Engineering*, vol. 12, pp. 44–51, 2016.

[122] H. Gerischer, C. Tobias, "Advances in electrochemistry and electrochemical engineering," *Advance in Chemical Physics*, vol. 13, pp. 2336–2344, 1984.

[123] D. A. G. Bruggeman, "Berechnung verschiedener physikalischer Konstanten von heterogenen Substanzen. I. Dielektrizitätskonstanten und Leitfähigkeiten der Mischkörper aus isotropen Substanzen," *Annalen der Physik*, vol. 5, no. 24, pp. 636–664, 1935.

[124] C. Sequeira, A. Hooper, "The study of lithium electrode reversibility against (PEO)xLiF3CSO3 polymeric electrolytes," *Solid State Ionics*, vol. 9–10, pp. 1131–1138, 1983.

[125] G. Richardson *et al.*, "An application of irreversible thermodynamics to the study of diffusion," *Journal of Applied Mathematics*, 2019.

[126] Z. Mao, *et al.*, "Dynamics of a Blended Lithium-Ion Battery Electrode During Galvanostatic Intermittent Titration Technique.," *Electrochimica Acta*, vol. 222, pp. 1741–1750, 2016.

[127] S. Krachkovskiy *et al.*, "Determination of mass transfer parameters and ionic association of LiPF6 : Organic carbonates solutions," *Journal of The Electrochemical Society*, vol. 164, no. 4, A912–A916, 2017.

[128] Z. Feng *et al.*, "Evaluating transport properties and ionic dissociation of LiPF6 in concentrated electrolyte," *Journal of The Electrochemical Society*, vol. 164, no. 12, A2434–A2440, 2017.

[129] N. Stolwijk *et al.*, "On the extraction of ion association data and transference numbers from ionic diffusivity and conductivity data in polymer electrolytes," *Electrochimica Acta*, vol. 102, pp. 451–458, 2013.

[130] E. Prada *et al.*, "Simplified electrochemical and thermal model of LiFePO4-Graphite Li-Ion batteries for fast charge applications," *Journal of Electrochemical Society*, vol. 159, no. 9, A1508—A1519, 2012.

[131] O. Pecher *et al.*, "Challenges and new opportunities of in situ NMR characterization of electrochemical processes," *Electrochemical Storage Materials*, p. 020 011, 2016.

[132] S. Krachkovskiy *et al.*, "Visualization of steady-state ionic concentration profiles formed in electrolytes during Li-Ion battery operation and determination of mass-transport properties by in situ magnetic resonance imaging," *Journal of the American Chemical Society*, vol. 138, no. 25, pp. 7992–7999, 2016.

[133] A. Kosakian, M. Secanell, "Estimating charge-transport properties of fuel-cell and electrolyzer catalyst layers via electrochemical impedance spectroscopy," *Electrochimica Acta*, vol. 367, p. 137 521, 2021.

[134] A. Bandarenka, "Exploring the interfaces between metal electrodes and aqueous electrolytes with electrochemical impedance spectroscopy," *The Analyst*, vol. 138, no. 19, p. 5540, 2013.

[135] M. Gouverneur, *et al.*, "Direct determination of ionic transference numbers in ionic liquids by electrophoretic NMR," *Physical Chemistry Chemical Physics*, vol. 17, pp. 30 680–30 686, 2015.

[136] K. Xu, "Navigating the minefield of battery literature," *Communications Materials*, vol. 3, p. 31, 2022.

[137] A.L. Levy, "Difficulties in the Hittorf method for determining transference numbers," *Journal of Chemical Education*, vol. 29, no. 8, p. 384, 1952.

[138] G. Richardson *et al.*, "The effect of ionic aggregates on the transport of charged species in lithium electrolyte solutions," *Journal of Electrochemical Society*, vol. 165, no. 9, 2018.

[139] A. Nyman *et al.*, "Electrochemical characterisation and modelling of the mass transport phenomena in LiPF6–EC–EMC electrolyte," *Electrochimica Acta*, vol. 53, no. 22, pp. 6356–6365, 2008.

[140] L. Valøen and J. Reimers, "Three-dimensional multi-particle electrochemical model of LiFePO4 cells based on a resistor network methodology," *Journal of Electrochemical Society*, vol. 152, A882, 2005.

[141] I. Villaluenga *et al.*, "Negative stefan-maxwell diffusion coefficients and complete electrochemical transport characterization of homopolymer and block copolymer electrolytes," *Journal of Electrochemical Society*, vol. 165, no. 11, 2018.

[142] S. Stewart, J. Newman, "The use of UV/vis absorption to measure diffusion coefficients in lipf6 electrolytic solutions," *Journal of Electrochemical Society*, vol. 155, no. 1, F13, 2008.

[143] M. Xu, X. Wang, "Electrode thickness correlated parameters estimation for Li-ion NMC battery electrochemical model," *Journal of Electrochemical Society*, vol. 77, p. 491, 2017.

[144] F. Cadiou *et al.*(), "Numerical Prediction of Multiscale Electronic Conductivity of Lithium-Ion Battery Positive Electrodes," *Journal of Electrochemistry Society*, vol. 166, no. 8, A1692, 2019.

[145] J. Schmalstieg *et al.*, "Full cell parameterization of a high-power Lithium-ion battery for a physico-chemical model: Part I. physical and electrochemical parameters," *Journal of Electrochemical Society*, vol. 165, A3799, 2018.

[146] M. Safari, C. Delacourt, "Mathematical modeling of lithium iron phosphate electrode: Galvanostatic charge/discharge and path dependence," *Journal of The Electrochemical Society*, vol. 158, no. 2, A63, 2011.

[147] Z. Ruifeng *et al.*, "A study on the open circuit voltage and state of charge characterization of high capacity lithium-ion battery under different temperature," *Energies*, vol. 11, no. 9, p. 2408, 2018.

[148] M. Secanell *et al.*, "Openfcst: An open-source mathematical modelling software for polymer electrolyte fuel cells," *ECS Transactions*, vol. 64, no. 3, pp. 655–680, 2014.

[149] P.R. Amestoy *et al.*, "Multifrontal parallel distributed symmetric and unsymmetric solvers," *Computer Methods in Applied Mechanics and Engineering*, vol. 184, no. 2–4, pp. 512–520, 2000.

[150] D. Arndt, *et al.*, "The deal.II library, Version 9.4," *Journal of Numerical Mathematics*, vol. 30, no. 3, pp. 231–246, 2022.

[151] A. Einstein, "On the motion of small particles suspended in liquids at rest required by the molecular-kinetic theory of heat.," *Annalen der Physik*, vol. 17, pp. 549–560, 1905.

[152] V. Blickle, *et al.*, "Einstein relation generalized to nonequilibrium," *Physical Review Letters*, vol. 98, no. 21, p. 210 601, 2006.

[153] R. Laity, "An application of irreversible thermodynamics to the study of diffusion," *Journal of Physical Chemistry*, vol. 63, no. 1, pp. 80–83, 1959.

[154] M. Farkhondeh *et al.*, "Full-range simulation of a commercial LiFePO4 electrode accounting for bulk and surface effects: A comparative analysis," *Journal of The Electrochemical Society*, vol. 161, no. 3, A201–A212, 2014.

[155] C. Truesdell, "Mechanical basis of diffusion," *The Journal of Chemical Physics*, vol. 37, no. 10, pp. 2336–2344, 1962.

[156] O. Lamm, "Studies in the kinematics of isother- mal diffusion. a macro-dynamical theory of multicomponent fluid diffusion," *Advance in Chemical Physics*, vol. 6, pp. 291–313, 1964.

[157] A.A. Franco, C.Frayret, *Advances in Batteries for Medium and Large-Scale Energy Storage*. Woodhead Publishing Series in Energy, 2015.

[158] I. Mele, *et al.*, "Advanced Porous Electrode Modelling Framework Based on More Consistent Virtual Representation of the Electrode Topology.," *Journal of Electrochemical Society*, vol. 167, p. 060 531, 2020.

[159] R.B. Smith, M.Z. Bazant, "Multiphase porous electrode theory," *Journal of Electrochemical Society*, vol. 164, no. 11, E3291–E3310, 2017.

[160] D. Miranda, *et al.*, "Computer simulations of the influence of geometry in the performance of conventional and unconventional lithium-ion batteries," *Applied Energy*, vol. 165, pp. 318–328, 2016.

[161] V. Zadin, D. Brandell, "Modelling polymer electrolytes for 3d-microbatteries using finite element analysis," *Electrochemica Acta*, vol. 57, pp. 237–243, 2011.

[162] T.M. Clancy, J.F. Rohan, "Simulations of 3d nanoscale architectures and electrolyte characteristics for li-ion microbatteries," *Journal of Energy Storage*, vol. 23, pp. 1–8, 2019.

[163] S. Dargaville, T.W. Farrell, "Predicting active material utilization in LiFePO4 electrodes using a multiscale mathematical model," *Journal of Electrochemical Society*, vol. 157, no. 7, A830–A840, 2010.

[164] J. Zheng, X. Li, "Characteristics of xLiFePO4·y Li3V2(PO4)3 electrodes for lithium batteries," *Ionics*, vol. 15, p. 753, 2009.

[165] M.Z. Bazant, "Theory of Chemical Kinetics and Charge Transfer based on Nonequilibrium Thermodynamics," *Accounts of Chemical Research*, vol. 46, no. 5, pp. 1144–1160, 2013.

[166] S. Orangi, A.H. Strømman, "A Techno-Economic Model for Benchmarking the Production Cost of Lithium-Ion Battery Cells," *Batteries*, vol. 8, no. 8, p. 83, 2022.

[167] R. Horn, C. Johnson, *Matrix Analysis*, 2nd ed. Cambridge University, 2012.

[168] G. Holzapfel, *Nonlinear Solid Mechanics a Continuum Approach for Engineering*, 1st ed. John Wiley and Sons, 2000.

[169] A. Moéz, "Generalized Frobenius inner products," *Mathematische Annalen*, vol. 141, no. 2, pp. 107–112, 1960.

[170] J. Song, M.Z. Bazant, "Effects of Nanoparticle Geometry and Size Distribution on Diffusion Impedance of Battery Electrodes," *Journal of Electrochemical Society*, vol. 160, no. 1, A15, 2013.

[171] J.H. Cushman, *et al.*, "A primer on upscaling tools for porous media," *Advances in Water Resources*, vol. 25, no. 8–12, p. 1043, 2002.

[172] G. Richardson, *et al.*, "Multiscale modelling and analysis of lithium-ion battery charge and discharge," *Journal of Engineering Mathematics*, vol. 72, p. 41, 2012.

Appendix A: Extended Derivations

This appendix provides mathematical proofs of some of the steps taken in Section 2 and 3 that do not provide further scientific insight into the physics of the equations but are required for completeness.

A.1 Derivation for SOC and C-rate

The state of charge (SOC) in a system is the fraction of the cathode available for Lithium intercalation. Because the application in section 3.2.1 is for a constant current, the SOC will be a linear function of time,

$$SOC(t) = c - \frac{1}{b}t$$

where b and c are constants. For discharge, the cell will begin full charged (i.e., $SOC = 1$), thus making $c = 1$. The second term will be the non-dimensional fraction of filled cathodic active material. Therefore, b is just the total time required to discharge the cell.

$$SOC(t) = 1 - \frac{1}{t_{total}}t$$

The total time of discharge will be dictated by the total amount of solid Lithium that has intercaled into the cathode, i.e., its saturation concentration. Using the principle,

$$\epsilon c_{sat} = r_{Li_{(s)}} t_{total}$$

where $r_{Li_{(s)}}$ is the rate at which solid Lithium is created in M/s, the SOC will be,

$$SOC(t) = 1 - \frac{r_{Li_{(s)}}}{c_{sat}}t$$

The reaction rate can then be expressed in terms of charge, by considering the number of Coulomb's transferred per mole of solid Lithium that is created. This quantity would be equivalent to the average source term in the cathode, i.e.,

$$S_{Li_{(s)},ave} = z_{Li^+} F r_{Li_{(s)}}$$

Finally, the average source term in the cathode will just be the current density being passed into the cathode divided by the thickness of the cathode, assuming zero charge storage (as discussed in section 2.1.2.2), i.e.,

$$S_{Li_{(s)},ave} = \frac{\mathbf{i}}{\delta_c}$$

Substituting all identities in gives the expression provided in section 3.2.1,

$$SOC(t) = 1 - \frac{\mathbf{i}}{z_{Li^+} F \delta_c \epsilon_c c_{sat}} t \tag{1.4}$$

The above derivation will be recycled to obtain an explicit expression for the C-rate. The C-rate is defined as the number of identical batteries that could be discharged in one hour. Alternatively, this is equivalent to 1 hour divided by the time it takes to discharge one battery, i.e.,

$$\text{C-rate} = \frac{1 \text{ hr}}{t_{total}}$$

Then, substituting the equalities above for the total time required to discharge the battery, t_{total}, the C-rate is given by,

$$\text{C-rate} = \frac{\mathbf{i}(1 \text{ hr})}{z_{Li^+} F \delta_c \epsilon_c c_{sat}} \tag{1.5}$$

Where the current, $\mathbf{i}$, is multiplied by 3600 to convert between A to C/hr.

A.2 Derivation between equations (2.18) to (2.21)

Beginning with,

$$\begin{aligned} & c_e\big(\nu_+ \nabla \ln(m_+ \gamma_+) + \nu_- \nabla \ln(m_- \gamma_-)\big) \\ & \quad = -\frac{c_0}{c_T}\left(\Big(\frac{1}{\mathscr{D}_{0+}} - \frac{z_+}{z_-}\frac{1}{\mathscr{D}_{0-}}\Big)\boldsymbol{N}_+ + \frac{1}{z_- \mathscr{D}_{0-}}\frac{\mathbf{i}}{F}\right) \end{aligned} \tag{2.18}$$

and combining term by bringing the ν_i terms into the exponents,

$$c_e \nabla \ln \left(m_+^{\nu_+} \gamma_+^{\nu_+} m_-^{\nu_-} \gamma_-^{\nu_-} \right) = -\frac{c_0}{c_T} \left(\left(\frac{1}{\mathscr{D}_{0+}} - \frac{z_+}{z_-} \frac{1}{\mathscr{D}_{0-}} \right) \boldsymbol{N}_+ + \frac{1}{z_- \mathscr{D}_{0-}} \frac{\mathbf{i}}{F} \right)$$

Equation (2.15), which is given by,

$$m_e = \frac{m_+}{\nu_+} = \frac{m_-}{\nu_-} \tag{2.15}$$

can be substituted into Equation 2.18 in place of m_- to obtain,

$$c_e \nabla \ln \left(m_+^{\nu_+} \left(\frac{m_+ \nu_-}{\nu_+} \right)^{\nu_-} \gamma_+^{\nu_+} \gamma_-^{\nu_-} \right) = -\frac{c_0}{c_T} \left(\left(\frac{1}{\mathscr{D}_{0+}} - \frac{z_+}{z_-} \frac{1}{\mathscr{D}_{0-}} \right) \boldsymbol{N}_+ + \frac{1}{z_- \mathscr{D}_{0-}} \frac{\mathbf{i}}{F} \right)$$

Then, separating the ν_i terms into a new gradient,

$$c_e \left(\nabla \ln \left(m_+^{\nu_+} m_+^{\nu_-} \gamma_+^{\nu_+} \gamma_-^{\nu_-} \right) + \nabla \ln \left(\frac{\nu_-}{\nu_+} \right)^{\nu_-} \right) = -\frac{c_0}{c_T} \left(\left(\frac{1}{\mathscr{D}_{0+}} - \frac{z_+}{z_-} \frac{1}{\mathscr{D}_{0-}} \right) \boldsymbol{N}_+ + \frac{1}{z_- \mathscr{D}_{0-}} \frac{\mathbf{i}}{F} \right)$$

The second gradient will fall to zero because all of its components are constants, resulting in,

$$c_e \nabla \ln \left(m_+^{(\nu_+ + \nu_-)} \gamma_+^{\nu_+} \gamma_-^{\nu_-} \right) = -\frac{c_0}{c_T} \left(\left(\frac{1}{\mathscr{D}_{0+}} - \frac{z_+}{z_-} \frac{1}{\mathscr{D}_{0-}} \right) \boldsymbol{N}_+ + \frac{1}{z_- \mathscr{D}_{0-}} \frac{\mathbf{i}}{F} \right) \tag{2.19}$$

Then applying Equation (2.20), given by,

$$\gamma_{+-}^{(\nu_+ + \nu_-)} = \gamma_+^{\nu_+} \gamma_-^{\nu_-} \tag{2.20}$$

to Equation (2.19),

$$c_e \nabla \ln \left(m_+^{(\nu_+ + \nu_-)} \gamma_{+-}^{(\nu_+ + \nu_-)} \right) = -\frac{c_0}{c_T} \left(\left(\frac{1}{\mathscr{D}_{0+}} - \frac{z_+}{z_-} \frac{1}{\mathscr{D}_{0-}} \right) \boldsymbol{N}_+ + \frac{1}{z_- \mathscr{D}_{0-}} \frac{\mathbf{i}}{F} \right)$$

Then, bringing the exponent in front,

$$c_e (\nu_+ + \nu_-) \nabla \ln \left(m_+ \gamma_{+-} \right) = -\frac{c_0}{c_T} \left(\left(\frac{1}{\mathscr{D}_{0+}} - \frac{z_+}{z_-} \frac{1}{\mathscr{D}_{0-}} \right) \boldsymbol{N}_+ + \frac{1}{z_- \mathscr{D}_{0-}} \frac{\mathbf{i}}{F} \right)$$

and reapplying Equation (2.15),

$$(c_+ + c_-) \nabla \ln \left(m_+ \gamma_{+-} \right) = -\frac{c_0}{c_T} \left(\left(\frac{1}{\mathscr{D}_{0+}} - \frac{z_+}{z_-} \frac{1}{\mathscr{D}_{0-}} \right) \boldsymbol{N}_+ + \frac{1}{z_- \mathscr{D}_{0-}} \frac{\mathbf{i}}{F} \right) \tag{2.21}$$

A.3 Derivation between equations (2.23) to (2.24)

Beginning with,

$$(c_+ + c_-)\left(1 + \frac{\partial \ln \gamma_{+-}}{\partial \ln m_+}\right)\nabla \ln m_+ = -\frac{c_0}{c_T}\left(\left(\frac{1}{\mathscr{D}_{0+}} - \frac{z_+}{z_-}\frac{1}{\mathscr{D}_{0-}}\right)\boldsymbol{N}_+ + \frac{1}{z_-\mathscr{D}_{0-}}\frac{\mathbf{i}}{F}\right) \quad (2.23)$$

we will first isolate for the flux of cations, $\boldsymbol{N}_+$,

$$\begin{aligned}\boldsymbol{N}_+ = &-\frac{c_T(c_+ + c_-)}{c_0}\Big(\frac{1}{\mathscr{D}_{0+}} - \frac{z_+}{z_-}\frac{1}{\mathscr{D}_{0-}}\Big)^{-1}\left(1 + \frac{\partial \ln \gamma_{+-}}{\partial \ln m_+}\right)\nabla \ln m_+ \\ &- \frac{1}{z_-\mathscr{D}_{0-}}\Big(\frac{1}{\mathscr{D}_{0+}} - \frac{z_+}{z_-}\frac{1}{\mathscr{D}_{0-}}\Big)^{-1}\frac{\mathbf{i}}{F}\end{aligned}$$

Eliminating the -1 exponent,

$$\begin{aligned}\boldsymbol{N}_+ = &\frac{c_T(c_+ + c_-)}{c_0}\left(\frac{z_-\mathscr{D}_{0+}\mathscr{D}_{0-}}{z_+\mathscr{D}_{0+} - z_-\mathscr{D}_{0-}}\right)\left(1 + \frac{\partial \ln \gamma_{+-}}{\partial \ln m_+}\right)\nabla \ln m_+ \\ &+ \frac{1}{z_-\mathscr{D}_{0-}}\left(\frac{z_-\mathscr{D}_{0+}\mathscr{D}_{0-}}{z_+\mathscr{D}_{0+} - z_-\mathscr{D}_{0-}}\right)\frac{\mathbf{i}}{F}\end{aligned}$$

and eliminating factors in the current term,

$$\begin{aligned}\boldsymbol{N}_+ = &\frac{c_T(c_+ + c_-)}{c_0}\left(\frac{z_-\mathscr{D}_{0+}\mathscr{D}_{0-}}{z_+\mathscr{D}_{0+} - z_-\mathscr{D}_{0-}}\right)\left(1 + \frac{\partial \ln \gamma_{+-}}{\partial \ln m_+}\right)\nabla \ln m_+ \\ &+ \left(\frac{z_+\mathscr{D}_{0+}}{z_+\mathscr{D}_{0+} - z_-\mathscr{D}_{0-}}\right)\frac{\mathbf{i}}{z_+F}\end{aligned}$$

Then, recalling electroneutrality for the binary electrolyte,

$$z_+c_+ = -z_-c_-$$

Substituting in for c_-,

$$\begin{aligned}\boldsymbol{N}_+ = &\frac{c_T}{c_0}\Big(c_+ - \frac{c_+z_+}{z_-}\Big)\left(\frac{z_-\mathscr{D}_{0+}\mathscr{D}_{0-}}{z_+\mathscr{D}_{0+} - z_-\mathscr{D}_{0-}}\right)\left(1 + \frac{\partial \ln \gamma_{+-}}{\partial \ln m_+}\right)\nabla \ln m_+ \\ &+ \left(\frac{z_+\mathscr{D}_{0+}}{z_+\mathscr{D}_{0+} - z_-\mathscr{D}_{0-}}\right)\frac{\mathbf{i}}{z_+F}\end{aligned}$$

and bringing through the brackets,

$$\begin{aligned}\boldsymbol{N}_+ = &-\frac{c_Tc_+}{c_0}\left(\frac{\mathscr{D}_{0+}\mathscr{D}_{0-}(z_+ - z_-)}{z_+\mathscr{D}_{0+} - z_-\mathscr{D}_{0-}}\right)\left(1 + \frac{\partial \ln \gamma_{+-}}{\partial \ln m_+}\right)\nabla \ln m_+ \\ &+ \left(\frac{z_+\mathscr{D}_{0+}}{z_+\mathscr{D}_{0+} - z_-\mathscr{D}_{0-}}\right)\frac{\mathbf{i}}{z_+F}\end{aligned} \quad (2.24)$$

A.4 Derivation for molality to molarity factor

This section will provide a step-by-step derivation for how to the molality correction factor can be expressed in terms of the specific volume and concentration of the ionic salt for a 1:1 binary electrolyte.

Beginning with the molality to molarity factor from Equation (2.30),

$$1 - \frac{d \ln c_0}{d \ln c_+}$$

The derivation begins by separating the derivative term by introducing a dummy variable, x (x was chosen because using a spacial coordinate gives physical meaning to this derivation),

$$1 - \left(\frac{d \ln c_0}{dx}\right)\left(\frac{d \ln c_+}{dx}\right)^{-1}$$

Then, taking the derivative through the logarithm,

$$1 - \left(\frac{1}{c_0}\frac{dc_0}{dx}\right)\left(\frac{1}{c_+}\frac{dc_+}{dx}\right)^{-1} = 1 - \frac{c_+}{c_0}\frac{dc_0/dx}{dc_+/dx}$$

The following identity states that the sum of partial volumes for each species in solution is equal to the total volume. This requirement is true for all solutions.

$$\sum_i c_i \bar{v}_i = c_e \bar{v}_e + c_0 \bar{v}_0 = 1$$

Rearranging for the concentration of the solvent,

$$c_0 = \frac{1}{\bar{v}_0}(1 - c_e \bar{v}_e)$$

This identity can be applied to determine the derivative of the solvent concentration with respect to the cation concentration,

$$\frac{dc_0}{dx} = -\frac{\bar{v}_e}{\bar{v}_0}\frac{dc_+}{dx}$$

By inserting these two identities into the above equation, one would receive:

$$1 - \frac{c_+}{\frac{1}{\bar{v}_0}(1 - c_+ \bar{v}_e)}\frac{-\frac{\bar{v}_e}{\bar{v}_0}(dc_+/dx)}{(dc_+/dx)}$$

Which, when terms are eliminated, returns,

$$1 - \frac{d \ln c_0}{d \ln c_+} = \frac{1}{1 - \bar{v}_e c_+} \tag{2.31}$$

A.5 Derivation between equations (2.42) to (2.43)

Regarding the derivation from Equation (2.42) to Equation (2.43):

$$\begin{aligned} c_+\nabla\bar{\mu}_+ = \frac{RT}{c_T}\Bigg[&\frac{c_+}{\mathscr{D}_{+-}}\bigg(\frac{z_+c_T\mathscr{D}_e}{z_-c_0}\Big(1+\frac{\partial\ln\gamma_{+-}}{\partial\ln m_+}\Big)\Big(1-\frac{d\ln c_0}{d\ln c_+}\Big)\nabla c_+ + \frac{\mathbf{i}t_-^0}{z_-F}\bigg) \\ &+\Big(\frac{z_+c_+}{z_-\mathscr{D}_{+-}}-\frac{c_0}{\mathscr{D}_{0+}}\Big)\bigg(-\frac{c_T\mathscr{D}_e}{c_0}\Big(1+\frac{\partial\ln\gamma_{+-}}{\partial\ln m_+}\Big)\Big(1-\frac{d\ln c_0}{d\ln c_+}\Big)\nabla c_+ + \frac{\mathbf{i}t_+^0}{z_+F}\bigg)\Bigg] \end{aligned} \tag{2.42}$$

Combine like terms for $\mathbf{i}$ and ∇c_+,

$$\begin{aligned} c_+\nabla\bar{\mu}_+ = \frac{RT}{c_T}\Bigg[&\bigg(\frac{c_+}{\mathscr{D}_{+-}}\frac{t_-^0}{z_-}+\Big(\frac{z_+c_+}{z_-\mathscr{D}_{+-}}-\frac{c_0}{\mathscr{D}_{0+}}\Big)\frac{t_+^0}{z_+}\bigg)\frac{\mathbf{i}}{F} \\ &+\bigg(\frac{z_+c_+}{z_-\mathscr{D}_{+-}}-\frac{z_+c_+}{z_-\mathscr{D}_{+-}}+\frac{c_0}{\mathscr{D}_{0+}}\bigg)\frac{c_T\mathscr{D}_e}{c_0c_+}\Big(1+\frac{\partial\ln\gamma_{+-}}{\partial\ln m_+}\Big)\Big(1-\frac{d\ln c_0}{d\ln c_+}\Big)\nabla c_+\Bigg] \end{aligned}$$

Dividing by c_+ and simplifying the two coefficient terms,

$$\nabla\bar{\mu}_+ = \frac{RT}{c_T}\Bigg[\bigg(\frac{1}{z_-\mathscr{D}_{+-}}-\frac{c_0t_+^0}{z_+c_+\mathscr{D}_{0+}}\bigg)\frac{\mathbf{i}}{F}+\frac{c_T\mathscr{D}_e}{c_+\mathscr{D}_{0+}}\Big(1+\frac{\partial\ln\gamma_{+-}}{\partial\ln m_+}\Big)\Big(1-\frac{d\ln c_0}{d\ln c_+}\Big)\nabla c_+\Bigg]$$

Then, applying electroneutrality, $z_+\nu_+ = -z_-\nu_-$, dividing by z_+F, and further simplifying,

$$\frac{1}{z_+F}\nabla\bar{\mu}_+ = \frac{RT}{c_Tz_-z_+F^2}\bigg(\frac{1}{\mathscr{D}_{+-}}+\frac{c_0t_+^0}{c_-\mathscr{D}_{0+}}\bigg)\mathbf{i}+\frac{RT\mathscr{D}_e}{z_+c_+F\mathscr{D}_{0+}}\Big(1+\frac{\partial\ln\gamma_{+-}}{\partial\ln m_+}\Big)\Big(1-\frac{d\ln c_0}{d\ln c_+}\Big)\nabla c_+$$

Applying equations (2.25) and (2.26), the ratio, $\mathscr{D}_e/z_+\mathscr{D}_{0+}$ in the last term can be manipulated as follows:

$$\frac{\mathscr{D}_e}{z_+\mathscr{D}_{0+}} = \frac{1}{z_+\mathscr{D}_{0+}}\frac{\mathscr{D}_{0+}\mathscr{D}_{0-}(z_- - z_+)}{z_-\mathscr{D}_{0-}-z_+\mathscr{D}_{0+}} = \frac{z_-\mathscr{D}_{0-}}{z_-\mathscr{D}_{0-}-z_+\mathscr{D}_{0+}}\bigg(\frac{1}{z_+}-\frac{1}{z_-}\bigg) = t_-^0\bigg(\frac{1}{z_+}-\frac{1}{z_-}\bigg)$$

Substituting in,

$$\begin{aligned} \frac{1}{z_+F}\nabla\bar{\mu}_+ =&\frac{RT}{c_Tz_-z_+F^2}\bigg(\frac{1}{\mathscr{D}_{+-}}+\frac{c_0t_+^0}{c_-\mathscr{D}_{0+}}\bigg)\mathbf{i} \\ &+\frac{RTt_-^0}{c_+F}\Big(\frac{1}{z_+}-\frac{1}{z_-}\Big)\Big(1+\frac{\partial\ln\gamma_{+-}}{\partial\ln m_+}\Big)\Big(1-\frac{d\ln c_0}{d\ln c_+}\Big)\nabla c_+ \end{aligned}$$

Finally, simplifying for the current, $\mathbf{i}$,

$$\begin{aligned} &\mathbf{i}\bigg[\frac{-RT}{c_Tz_-z_+F^2}\bigg(\frac{1}{\mathscr{D}_{+-}}+\frac{c_0t_+^0}{c_-\mathscr{D}_{0+}}\bigg)\bigg] \\ &=\bigg[-\frac{1}{z_+F}\nabla\bar{\mu}_+ + \frac{RTt_-^0}{c_+F}\Big(\frac{1}{z_+}-\frac{1}{z_-}\Big)\Big(1+\frac{\partial\ln\gamma_{+-}}{\partial\ln m_+}\Big)\Big(1-\frac{d\ln c_0}{d\ln c_+}\Big)\nabla c_+\bigg] \end{aligned} \tag{2.43}$$

A.6 Derivation between equations (2.46) and (2.47)

Regarding the derivation from Equation (2.46) to Equation (2.47):

$$\begin{aligned}\mathbf{i} =&\kappa\Bigg[-\frac{1}{z_+F}\nabla\big(\mu_+^{\ominus}+RT\ln\left(m_+\gamma_+\lambda_+^{\ominus}\right)+z_+F\phi_m\big)\\&+\frac{RTt_-^0}{c_+F}\Big(\frac{1}{z_+}-\frac{1}{z_-}\Big)\Big(1+\frac{\partial\ln\gamma_{+-}}{\partial\ln m_+}\Big)\Big(1-\frac{d\ln c_0}{d\ln c_+}\Big)\nabla c_+\Bigg]\end{aligned}\tag{2.46}$$

Bringing the gradients through the brackets and eliminating constant terms,

$$\mathbf{i}=\kappa\Bigg[-\nabla\phi_m-\frac{RT}{z_+F}\nabla\ln\left(m_+\gamma_+\right)+\frac{RTt_-^0}{c_+F}\Big(\frac{1}{z_+}-\frac{1}{z_-}\Big)\Big(1+\frac{\partial\ln\gamma_{+-}}{\partial\ln m_+}\Big)\Big(1-\frac{d\ln c_0}{d\ln c_+}\Big)\nabla c_+\Bigg]$$

Through the use of Equation (2.22) and (2.29), the concentration gradient term can be reverted to a previous form:

$$\mathbf{i}=\kappa\Bigg[-\nabla\phi_m-\frac{RT}{z_+F}\nabla\ln\left(m_+\gamma_+\right)+\frac{RTt_-^0}{F}\Big(\frac{1}{z_+}-\frac{1}{z_-}\Big)\nabla\ln\left(m_+\gamma_{+-}\right)\Bigg]$$

Then, recalling electroneutrality, $z_+\nu_+ + z_-\nu_- = 0$,

$$\mathbf{i}=\kappa\Bigg[-\nabla\phi_m-\frac{RT}{z_+F}\nabla\ln\left(m_+\gamma_+\right)+\frac{RTt_-^0}{z_+\nu_+F}(\nu_++\nu_-)\nabla\ln\left(m_+\gamma_{+-}\right)\Bigg]$$

Then, by Equation (2.20), the electrolyte activity coefficient can be split into cation and anion terms,

$$\mathbf{i}=\kappa\Bigg[-\nabla\phi_m-\frac{RT}{z_+F}\nabla\ln\left(m_+\gamma_+\right)+\frac{RTt_-^0}{z_+\nu_+F}\big(\nu_+\nabla\ln\left(m_+\gamma_+\right)+\nu_-\nabla\ln\left(m_+\gamma_-\right)\big)\Bigg]$$

Combining like terms,

$$\mathbf{i}=\kappa\Bigg[-\nabla\phi_m+\frac{RT}{F}\Bigg(\frac{t_-^0\nu_-}{z_+\nu_+}\nabla\ln\left(m_+\gamma_-\right)+\frac{(t_-^0-1)}{z_+}\nabla\ln\left(m_+\gamma_+\right)\Bigg)\Bigg]$$

By electroneutrality and the identity, $t_+^0 + t_-^0 = 1$,

$$\mathbf{i}=\kappa\Bigg[-\nabla\phi_m-\frac{RT}{F}\Bigg(\frac{t_-^0}{z_-}\nabla\ln\left(m_+\gamma_-\right)+\frac{t_+^0}{z_+}\nabla\ln\left(m_+\gamma_+\right)\Bigg)\Bigg]$$

Then, applying equations (2.22) and (2.29) again,

$$\begin{aligned}\mathbf{i}=\kappa\Bigg[-\nabla\phi_m-&\frac{RT}{c_+F}\Bigg(\frac{t_-^0}{z_-}\Big(1+\frac{\partial\ln\gamma_-}{\partial\ln m_+}\Big)+\frac{t_+^0}{z_+}\Big(1+\frac{\partial\ln\gamma_+}{\partial\ln m_+}\Big)\Bigg)\\&\Big(1-\frac{d\ln c_0}{d\ln c_+}\Big)\nabla c_+\Bigg]\end{aligned}\tag{2.47}$$

A.7 Derivation for Equilibrium Current Density

This appendix will outline the derivation form of the Butler-Volmer equation most often used in battery literature.

As discussed in Section 2.1.3.2, the general reaction being modelled is,

$$R^+ + e^- \leftrightharpoons P \tag{2.66}$$

where the reaction is taking place at a reference electrode with solid potential ϕ_R. When applying electrochemical equilibrium, results in,

$$\bar{\mu}_R + \bar{\mu}_{e^-} = \bar{\mu}_P$$

Recalling the electrochemical potential definition, i.e.,

$$\bar{\mu}_i = \mu_i^{\ominus} + RT \ln a_i + z_i F \phi_m \tag{2.13}$$

and applying it to each term in (2.66),

$$\left(\mu_R^{\ominus} + RT \ln a_R + F\phi_m\right) + \left(\mu_{e^-}^{\ominus} - F\phi_R\right) = \left(\mu_P^{\ominus} + RT \ln a_P\right) \tag{2.13}$$

where the activity of an electron is taken as 1. After cancelling terms and rearranging,

$$\phi_R = \phi_m + \frac{1}{F}\left(\mu_R^{\ominus} + \mu_{e^-}^{\ominus} - \mu_P^{\ominus} + RT \ln\left(\frac{a_R}{a_P}\right)\right)$$

The combination of reference potentials ($\mu_R^{\ominus}$, $\mu_{e^-}^{\ominus}$, and $\mu_P^{\ominus}$) describes the open-cell potential that develops between the electrolyte and the reference electrode. For a working electrode made of the same material as the reference electrode, this combination will be equivalent to $FE^{eq,\ominus}$.

$$\mu_R^{\ominus} + \mu_{e^-}^{\ominus} - \mu_P^{\ominus} = FE^{eq,\ominus}$$

Substituting ϕ_R into Equation (2.85) gives,

$$\mathbf{i} = \mathbf{n} i_{eq}\Bigg[\exp\left(-\frac{\alpha F}{RT}\left(\phi_s - \phi_m - E^{eq,\ominus} - \frac{RT}{F}\ln\left(\frac{a_R}{a_P}\right)\right)\right) - \exp\left(\frac{(1-\alpha)F}{RT}\left(\phi_s - \phi_m - E^{eq,\ominus} - \frac{RT}{F}\ln\left(\frac{a_R}{a_P}\right)\right)\right)\Bigg]$$

Then, splitting the exponential and cancelling it with the logarithm of the activity term, gives,

$$\mathbf{i} = \mathbf{n} i_{eq} \left[\left(\frac{a_R}{a_P} \right)^{\alpha} \exp\left(- \frac{\alpha F}{RT} \left(\phi_s - \phi_m - E^{eq,\ominus} \right) \right) - \left(\frac{a_R}{a_P} \right)^{(\alpha-1)} \exp\left(\frac{(1-\alpha)F}{RT} \left(\phi_s - \phi_m - E^{eq,\ominus} \right) \right) \right]$$

Recall the activity of each ionic species,

$$a_i = m_i \gamma_i \lambda_i^{\ominus} \tag{2.14}$$

which, when applying the definition of molality from Equation (2.29), becomes,

$$a_i = \frac{c_i \gamma_i \lambda_i^{\ominus}}{c_0 M_0}$$

Substituting in, the c_0 and M_0 will cancel, as will λ_i^{Θ}, as it is characteristic to the electrolyte as a whole and only a function of pressure and temperature, which are properties common to all species. Therefore,

$$\mathbf{i} = \mathbf{n} i_{eq} \left[\left(\frac{c_R \gamma_R}{c_P \gamma_P} \right)^{\alpha} \exp\left(- \frac{\alpha F}{RT} \left(\phi_s - \phi_m - E^{eq,\ominus} \right) \right) - \left(\frac{c_R \gamma_R}{c_P \gamma_P} \right)^{(\alpha-1)} \exp\left(\frac{(1-\alpha)F}{RT} \left(\phi_s - \phi_m - E^{eq,\ominus} \right) \right) \right]$$

Bazant discusses the application of the activity coefficients in the BV equations in ref [165]. In equation (12) he isolates a correction factor that accounts for the effects of concentrated solutions, i.e.,

$$\left(\frac{\gamma_R^{1-\alpha} \gamma_P^{\alpha}}{\gamma_{\ddagger}} \right)$$

where $\gamma_{\ddagger}$ is the activity coefficient of the transition state.

However, not only is the activity coefficient of the transition state difficult to obtain, but the correction factor has a minor effect on the resulting current and the work in references [7, 61, 118, 125] merely assumes linear activity, scaling with concentration, even for highly concentrated solutions. Therefore, the activity of each species will

instead be presented as a ratio of its concentration with its reference concentration, i.e.,

$$\mathbf{i} = \mathbf{n} i_{eq} \Bigg[\Big(\frac{c_R}{c_R^{ref}} \Big)^{\alpha} \Big(\frac{c_P}{c_P^{ref}} \Big)^{-\alpha} \exp\Bigg(- \frac{\alpha F}{RT} \big(\phi_s - \phi_m - E^{eq,ref} \big) \Bigg) - \Big(\frac{c_R}{c_R^{ref}} \Big)^{(\alpha-1)} \Big(\frac{c_P}{c_P^{ref}} \Big)^{(1-\alpha)} \exp\Bigg(\frac{(1-\alpha)F}{RT} \big(\phi_s - \phi_m - E^{eq,ref} \big) \Bigg) \Bigg]$$

Then, by pulling out common factors,

$$\mathbf{i} = \mathbf{n} i_{eq} \Big(\frac{c_P}{c_P^{ref}} \Big)^{-\alpha} \Big(\frac{c_R}{c_R^{ref}} \Big)^{(\alpha-1)} \Bigg[\Big(\frac{c_R}{c_R^{ref}} \Big) \exp\Bigg(- \frac{\alpha F}{RT} \big(\phi_s - \phi_m - E^{eq,ref} \big) \Bigg) - \Big(\frac{c_P}{c_P^{ref}} \Big) \exp\Bigg(\frac{(1-\alpha)F}{RT} \big(\phi_s - \phi_m - E^{eq,ref} \big) \Bigg) \Bigg]$$

This form of the BV equation is very similar to the form in Equation (2.79) except for the prefactor of exchange current density, i_{ref}, i.e.,

$$\mathbf{i} = \mathbf{n} i_{ref} \Bigg[\Big(\frac{c_R}{c_R^{ref}} \Big) \exp\Bigg(- \frac{\alpha F}{RT} (\phi_s - \phi_m - E^{eq,ref}) \Bigg) - \Big(\frac{c_P}{c_P^{ref}} \Big) \exp\Bigg(\frac{(1-\alpha)F}{RT} (\phi_s - \phi_m - E^{eq,ref}) \Bigg) \Bigg] \tag{2.79}$$

Setting the two prefactors equal gives,

$$i_{ref} = i_{eq} \Big(\frac{c_P}{c_P^{ref}} \Big)^{-\alpha} \Big(\frac{c_R}{c_R^{ref}} \Big)^{(\alpha-1)}$$

and then rearranging for i_{eq},

$$i_{eq} = i_{ref} \Big(\frac{c_P}{c_P^{ref}} \Big)^{\alpha} \Big(\frac{c_R}{c_R^{ref}} \Big)^{1-\alpha} \tag{2.82}$$

A.8 Derivation for U and U' relationship

Beginning with Equation (2.111), having substituted Equation (2.114) in for i_{eq},

$$S_{Li_{(s)}} = i_{ref,c} \frac{A_v}{F} \theta^{\alpha_c} (1-\theta)^{1-\alpha_c} \Big(\frac{c_{Li^+}}{c_{Li^+}^{ref}} \Big)^{1-\alpha_c} \Bigg[\exp\Bigg(- \frac{\alpha_c F}{RT} (\phi_s - \phi_R - U) \Bigg) - \exp\Bigg(\frac{(1-\alpha_c)F}{RT} (\phi_s - \phi_R - U) \Bigg) \Bigg]$$

Bringing the factors containing θ inside the brackets and removing a $(1-\theta)$ from the first term and a θ term from the second,

$$S_{Li_{(s)}} = i_{ref,c}\frac{A_v}{F}\left(\frac{c_{Li^+}}{c_{Li^+}^{ref}}\right)^{1-\alpha_c}\Bigg[(1-\theta)\big(\theta^{\alpha_c}(1-\theta)^{-\alpha_c}\big)\exp\left(-\frac{\alpha_c F}{RT}(\phi_s-\phi_R-U)\right) - \theta\big(\theta^{\alpha_c-1}(1-\theta)^{1-\alpha_c}\big)\exp\left(\frac{(1-\alpha_c)F}{RT}(\phi_s-\phi_R-U)\right)\Bigg]$$

Then, using the logarithm/exponential identities, the equation will becomes,

$$S_{Li_{(s)}} = i_{ref,c}\frac{A_v}{F}\left(\frac{c_{Li^+}}{c_{Li^+}^{ref}}\right)^{1-\alpha_c} \Bigg[(1-\theta)\exp\left(-\alpha_c\ln\left(\frac{1-\theta}{\theta}\right)\right)\exp\left(-\frac{\alpha_c F}{RT}(\phi_s-\phi_R-U)\right) - \theta\exp\left((1-\alpha_c)\ln\left(\frac{1-\theta}{\theta}\right)\right)\exp\left(\frac{(1-\alpha_c)F}{RT}(\phi_s-\phi_R-U)\right)\Bigg]$$

And finally, by combining the exponential terms,

$$S_{Li_{(s)}} = i_{ref,c}\frac{A_v}{F}\left(\frac{c_{Li^+}}{c_{Li^+}^{ref}}\right)^{1-\alpha_c} \Bigg[(1-\theta)\exp\left(-\frac{\alpha_c F}{RT}\left(\phi_s-\phi_R-U+\frac{RT}{F}\ln\left(\frac{1-\theta}{\theta}\right)\right)\right) - \theta\exp\left(\frac{(1-\alpha_c)F}{RT}\left(\phi_s-\phi_R-U+\frac{RT}{F}\ln\left(\frac{1-\theta}{\theta}\right)\right)\right)\Bigg]$$

Now, by comparing this with Equation (2.115), where i_{eq} is substituted by Equation (2.116), i.e.,

$$S_{Li_{(s)}} = i_{ref,c}\frac{A_v}{F}\left(\frac{c_{Li^+}}{c_{Li^+}^{ref}}\right)^{1-\alpha_c}\Bigg[(1-\theta)\exp\left(-\frac{\alpha_c F}{RT}(\phi_s-\phi_R-U')\right) - \theta\exp\left(\frac{(1-\alpha_c)F}{RT}(\phi_s-\phi_R-U')\right)\Bigg]$$

It becomes apparent this Equation (2.117) follows,

$$U' + \frac{RT}{F}\ln\left(\frac{1-\theta}{\theta}\right) = U \tag{2.117}$$

A.9 Derivation for Newton Linearization

For this derivation, the residual term, $R(\mathbf{u}^{(m)})$ is trivial. The complexity arises in the Jacobian term, $\delta R(\mathbf{u}^{(m)})$.

The Jacobian term is given by,

$$\begin{aligned}\delta R(\mathbf{u}^{(m)}) = \delta\Bigg[& \sum_{p=n-k+1}^{n+1} \frac{\boldsymbol{A}\alpha_p}{\tau}\mathbf{u}^{(p,m)} \\ & - \nabla\cdot\big(\boldsymbol{B}(\mathbf{u}^{(n+1,m)})\nabla\mathbf{u}^{(n+1,m)}\big) \\ & - \big(\mathbf{i}(\mathbf{u}^{(n+1,m)})\cdot\nabla t_+^0(\mathbf{u}^{(n+1,m)})\big)\mathbf{g} \\ & - \mathbf{f}(\mathbf{u}^{(n+1,m)})\Bigg]\end{aligned}$$

Because the variation is distributive, it can be applied to each term,

$$\begin{aligned}\delta R(\mathbf{u}^{(m)}) = & \delta\Bigg[\sum_{p=n-k+1}^{n+1} \frac{\boldsymbol{A}\alpha_p}{\tau}\mathbf{u}^{(p,m)}\Bigg] \\ & - \delta\Big[\nabla\cdot\big(\boldsymbol{B}(\mathbf{u}^{(n+1,m)})\nabla\mathbf{u}^{(n+1,m)}\big)\Big] \\ & - \delta\Big[\big(\mathbf{i}(\mathbf{u}^{(n+1,m)})\cdot\nabla t_+^0(\mathbf{u}^{(n+1,m)})\big)\mathbf{g}\Big] \\ & - \delta\mathbf{f}(\mathbf{u}^{(n+1,m)})\end{aligned}$$

Allowing the variation into each term by recognizing that it is associative and applying the product rule,

$$\begin{aligned}\delta R(\mathbf{u}^{(m)}) = & \sum_{p=n-k+1}^{n+1} \frac{\boldsymbol{A}\alpha_p}{\tau}\delta\mathbf{u} \\ & - \nabla\cdot\big(\delta\boldsymbol{B}(\mathbf{u}^{(n+1,m)})\nabla\mathbf{u}^{(n+1,m)} + \boldsymbol{B}(\mathbf{u}^{(n+1,m)})\nabla\delta\mathbf{u}\big) \\ & - \big(\delta\mathbf{i}(\mathbf{u}^{(n+1,m)})\cdot\nabla t_+^0(\mathbf{u}^{(n+1,m)}) + \mathbf{i}(\mathbf{u}^{(n+1,m)})\cdot\nabla\delta t_+^0(\mathbf{u}^{(n+1,m)})\big)\mathbf{g} \\ & - \delta\mathbf{f}(\mathbf{u}^{(n+1,m)})\end{aligned}$$

Then, applying the identity,

$$\delta f(u) = \frac{\partial f}{\partial u}\delta u$$

the Jacobian term becomes,

$$\begin{aligned}
\delta R(\mathbf{u}^{(m)}) = & \sum_{p=n-k+1}^{n+1} \frac{\boldsymbol{A}\alpha_p}{\tau}\delta\mathbf{u} \\
& - \nabla\cdot\left(\left.\frac{\partial \boldsymbol{B}(\mathbf{u})}{\partial u_k}\right|_{\mathbf{u}=\mathbf{u}^{(n+1,m)}} \delta u_k \nabla\mathbf{u}^{(n+1,m)} + \boldsymbol{B}(\mathbf{u}^{(n+1,m)})\nabla\delta\mathbf{u}\right) \\
& - \left(\left(\left.\frac{\partial \mathbf{i}(\mathbf{u})}{\partial u_k}\right|_{\mathbf{u}=\mathbf{u}^{(n+1,m)}} \delta u_k\right)\cdot\left(\left.\frac{\partial t_+^0(\mathbf{u})}{\partial u_l}\right|_{\mathbf{u}=\mathbf{u}^{(n+1,m)}} \nabla u_l\right)\right)\mathbf{g} \\
& - \left(\mathbf{i}(\mathbf{u}^{(n+1,m)})\cdot\nabla\left(\left.\frac{\partial t_+^0(\mathbf{u})}{\partial u_k}\right|_{\mathbf{u}=\mathbf{u}^{(n+1,m)}} \delta u_k\right)\right)\mathbf{g} \\
& - \left.\frac{\partial \mathbf{f}(\mathbf{u})}{\partial u_k}\right|_{\mathbf{u}=\mathbf{u}^{(n+1,m)}} \delta u_k
\end{aligned}$$

Then, applying the product rule for the gradient to the fourth term,

$$\begin{aligned}
\delta R(\mathbf{u}^{(m)}) = & \sum_{p=n-k+1}^{n+1} \frac{\boldsymbol{A}\alpha_p}{\tau}\delta\mathbf{u} \\
& - \nabla\cdot\left(\left.\frac{\partial \boldsymbol{B}(\mathbf{u})}{\partial u_k}\right|_{\mathbf{u}=\mathbf{u}^{(n+1,m)}} \delta u_k \nabla\mathbf{u}^{(n+1,m)} + \boldsymbol{B}(\mathbf{u}^{(n+1,m)})\nabla\delta\mathbf{u}\right) \\
& - \left(\left(\left.\frac{\partial \mathbf{i}(\mathbf{u})}{\partial u_k}\right|_{\mathbf{u}=\mathbf{u}^{(n+1,m)}} \delta u_k\right)\cdot\left(\left.\frac{\partial t_+^0(\mathbf{u})}{\partial u_l}\right|_{\mathbf{u}=\mathbf{u}^{(n+1,m)}} \nabla u_l\right)\right)\mathbf{g} \\
& - \left(\mathbf{i}(\mathbf{u}^{(n+1,m)})\cdot\left(\nabla\left.\frac{\partial t_+^0(\mathbf{u})}{\partial u_k}\right|_{\mathbf{u}=\mathbf{u}^{(n+1,m)}} \delta u_k + \left.\frac{\partial t_+^0(\mathbf{u})}{\partial u_k}\right|_{\mathbf{u}=\mathbf{u}^{(n+1,m)}} \nabla\delta u_k\right)\right)\mathbf{g} \\
& - \left.\frac{\partial \mathbf{f}(\mathbf{u})}{\partial u_k}\right|_{\mathbf{u}=\mathbf{u}^{(n+1,m)}} \delta u_k
\end{aligned}$$

Finally, by applying the chain rule again,

$$\begin{aligned}
\delta R(\mathbf{u}^{(m)}) = & \sum_{p=n-k+1}^{n+1} \frac{\boldsymbol{A}\alpha_p}{\tau}\delta\mathbf{u} \\
& - \nabla\cdot\left(\left.\frac{\partial \boldsymbol{B}(\mathbf{u})}{\partial u_k}\right|_{\mathbf{u}=\mathbf{u}^{(n+1,m)}} \delta u_k \nabla\mathbf{u}^{(n+1,m)} + \boldsymbol{B}(\mathbf{u}^{(n+1,m)})\nabla\delta\mathbf{u}\right) \\
& - \left(\left(\left.\frac{\partial \mathbf{i}(\mathbf{u})}{\partial u_k}\right|_{\mathbf{u}=\mathbf{u}^{(n+1,m)}} \delta u_k\right)\cdot\left(\left.\frac{\partial t_+^0(\mathbf{u})}{\partial u_l}\right|_{\mathbf{u}=\mathbf{u}^{(n+1,m)}} \nabla u_l\right)\right)\mathbf{g} \\
& - \left(\mathbf{i}(\mathbf{u}^{(n+1,m)})\cdot\left(\left.\frac{\partial^2 t_+^0(\mathbf{u})}{\partial u_k \partial u_l}\right|_{\mathbf{u}=\mathbf{u}^{(n+1,m)}} \delta u_k \nabla u_l^{(n+1,m)} + \left.\frac{\partial t_+^0(\mathbf{u})}{\partial u_k}\right|_{\mathbf{u}=\mathbf{u}^{(n+1,m)}} \nabla\delta u_k\right)\right)\mathbf{g} \\
& - \left.\frac{\partial \mathbf{f}(\mathbf{u})}{\partial u_k}\right|_{\mathbf{u}=\mathbf{u}^{(n+1,m)}} \delta u_k
\end{aligned}$$

Finally, cleaning up some terms,

$$\begin{aligned}
\delta R(\mathbf{u}^{(m)}) = & \sum_{p=n-k+1}^{n+1} \frac{\boldsymbol{A}\alpha_p}{\tau}\delta\mathbf{u} \\
& - \nabla\cdot\left(\boldsymbol{B}(\mathbf{u}^{(n+1,m)})\nabla\delta\mathbf{u}\right) \\
& - \nabla\cdot\left(\left.\frac{\partial\boldsymbol{B}(\mathbf{u})}{\partial u_k}\right|_{\mathbf{u}=\mathbf{u}^{(n+1,m)}}\delta u_k\nabla\mathbf{u}^{(n+1,m)}\right) \\
& - \left(\left(\left.\frac{\partial\mathbf{i}(\mathbf{u})}{\partial u_k}\right|_{\mathbf{u}=\mathbf{u}^{(n+1,m)}}\delta u_k\right)\cdot\left(\left.\frac{\partial t_+^0(\mathbf{u})}{\partial u_l}\right|_{\mathbf{u}=\mathbf{u}^{(n+1,m)}}\nabla u_l\right)\right)\mathbf{g} \\
& - \left(\mathbf{i}(\mathbf{u}^{(n+1,m)})\cdot\left(\left.\frac{\partial t_+^0(\mathbf{u})}{\partial u_k}\right|_{\mathbf{u}=\mathbf{u}^{(n+1,m)}}\nabla\delta u_k\right)\right)\mathbf{g} \\
& - \left(\mathbf{i}(\mathbf{u}^{(n+1,m)})\cdot\left(\left.\frac{\partial^2 t_+^0(\mathbf{u})}{\partial u_k\partial u_l}\right|_{\mathbf{u}=\mathbf{u}^{(n+1,m)}}\delta u_k\nabla u_l^{(n+1,m)}\right)\right)\mathbf{g} \\
& - \left.\frac{\partial\mathbf{f}(\mathbf{u})}{\partial u_k}\right|_{\mathbf{u}=\mathbf{u}^{(n+1,m)}}\delta u_k
\end{aligned}$$

This can then be inserted as the $\delta R(\mathbf{u}^{(m)})$ term in Equation (2.135) to receive Equation (2.136).

A.10 Derivation for Spatial Discretization

This appendix section will outline the process in which the discretized weak form of the system of governing equations was obtained. Note this is general enough to encompass either system outlined in section 2. Beginning with the weak form of the equations, i.e., Equation (2.139), the test functions, as outlined in Equation (2.140), will be implemented. The summations have been dropped and the indices are pre-

sented as a superscript, i.e.,

$$
\begin{aligned}
&\int_\Omega \bar{v}^i\psi^i \frac{\boldsymbol{A}\alpha_{n+1}}{\tau}\delta\bar{\mathbf{u}}^j\psi^j d\Omega \\
&+ \int_\Omega \big(\nabla(\bar{v}^i\psi^i)\big)\cdot\big(\boldsymbol{B}(\mathbf{u}^{(n+1,m)})\nabla(\delta\bar{\mathbf{u}}^j\psi^j)\big)d\Omega \\
&+ \int_\Omega \big(\nabla(\bar{v}^i\psi^i)\big)\cdot\left(\left.\frac{\partial\boldsymbol{B}(\mathbf{u})}{\partial u_k}\right|_{\mathbf{u}=\mathbf{u}^{(n+1,m)}}\delta\bar{u}_k^j\psi^j\nabla\mathbf{u}^{(n+1,m)}\right)d\Omega \\
&- \int_\Omega \bar{v}^i\psi^i\left(\left(\left.\frac{\partial\mathbf{i}(\mathbf{u})}{\partial u_k}\right|_{\mathbf{u}=\mathbf{u}^{(n+1,m)}}\delta\bar{u}_k^j\psi^j\right)\cdot\left(\left.\frac{\partial t_+^0(\mathbf{u})}{\partial u_l}\right|_{\mathbf{u}=\mathbf{u}^{(n+1,m)}}\nabla u_l\right)\right)\mathbf{g}d\Omega \\
&- \int_\Omega \bar{v}^i\psi^i\left(\mathbf{i}(\mathbf{u}^{(n+1,m)})\cdot\left(\left.\frac{\partial t_+^0(\mathbf{u})}{\partial u_k}\right|_{\mathbf{u}=\mathbf{u}^{(n+1,m)}}\nabla(\delta\bar{u}_k^j\psi^j)\right)\right)\mathbf{g}d\Omega \\
&- \int_\Omega \bar{v}^i\psi^i\left(\mathbf{i}(\mathbf{u}^{(n+1,m)})\cdot\left(\left.\frac{\partial^2 t_+^0(\mathbf{u})}{\partial u_k\partial u_l}\right|_{\mathbf{u}=\mathbf{u}^{(n+1,m)}}\delta\bar{u}_k^j\psi^j\nabla u_l^{(n+1,m)}\right)\right)\mathbf{g}d\Omega \\
&- \int_\Omega \bar{v}^i\psi^i\left.\frac{\partial\mathbf{f}(\mathbf{u})}{\partial u_k}\right|_{u=u^{(n+1,m)}}\delta\bar{u}_k^j\psi^j d\Omega \\
&= -\int_\Omega \bar{v}^i\psi^i\sum_{p=n-k+1}^{n+1}\frac{\boldsymbol{A}\alpha_p}{\tau}\mathbf{u}^{(p,m)}d\Omega \\
&- \int_\Omega \big(\nabla(\bar{v}^i\psi^j)\big)\cdot\big(\boldsymbol{B}(\mathbf{u}^{(n+1,m)})\nabla\mathbf{u}^{(n+1,m)}\big)d\Omega \\
&+ \int_\Omega \bar{v}^i\psi^i\left(\mathbf{i}(\mathbf{u}^{(n+1,m)})\cdot\left(\left.\frac{\partial t_+^0(\mathbf{u})}{\partial u_k}\right|_{\mathbf{u}=\mathbf{u}^{(n+1,m)}}\nabla u_k^{(n+1,m)}\right)\right)\mathbf{g}d\Omega \\
&+ \int_\Omega \bar{v}^i\psi^i\mathbf{f}(\mathbf{u}^{(n+1,m)})d\Omega
\end{aligned}
$$

The equation vector is now going to be opened up using index notation. The indices are denoted as subscripts to distinguish them from the DOF indices in the superscript. It is important to realize that these dimensions are independent from each other can therefore vectors and tensors will operate as a scalar when manipulating the other index (e.g., spatial gradients acting upon the shape functions should not be applied

to $\boldsymbol{A}$ or $\boldsymbol{B}$). The equaton is therefore now,

$$
\begin{aligned}
&\int_\Omega \bar{v}^i\psi^i \frac{A_{ab}\alpha_{n+1}}{\tau}\delta\bar{u}_b^j\psi^j d\Omega \\
&+ \int_\Omega \big(\nabla(\bar{v}^i\psi^i)\big)\cdot\big(B_{ab}(\mathbf{u}^{(n+1,m)})\nabla(\delta\bar{u}_b^j\psi^j)\big)d\Omega \\
&+ \int_\Omega \big(\nabla(\bar{v}^i\psi^i)\big)\cdot\left(\left.\frac{\partial B_{ab}(\mathbf{u})}{\partial u_k}\right|_{\mathbf{u}=\mathbf{u}^{(n+1,m)}}\delta\bar{u}_k^j\psi^j\nabla u_b^{(n+1,m)}\right)d\Omega \\
&- \int_\Omega \bar{v}^i\psi^i\left(\left(\left.\frac{\partial \mathbf{i}(\mathbf{u})}{\partial u_k}\right|_{\mathbf{u}=\mathbf{u}^{(n+1,m)}}\delta\bar{u}_k^j\psi^j\right)\cdot\left(\left.\frac{\partial t_+^0(\mathbf{u})}{\partial u_l}\right|_{\mathbf{u}=\mathbf{u}^{(n+1,m)}}\nabla u_l\right)\right)g_a d\Omega \\
&- \int_\Omega \bar{v}^i\psi^i\left(\mathbf{i}(\mathbf{u}^{(n+1,m)})\cdot\left(\left.\frac{\partial t_+^0(\mathbf{u})}{\partial u_k}\right|_{\mathbf{u}=\mathbf{u}^{(n+1,m)}}\nabla(\delta\bar{u}_k^j\psi^j)\right)\right)g_a d\Omega \\
&- \int_\Omega \bar{v}^i\psi^i\left(\mathbf{i}(\mathbf{u}^{(n+1,m)})\cdot\left(\left.\frac{\partial^2 t_+^0(\mathbf{u})}{\partial u_k\partial u_l}\right|_{\mathbf{u}=\mathbf{u}^{(n+1,m)}}\delta\bar{u}_k^j\psi^j\nabla u_l^{(n+1,m)}\right)\right)g_a d\Omega \\
&- \int_\Omega \bar{v}^i\psi^i\left.\frac{\partial f_a(\mathbf{u})}{\partial u_k}\right|_{u=u^{(n+1,m)}}\delta\bar{u}_k^j\psi^j d\Omega \\
&= -\int_\Omega \bar{v}^i\psi^i\sum_{p=n-k+1}^{n+1}\frac{A_{ab}\alpha_p}{\tau}u_b^{(p,m)}d\Omega \\
&- \int_\Omega \big(\nabla(\bar{v}^i\psi^j)\big)\cdot\big(B_{ab}(\mathbf{u}^{(n+1,m)})\nabla u_b^{(n+1,m)}\big)d\Omega \\
&+ \int_\Omega \bar{v}^i\psi^i\left(\mathbf{i}(\mathbf{u}^{(n+1,m)})\cdot\left(\left.\frac{\partial t_+^0(\mathbf{u})}{\partial u_k}\right|_{\mathbf{u}=\mathbf{u}^{(n+1,m)}}\nabla u_k^{(n+1,m)}\right)\right)g_a d\Omega \\
&+ \int_\Omega \bar{v}^i\psi^i f_a(\mathbf{u}^{(n+1,m)})d\Omega
\end{aligned}
$$

The test function and variation coefficients, $\bar{v}^i$ and $\delta\bar{\mathbf{u}}^j$, are constant and can therefore be brought out from the gradient terms. Also, v is common to all terms and will therefore be divided out of the equation all together. Finally, rearranging terms

slightly for readability, the discretized form becomes,

$$
\begin{aligned}
&\int_{\hat{\Omega}} \frac{A_{ac}\alpha_{n+1}}{\tau}\psi^i\psi^j\delta\bar{u}_c^j d\hat{\Omega} \\
&+ \int_{\hat{\Omega}} B_{ac}(\mathbf{u}^{(n+1,m)})\big(\nabla\psi^i\cdot\nabla\psi^j\big)\delta\bar{u}_c^j d\hat{\Omega} \\
&+ \int_{\hat{\Omega}} \left(\left.\frac{\partial B_{ab}(\mathbf{u})}{\partial u_k}\right|_{\mathbf{u}=\mathbf{u}^{(n+1,m)}}\right)\big(\nabla\psi^i\cdot\nabla u_b^{(n+1,m)}\big)\psi^j\delta\bar{u}_k^j d\hat{\Omega} \\
&- \int_{\hat{\Omega}} \left(\left.\frac{\partial t_+^0(\mathbf{u})}{\partial u_l}\right|_{\mathbf{u}=\mathbf{u}^{(n+1,m)}}\right)\left(\left(\left.\frac{\partial \mathbf{i}(\mathbf{u})}{\partial u_k}\right|_{\mathbf{u}=\mathbf{u}^{(n+1,m)}}\right)\cdot\nabla u_l\right) g_a\psi^i\psi^j\delta\bar{u}_k^j d\hat{\Omega} \\
&- \int_{\hat{\Omega}} \left(\left.\frac{\partial t_+^0(\mathbf{u})}{\partial u_k}\right|_{\mathbf{u}=\mathbf{u}^{(n+1,m)}}\right)\Big(\mathbf{i}(\mathbf{u}^{(n+1,m)})\cdot\nabla\psi^j\Big) g_a\psi^i\delta\bar{u}_k^j d\hat{\Omega} \\
&- \int_{\hat{\Omega}} \left(\left.\frac{\partial^2 t_+^0(\mathbf{u})}{\partial u_k\partial u_l}\right|_{\mathbf{u}=\mathbf{u}^{(n+1,m)}}\right)\Big(\mathbf{i}(\mathbf{u}^{(n+1,m)})\cdot\nabla u_l^{(n+1,m)}\Big) g_a\psi^i\psi^j\delta\bar{u}_k^j d\hat{\Omega} \\
&- \int_{\hat{\Omega}} \left(\left.\frac{\partial f_a(\mathbf{u})}{\partial u_k}\right|_{u=u^{(n+1,m)}}\right)\psi^i\psi^j\delta\bar{u}_k^j d\hat{\Omega} \\
&= -\int_{\hat{\Omega}} \sum_{p=n-k+1}^{n+1} \frac{A_{ab}\alpha_p}{\tau} u_b^{(p,m)}\psi^i d\hat{\Omega} \\
&- \int_{\hat{\Omega}} B_{ab}(\mathbf{u}^{(n+1,m)})\big(\nabla\psi^j\cdot\nabla u_b^{(n+1,m)}\big) d\hat{\Omega} \\
&+ \int_{\hat{\Omega}} \left(\left.\frac{\partial t_+^0(\mathbf{u})}{\partial u_k}\right|_{\mathbf{u}=\mathbf{u}^{(n+1,m)}}\right)\Big(\mathbf{i}(\mathbf{u}^{(n+1,m)})\cdot\nabla u_k^{(n+1,m)}\Big) g_a\psi^i d\hat{\Omega} \\
&+ \int_{\hat{\Omega}} f_a(\mathbf{u}^{(n+1,m)})\psi^i d\hat{\Omega}
\end{aligned}
$$

Finally, the variation is pulled out of the RHS, thus creating a new free variable and turning the bracketed term into a matrix. Each term within this matrix is the

corresponding variational contribution to the Jacobian matrix.

$$
\begin{aligned}
&\Bigg[\int_{\hat{\Omega}} \frac{A_{ac}\alpha_{n+1}}{\tau}\psi^i\psi^j d\hat{\Omega} \\
&+ \int_{\hat{\Omega}} B_{ac}(\mathbf{u}^{(n+1,m)})\big(\nabla\psi^i\cdot\nabla\psi^j\big)d\hat{\Omega} \\
&+ \int_{\hat{\Omega}} \left(\frac{\partial B_{ab}(\mathbf{u})}{\partial u_k}\bigg|_{\mathbf{u}=\mathbf{u}^{(n+1,m)}}\delta_{kc}\right)\big(\nabla\psi^i\cdot\nabla u_b^{(n+1,m)}\big)\psi^j d\hat{\Omega} \\
&- \int_{\hat{\Omega}} \left(\frac{\partial t_+^0(\mathbf{u})}{\partial u_l}\bigg|_{\mathbf{u}=\mathbf{u}^{(n+1,m)}}\right)\left(\left(\frac{\partial \mathbf{i}(\mathbf{u})}{\partial u_k}\bigg|_{\mathbf{u}=\mathbf{u}^{(n+1,m)}}\delta_{kc}\right)\cdot\nabla u_l\right) g_a\psi^i\psi^j d\hat{\Omega} \\
&- \int_{\hat{\Omega}} \left(\frac{\partial t_+^0(\mathbf{u})}{\partial u_k}\bigg|_{\mathbf{u}=\mathbf{u}^{(n+1,m)}}\delta_{kc}\right)\Big(\mathbf{i}(\mathbf{u}^{(n+1,m)})\cdot\nabla\psi^j\Big) g_a\psi^i d\hat{\Omega} \\
&- \int_{\hat{\Omega}} \left(\frac{\partial^2 t_+^0(\mathbf{u})}{\partial u_k\partial u_l}\bigg|_{\mathbf{u}=\mathbf{u}^{(n+1,m)}}\delta_{kc}\right)\Big(\mathbf{i}(\mathbf{u}^{(n+1,m)})\cdot\nabla u_l^{(n+1,m)}\Big) g_a\psi^i\psi^j d\hat{\Omega} \\
&- \int_{\hat{\Omega}} \left(\frac{\partial f_a(\mathbf{u})}{\partial u_k}\bigg|_{u=u^{(n+1,m)}}\delta_{kc}\right)\psi^i\psi^j d\hat{\Omega}\Bigg]\delta\bar{u}_c^j \\
&= -\int_{\hat{\Omega}} \sum_{p=n-k+1}^{n+1} \frac{A_{ab}\alpha_p}{\tau}u_b^{(p,m)}\psi^i d\hat{\Omega} \\
&- \int_{\hat{\Omega}} B_{ab}(\mathbf{u}^{(n+1,m)})\big(\nabla\psi^j\cdot\nabla u_b^{(n+1,m)}\big)d\hat{\Omega} \\
&+ \int_{\hat{\Omega}} \left(\frac{\partial t_+^0(\mathbf{u})}{\partial u_k}\bigg|_{\mathbf{u}=\mathbf{u}^{(n+1,m)}}\right)\Big(\mathbf{i}(\mathbf{u}^{(n+1,m)})\cdot\nabla u_k^{(n+1,m)}\Big) g_a\psi^i d\hat{\Omega} \\
&+ \int_{\hat{\Omega}} f_a(\mathbf{u}^{(n+1,m)})\psi^i d\hat{\Omega}
\end{aligned}
$$

This equation could be recommitted to tensor notation with the use of the Kronecker product (second order tensor product), $\otimes$, to create a fourth order RHS matrix [167]. However, this can be very confusing as it is not clear which dimension is being operated on.

Appendix B: OpenFCST PRM Files

B.1 app_lib_electrolyte main and data PRM Files

Listing B.1: `main.prm`

```
#####################################################################
#   $Id: $
#
#  This file is used to simulate app_lib_electrolyte
#  and obtain the voltage required to sustain a given
#  current passing though.
#
#  Copyright (C) 2022 by Marc Secanell and Cameron Fenske
#
#####################################################################

subsection Simulator

 set simulator name = app_lib_electrolyte
 set simulator parameter file name = data.prm
 set nonlinear solver name = None
 set transient solver name = BDF
 set Analysis type = Analysis

end
```

Listing B.2: `data.prm`

```
#############################################################################
#   $Id: $
#
#  This file is used to simulate app_lib_electrolyte
#  and obtain the voltage required to sustain a given
#  current passing though.
#
#  Copyright (C) 2022 by Marc Secanell and Cameron Fenske
#
#############################################################################

#############################################################################
subsection Grid generation
 set Type of mesh = GridExternal
 set File name = ../analysis/Mesh.msh
 set File type = msh
 set Initial refinement = 0
 set Planar electrode width = 0.0001
end
#############################################################################

#############################################################################
subsection Discretization
 set Boundary fluxes = true
end
#############################################################################

#############################################################################
subsection Initial Solution
 set Initial solution output filename = Step00000
 set Output initial solution          = false
end
#############################################################################

#############################################################################
subsection Adaptive refinement
 set Number of Refinements = 1
 set Refinement            = adaptive  #global | adaptive
 set Output initial mesh     = false
 set Output final solution   = true
 set Output intermediate solutions = true
end
#############################################################################
```

```
#############################################################################
subsection Output
 subsection Data
  set Print solution = true
  set Print only the last time layer data = true
 end
end
#############################################################################

#############################################################################
subsection Output Variables
 set Compute boundary responses = true
 set num_output_vars = 1
 set Output boundary id = 6
end
#############################################################################

#############################################################################
subsection Fuel cell data
 subsection Lithium Ion Separator Layer
  set Material id = 1
  set Lib layer type = LibSeparator
  set Porosity = 0.55
 end
 subsection Operating conditions
  subsection Steady-state conditions
   set Temperature cell [K] = 363
  end
 end
end
#############################################################################

#############################################################################
subsection Materials
 set Electrolyte Chemistry = LiTFSI_PEO
end
#############################################################################

#############################################################################
subsection Equations

 subsection Lithium Ion Diffusion Equation

  subsection Initial data
```

```
    set lithium_ion_concentration = 1:2.76
   end

   subsection Boundary data
    set lithium_ion_concentration =
    set Constant Lithium Ion Flux Boundary Conditions
                                        = 5: 0.0
    set BV Reaction Boundary Conditions (Current)
                                        = 6: 0.0002, 7: -0.0002
    set BV Reaction Boundary Conditions (Voltage) =
   end

  end

  subsection Lithium Charge Transport Equation

   subsection Initial data
    set lithium_electronic_potential = 1:0.0
   end

   subsection Boundary data
    set lithium_electronic_potential =
    set Constant Current Boundary Conditions = 5:0.0
    set BV Reaction Boundary Conditions (Current)
                                        = 6: 0.0002
    set BV Reaction Boundary Conditions (Voltage)
                                        = 7: 0.0
   end

  end

end
##########################################################################

##########################################################################
subsection Newton
 set Max steps          = 100
 set Tolerance          = 1.e-8
 set Debug level        = 5
end
##########################################################################

##########################################################################
subsection Transient
 set Adaptive time stepping algorithm = None
```

```
  set Total time of simulation, [s] = 900
  set Initial time step, [s] = 1
  set Create detailed simulation report = true
end
################################################################################
```

B.2 app_lib_macro_scale main and data PRM Files

Listing B.3: `main.prm`

```
#####################################################################
#
#   This file is used to simulate app_lib_macro_scale.
#
#   This application runs the macro-scale Lithium-ion
#   battery model. It couples charge and mass transport
#   in a separator and porous cathode, along with the
#   reactions between them, using BV kinetics.
#
#
#   Copyright (C) 2022 by Marc Secanell and Cameron Fenske
#
#####################################################################

subsection Simulator
 set simulator name = app_lib_macro_scale
 set simulator parameter file name = data.prm
 set nonlinear solver name = Newton3pp
 set transient solver name = BDF
 set Analysis type = Analysis
end
```

Listing B.4: `data.prm`

```
#############################################################################
#   $Id: $
#
#   This file is used to simulate app_lib_macro_scale.
#   This file will be called by the main.prm file.
#
#   Copyright (C) 2022 by Marc Secanell and Cameron Fenske
#
#############################################################################

#############################################################################
subsection Grid generation
 set Type of mesh = GridExternal
 set File name = ../analysis/MacroScaleMesh.msh
 set File type = msh
 set Initial refinement = 0
 set Planar electrode width = 0.000005
end
#############################################################################

#############################################################################
subsection Initial Solution
 set Read in initial solution from file = false
 set Output initial solution = false
 set Output solution for transfer = false
 set Initial solution output filename = Step00000
end
#############################################################################

#############################################################################
subsection Adaptive refinement
 set Refinement = global
 set Number of Refinements = 1
 set Output initial mesh = false
 set Output intermediate solutions = false
 set Output final solution = true
 set Output intermediate responses = false
 set Use nonlinear solver for linear problem = false
end
#############################################################################

#############################################################################
subsection System management
```

```
 set Number of solution variables = 4

 subsection Solution variables
  set Solution variable 1 = solid_lithium_concentration
  set Solution variable 2 = electronic_electrical_potential
  set Solution variable 3 = lithium_ion_concentration
  set Solution variable 4 = lithium_electronic_potential
 end

 subsection Equations
  set Equation 1 = Ficks Transport Equation - solid_lithium
  set Equation 2 = Electron Transport Equation
  set Equation 3 = Lithium Ion Diffusion Equation
  set Equation 4 = Lithium Charge Transport Equation
 end

end
#############################################################################

#############################################################################
subsection Fuel cell data
 subsection Operating conditions
  subsection Steady-state conditions
   set Temperature cell [K] = 363.0
  end
 end
 subsection Lithium Ion Separator Layer
  set Material id = 1
  set Lib layer type = LibSeparator
  set Porosity = 0.55
 end
 subsection Lithium Ion Porous Cathode Layer
  set Material id = 2
  set Porous Electrode layer type = HomogeneousElectrode
  set Porosity = 0.37
 end
 subsection Cathodic Current Collector Layer
  set Material id = 3
  set Solid material type = Steel_4340
 end
end
#############################################################################

#############################################################################
```

```
subsection Materials
 set Electrolyte Chemistry = LiTFSI_PEO
end
#####################################################################

#####################################################################
subsection Equations

 subsection Ficks Transport Equation - solid_lithium
  subsection Initial data
    set solid_lithium_concentration = 1: 0.0, 2:1.0
  end
  subsection Boundary data
   set solid_lithium_concentration = 6:0.0
   set species_flux = 5:0.0, 7:0
  end
 end

 subsection Electron Transport Equation
  subsection Initial data
   set electronic_electrical_potential = 1: 0.0, 2:0.0
  end
  subsection Boundary data
   set electronic_electrical_potential = 7:0.0
   set current_flux = 5:0.0, 6:0
  end
 end

 subsection Lithium Ion Diffusion Equation
  subsection Initial data
   set lithium_ion_concentration = 1: 1.0, 2:1.0
  end
  subsection Boundary data
   set lithium_ion_concentration =
   set Constant Lithium Ion Flux Boundary Conditions = 5:0, 7:0
   set BV Reaction Boundary Conditions (Current) = 6:0.002
   set BV Reaction Boundary Conditions (Voltage) =
  end
 end

 subsection Lithium Charge Transport Equation
  subsection Initial data
   set lithium_electronic_potential = 1: -4.3, 2:-4.3
  end
  subsection Boundary data
```

```
    set lithium_electronic_potential =
    set Constant Current Boundary Conditions = 5:0.0, 7:0
    set BV Reaction Boundary Conditions (Current) = 6:0.002
    set BV Reaction Boundary Conditions (Voltage) =
   end
  end

end
##########################################################################

##########################################################################
subsection Discretization
 set Boundary fluxes = true
 set Element = FESystem[FE_Q(1)^4]
 subsection Matrix
  set Quadrature cell = -1
  set Quadrature face = -1
 end
 subsection Residual
  set Quadrature cell = -1
  set Quadrature face = -1
 end
end
##########################################################################

##########################################################################
subsection Output Variables
 set Compute boundary responses = true
 set num_output_vars = 1
 set Output boundary id = 6
 set Output_var_0 = solid_electrode_potential
end
##########################################################################

##########################################################################
subsection Output
 subsection Data
  set Output format = vtk
  set Print solution = true
  set Print only the last time layer data = true
 end
 subsection Grid
  set Format = eps
 end
end
```

```
#############################################################################


#############################################################################
subsection Transient
  set Adaptive time stepping algorithm  = None
  set Total time of simulation, [s] = 400
  set Initial time step, [s] = 0.01
  set Create detailed simulation report = true
end
#############################################################################

#############################################################################
subsection Newton
  set Max steps = 100
  set Tolerance = 1.e-8
  set Debug level = 5
end
#############################################################################
```